UNIVERSIDAD AUTONOMA
DE MADRID

FACULTAD DE CIENCIAS
Dpto. de FÍSICA DE MATERIALES

EFECTOS ISOTÓPICOS EN LOS PROCESOS DE PRODUCCIÓN Y ALMACENAMIENTO DE HIDRÓGENO

Memoria presentada por

FABRICE LEARDINI

para optar al grado de Doctor en Ciencias Físicas
por la Universidad Autónoma de Madrid

UNIVERSIDAD AUTÓNOMA DE MADRID

FACULTAD DE CIENCIAS
DEPARTAMENTO DE FÍSICA DE MATERIALES

EFECTOS ISOTÓPICOS EN LOS PROCESOS DE PRODUCCIÓN Y ALMACENAMIENTO DE HIDRÓGENO

Memoria presentada por
Fabrice Leardini
para optar al grado de Doctor en Ciencias Físicas

Director: Carlos Sánchez López

Madrid, Mayo de 2007

La Primavera
Celia y Antonio Juárez Leardini

Para ser original hay que volver a los orígenes
Antonio Gaudí

Indice

Capítulo 1

Introducción

1.1 El hidrógeno como vector energético

Actualmente la ciencia se desarrolla en gran medida en las interfases entre las distintas áreas de conocimiento. Tal es el caso del hidrógeno, concebido desde el punto de vista de su uso como vector energético. En este campo confluyen la Química y la Física, ambas, a su vez, desde múltiples puntos de vista.

El enlace químico de la molécula de H_2 constituye una forma localizada de energía que podemos transportar y almacenar. Por ello, el hidrógeno se perfila como un firme candidato para sustituir a los combustibles fósiles. Sin embargo, a diferencia de éstos, no existen yacimientos de hidrógeno molecular en nuestro planeta, ni está presente en nuestra atmósfera, debido a que la velocidad media de la molécula de H_2 es superior a la velocidad de escape del campo gravitatorio terrestre. De acuerdo con esta afirmación, el hidrógeno no ha de ser considerado como una fuente de energía, sino como un vector energético, un combustible que ha de ser creado a partir de las fuentes primarias de energía.

La posible utilización de hidrógeno como vector energético pasa actualmente por la investigación en tres aspectos fundamentales, que abarcan campos como la termodinámica, la física de materiales, la física de superficies, la catálisis química o la electroquímica:

i) producción de H_2
ii) transporte y acumulación de H_2
iii) obtención de energía útil a partir de H_2

En estos campos, existen numerosas vías de investigación abiertas en todo el mundo, y tanto la UE, como EEUU y Japón, cuentan con programas específicos para desarrollar el uso del H_2 como combustible.

1.1.1 Producción de hidrógeno

La producción de hidrógeno exige transformar la energía primaria en energía química, esto es, crear los enlaces H-H a partir de una materia prima que contenga hidrógeno usando energía luminosa, térmica o eléctrica.

En la actualidad se utilizan, básicamente, dos procesos de producción de hidrógeno a nivel industrial: a partir de combustibles fósiles (reformado de gas natural, oxidación parcial de hidrocarburos y gasificación del carbón) y mediante la electrolisis de agua. Anualmente se producen más de 50 millones de toneladas de hidrógeno en el mundo, el 96% de las cuales procede de los combustibles fósiles (48% del gas natural, 30% de hidrocarburos y 18% del carbón) y sólo el 4% provienen de la electrolisis de agua [1.1].

Desde un punto de vista ambiental, la forma más adecuada de obtener H_2 es mediante la descomposición de agua, realizada con energía eléctrica (electrolisis) o luminosa (fotolisis) procedentes de las fuentes de energía renovables. Sin embargo, la eficiencia energética de estos procesos es aún modesta, lo que hace que sea necesario desarrollar electro- y fotocatalizadores con mejores rendimientos.

1.1.2 Transporte y almacenamiento de hidrógeno

El transporte de hidrógeno para usos industriales se lleva a cabo mediante redes de tuberías y canalizaciones tendidas desde los centros de producción hasta los usuarios de grandes consumos (generalmente cercanos). Para los pequeños usuarios el hidrógeno se distribuye en contenedores a presión entre 200 y 350 bares. Por tanto, la tecnología necesaria para la distribución del H_2 no difiere sustancialmente de la utilizada actualmente para el transporte del gas natural o el petróleo.

En lo que se refiere al almacenamiento de H_2, sin embargo, nos encontramos ante uno de los retos más importantes que debemos hacer frente para conseguir implantar el uso del H_2 como combustible. La forma habitual de almacenamiento de H_2 es comprimir el gas y confinarlo a presiones entre 350 y 700 bares en depósitos protegidos. Otra alternativa para el almacenamiento de H_2 utilizada a escala industrial es la licuefacción, para la que se requieren tecnologías criogénicas (temperaturas por debajo de 20 K a 1 bar de presión). Sin embargo, de los métodos de almacenamiento conocidos, el más prometedor para las aplicaciones parece ser la acumulación en metales, formando compuestos conocidos como hidruros de metal [1.2]. Dentro de este campo, es necesario profundizar en el conocimiento de las reacciones de formación/descomposición de estos compuestos, con objeto de desarrollar acumuladores de H_2 con las características necesarias para su implantación. Por otro lado, la acumulación de hidrógeno en metales tiene un gran interés en la actualidad, debido a su uso como electrodos en baterías de tipo Ni/MH [1.3-5].

1.1.3 Obtención de energía útil a partir de H_2

El hidrógeno puede producir energía útil por combustión convencional, en un motor de combustión interna en la que se obtiene energía mecánica, o mediante la utilización de pilas de combustible, en las que se obtiene directamente energía eléctrica. En ambos casos, el producto de la combustión es esencialmente agua y dependerá de la pureza de los gases de partida (hidrógeno y oxígeno) el que se produzcan o no otros derivados como NO_x.

Las pilas de combustible son dispositivos electroquímicos formados por dos electrodos metálicos y un electrolito. En estos dispositivos, la molécula que se oxida se consume por lo que debe ser suministrada de forma continua (de ahí su nombre). Las pilas de combustible alimentadas por hidrógeno funcionan de forma que el H_2 (combustible) se oxida en el ánodo y el O_2 del aire se reduce en el cátodo. Se trata, por tanto, de un dispositivo de conversión directa de energía química en energía eléctrica.

1.2 Efectos isotópicos entre hidrógeno y deuterio

Un enfoque muy interesante para investigar los procesos fisicoquímicos en los que interviene el hidrógeno, consiste en el análisis de los efectos isotópicos entre sus dos isótopos estables: H y D. Desde el descubrimiento del deuterio en 1931 [1.6-9], los efectos isotópicos entre H y D se han investigado ampliamente. Hoy día, el análisis de los efectos isotópicos entre H y D está presente en numerosas ramas de la ciencia, como la medicina, la biología molecular, la química de los alimentos, la electroquímica, la catálisis química, la geología, la climatología, la física nuclear, la física de superficies o la astrofísica, por citar algunos ejemplos.

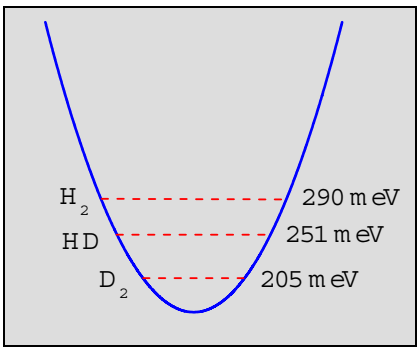

Fig.1.1. Esquema de niveles de energía fundamentales para las tres formas isotópicas del hidrógeno molecular. A la derecha se muestra la posición de estos niveles respecto al mínimo de potencial.

Los efectos isotópicos entre H y D tienen su origen en la naturaleza cuántica de los átomos. Las interacciones atómicas que determinan las propiedades de la materia se pueden describir mediante superficies de energía potencial. Estas superficies dependen fundamentalmente de la interacción eléctrica entre núcleos y electrones, de modo que no se ven esencialmente afectadas por la sustitución isotópica. Sin embargo, la física cuántica predice la existencia de niveles vibracionales de energía en los mínimos de estas superficies. Estos niveles están cuantizados. Su energía depende de la frecuencia de los modos de vibración, y ésta, a su vez, depende de la masa de los átomos. De este modo, los efectos isotópicos son más pronunciados entre H y D que entre cualquier otra pareja de isótopos (exceptuando la pareja H-T), debido a que la diferencia de masa relativa entre H y D es la mayor posible (sus masas están en relación ~1:2).

Para hacernos una idea de la magnitud de estos fenómenos, consideremos las tres formas isotópicas del hidrógeno molecular: H_2, HD y D_2. La Fig.1.1 muestra de forma esquemática los niveles de energía fundamentales (o energías de punto cero) de los tres isótopos moleculares. Nótese que las diferencias de energía de punto cero de los tres isotopólogos son incluso mayores que la magnitud de la energía térmica a temperatura ambiente (kT~25 meV a 300 K).

Desde el punto de vista de la Química-Física, los efectos isotópicos se pueden clasificar en dos grupos: termodinámicos y cinéticos. A continuación, se describirán algunos aspectos fundamentales de los efectos isotópicos atendiendo a esta clasificación.

1.2.1 Efectos isotópicos termodinámicos

Cuando una reacción química se encuentra en equilibrio, los efectos isotópicos H/D aparecen debido a la diferencia relativa entre los niveles de energía de ambos isótopos en los reactivos y en los productos (véase la Fig.1.2a). De modo general, puede decirse que la concentración del isótopo pesado, el D, será mayor en el lado de la reacción donde la diferencia de energías de punto cero sea mayor. Normalmente, esto sucede en el lado de la reacción donde el enlace es más fuerte.

1.2.2 Efectos isotópicos cinéticos

La cinética de las reacciones químicas en las que interviene el hidrógeno también se ve afectada por la sustitución isotópica H/D. El efecto isotópico cinético se explica normalmente en base a la Teoría de las Velocidades Absolutas de Eyring [1.10]. Esta Teoría postula que la reacción transcurre a través de un complejo activado (CA), un estado intermedio entre los reactivos y los productos. En la Fig.1.2b se muestra esquemáticamente la superficie de energía potencial durante el curso de una reacción química. El CA es, generalmente, un punto de silla en la superficie de energía potencial, esto es, tiene un máximo a lo largo de la coordenada de reacción y un mínimo en las coordenadas perpendiculares. Esto

hace que aparezca una estructura de niveles vibracionales en el CA, los cuales, nuevamente, dependerán de la masa de las partículas.

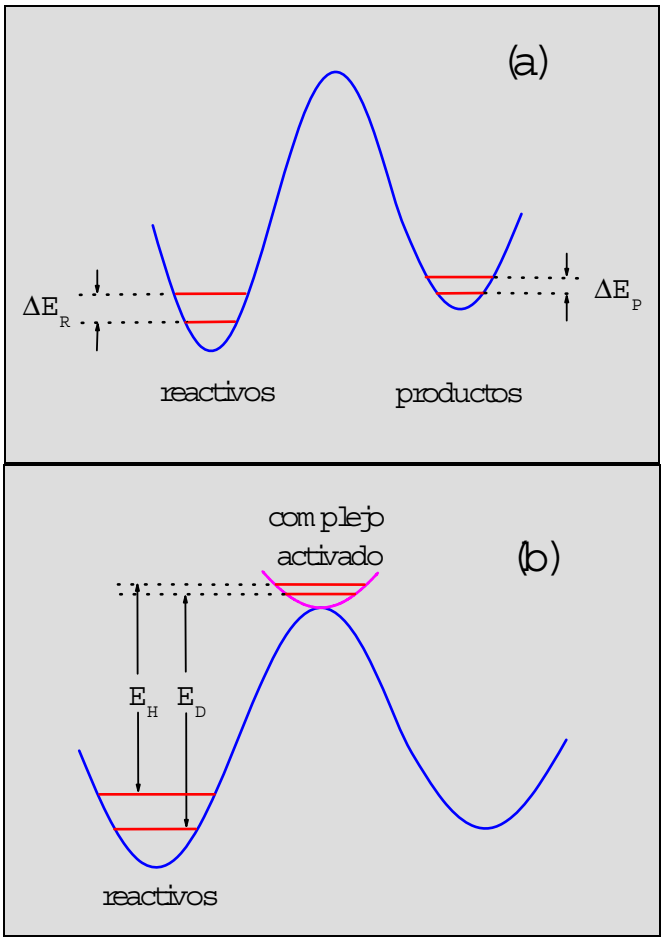

Fig.1.2. Representación esquemática de la superficie de energía potencial durante el curso de una reacción química (línea azul), cuando la reacción se encuentra en el equilibrio (a) y cuando ésta discurre fuera de él (b). Las líneas rojas representan los niveles de energía de punto cero de H y D en los distintos estados. (ΔE_R) y (ΔE_R) representan las diferencias entre las energías de punto cero en los reactivos y en los productos, mientras que E_H y E_D representan las energías de activación de la reacción para H y D, respectivamente.

De acuerdo con la Teoría de Eyring, la velocidad de la reacción está determinada por la energía que separa el estado inicial (reactivos) y el CA, conocida como energía de activación. Debido a la diferencia entre los niveles vibracionales de H y D en los reactivos y el CA, las energías de activación para ambos isótopos son diferentes. En general, las diferencias de energía de punto cero son mayores en los reactivos que en el CA, por lo que la velocidad de la reacción es mayor para el isótopo ligero. Esto es lo que se conoce como el efecto isotópico normal. Sin embargo, existen sistemas en los cuales ocurre un efecto isotópico inverso, esto es, la velocidad de reacción es mayor para D que para H.

1.3 Efectos isotópicos en los procesos de producción y almacenamiento de hidrógeno. Antecedentes y estado actual

La presente Tesis Doctoral se centrará en dos aspectos fundamentales relacionados con el hidrógeno como vector energético. Por un lado, en el proceso de producción de hidrógeno mediante disociación electrolítica de la molécula de H_2O. Por otro, en el almacenamiento de hidrógeno en metales, tanto por reacción sólido-gas como por vía electroquímica. El hilo conductor de la Tesis será el análisis de los efectos isotópicos entre H y D en estas reacciones. A continuación, se expondrán los aspectos fundamentales de las investigaciones realizadas hasta la fecha en estos campos.

1.3.1 Efectos isotópicos en la reacción de evolución de hidrógeno

La reacción catódica que tiene lugar durante la disociación electrolítica de la molécula de H_2O se conoce como reacción de evolución de hidrógeno (REH). Esta es, sin duda, la reacción electroquímica más estudiada [1.11, 12]. Es una de las reacciones más sencillas y a la vez más fundamentales dentro de la catálisis heterogénea, por lo que su estudio es esencial para poder entender reacciones más complejas. No obstante, esto no quiere decir que se conozcan completamente sus entresijos. A menudo ocurre que distintos métodos electroquímicos muestran resultados diferentes acerca del mecanismo por el que discurre la REH en un determinado cátodo. Por ello, el análisis de los efectos isotópicos H/D se ha usado tradicionalmente como un criterio adicional para discernir el mecanismo de la REH [1.13-20]. Existen numerosas investigaciones acerca de los efectos isotópicos H/D en la REH. En particular, en lo que se conoce como el factor de separación electroquímico [1.21-25]. Estas investigaciones se empezaron a desarrollar en los años 30, y tuvieron un especial auge dentro de la electroquímica en la década de los 60. A partir de entonces, el número de publicaciones sobre este tema ha ido disminuyendo, lo cual no implica que sea un tema cerrado. En el campo de la producción de H_2 por vía electroquímica, el objetivo fundamental es encontrar materiales que catalicen esta reacción con el mínimo coste energético posible [1.11, 12]. Este campo se conoce como electrocatálisis. Recientemente, han aparecido algunos trabajos que muestran ciertas correlaciones entre la actividad

electrocatalítica de un metal y su factor de separación electrolítico [1.26-28], lo cual abre nuevas vías de investigación en relación con la separación isotópica.

1.3.1 Efectos isotópicos en los procesos de almacenamiento de hidrógeno en metales

El campo del almacenamiento de H_2 en hidruros de metal mediante reacción sólido-gas es un campo de intensa actividad investigadora, donde existen cientos, quizá miles, de publicaciones (ver por ejemplo [1.29-33]). Históricamente, la primera aplicación de los hidruros de metal fue como moderadores/apantalladores en los reactores nucleares. En este contexto, el análisis de los efectos isotópicos H/D/T es un tema de gran importancia [1.34, 35]. Sin embargo, las investigaciones sobre los efectos isotópicos en hidruros han estado motivadas fundamentalmente por el uso de estos compuestos para la separación isotópica de H/D/T [1.36, 37]. Por otro lado, este tipo de investigaciones es también importante desde un punto de vista fundamental. El análisis de los efectos isotópicos resulta interesante para entender las propiedades de los hidruros [1.38, 39], así como sus mecanismos de formación /descomposición [1.40].

Cabe destacar que la mayoría de las investigaciones previas sobre los efectos isotópicos en hidruros de metal que se han realizado se refieren a los efectos isotópicos termodinámicos [1.40-47]. En lo que respecta a la cinética, hay algunos trabajos [1.48, 49] en los que se investiga la cinética de intercambio isotópico entre H_2 en fase gas y un deuteruro de metal (o viceversa). Asimismo, existen algunas investigaciones acerca del efecto isotópico en la difusión de H y D en metales [1.41, 50]. Sin embargo, el análisis de los efectos isotópicos H/D en los Espectros de Desorción Térmica (EDT) de los hidruros es un tema casi inexplorado. Hasta donde he podido saber, sólo existe un trabajo previo que investiga de forma cualitativa los efectos isotópicos en la desorción simultánea de H y D mediante EDT [1.51].

Actualmente, la principal aplicación de los hidruros de metal es su uso como electrodos en las baterías Ni/MH [1.3-5]. Sin embargo, en el campo del almacenamiento de hidrógeno en metales por vía electroquímica, el análisis de los efectos isotópicos es un tema apenas explorado. Cabe destacar los trabajos de Lewis y Flanagan [1.52, 53], quienes midieron las isotermas del hidruro y deuteruro de Pd por vía electroquímica. Más recientemente, ha aparecido un trabajo en el que se muestra un efecto isotópico muy notable en electrodos de Ti_2Ni [1.54].

1.4 Objetivos de la Tesis Doctoral

Como se dijo al principio de este capítulo, las interfases entre las distintas disciplinas son actualmente las áreas donde más se desarrolla (y donde más está por desarrollar) la ciencia. La presente Tesis Doctoral pretende abordar la producción y el almacenamiento de hidrógeno, dos temas específicamente

heterodisciplinares, usando un enfoque *transdisciplinar*: el análisis de los efectos isotópicos entre H y D. El objetivo fundamental de este trabajo no es tanto avanzar en el desarrollo de nuevos materiales capaces de producir y almacenar hidrógeno, sino poner de relieve cómo el análisis de los efectos isotópicos puede ayudarnos a conocer mejor estos procesos. Por este motivo, se han investigado los efectos isotópicos en materiales prototípicos, como el Pt (para la producción de hidrógeno por vía electroquímica), el Pd (para el estudio de la cinética de descomposición de los hidruros mediante reacción sólido-gas) y las aleaciones de tipo $LaNi_5$ (para los electrodos de hidruro metálico).

El primer objetivo de este trabajo ha sido el diseño y la puesta a punto de un sistema experimental basado en la espectrometría de masas que permita analizar la composición de mezclas H_2/HD/D_2. El análisis cuantitativo de la composición de un flujo gaseoso no es un asunto trivial. Más aún cuando se trata de analizar la composición isotópica de un flujo de hidrógeno. Como se verá más adelante, existen numerosos factores que afectan a la calibración del instrumento. La descripción y caracterización del sistema de análisis de gases se tratará en el Capítulo 2. Esta caracterización trasciende más allá del análisis de mezclas H_2/HD/D_2, extendiéndose también al de otros gases. Con ello se pretende dar una mayor versatilidad al sistema experimental, con objeto de aplicarlo a otros posibles usos en el futuro.

En el Capítulo 3, se abordará el estudio de los efectos isotópicos en la REH. El primer paso consistirá en recopilar y analizar, de forma crítica, las investigaciones relativas a la separación electrolítica de H y D realizadas hasta la fecha. De hecho, los trabajos realizados en este tema son muy heterogéneos y no existe ninguna revisión crítica global, que yo sepa. Además, debido a las recientes investigaciones que apuntan la existencia de una cierta correlación entre la actividad electrocatalítica y el factor de separación electrolítico, se dedicará una parte importante del Capítulo 3 a revisar las medidas del factor de separación electrolítico en los metales de transición. Este análisis permitirá profundizar en el conocimiento de la separación isotópica y su relación con la actividad electrocatalítica y la estructura electrónica de los cátodos metálicos. A continuación, se presentarán los resultados obtenidos de las medidas resueltas en tiempo del factor de separación en cátodos de Pt. Se analizará la dependencia del factor de separación con la densidad de corriente electrolítica y con la composición isotópica de los electrolitos. Finalmente, se presentarán algunos resultados complementarios que pretenden ilustrar la capacidad del sistema experimental como herramienta analítica en electroquímica.

En el Capítulo 4, se analizan los efectos isotópicos en la cinética de descomposición del hidruro-deuteruro de Pd mediante reacción sólido-gas. Para ello, se ha empleado la técnica de EDT, en la que conecta un calorímetro diferencial de barrido al sistema de análisis de gases. El objetivo de este trabajo consiste en determinar los mecanismos y los parámetros cinéticos del proceso de

descomposición de este hidruro. Asimismo, se ha investigado la forma en que se distribuyen los átomos de H y D en los tres isótopos moleculares. Este es un tema que no ha recibido, a mi juicio, la atención que merece, y que permite obtener información muy relevante acerca de la reacción de recombinación de los átomos de H y D en la superficie del Pd.

Por último, se ha investigado cómo afecta la sustitución isotópica a la estabilidad y a la cinética de carga/descarga de electrodos de tipo $LaNi_5$. Como se ha dicho anteriormente, este es un tema apenas explorado. El objetivo de este trabajo es sentar algunas bases para el uso del análisis de los efectos isotópicos como método para investigar las propiedades electroquímicas de este tipo de electrodos.

Finalmente, quisiera destacar que, dado su carácter fundamental e interdisciplinar, las investigaciones acerca de los efectos isotópicos H/D representan un marco excelente en el cual empezar a construir una carrera científica. Tal es el principal objetivo de la presente Tesis Doctoral.

1.5 Referencias

[1.1] Kothari R, Buddhi D, Sawhney RL 2006 *Renew. & Sust. Energy Rev.* doi:10.1016/j.rser.2006.07.012.

[1.2] Schlapbach L and Züttel A 2001 *Nature* **414** 353

[1.3] Cuevas F, Joubert J-M, Latroche M, Percheron-Guégan A 2001 *Appl. Phys. A* **72** 225

[1.4] Sakai T, Matsouka M and Iwakura C in '*Handbook on the Physics and Chemistry of Rare Earths*' vol. 21, ed. K.A. Geschneider, Jr Eyring and L. Eyring (1995, Elsevier) pp133-178

[1.5] Kleperis J, Wójcik G, Czerwinski A, Skowronski J, Kopczyk M and Beltowska-Brzezinska M 2001 *J. Solid State Electrochem.* **5** 229

[1.6] Urey HC, Brickwedde FG and Murphy GM 1932 *Phys. Rev.* **39** 164

[1.7] Urey HC, Brickwedde FG and Murphy GM 1932 *Phys. Rev.* **40** 1

[1.8] Urey HC, Brickwedde FG and Murphy GM 1932 *Phys. Rev.* **40** 464

[1.9] Washburn EW and Urey HC 1932 *Proc. Nat. Acad. Sci.* **18** 496

[1.10] Glasstone S, Laidler KJ and Eyring H *'The Theory of Rate Processes'* McGraw-Hill (1941 New York)

[1.11] Kita H 1966 *J. Electrochem. Soc.* **113** 1095

[1.12] Jaksic MM 2001 *Int. J. Hydrogen Energy* **26** 559

[1.13] Keii T and Kodera T 1957 *J. Res. Inst. Catalysis Hokkaido Univ.* **5** 105

[1.14] Conway BE and Salomon M 1964 *Ber. Bunsenges.* **68** 331

[1.15] Conway BE 1958 *Proc. Roy. Soc. (London)* **A247** 400

[1.16] Bockris JO'M and Srinivasan S 1964 *J. Electrochem. Soc.* **111** 844

[1.17] Horiuti J, Keii T and Hirota K 1951-3 *J. Res. Inst. Catalysis Hokkaido Univ.* **2** 1

[1.18] Bockris JO'M and Srinivasan S 1964 *J. Electrochem. Soc.* **111** 853

[1.19] Bockris JO'M and Srinivasan S 1964 *J. Electrochem. Soc.* **111** 858
[1.20] Okamoto G, Horiuti J and Hirota K 1936 *Sci. Pap. Inst. Phys. Chem. Res. Tokyo* **29** 223
[1.21] Topley B and Eyring H 1934 *J. Chem. Phys.* **2** 217

[1.22] Rowland PR 1968 *Nature* **218** 945
[1.23] Harada S 1996 *Mater. Transac. JIM* **37** 45
[1.24] Hammerli M, Mislan JP and Olmstead WJ 1970 *J Electrochem. Soc.* **117** 751
[1.25] Lewis GP and Ruetschi P 1962 *J. Phys. Chem.* **66** 1487
[1.26] Matsushima H, Nohira T and Ito Y 2004 *Electrochim. Acta* **49** 4181
[1.27] Stojic DLJ, Miljanic SS, Grozdic TD, Petkovska LT and Jaksic MM 2000 *Int. J. Hydrogen Energy* **25** 819
[1.28] Stojic DLJ, Miljanic SS, Grozdic TD, Bibic NM and Jaksic MM 1991 *Int. J. Hydrogen Energy* **16** 469
[1.29] 'Hydrogen in Metals I' *Topics in Applied Physics* vol 28 ed. G Alefeld and J Völk (1978, Berlin: Springer-Verlag)
[1.30] 'Hydrogen in Metals II' *Topics in Applied Physics* vol 29 ed. G Alefeld and J Völk (1978, Berlin: Springer-Verlag)
[1.31] 'Hydrogen in Metals III' *Topics in Applied Physics* vol 73 ed. H. Wipf (1997, Berlin: Springer-Verlag)
[1.32] 'Hydrogen in Intermetallic Compounds I' *Topics in Applied Physics* vol 63 ed. L. Schlapbach (1988, Berlin: Springer-Verlag)
[1.33] 'Hydrogen in Intermetallic Compounds II' *Topics in Applied Physics* vol 67 ed. L. Schlapbach (1992, Berlin: Springer-Verlag)
[1.34] Soda K, Iizuka E, Tsuchiya B, Morita K and Iwahara H 2002 *J. Nucl. Sci. Technol.* **39** 359
[1.35] Yamanaka S, Yamada K, Kurosaki K, Uno M, Takeda K, Anada H, Matsuda T and Kobayashi S 2002 *J. Alloys Comp.* **330/332** 99
[1.36] Andreev BM and Magomedbekov EP 2001 *Separation Science and Technology* **36** 2027
[1.37] Ducret D, Ballanger A, Steimetz J, Laquerbe C, Baudouin O and Sere Peyrigain P 2001 *Fusion Engineering and Design* **58/59** 417
[1.38] Läser R and Klatt KH 1983 *Phys. Rev. B* **28** 748
[1.39] Paul-Boncour V, Guillot M, Wiesinger G and André G 2005 *Phys. Rev. B* **72** 174430
[1.40] Andreev BM, Sicking GH and Magomedbekov EP '*Interaction of Hydrogen Isotopes with transition Metals and Intermetallic Compounds'* Springer Tracts in Modern Physics vol. 132, (1996, Springer-Verlag, Berlin)
[1.41] Sicking G 1984 *J. Less-Common Met.* **101** 169
[1.42] Wiswall RH and Reilly JJ 1972 *Inorg. Chem.* **11** 1691
[1.43] Lambert I, Percheron-Guégan A and Montel J 1977 *J. Chim. Phys.* **74** 380

[1.44] Cho S-W, Akiba E, Nakamura Y and Enoki H 2000 *J. Alloys Comp.* **297** 253
[1.45] Buchner H, in *Hydrides for Energy Storage*, Proc. Int. Symp. Geilo, Norway, August 1977. A.F. Andresen and A. J. Maeland Eds. Pergamon Press. p. 569
[1.46] Yawny A, Friedlmeier G and Bolcich JC 1989 *Int. J. Hydrogen Energy* **14** 587
[1.47] Nikolić R, Zmbov K and Veljković M 1993 *Int. J. Hydrogen Energy* **18** 743
[1.48] Outka D.A. and Foltz G.W. 1991 *J. Catalysis* **130** 268
[1.49] Foltz GW and Melius CF 1987 *J. Catalysis* **108** 409
[1.50] Völk J and Alefeld G 1978 Hydrogen in Metals I *Topics in Applied Physics* vol 28 ed G Alefeld and J Völk (Berlin: Springer-Verlag) pp321-348
[1.51] Hayasi 2003 *J. Alloys Comp.* **359** 281
[1.52] Flanagan TB and Lewis FA 1959 *Trans. Farad. Soc.* **55** 1409
[1.53] Flanagan TB 1961 *J. Phys. Chem.* **65** 280
[1.54] Luan B, Kennedy SJ, Liu HK and Dou SX 1998 *J. Alloys Comp.* **267** 224

Chapter 2

An experimental characterization of a QMS meter to be used as a gas analyzer

2.1 Introduction

This chapter is devoted to the analysis of the composition of gas mixtures by Quadrupole Mass Spectrometry (QMS). This technique plays a fundamental role in the investigation of the H/D isotope effects in hydrogen production and storage processes, as it will be shown in Chapters 3 and 4. However, the potential applications of QMS go beyond the field of isotope gas analysis. When coupled to an electrochemical cell, it allows to analyze the gases produced by the electrolysis. This coupling of both techniques technique is known as Electrochemical Mass Spectrometry (EMS). The gas analysis system can also be used to perform Thermal Desorption Spectroscopy (TDS), by connecting it to a differential scanning calorimeter (DSC).

Basically, a quadrupole mass spectrometer (QMS[1]) is an analytical instrument that generates and detects ions according to their mass-to-charge ratio. Therefore, it can be used to measure the partial pressures of the gases surrounding the ionizer. In spite the apparent simplicity of the above definition, a large number of physical and chemical phenomena are involved within the analytical procedure. Gas analysis by QMS is sensitive to many experimental factors, so a precise knowledge of the experimental technique is imperative whenever quantitative measurements are to be accomplished. For this reason, the first part of this chapter (section 2.2) concerns the detailed description of the experimental system used for gas analysis. Some general features of the gas analysis process are presented in section 2.3.

[1] The initials QMS will be used indistinctly to name the experimental technique and the experimental system.

In addition, the calibration of the QMS is completely necessary in order to perform quantitative measurements. Special attention has been paid to the isotope analysis in H_2-HD-D_2 mixtures. This is a delicate problem which is not treated with sufficient detail in previous works on H/D analysis by QMS. The detection sensitivities of the H_2, HD and D_2 molecules are investigated in section 2.4. In order to exploit at the maximum extent the capabilities of the gas analysis system, the detection sensitivities for Ar, H_2O and O_2 have been also investigated (section 2.5).

Finally, the temporal stability of the gas analysis system and the dependence of the obtained sensitivities with the chemical nature of the analyzed gases are discussed in section 2.6.

2.2 Description of the experimental system

The scheme of the experimental set-up used for gas analysis is depicted in Fig.2.1. The QMS consists of three parts: an ion source, an ion filter and an ion detector. It is placed inside a vacuum chamber connected to a pumping system. A special system for gas collection is also needed to maintain the high vacuum conditions inside the chamber of analysis, where there is a pressure meter, namely a combined sensor Pirani-Penning Balzers PKR 250 that allows measuring the total pressure in the range 10^{-9}-10^{3} mbar. In what follows, the different parts of the gas analysis system are described in detail.

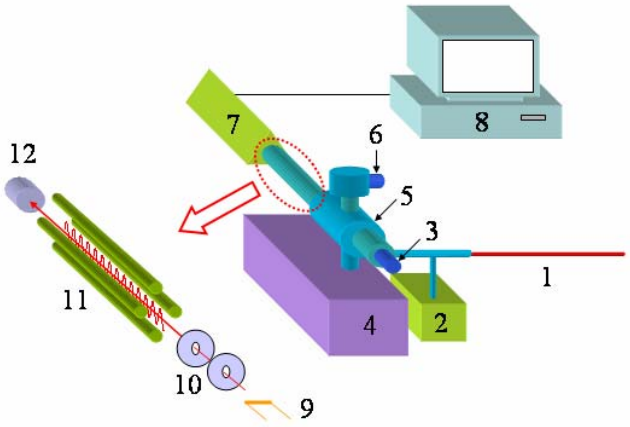

Fig.2.1. Scheme of the gas analysis system: (1) capillary tube; (2) rotary pump; (3) needle valve; (4) pumping system; (5) vacuum chamber; (6) Penning sensor; (7) electronic setup; (8) Quadstar 422 software; (9) ion source; (10) electrodes; (11) quadrupolar filter; (12) detectors.

2.2.1 Gas collection system

The gas collection system consists of a low conductance capillary tube and a needle valve that allows varying the flow of gases entering the chamber. To favour this flow through the capillary tube, a pressure gradient is created by a rotatory pump.

2.2.1.1 Capillary tube

The capillary tube is made in quartz. It has 100 μm internal diameter and 1m in length. It can be heated to avoid the condensation of gases, mainly water vapour.

The most important parameter characterizing the capillary tube is the transport time of the collected gases through it (τ_c). This time can be estimated from the ratio between the volume and the conductance of the capillary.

The conductance depends on the flow regime of gases through it. This regime can be estimated from the Knudsen number (κ) [2.1]:

$$\kappa = \frac{\lambda}{2r_c} \tag{2.1}$$

where λ is the mean free path of the molecules and r_c is the internal radius of the capillary. λ depends on pressure (P), temperature (T) and the cross section of molecule-molecule scattering (ϕ_0):

$$\lambda = \frac{kT}{\sqrt{2}P\phi_0} \tag{2.2}$$

where k is the Boltzmann's constant.

When κ>3, the flow of gases is said to be molecular. Under these conditions, molecule-molecule collisions are less probable than collisions between the molecules and the capillary walls and the flows of the molecular species are independent of each other. On the other hand, molecule-molecule collisions are dominant for κ<0.01, generating a continuous regime. By taking ϕ_0 values of molecule-molecule collisions (typically in the range of 10^{-20} m^2), κ values of the gas flow through the capillary can be calculated. At the end of the capillary where gases are collected, the pressure is about 10^5 Pa, what leads to $\lambda \sim 10^{-6}$ m and $\kappa \sim 10^{-2}$. At the opposite end, the pressure is reduced to ~1 Pa, what leads to κ values of about 10^3. Therefore, the gas flow through the capillary will change from a continuous to a molecular regime as the gas is going from the inlet to the outlet side of the capillary. The calculation of the conductance of the capillary when the gas flow changes from continuous to molecular regime is not a trivial task. In a

first approximation, one can consider separately the conductance in both regimes to obtain the lower and upper limits for the transport time.

The conductance of the capillary (C) in continuous regime can be calculated from Poiseuille's law [2.1]:

$$C = \frac{\pi \cdot r_c^{\,4}}{8 \cdot \eta \cdot L} \cdot \frac{P_i - P_o}{2} \tag{2.3}$$

where η is the viscosity coefficient of the gas, L is the length of the capillary and P_i and P_o are the pressures at the inlet and outlet sides of the capillary, respectively. By taking the viscosity coefficient of Ar at 293 K (η=2.22·10^{-5} Poise), P_i~10^5 Pa and P_o~1 Pa, it is obtained C~5.5·10^{-9} m^3 s^{-1} (0.33 sccm).

In the molecular regime, the flow of each species is determined by Maxwell's velocity distribution law, which implies a dependence of the mean velocity of the molecules (v) with their mass (m):

$$v = \sqrt{\frac{8kT}{\pi m}} \tag{2.4}$$

In this regime, the conductance of the capillary can be obtained by using the Clausing approximation [2.1]:

$$C = \frac{v}{4} \cdot a \cdot \mu = a \cdot \mu \cdot \sqrt{\frac{kT}{2\pi m}} \tag{2.5}$$

where a is the section of the capillary and μ is the transmission probability, which depends on the geometry of the capillary. In the limit $L/r_c \to \infty$, $\mu = 8r_c/3L$. The conductance of the capillary for Ar at 293 K calculated by using equation (2.5) is $C \approx 10^{-10}$ m^3 s^{-1} (6·10^{-3} sccm).

By taking the estimated conductance values of continuous and molecular flows, the obtained lower and upper limits for the transport time of Ar gas are $1.4 < \tau_c < 78.5$ s. The upper limit for the transport time of H_2 through the capillary is reduced to 17.5 s due to its lower molecular mass compared to Ar. In principle, it is expected that τ_c will be nearer to the value calculated considering a continuous flow, because the molecular regime will only occur in a small section of the capillary. This view has been confirmed experimentally. τ_c values obtained from the calibration experiments of the gas analysis system (see sections 2.4.2 and 3.4.2) are of about 5 s.

2.2.1.2 Needle valve

The inlet flux of gases into the analysis chamber can be controlled by means of a needle valve Balzers UDV 040 which allows regulating the inlet flux between 10^{-9} and 600 mbar l s^{-1}.

The gas flow regime through the valve is a molecular one because the mean free path of the molecules at its inlet (λ~0.1 m) is much higher than the dimensions of the hole. It must be mentioned that the conductance of the needle valve is influenced by the temperature. Therefore, room temperature fluctuations can be a source of instabilities during the measurements.

2.2.2 Analysis chamber

The analysis chamber where the QMS is placed is all constructed in stainless steel and it can be heated to degasify its surfaces when necessary. The chamber is connected to a pumping system Balzers TSU 064 D consisting of a primary membrane pump MZ2T, a turbomolecular pump TMU 064 and a controller TCP 015. It has a nominal pump speed of 50 l s^{-1} and reaches a residual pressure in the range of 10^{-9} mbar. However, the pump speed for light molecules, such as H_2, HD and D_2 is lower and follows a linear dependence with the square root of their molecular masses [2.2].

The flow regime of gases inside the analysis chamber is a molecular one because the large values of the mean free path of the molecules at the pressure and temperature conditions inside it (P~10^{-8}-10^{-6} mbar, λ~10^{5}-10^{3} m).

The partial pressure of each molecular species inside the chamber can be obtained by computing the inlet and outlet flows of gases. Due to the low conductance of the gas collection system, only a small portion of the collected gases passes through it. Therefore, the flow of molecules of the specie χ that enters the analysis chamber ($dN_\chi^i(t)/dt$) obey the equation:

$$\frac{dN_\chi^i(t)}{dt} = \alpha_\chi \cdot f_\chi(t) \tag{2.6}$$

where $f_\chi(t)$ is the partial flow of the specie χ in the collected gases, *i.e.*, the ratio of the χ flow ($F_\chi(t)$) to the total flow:

$$f_\chi(t) = \frac{F_\chi(t)}{\sum_\delta F_\delta(t)} \tag{2.7}$$

The value of the factor α_χ can be regulated by means of the needle valve. On the other hand, it depends on the mass of the species because of the molecular flow

of gases through the capillary tube and the needle valve. In mass spectrometry, the effects that depend on the mass of the atoms or molecules are generally called 'mass discrimination effects'.

The outlet flow of a certain specie χ ($dN_\chi^o(t)/dt$) due to the action of the pumping system, depends on the pumping speed for this specie (B_χ), the increment of its partial pressure inside the chamber ($p_\chi(t)$-p_χ^0), and the temperature:

$$\frac{dN_\chi^o(t)}{dt} = \frac{B_\chi \cdot \left(p_\chi(t) - p_\chi^o\right)}{k \cdot T} \tag{2.8}$$

where p_χ^o is the partial pressure of the specie χ in the residual atmosphere of the chamber. By combining (2.6) and (2.8), one obtains that the variation of the number of molecules of the specie χ inside the chamber obeys the equation:

$$\frac{dN_\chi(t)}{dt} = \frac{dN_\chi^i(t)}{dt} - \frac{dN_\chi^o(t)}{dt} = \alpha_\chi \cdot f_\chi(t) - \frac{B_\chi \cdot \left(p_\chi(t) - p_\chi^0\right)}{k \cdot T} \tag{2.9}$$

By taking the equation of state of an ideal gas and considering that $f_\chi(t)$ is constant, the solution of equation (2.9) is:

$$p_\chi(t) - p_\chi^0 = \frac{kT \cdot \alpha_\chi \cdot f_\chi}{B_\chi}\left(1 - e^{-\frac{B_\chi}{V_a}t}\right) \tag{2.10}$$

where V_a is the chamber volume. According to this expression, the stationary value of the specie χ partial pressure inside the chamber is:

$$p_\chi - p_\chi^0 = \frac{kT \cdot \alpha_\chi \cdot f_\chi}{B_\chi} \tag{2.11}$$

whereas the time constant to reach this stationary state is:

$$\tau_\chi = \frac{V_a}{B_\chi} \tag{2.12}$$

Equation (2.11) allows to make an estimation of the inlet flow of gases entering the analysis chamber at the usual measurement conditions (P~$4 \cdot 10^{-6}$ mbar, B~50 l s^{-1}), of the order of $2 \cdot 10^{-4}$ mbar l s^{-1}.

On the other hand, τ_χ can be estimated from equation (2.12). By taking V_a~2 l and B~50 l s^{-1}, the time constant of gases in the analysis chamber is of the order of 0.04 s. This time constant is much lower than the estimated transport time through the gas collection system, τ_c. This implies that the partial flow of the collected gases can be considered constant during the typical response times of the gas analysis chamber. In this case, the relation between the gas partial pressure and its partial flow can be approximated by equation (2.11).

It is worthwhile to say that beside the explicit dependence on temperature shown in equation (2.11), the pumping speed and the conductance of the different parts of the system (specially the needle valve) can depend on temperature.

2.2.3 Quadrupole Mass Spectrometer

It has been stated above that a QMS 200 (from Balzers) partial pressure analyzer is located inside the high vacuum chamber. The QMS 200 is composed of three different parts: the ion source, the quadrupolar filter and the ion detector. These parts are described in detail below.

2.2.3.1 Ion source

The gaseous species (molecules or atoms) collected inside the analysis chamber are ionised by bombardment with electrons that are thermoionically emitted by a filament cathode. The QMS Balzers 200 has two W filaments. The geometry of the ion source can be seen in Fig.2.2. A high current (typically 2.75 A) passes through the filament (filament current) to heat it and facilitate the electron emission process. A cut off must be imposed to the filament current (typically 3.5 A) in order to avoid filament melting. The emitted electrons are accelerated by a voltage gradient imposed between the filament and an auxiliary electrode (the cylindrical grid appearing in Fig.2.2) in order to reach a definite energy before impacting the atoms or molecules.

Fig.2.2. View of the ion source.

Both the electron beam intensity and energy must be kept constant in order to accomplish stable measurements. To this purpose, it is required a clean filament surface. Impurities (such as H, O and C) adsorbed at the W filament surface can change its work function and affect the electron emission process. In addition, several reactions catalysed by the poisoned hot filament can take place [2.3,2.4] once H_2 or other reactive gases are introduced inside the chamber (see section 2.3.3). This can modify the partial pressures of the gases and affect the results of the measurements. The filament surface can be cleaned by passing a higher filament current through it (such as the emission current reaches 10 mA) during 1 min to produce the thermal desorption of the impurity atoms. Cleaning of the filament improves the stability of the electron emission process and reduces the effect of the filament-catalyzed reactions.

When an electron impacts an atom or molecule, several ions can be formed. For instance, the ionisation of Ar can produce Ar^+ and Ar^{2+}, whereas the ionisation of H_2 can give H^+ and H_2^+. The ionic structures and their relatives abundances produced from a certain specie is known as its 'cracking pattern'. These patterns depend on the electron beam energy and intensity. In most cases, the precise determination of cracking patterns is essential for quantitative analysis of the obtained mass spectra.

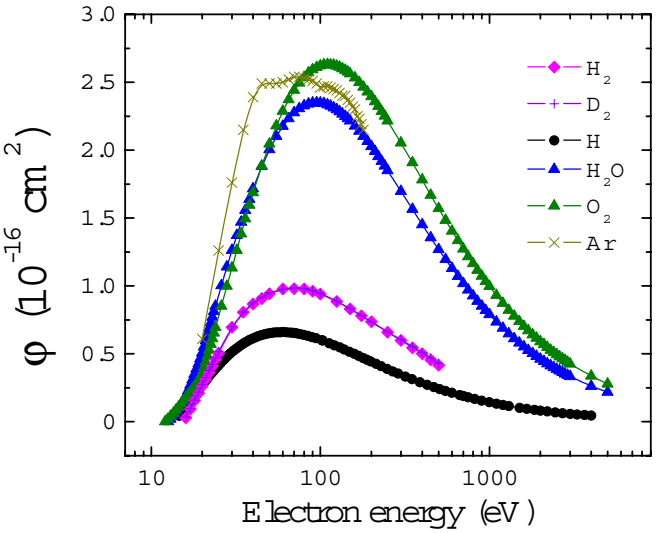

Fig.2.3. Electron-impact ionization cross sections for single ionization of H_2 [2.5], D_2 [2.5], H [2.6], H_2O [2.6], O_2 [2.7] and Ar [2.8] as a function of the energy of the incident electrons.

The electron-impact ionisation cross section for the formation of a given ion (φ^{χ}) depends on the electronic structure of the parent atom/molecule and on the energy of the incident electrons. In Fig.2.3, those cross sections for single ionization of H_2, D_2, H, H_2O, O_2 and Ar have been plotted as a function of the energy of the incident electrons. From this figure it can be seen that the electron energy must be tuned between 60 and 110 eV in order to maximize the number of produced ions and, so, the QMS sensitivity. In particular, the maximum φ^{χ} value is found at 70 eV for H_2, D_2 and Ar. It is worth to note that there are not significant isotope effects in the ionization cross sections of H_2 and D_2, being those values equal within ±2 %.

On the other hand, it has to be mentioned that the number of produced ions does not necessarily varies linearly with the electron beam intensity, as could be intuitively felt. This is due to the presence of spatial charge effects in the ionization source, mainly at high intensities of the e^--beam [2.9]. Spatial charge effects can change the energy of the incident electrons and modify the electron-impact ionization cross sections.

Fig.2.4. Frontal (up) and vertical (bottom) views of the electrode assembly surrounding the ion source.

There are various tuneable electrodes surrounding the ionisation source which have different functions. Some of them filter the electrons to avoid that they reach the ion filter and the detector (Extraction Voltage). Other electrodes are used to focus the produced ions (Focus and Ion Reference Voltages) and to vary their energy to enter the ion filter (Field Axis Voltage). The frontal and vertical views of the electrode assembly surrounding the ion source are shown in Fig. 2.4.

2.2.3.2 Ion filter

Ions produced in the ion source enter the ion filter after being properly focalized. A quarupolar filter consists of four cylindrical electrodes located at the edges of a square prism. The voltage applied to the electrodes is composed by a high frequency ($V\cos(\omega t)$) component and a continuous one (U). The dynamic equations of the ions in the quadrupolar field generated by the electrodes are known as Mathieu differential equations. Their solutions split into two groups: stable and unstable. In the first group, the amplitude of the trajectories is confined and the ions can pass through the filter and reach the detectors. In the second group, the amplitudes continuously grow and the ions are neutralised by the electrodes and pumped out of the system. The stability of the trajectories depends on the parameters U, V and ω, the distance between the electrodes and the mass-to-charge ratio (m/q) of the ions. Therefore, one can filter the ions according to their m/q values by tuning the parameters U and V of the applied voltage. It should be noted that different ions with the same m/q value will contribute to the same current peak of the mass spectra. Usually, m/q values are expressed in atomic units, *i.e.*, q in electron charge units and m is the mass number of the atomic/molecular ion.

The ion transmittance through the filter depends on the energy and the angular distribution with which they enter the filter [2.10]. In turn, these characteristics are affected by the fringing fields present at the different parts of the system. The interaction of the ions with the fringing fields depends on their m/q value. As a consequence, there is another mass discrimination effect in the gas analysis process associated with the transmittance of the ions through the quadrupolar filter.

Another important parameter of the ion filter is its resolving power, defined as the ratio between the m/q value at the maximum of a certain current peak of the spectra and its width. Although there is not a unique definition, the peak width is usually defined as the difference in m/q units between m/q values on either side of the peak at which the current has dropped to 10 % of the peak height. If the current peak is such that the signal does not drop to 10 % or less of the peak height, this indicates overlapping of adjacent peaks. The resolving power is a measurement of the ability of the QMS to separate ions according to their m/q values. It depends on the quotient U/V and on the number of cycles that the ions experiment inside the quadrupolar filter. This number is proportional to ω and inversely proportional to the speed of the ions along the axis of the filter. In general, higher the resolving

power is, the lower the height of the peaks and the sensitivity of the QMS. Therefore, there is a compromise between a high resolution and a high resolving power.

2.2.3.3 Ion detectors

Once the ions are separated according to their *m/q* values, they are electrically detected. The QMS has two different detectors: a Faraday cup and a secondary electron multiplier detector (SEMD).

The Faraday cup is a metallic electrode where the ions strike and give up their charge. The resulting current is converted in a sensitive current-to-voltage converter, yielding an output signal proportional to the ion current. The limit of measurement is between 10^{-16} A and 10^{-14} A, depending on the time constant of the current-to-voltage converter.

The SEMD should be used whenever the ionic currents are very small or the ion formation processes very fast. It consists of a dynode system that amplifies the ionic currents to reach gains ranging from 10^2 to 10^5. The gain depends on the mass and chemical nature of the ions [2.11] and on the SEMD operating parameters and it has to be calibrated for each ion whenever quantitative results are required.

2.2.4 Detection sensitivity of the QMS

The detection sensitivity is perhaps the most important and significant parameter of the QMS. The detection sensitivity ($s_{m/q}^{\chi}$) of a particular gas specie (χ) is usually defined as the ratio of the change in current peak height associated with an ion produced from this specie ($i_{m/q}$-$i_{m/q}^{0}$) to the change in the partial pressure of the same specie in the analysis chamber (p_{χ}-p_{χ}^{0}):

$$i_{m/q} - i_{m/q}{}^{0} = s_{m/q}{}^{\chi} \cdot \left(p_{\chi} - p_{\chi}^{0}\right) \tag{2.13}$$

where $i_{m/q}^{0}$ is the signal corresponding to the residual gas partial pressure, p_{χ}^{0}.

The factor $s_{m/q}^{\chi}$ is proportional to the electron impact ionization cross section of the atoms/molecules, to the ionic transmittance through the ion filter and the different electrodes and to the ionic detection effectiveness. It must be noted that equation (2.13) does not necessarily implies a linear correlation between the height of current peaks and the partial pressures of the corresponding gases because $s_{m/q}^{\chi}$ can depend on the gas partial pressure.

For the present purposes, however, it is more convenient to relate the ionic currents to the partial flow of the gaseous species collected for analysis. By combining equations (2.11) and (2.13) it is obtained:

$$i_{m/q} - i_{m/q}{}^{0} = \sigma_{m/q}{}^{\chi} \cdot f_{\chi} \tag{2.14}$$

where:

$$\sigma_{m/q}{}^{\chi} = \frac{kT \cdot \alpha_{\chi} \cdot s_{m/q}{}^{\chi}}{B_{\chi}} \tag{2.15}$$

$\sigma_{m/q}{}^{\chi}$ is the most convenient definition of the detection sensitivity because it includes all the variables present in the analytical procedure. It depends on the nature of the analyzed gas species due to differences between e^--impact ionization cross sections of the atoms or molecules and to mass discrimination effects in gas collection, ionization, filter and detection processes.

2.2.5 Total pressure meter

In addition to the QMS, there is a total pressure meter inside the vacuum chamber. It consists of a combined sensor Pirani-Penning Compact FullRange Gauge PKR 250 (from Balzers). The Pirani is a thermal conductivity sensor that measures absolute pressure by detecting heat losses from a heated fine wire. It operates in the range 10^{-5}-10^{3} mbar. The Penning sensor is a cold cathode ionization gauge in which ionization is produced by electrons emitted from an unheated cathode. A magnetic field is used to lengthen the electron path and so increase the number of ions produced. The operation range of the Penning sensor is between 10^{-9}-10^{-5} mbar.

2.3 Gas analysis by QMS

2.3.1 Influence of the operating parameters on the mass spectra

Prior to gas analysis, it is important to choose the operating parameters of the experimental system and to define a convenient measurement protocol.

Gas analyses have been always made by fixing the needle valve at a definite position to reach a total gas pressure inside the analysis chamber of about $4 \cdot 10^{-6}$ mbar. According to equation (2.13), the ionic signals corresponding to the analyzed gas mixtures should increase by raising the gas partial pressures inside the chamber. However, the signals saturate at high pressures, leading to complex pressure-dependences of the detection sensitivities and to a difficult quantitative gas analysis. Moreover, high pressures diminish the lifetime of the ion source. Therefore, there is a compromise among high detection sensitivity, high ion source lifetime and a good linearity of the ionic signals with partial pressures. The selected operating total pressure fulfils all these conditions reasonably well.

Experimental measurements have been made by setting the QMS parameters either to Set A or to Set B values, as shown in Table 2.1.

Table 2.1. QMS operating parameters used for gas analysis

Operating Parameters	Set A	Set B
e^--beam energy (eV)	98	85
e^--beam intensity (mA)	2	1.5
Ion Reference voltage (V)	150	150
Focus voltage (V)	0	0
Field Axis voltage (V)	7	7
Extract voltage (V)	6	19

The influence of the QMS operating parameters on the recorded mass spectra (for a mixture of 0.7 sccm-H_2 and 28.8 sccm-Ar) can be seen in Fig.2.5. The mass spectra consist of a series of current peaks at definite *m/q* values corresponding to the different ions formed in the ionization source. The change of the QMS operating parameters from Set A to Set B values results in a decrease of the background currents (offset) of roughly one order of magnitude. On the other hand, an increase of the heights of the current peaks is observed when using Set B parameters. From these spectra, the QMS resolving power can be obtained. With Set A parameters, resolving powers at *m/q*=2 and *m/q*=40 (corresponding to H_2^+ and Ar^+ ions) are equal to 2.45 and 49.9, respectively. These values are not essentially changed when using Set B parameters (are equal to 2.70 and 49.8 for *m/q*=2 and *m/q*=40, respectively).

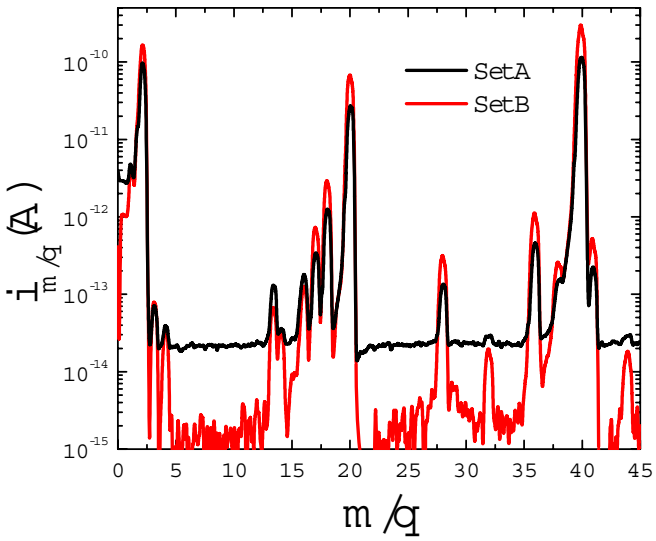

Fig.2.5. Mass spectra of a H_2-Ar mixture with two different sets (A and B) of operating parameters of the QMS (see Table 2.1).

Gas analysis is usually accomplished by monitoring the heights of selected current peaks, *i.e.*, the peak currents. Therefore, the offset of the instrument and the *m/q* value of the current peak maximum in the spectra must be determined before accomplishing the measurements.

2.3.2 Analysis of the residual atmosphere in the vacuum chamber

Several probes have been done to know the composition of the vacuum chamber residual atmosphere.

Fig.2.6 shows a mass spectra of the residual atmosphere between *m/q*=0 and 100. It can be seen that i_{18} peak current is at least one order of magnitude higher than any other one, followed by i_1, i_2, i_{28}, i_4, i_{32} and i_{44}. This reveals that the residual atmosphere is mainly composed by H_2O and at a lower level H_2, N_2, D_2, O_2 and CO_2. It is worth to note, however, that the residual atmosphere composition depends on the history of use of the instrument.

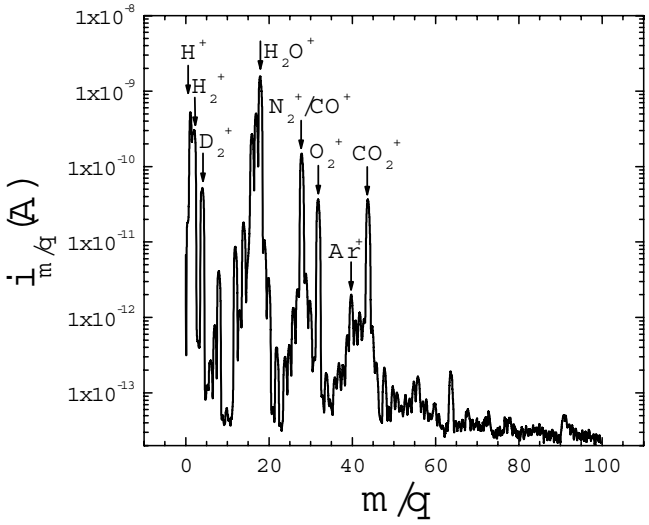

Fig.2.6. Mass spectrum of the residual atmosphere in the vacuum chamber. Ions corresponding to the main current peaks have been indexed. The spectrum has been recorded with the SEMD.

A nice demonstration of the presence of a H_2O-rich residual atmosphere in the vacuum chamber has been obtained from the time evolution of the ionic signals during long-duration measurements. Daily temperature variations induce the condensation/desorption of water vapour at/from the chamber walls, changing the molar fractions of the gases inside it and affecting the relative intensities of the current peaks of the mass spectra. The influence of the ambient temperature on i_{18} peak current is shown in Fig.2.7. The ionic currents coming from the ionization of

other molecules present in the residual atmosphere, such as O_2 and CO/N_2, vary inversely to that shown in Fug.2.7. This is a secondary effect related to the increment of the H_2O pressure that decreases the partial pressures of the other gases. The total pressure monitored by the Penning sensor is also sensitive to ambient temperature variations and has a similar evolution to i_{18}, as can be seen in Fig.2.8. This correlation implies that the main component in the residual atmosphere is H_2O. The slope of the straight line in Fig.2.8 can be used to calibrate the H_2O sensitivity of the QMS with respect to the Penning sensor sensitivity. The obtained result is $(1.26\pm0.01)\cdot10^{-5}$ A mbar^{-1} for Set A QMS operating parameters.

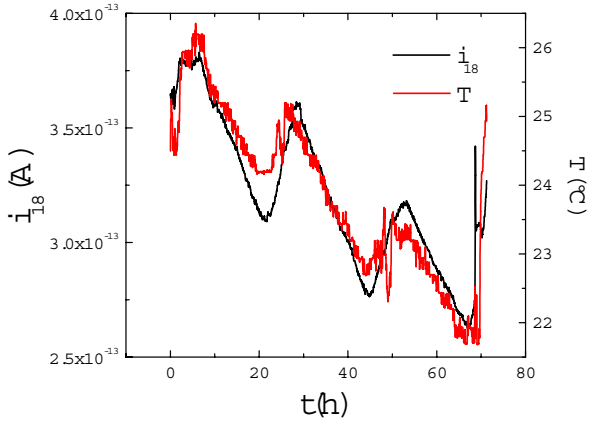

Fig.2.7. Time evolution of ambient temperature (red line) and of the residual H_2O partial pressure (black line) in the vacuum chamber.

It is worthwhile mention the strong influence of the Penning sensor on the residual H_2 partial pressure in the analysis chamber. The i_2 peak current is lowered from 10^{-12} to 10^{-13} A when switching off the Penning sensor. This effect is attributed to the desorption of H_2 molecules from the chamber walls induced by the ionizing current of the Penning sensor.

Given that the gases collected for analysis are drift trough the capillary tube by means of a rotary pump, it is important to check for hydrocarbon partial pressures inside the chamber that could come from pump oil. No important peak currents due to these hydrocarbons have been observed in the *m/q* scans, such as that appearing in Fig.2.6. In addition, a second argument to rule out the presence of significant amounts of hydrocarbons in the vacuum chamber is obtained from the analysis of the i_1 peak current, corresponding to H^+ ions. This peak current can be well expressed as a linear combination of i_2 and i_{18}:

$$i_1 = a_{1/2} i_2 + a_{1/18} i_{18} \tag{2.16}$$

what indicates that the only sources of H^+ ions in the vacuum chamber are H_2 and H_2O and, thus, the partial pressures of hydrocarbons must be negligible. The $a_{1/2}$ coefficient is the ratio between H^+ and H_2^+ ionic contributions coming from the ionization of H_2, *i.e.*, represent the cracking pattern of H_2. Similarly, the $a_{1/18}$ coefficient represents the ratio between H^+ and H_2O^+ ionic contributions coming from the ionization of H_2O. The values of these coefficients have been obtained from the analysis of i_1, i_2 and i_{18} peak currents during long time measurements of the residual atmosphere partial pressures in the vacuum chamber and are listed in Table 2.2. It can be seen that the change of the QMS operating parameters affects the cracking patterns of H_2 and H_2O molecules.

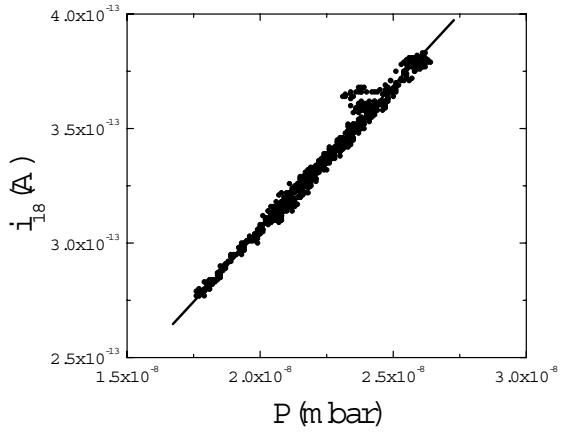

Fig.2.8. Relation between total pressure, monitored by the Penning sensor, and the H_2O partial pressure, monitored by i_{18} peak current, within the vacuum chamber. The solid line represents the linear fit of the experimental data.

Table 2.2. Influence of the QMS operating parameters on the H_2 and H_2O cracking patterns.

QMS parameters	$a_{1/2}$	$a_{1/18}$
Set A	0.066	0.155
Set B	0.087	0.248

2.3.3 Interference of the analyzed gases with the residual atmosphere in the vacuum chamber

The collection of a gas mixture into the analysis chamber modifies the partial pressures of the chemical species forming that mixture and, in addition, the partial

pressures of other species in the residual atmosphere can also change. On the other hand, the exposure of the QMS to chemically active gases may also result in changes in the composition of the residual atmosphere. In particular, H_2O, CO_x and C_mH_n can result from H-plasma interactions with the surface oxides and carbon compounds present in the hot ionizing filament or at the chamber walls [2.3,2.4]. These processes may lead to apparent changes of the QMS sensitivities. The H-plasma induced H_2O formation is of significant interest because it can affect the results of the analysis of the H_2/H_2O mixtures.

In order to check the role of the H_2-induced H_2O formation, some experiments have been performed by introducing H_2-Ar and D_2-Ar mixtures into the QMS. Significant amounts of water molecules have been observed whenever H_2 is introduced into the chamber. In order to quantify this effect the i_{18} peak current (corresponding to H_2O^+ ions) has been plotted against i_2. A typical correlation between i_{18} and i_2 obtained from these experiments is shown in Fig.2.9. The slopes of the i_{18} *vs.* i_2 plots range between $2 \cdot 10^{-3}$ and $5 \cdot 10^{-3}$. No appreciable influence of the QMS operating parameters and of the Penning sensor on these values has been observed. It is worth to say that hysteretic responses of the H_2O^+ ion concentration versus the H_2^+ one have been sometimes observed.

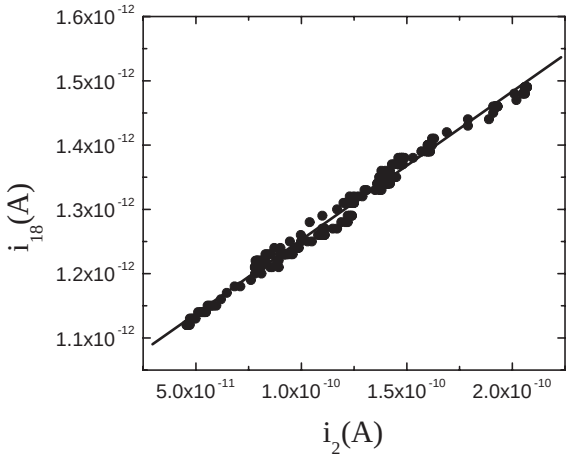

Fig.2.9. Correlation between the i_{18} and i_2 peak currents observed in the analysis of H_2-Ar mixtures. This correlation has been attributed to the H_2-induced H_2O production inside the analysis chamber. The solid line represents the linear fit of the experimental data.

A similar correlation between the HDO and the D_2 partial pressures has been observed in the D_2-Ar analyses. The obtained slopes of the i_{19} *vs.* i_4 plots are close to those ones from the i_{18} *vs.* i_2 plots. Unfortunately, the D_2O partial pressure could

not be measured in these experiments due to the additional contribution of the $^{40}Ar^{2+}$ ion to the i_{20} peak current.

The increment of the H_2O partial pressure can not be attributed to the H_2O impurities present in the used gases. The H_2O level in the H_2-Ar mixture is of a few ppm, whereas the slopes of the i_{18} *vs.* i_2 plots are in the range of 10^{-3}. Other possible explanations for the observed correlation between the H_2O and H_2 partial pressures could be the H_2 displacement of adsorbed water molecules at the chamber walls or the H_2O drift through the H_2 pipeline. However, these possibilities are ruled out by the fact that the H_2O partial pressure does not correlate with the D_2 one in the D_2-Ar probes, whereas the HDO partial pressure does it. On the other hand, the magnitude of the H_2O (HDO) partial pressure increase in the analysis chamber induced by the H_2 (D_2) gas is in agreement with the previous investigations on the H_2-induced H_2O production [2.3,2.4]. One may conclude that the observed correlation between the water and the hydrogen partial pressures is caused by H_2-induced H_2O formation inside the analysis chamber.

The reverse effect, *i.e.*, the H_2O-induced H_2 formation, has been also observed. However, this process seems to occur within the Penning sensor. The analysis of H_2O-Ar mixtures coming from the thermal desorption of $Mg(OH)_2$ (see section 2.5.2) has shown that the ratio between the i_2 and i_{18} peak currents is raised from 0.02 to 0.5 when switching on the Penning sensor.

Finally, it is worth to say that apparent changes in the chemical composition of the residual atmosphere can be eventually induced by the variation of the offset of the instrument. This effect seems to be related to the electronic setup of the QMS and is usually observed when a certain peak current (coming from the ionization of the analyzed gas mixture) changes of scale. In any case, it is easy to identify this effect and to correct the experimental data.

2.4 Hydrogen isotope analysis

The H_2-HD-D_2 analysis has some specific features with respect to the analysis of other gas mixtures. On the one hand, the ionization of H_2-HD-D_2 mixtures in the QMS and the subsequent reactions taking place inside it can produce up to 9 different ions between m/q=1 and 6. This implies that there are some ions which have the same m/q ratio and, then, contribute to the same current peak of the mass spectra. On the other hand, isotope exchange reactions can occur during the analytical procedure and modify the experimental results. In addition, as it has been stated above, mass discrimination effects can be present in several steps of the whole measurement process. Therefore, the detection sensitivities for different gas species will be, in general, different. This will occur even for different isotopes of the same species, such as H_2, HD and D_2. Therefore, the detection sensitivities of the hydrogen molecular isotopes must be determined in order to accomplish quantitative measurements. Several probes must be done in order to check the reproducibility of the obtained results.

2.4.1 Ionic contribution to the peak currents of the mass spectra

In order to relate the current peaks of the mass spectra to the partialflows of the analysed H_2-HD-D_2-Ar mixtures, it is necessary to separate the contribution of different ions to each current peak. The hydrogen-deuterium ions and their reaction mechanisms observed at each m/q value are listed in Table 2.3 [2.12]. Three body reactions for the formation of triatomic ions have been omitted because they are negligible at the usual pressures and temperatures in the analysis chamber.

Table 2.3. H-D ions and their reaction mechanisms observed at m/q values between 1 and 6.

m/q	**Ion**	**Reaction mechanism**	
1	H^+	$H_2 + e^- \rightarrow H^+ + H + 2e^-$	(2.17a)
		$HD + e^- \rightarrow H^+ + D + 2e^-$	(2.17b)
2	D^+	$D_2 + e^- \rightarrow D^+ + D + 2e^-$	(2.18a)
		$HD + e^- \rightarrow D^+ + H + 2e^-$	(2.18b)
	H_2^+	$H_2 + e^- \rightarrow H_2^+ + 2e^-$	(2.19a)
		$H^+ + H_2 \rightarrow H_2^+ + H$	(2.19b)
		$H^+ + HD \rightarrow H_2^+ + D$	(2.19c)
3	HD^+	$HD + e^- \rightarrow HD^+ + 2e^-$	(2.20a)
		$H^+ + D_2 \rightarrow HD^+ + D$	(2.20b)
		$H^+ + HD \rightarrow HD^+ + H$	(2.20c)
		$D^+ + H_2 \rightarrow HD^+ + H$	(2.20d)
		$D^+ + HD \rightarrow HD^+ + H$	(2.20e)
	H_3^+	$H_2^+ + H_2 \rightarrow H_3^+ + H$	(2.21a)
		$H_2^+ + HD \rightarrow H_3^+ + D$	(2.21b)
4	D_2^+	$D_2 + e^- \rightarrow D_2^+ + 2e^-$	(2.22a)
		$D^+ + D_2 \rightarrow D_2^+ + D$	(2.22b)
		$D^+ + HD \rightarrow D_2^+ + H$	(2.22c)
	H_2D^+	$H_2^+ + D_2 \rightarrow H_2D^+ + D$	(2.23a)
		$H_2^+ + HD \rightarrow H_2D^+ + H$	(2.23b)
		$HD^+ + H_2 \rightarrow H_2D^+ + H$	(2.23c)
		$HD^+ + HD \rightarrow H_2D^+ + H$	(2.23d)
5	HD_2^+	$D_2^+ + H_2 \rightarrow HD_2^+ + H$	(2.24a)
		$D_2^+ + HD \rightarrow HD_2^+ + D$	(2.24b)
		$HD^+ + D_2 \rightarrow HD_2^+ + D$	(2.24c)
		$HD^+ + HD \rightarrow HD_2^+ + H$	(2.24d)
6	D_3^+	$D_2^+ + D_2 \rightarrow D_3^+ + D$	(2.25a)
		$D_2^+ + HD \rightarrow D_3^+ + H$	(2.25b)

The contribution of different ions to each current peak can be known by using different combinations of gases. For instance, the molecular ions containing D atoms are not present in the spectra if H_2-Ar mixtures are analysed. Reciprocally, ions containing H atoms are absent by using D_2-Ar mixtures. Following this idea, calibration probes with different combination of gases have been done to determine the ionic contribution to the mass spectra.

2.4.2 H_2 sensitivity

The H_2 sensitivity has been determined by analyzing H_2-Ar mixtures. To this aim, a constant Ar flow (28.8 sccm) has been mixed with a variable H_2 flow in a PVC pipeline connected to the gas analysis system. The Ar flow has been fixed with a flow meter and controller Ucar F 201C-UA, whereas the H_2 flow has been regulated by using conventional valves and measured with a flowmeter Aalborg GFM-171. The typical profile of the H_2 flow variation is shown in Fig.2.10. In order to check for the hysteresis effect on the H_2 analysis, the flow profile has been composed by a sequence of increasing and decreasing flow steps.

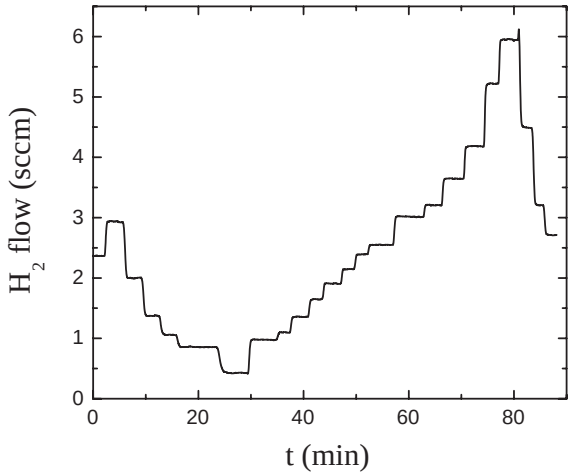

Fig.2.10. Typical H_2 flow profile during the calibration experiments with H_2-Ar mixtures.

The time evolution of i_2 peak current, corresponding to H_2^+ ions, within a given H_2 flow step is shown in Fig.2.11. The ionic current tends to be stationary with a time constant corresponding to the transport time of H_2 gas through the pipeline and the gas analysis system. Time constants of i_1, i_2 and i_3 peak currents are plotted in Fig.2.12 as a function of the H_2 flow. The decrease of time constants when increasing the H_2 flow is due to H_2 transport through the PVC pipeline. This transport time tends to zero at high H_2 flows. Therefore, limiting values of the time

constants allow obtaining an estimation of the transport time of H_2 through the gas analysis system, of the order of 5 s (dashed line in Fig.2.12).

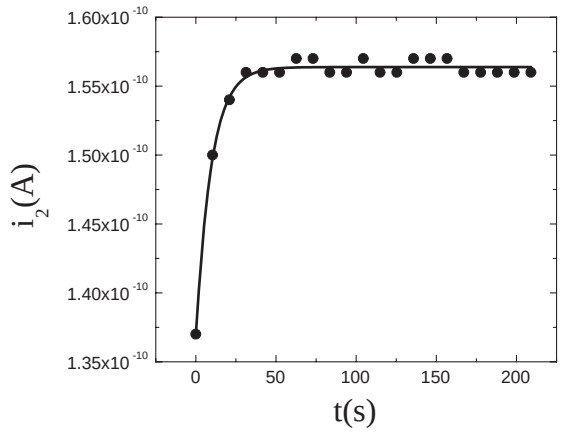

Fig.2.11. Time evolution of i_2 during a typical H_2 flow step. The line represents the fit of the experimental points to the function $i_2(t)=i_2^*+Aexp(-t/\tau_2)$.

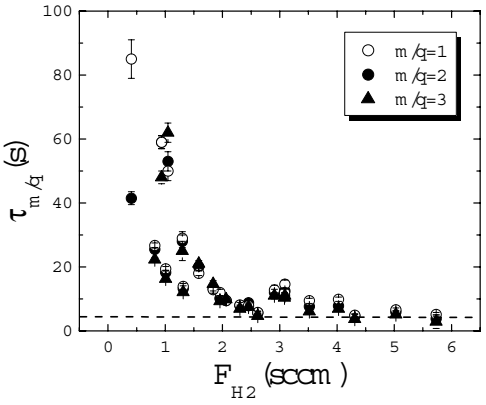

Fig.2.12. Time constants of i_1, i_2 and i_3 peak currents as a function of the H_2 flow. Dashed line represents the limiting value corresponding to the transport time of H_2 through the gas analysis system.

A linear correlation has been found between the stationary values of i_2 peak current and the H_2 partial flow in the analyzed gas mixtures, as can be seen in Fig.2.13. This implies that H_2^+ ions are formed according to reaction (2.19a), and the influence of the second order reactions (2.19b-c) and (2.21a-b) on the H_2^+ concentration is negligible.

The slope obtained from the least square fit of the plot in Fig.2.13 is the QMS sensitivity, σ_2^{H2}, defined in section 2.2.4. The influence of the QMS operating parameters and the Penning sensor on σ_2^{H2} can be seen in Table 2.4. Up to five measurements were done at the same experimental conditions in order to check the reproducibility of the gas analysis system. The standard deviation of the sensitivity is about 2 % in all cases, although the error in the determination of each single sensitivity value is <1 %. It is observed that the change from Set A to Set B parameters produces a sensitivity increase of a factor about 2. No influence of the Penning sensor on σ_2^{H2} values has been observed.

Table 2.4. Influence of the QMS operating parameters and of the Penning sensor on the H_2 detection sensitivity and on the i_1/i_2 and i_3/i_2^2 ratios.

QMS parameters	Penning sensor	# probes	σ_2^{H2}(A)	$a_{1/2}$	$a_{3/2}$(A^{-1})
Set A	On	5	$(2.75\pm0.05)\cdot10^{-9}$	$(6.8\pm0.2)\cdot10^{-2}$	$(7.6\pm0.6)\cdot10^{6}$
Set B	On	1	$(4.76\pm0.07)\cdot10^{-9}$	$(9.87\pm0.04)\cdot10^{-2}$	$(3.6\pm0.3)\cdot10^{6}$
	Off	2	$(4.8\pm0.1)\cdot10^{-9}$	$(8\pm2)\cdot10^{-2}$	$(3.8\pm0.3)\cdot10^{6}$

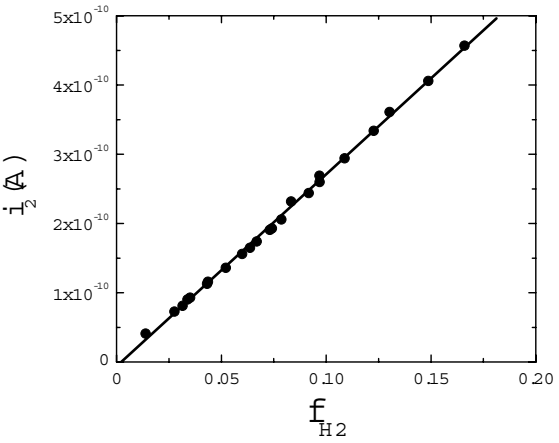

Fig.2.13. Plot of the i_2 stationary values as a function of the partial H_2 flow in H_2-Ar mixtures. Black points are the experimental values, whereas the line represents the least square fit of the experimental data.

To make an estimation of the detection limit of the whole experimental system for H_2, one should consider the case of small H_2 flows (compared to the carrier Ar flow). In this case, the H_2 partial flow can be considered proportional to the H_2 flow and, according to equation (2.14), the i_2 peak current will be directly proportional to the H_2 flow. The constant of proportionality is the absolute detection sensitivity (*i.e.*, the ionic current per H_2 mol-per-second). Absolute H_2 detection sensitivities at m/q=2 are $1.28 \cdot 10^{-4}$ and $2.23 \cdot 10^{-4}$ A $mol^{-1}H_2$ s for Set A and Set B parameters, respectively. These values imply that the minimum detectable H_2 flow in our experimental system is of the order of 10^{-9}-10^{-8} $molH_2$ s^{-1}, given that the minimum ionic current increments detectable with the Faraday detector are typically in the range of 10^{-13}-10^{-12} A. The use of the SEMD detector can decrease the minimum detectable H_2 flow in 2 or 3 orders of magnitude.

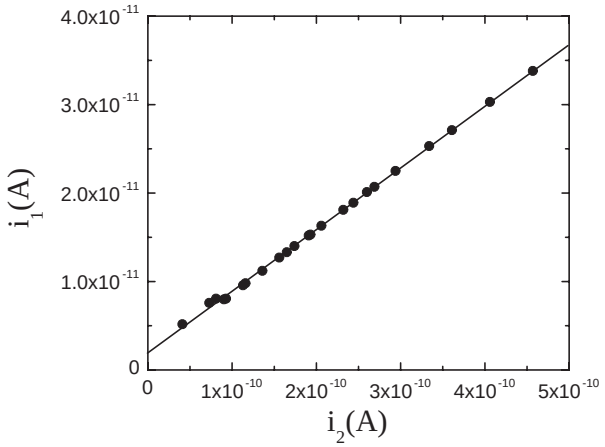

Fig.2.14. Experimental correlation between i_1 and i_2 peak currents observed during the analysis of H_2-Ar mixtures. Black points are the experimental values, whereas the line represents the least square fit of the experimental data.

The i_1 peak current has been also found proportional to the H_2 partial flow, what implies that H^+ ions are formed by means of reaction (2.17a). In this case, however, it is more convenient to relate i_1 with i_2 instead of the partial H_2 flow:

$$i_1 = a_{1/2} i_2 \tag{2.24}$$

A linear correlation is observed between both peak currents, as it can be seen in Fig.2.14. The $a_{1/2}$ coefficients, obtained from the linear fit of experimental data, are shown in Table 2.4. Typical errors in $a_{1/2}$ are lower than 1 %. However, the

errors appearing in Table 2.4 have been taken from the standard deviation of all the measurements, of the order of 8 %. Note that $a_{1/2}$ values are in agreement with those obtained during the analysis of the residual atmosphere in the vacuum chamber (see Table 2.2).

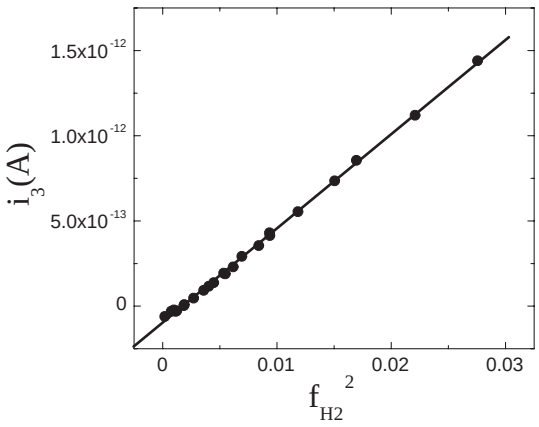

Fig.2.15. Experimental correlation between i_3 peak current (due to the H_3^+ ion) and the square of the H_2 partial flow. The solid line is the linear fit to the experimental data.

The i_3 peak current has been found to vary as the square of the H_2 partial flow, as shown in Fig.2.15. In principle, this peak current is due to the contribution of H_3^+ and HD^+ ions. The former is formed by the bimolecular reaction (2.21a) between a H_2^+ molecular ion and a H_2 molecule, what is consistent with a quadratic H_2 partial flow dependence. The contribution of the HD^+ ion to the i_3 peak current comes from the ionization of HD molecules present in the H_2 gas, giving a linear dependence with the H_2 flow, instead of a quadratic one. Therefore, from the experimental correlation shown in Fig.2.15 it can be concluded that the i_3 peak current is mainly due to the contribution of the H_3^+ ion. The isotopic fraction of HD molecules in H_2 should be of the order of 10^{-4}, *i.e.*, the natural isotopic fraction of H and D in the earth, although this fraction could be lowered to about 10^{-5} due to the isotope fractionation occurring during the H_2 production and purification processes. The quotient between i_3 and i_2 peak currents is about 10^{-3}, *i.e.*, one or two orders of magnitude higher than the expected HD/H_2 ratio. This fact supports the hypothesis that, in the analysis of H_2+Ar mixtures, the i_3 peak current is mainly due to the H_3^+ ionic contribution. It is concluded that for determining the HD concentration in hydrogen mixtures with a low HD/H_2 ratio (lower than about 0.1), the precise calibration of the H_3^+ ion contribution to the i_3 peak is imperative. To

this purpose, it is useful to relate i_3 peak current corresponding to H_3^+ ions with the square of i_2:

$$i_3 = a_{3/2} i_2^{\,2} \tag{2.25}$$

The obtained values of the $a_{3/2}$ parameter are also included in Table 2.4. These values must be used to subtract the H_3^+ ionic contribution to i_3 whenever quantitative HD measurements are to be done.

On the other hand, according to the observed i_3/i_2 ratios, it is deduced that the overall H_2^+ ion concentration is not essentially affected by the second order reaction (2.21a) and, thus, the relation between i_2 peak current and the H_2 partial flow keeps linear. However, this linearity would be disrupted at higher H_2 partial pressures inside the analysis chamber.

2.4.3 D_2 sensitivity

The D_2 detection sensitivity has been obtained from the analysis of D_2-Ar mixtures. The experimental procedure is similar to that described in the preceding section for the analysis of H_2-Ar mixtures.

The dependence of i_4 peak current, corresponding to D_2^+ ions, with the partialD_2 flow in the analyzed gas mixtures is shown in Fig.2.16. A clear influence of the Penning sensor on i_4 values is seen. Switching on the Penning sensor decreases the D_2 sensitivity, σ_4^{D2}, by roughly a 10 %. This behaviour has been ascribed to ion-molecule isotope exchange reactions between D_2 and H-containing molecules present in the residual atmosphere in the analysis chamber, mainly H_2O and H_2. Such reactions decrease the D_2 concentration in the analysis chamber and, therefore, lower D_2^+ ionic currents are observed. This hypothesis is further supported from the analysis of the HD^+ and H_2^+ ionic currents dependence with the D_2 partial flow, as it will be shown below. Therefore, one may conclude that the Penning sensor should be switched off whenever quantitative D_2 or H_2-HD-D_2 analyses are to be done.

Table 2.5. Influence of the QMS operating parameters and of the Penning sensor on the D_2 detection sensitivity and on the i_2/i_4 and i_6/i_4^2 ratios.

QMS parameters	Penning sensor	# probes	σ_4^{D2}(A)	$a_{2/4}$	$a_{6/4}$(A^{-1})
Set A	On	4	$(6\pm2)\cdot10^{-10}$	-	$(1.4\pm0.1)\cdot10^{7}$
	Off	1	$(6.6\pm0.1)\cdot10^{-10}$	$(1.46\pm0.01)\cdot10^{-2}$	$(1.2\pm0.1)\cdot10^{7}$
Set B	On	3	$(8.7\pm0.5)\cdot10^{-10}$	-	$(6.7\pm0.2)\cdot10^{6}$
	Off	3	$(9.4\pm0.5)\cdot10^{-10}$	$(1.37\pm0.02)\cdot10^{-2}$	$(5.8\pm0.3)\cdot10^{6}$

The D_2 detection sensitivities are listed in Table 2.5. Absolute detection sensitivities (for low D_2 flows compared to the Ar flow) with Set A and Set B

parameters are equal to $3.1 \cdot 10^{-5}$ and $4.4 \cdot 10^{-5}$ A $mol^{-1}D_2$ s, respectively (Penning sensor off). When comparing σ_4^{D2} values with these obtained for H_2 (Table 2.4), an important isotope effect is observed. This is attributed to the mass discrimination effects present in gas collection, ionization, filtering and detection processes described in section 2.2. This point will be discussed in detail in section 2.6.2.

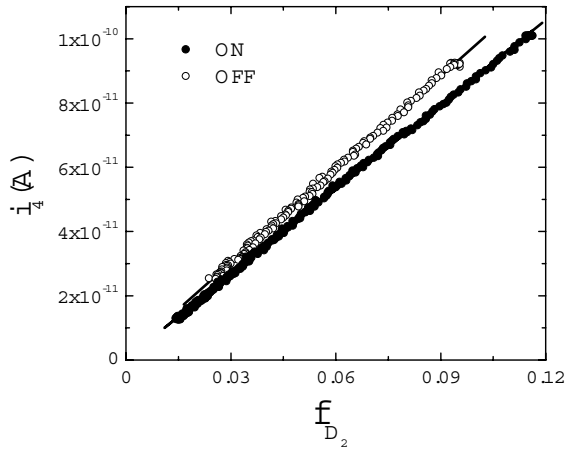

Fig.2.16. Plot of i_4 peak current as a function of the D_2 partial flow in D_2-Ar mixtures. The influence of the Penning sensor on i_4 is shown. Full and open circles have been respectively obtained by switching on and off the Penning sensor. The solid lines represent the least square fit of experimental data points.

Due to the fact that D_2 gas used for calibration experiments is not isotopically pure (the H concentration is ~1.5 %), a small amount of H_2 and HD molecules are also present in the analyzed D_2-Ar mixtures. Equilibrium is assumed among the three molecular isotopes, according to the isotope exchange reaction:

$$H_2 + D_2 \Leftrightarrow 2HD \tag{2.28}$$

Therefore, the relative concentrations of the hydrogen molecular isotopes are determined by the equilibrium constant:

$$K_{eq} = \frac{[HD]^2}{[H_2] \cdot [D_2]} \tag{2.29}$$

which is equal to 3.27 at 298 K [2.13]. This value implies that the H_2 concentration in the analyzed gas mixtures is about two orders of magnitude lower than the HD one. Therefore, it can be reasonably assumed that nearly all the H atoms are forming HD molecules.

The i_3 peak current is plotted in Fig.2.17 as a function of the D_2 partial flow. Due to the low H_2 content in the analyzed gas, the influence of H_3^+ ions to i_3 can be neglected and it can be safely assumed that this peak current corresponds exclusively to HD^+ ions. Again, a clear influence of the Penning sensor is observed. The measurements done with the Penning sensor switched off show a linear correlation between i_3 and f_{D2}, as expected. However, a non-linear behaviour is observed when switching on the Penning sensor. Moreover, higher HD^+ ionic signals are observed in this case. These phenomena have been also attributed to the above mentioned isotope exchange reactions taking place within the total pressure analyzer. The higher HD^+ ionic currents concur with the lower D_2^+ signals observed when switching off the Penning sensor.

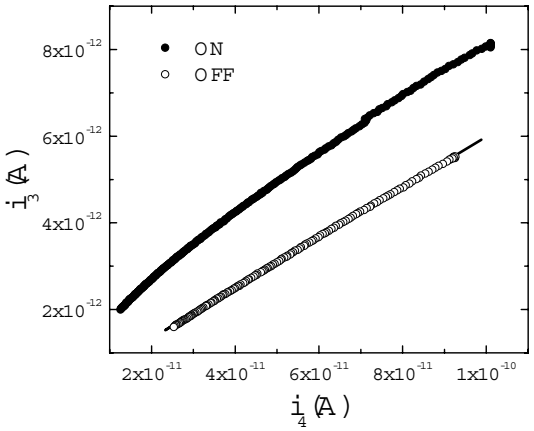

Fig.2.17. Experimental correlation between the i_3 peak current (corresponding to HD^+ ions) and the D_2 partial flow. Full and open circles refer to calibration experiments with the Penning sensor switched on and off, respectively. The solid line is the linear fit to the experimental data with the Penning sensor switched off.

The Penning sensor has also a strong effect on the i_2 peak current. This current is plotted in Fig.2.18 as a function of i_4. Again, a linear relation is obtained when the sensor is switched off, but this relation is non-linear when it is on. In principle, i_2 should be exclusively attributed to D^+ ions, because the estimated H_2 concentration in D_2 gas is about 0.01% (see above) and the observed i_2/i_4 ratio is two orders of magnitude higher, as can be seen in Table 2.5. However, the increment of i_2 peak current observed when the sensor is switched on seems to be

related to the contribution of H_2^+ ions formed by isotope exchange between D_2 molecules and the residual gas atmosphere in the Penning sensor.

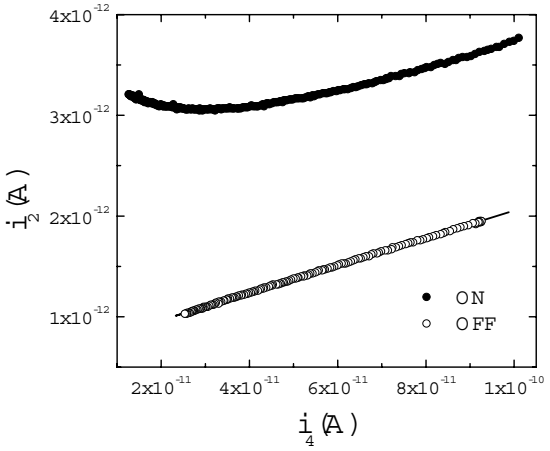

Fig.2.18. Experimental correlation between i_2 and i_4 peak currents obtained from the analysis of D_2-Ar mixtures. Full and open circles refer to calibration experiments with the Penning sensor switched on and off, respectively. The solid line represents the linear fits to the experimental data obtained with the Penning sensor switched off.

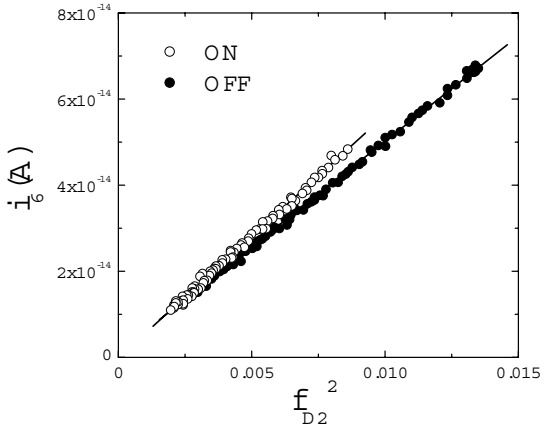

Fig.2.19. Experimental correlation between the i_6 peak current (corresponding to D_3^+ ions) and the square of the D_2 partial flow. Full and open circles refer to calibration experiments with the Penning sensor switched on and off, respectively. The solid lines are the least square fits to the experimental data.

Finally, the D_3^+ ionic signal has been analyzed. In Fig.2.19, the i_6 peak current is plotted versus the square of the D_2 partial flow. The linear correlation observed in this figure indicates that D_3^+ ions are formed according to reaction (2.25a). The observed i_6/i_4^2 ratios are listed in Table 2.5. The higher i_6 values observed when the Penning sensor is switched on seems to be due to the additional formation of D_3^+ ions within the ion source of this sensor.

2.4.4 Influence of isotope exchange reactions

In this section, the influence of isotope exchange reactions on the analysis of H_2-HD-D_2 mixtures is investigated. This is an important task because those reactions can alter the relative populations of H_2, HD and D_2 molecules during the measurement itself, and, therefore, modify the experimental results.

Two types of isotope exchange reactions will be distinguished: i) between neutral molecules and ii) between molecular ions and neutral molecules. The former reactions can be homogeneous or catalysed by the surfaces present in the experimental system. They can occur during the transport of gases to the analysis chamber or within it. On the other hand, ion-molecule reactions occur in the ionization sources of the QMS and the Penning sensor.

The influence of the homogeneous exchange reaction (2.28) during the transport of molecules to the analysis chamber and within it, is now examined. Numerous investigations (see for example [2.14] and references therein) on the kinetics and mechanism of the homogeneous reaction (2.28) have been carried out since the first series of experiments accomplished by Farkas and Farkas [2.15] in 1935. These studies were performed in single pulse shock tubes with H_2-D_2-Ar mixtures. Although the experimental results obtained by various authors differ considerably, no HD formation has been observed below 1100 K. This result excludes the possibility of having an isotope exchange via reaction (2.28) at the pressure and temperature conditions of the present experiments. Further evidences on the negligible rates of the forward and reverse reactions of isotope exchange (2.28) at RT have been found. Hydrogen isotopic mixtures prepared at some temperature and stored in an inert vessel (of glass, for example) at RT, had H_2, HD and D_2 relative concentrations given by the equilibrium constant at the preparation temperature, even if the mixtures were stored for a long period [2.16,2.17]. It is concluded that the measured H_2, HD and D_2 flows are not essentially influenced by the homogeneous exchange reaction (2.28) during the transport of molecules to the analysis chamber.

The influence of homogeneous exchange reactions between hydrocarbons and water impurities, present in the experimental system, with hydrogen molecular isotopes can also be neglected. Rate constants of the isotope exchange between D_2O and H_2 were reported by Lécluse and Robert [2.18]. The same authors also reported the rate constants of isotopic exchange between CD_4 and H_2. Their results can be used to estimate the rates of isotopic exchange reactions between hydrogen

molecules and hydrocarbons. Taking into account the values of these rate constants, very long times would be required to produce an appreciable effect in the relative H_2, HD and D_2 populations. In addition, Lécluse and Robert found that the catalytic effects on charcoal, silica, phyllosilicates and iron were negligible, what excludes the possibility of having a catalytic effect induced by the surfaces present in our experimental system (PVC tubing, quartz capillary tube and stainless steel) over the typical time scales of the gas analysis process.

On the other hand, the rate constants of ion-molecule isotope exchange are usually much higher than between neutral molecules. Indeed, the results presented in the preceding section have shown the influence of isotope exchange between D_2 and H-containing molecules that take place within the Penning sensor. Such reactions increase the HD concentration in the analysis chamber at the expense of the D_2 one.

In order to investigate the role of ion-molecule isotope exchange within the ionization source of the QMS, calibration experiments have been done with H_2-D_2-Ar mixtures with the Penning sensor switched off. Typical temporal profiles of the H_2 and D_2 flows during these experiments are shown in Fig.2.20. It can be seen that the H_2 and D_2 flows were profiled by maintaining one constant and varying the other one and vice versa. The Ar flow was constant and equal to 28.8 sccm.

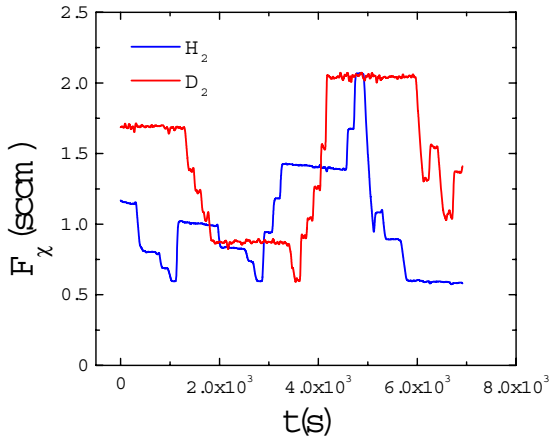

Fig.2.20. Temporal profiles of H_2 (blue line) and D_2 (red line) flows during the analysis of H_2-D_2-Ar mixtures.

According to the results obtained in section 2.4.3, the D_2 concentration can be monitored by measuring i_4, which correspond to D_2^+ ions. The observed correlation between D^+ and D_2^+ ionic currents must be used to subtract the D^+ contribution to i_2 and then calculate the H_2^+ ionic current. H_2^+ and D_2^+ ionic currents have been

plotted as a function of the H_2 and D_2 partial flows, respectively, and results are shown in Fig.2.21. As for the analysis of H_2-Ar and D_2-Ar mixtures, linear behaviours are observed. The sensitivities σ_2^{H2} and σ_4^{D2} obtained from the slopes of the linear fits of the data appear in Table 2.6. No significant differences (<5 %) are observed between these values and those obtained in the analysis of H_2-Ar and D_2-Ar mixtures (see Tables 2.4 and 2.5).

Table 2.6. Influence of the QMS operating parameters on the H_2 and D_2 detection sensitivities obtained from the analysis of H_2-D_2-Ar mixtures.

QMS parameters	# probes	σ_2^{H2}(A)	σ_4^{D2}(A)
Set A	1	$(2.75\pm0.05)\cdot10^{-9}$	$(6.3\pm0.1)\cdot10^{-10}$
Set B	2	$(4.5\pm0.1)\cdot10^{-9}$	$(9.9\pm0.4)\cdot10^{-2}$

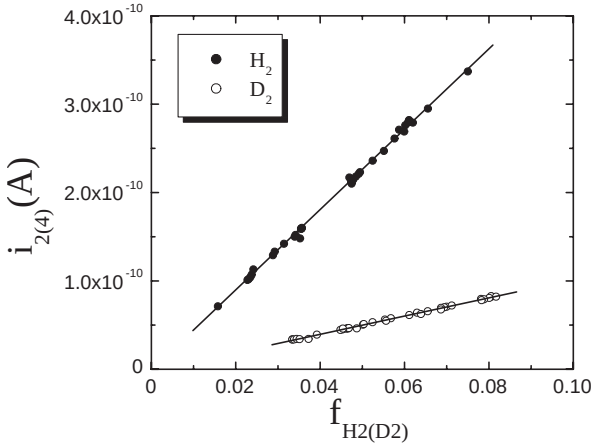

Fig.2.21. Experimental correlation between the H_2^+ and D_2^+ ionic currents with the H_2 and D_2 partial flows, respectively, obtained from the analysis of H_2-D_2-Ar mixtures. The solid lines are the least square fits to the experimental data.

On the other hand, small amounts of HD^+ ions are formed within the ionization source of the QMS during the analysis of H_2-D_2-Ar mixtures. The HD^+ ionic current has been calculated by subtracting the H_3^+ ionic contribution to i_3. By comparing HD^+ ionic currents obtained with D_2-Ar and H_2-D_2-Ar mixtures, it can be concluded that the mole number of HD^+ ions formed by isotope exchange is below 2 % of the D_2^+ one. The mechanism of HD^+ ion formation has been deduced from the observed correlation between HD^+ ionic current and the product of D_2 and

H_2O concentrations, as shown in Fig.2.22. This reveals that HD^+ is formed during the measurements according to the exchange reaction:

$$D_2^+ + H_2O \rightarrow HD^+ + HDO \tag{2.30}$$

The isotope exchange reaction (2.30) has also been observed by Stahl *et al.* [2.19] when analysing D_2 gas by mass spectrometry.

In summary, it can be concluded that the relative concentrations H_2 and D_2 molecules in the analyzed H_2-D_2-Ar mixtures are not essentially affected by isotope exchange reactions occurring during gas transport, within the analysis chamber or at the ion source of the QMS. Therefore, the influence of isotope exchange reactions on the quantitative analysis of H_2-D_2 mixtures can be neglected.

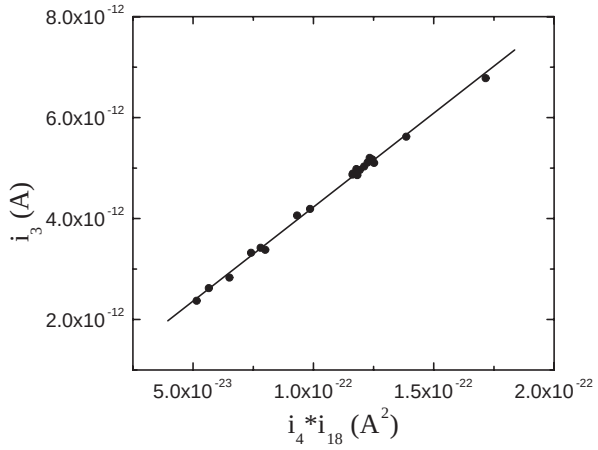

Fig.2.22. Experimental correlation between the i_3 peak current corresponding to HD^+ ions and the product of i_4 and i_{18}, corresponding to D_2^+ and H_2O^+ ions, respectively, obtained during the analysis of H_2-D_2-Ar mixtures. The solid line represents the linear fit to the experimental data.

2.4.5 HD sensitivity

Due to the strong isotope effect observed when comparing the H_2 and D_2 detection sensitivities, it is expected that mass discrimination effects also affect the sensitivity of HD. Additional experimental probes have been done to determine the HD sensitivity. However, due to the difficulty to prepare pure HD, the determination of σ_3^{HD} has been based on experiments with H_2-HD-D_2-Ar mixtures instead of HD-Ar. Hydrogen molecular isotopic mixtures have been prepared in two different ways, which are described in detail below.

Firstly, H_2-HD-D_2 mixtures have been obtained from a mixture of H_2 and D_2 gases. The H_2-D_2 mixture has been done in a Sievert's type apparatus and it has been stored into an Al bottle. It is worth to note that H_2 and D_2 molecules have to form a homogeneous mixture when mixed in the Sievert's apparatus. To make an estimation of the time required to this aim, the diffusion coefficient of H_2 in D_2 must be considered. At 1 atm and 288 K it is equal to 1.240 cm^2 s^{-1} [2.20]. This value implies that the time required to forming a homogeneous H_2-D_2 mixture in the mixing volume of the Sievert's apparatus is of the order of 2 hours.

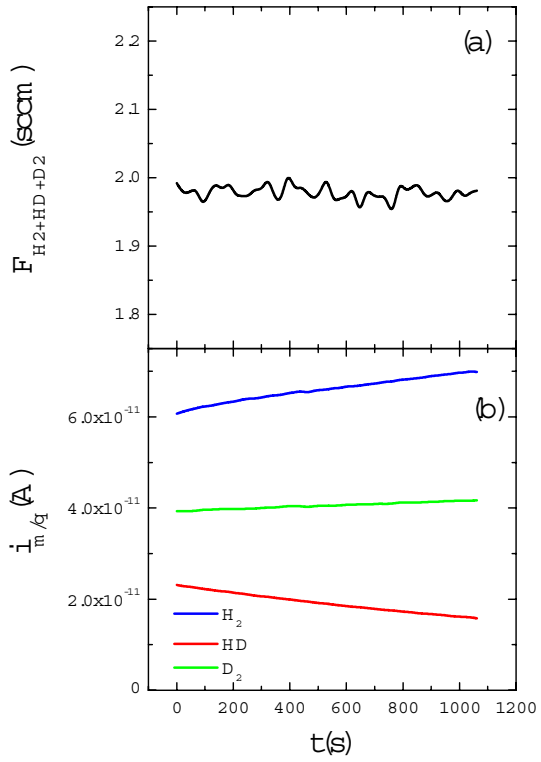

Fig.2.23. Temporal profiles of the total H_2-HD-D_2 flow (a) and the QMS peak currents corresponding to H_2^+, HD^+ and D_2^+ ions (b).

On the other hand, in order to form HD molecules from isotope exchange between H_2 and D_2, some catalyst must be used because, as it has been stated in section 2.4.4, reaction rates of the homogeneous exchange reaction (2.28) are very low at the experimental conditions of pressure and temperature in the H_2-D_2 bottle. It was found that the stainless steel pressure regulator connected to the H_2-D_2 bottle slowly catalyzes (within a period of several hours) the isotope exchange reaction

(2.28). This finding was used to produce a H_2-HD-D_2 isotopic mixture in the pressure regulator volume from a portion of the H_2-D_2 gas stored in the bottle. The rest of H_2 and D_2 molecules were maintained separately from the H_2-HD-D_2 mixture by closing the valve of the H_2-D_2 bottle. The idea was to produce a gas flow with variable isotopic composition to determine σ_3^{HD}. When opening simultaneously the valve of the H_2-D_2 bottle and the exit valve of the pressure regulator, a constant flow with variable isotope composition was created. This flow was mixed with a constant Ar flow (28.8 sccm) before entering the gas analysis system. The temporal profiles of the total H_2+HD+D_2 flow (measured with a flow-meter) and of the i_2, i_3 and i_4 peak currents corresponding to H_2^+, HD^+ and D_2^+ ions, respectively, are plotted in Fig.2.23a and b, respectively. The total H_2-HD-D_2 flow produced in this way had a good stability.

Fluctuations in the gas flow signal shown in Fig.2.23a are within ±1% and are mainly attributed to the electric noise in the output signal of the flowmeter. In spite of the constancy of the total H_2-HD-D_2 flow, variable partial flows of H_2, HD and D_2 were obtained (see the time evolution of the i_2, i_3 and i_4 peak currents in Fig.2.23b. By using σ_2^{H2} and σ_4^{D2} values obtained in sections 2.4.2 and 2.4.3, the H_2 and D_2 flows can be calculated from i_2 and i_4 and then substracted from the total H_2-HD-D_2 flow to obtain the HD flow. Then, HD^+ ionic contribution to i_3 can be related to the partial HD flow of the analyzed gas mixture to determine σ_3^{HD}, as shown in Fig.2.24.

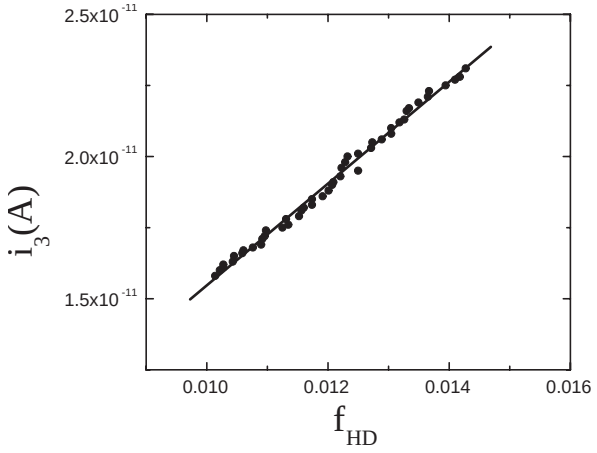

Fig.2.24. Experimental correlation between the i_3 peak current corresponding to HD^+ ions and the HD relative flow obtained from the analysis of H_2-HD-D_2-Ar mixtures. The solid line is the least square fit to the experimental data.

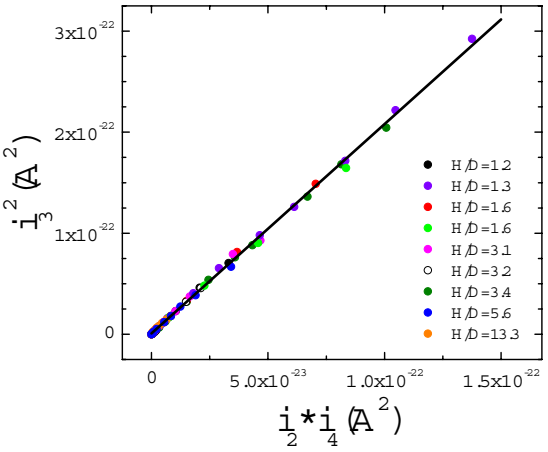

Fig.2.25. Plot of the square of HD^+ ionic current *vs.* the product of H_2^+ and D_2^+ ones obtained from the analysis of H_2-HD-D_2 mixtures evolved from the electrolysis of 0.1M LiOH-LiOD electrolytes. The legend shows the H/D ratio in the evolved gases. The solid line is the linear fit to the experimental data.

The second method used to determine the HD detection sensitivity is based on the analysis of H_2-HD-D_2 flows evolved from the electrolysis of H_2O/HDO/D_2O mixtures. This subject will be treated in detail in Chapter 3, which is devoted to the investigation of H/D electrolytic separation factors. Pt foils were used as cathodes during the hydrogen-deuterium evolution reaction (HER-DER) in 0.1M LiOH-LiOD electrolytes. On applying a constant electrolytic current through the cell, the H_2-HD-D_2 flow reaches, after a transient time (see section 3.4.3.1), a steady state value proportional to the electrolytic current imposed to the cell, according to Faraday's law. By changing the H/D ratio in the electrolytes, the mole fractions of H_2, HD and D_2 in the evolved gases are also varied. However, the relation among the hydrogen molecular isotopes is independent of the electrolytic current, the H/D ratio in the evolved gases and the Pt electrodes used for the HER-DER and is only determined by the equilibrium constant of reaction (2.28), given by equation (2.29). In Fig.2.25, the square of HD^+ ionic current is plotted against the product of H_2^+ and D_2^+ ones for various gas mixtures with different H/D ratios. A nice agreement is observed among the different experimental data appearing in this figure. According to equations (2.14) and (2.29), the slope (Λ) of the experimental points in this figure must be equal to:

$$\Lambda = \frac{\sigma_2^{H2}\sigma_4^{D2}}{\left(\sigma_3^{HD}\right)^2} K_{eq} \tag{2.31}$$

Therefore, equation (2.31) allows determining σ_3^{HD} from Λ, σ_2^{H2}, σ_4^{D2} and K_{eq} values. σ_3^{HD} values obtained from these two methods with Set A and Set B QMS parameters are listed in Table 2.7. It can be seen that σ_3^{HD} values lie between σ_2^{H2} and σ_4^{D2} ones. It can also be observed that the change of the operating parameters does not essentially affect to the HD detection sensitivity.

Table 2.7. Influence of the QMS operating parameters on HD detection sensitivity.

QMS parameters	σ_3^{HD}(A)
Set A	$(1.7\pm0.1)\cdot10^{-9}$
Set B	$(1.8\pm0.1)\cdot10^{-9}$

2.5 Other gases

2.5.1 Ar sensitivity

The Ar detection sensitivity has been obtained from the analysis of the H_2-Ar, D_2-Ar and H_2-D_2-Ar mixtures already described in sections 2.4.2-2.4.5. Although the Ar flow was maintained constant in these experiments, the variation of H_2 and D_2 flows produced a variation of the partial Ar flow.

The main current peak coming from the ionization of the Ar atoms is due to the $^{40}Ar^+$ ion. The typical experimental correlation between the i_{40} peak current and the partial Ar flow of the analysed gas mixtures is shown in Fig.2.26. The Ar detection sensitivity (σ_{40}^{Ar}) has been obtained from the slope of these plots. It can be seen that the dispersion of the experimental points in Fig.2.26 is higher than those obtained for H_2, HD and D_2 (see Figs.2.13, 2.16 and 2.24). In addition, the standard deviation among the individual σ_{40}^{Ar} values obtained in different experiments is also higher. Those effects have been attributed to the higher values of the partialAr flow as compared to the H_2, HD and D_2 ones. The measurements at high partial flows are less sensitive than at low ones due to the appearance of non-linear effects.

Table 2.8. Influence of the QMS operating parameters and of the Penning sensor on the Ar detection sensitivity.

QMS parameters	Penning sensor	# probes	σ_{40}^{Ar}(A)
Set A	On	6	$(1.2\pm0.2)\cdot10^{-10}$
	Off	2	$(1.2\pm0.2)\cdot10^{-10}$
Set B	On	3	$(3.4\pm0.3)\cdot10^{-10}$
	Off	9	$(3.3\pm0.3)\cdot10^{-10}$

The mean σ_{40}^{Ar} values obtained from all the calibration experiments are listed in Table 2.8. No influence of the Penning sensor on σ_{40}^{Ar} can be observed. By contrast, the change from Set A to Set B operating parameters has a strong influence on σ_{40}^{Ar}, as for the H_2, HD and D_2 detection sensitivities.

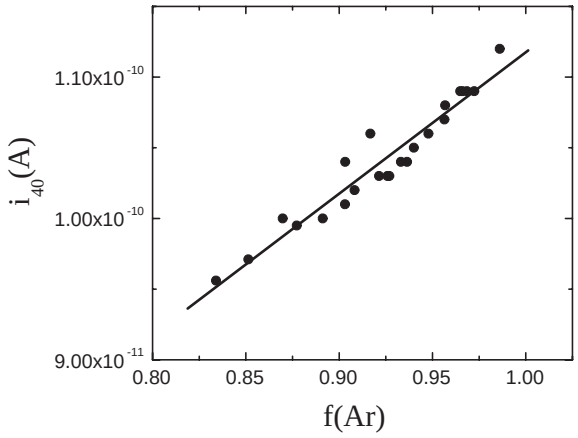

Fig.2.26. Plot of the i_{40} peak current as a function of the partial Ar flow obtained from the analysis of a D_2-Ar mixture. The solid line is the linear fit to the experimental data.

The $^{36}Ar^+$ ionic contribution to i_{36} has been also investigated. The typical correlation between the i_{36} and i_{40} peak currents is plotted in Fig.2.27. A linear dependence is observed, whose slope is equal to $a_{36/40}=(3.49\pm0.01)\cdot10^{-3}$. This value is slightly higher than the natural $^{36}Ar/^{40}Ar$ isotopic ratio, equal to $3.38\cdot10^{-3}$. This difference can be attributed to an isotopic composition of the Ar gas different from the natural composition, but also to the mass discrimination effects present in the gas analysis process due to the 10 % of difference between the atomic masses of both isotopes.

The ratio between the $^{40}Ar^{2+}$ and the $^{40}Ar^+$ peak currents coming from the ionization of ^{40}Ar has been also determined, as shown in Fig.2.28. This ratio is equal to $a_{20/40}=0.392\pm0.002$ and 0.313 ± 0.002 for Set A and Set B parameters, respectively. The corresponding ratio between the $^{36}Ar^{2+}$ and the $^{36}Ar^+$ peak currents could not be obtained due to the influence of the H_2O^+ ionic contribution to the i_{18} peak current. However, this ratio is estimated to be equal to $a_{20/40}$. From the obtained $a_{36/40}$ and $a_{20/40}$ factors and the typical i_{40} peak current values it is deduced that the ionic contribution of the $^{36}Ar^{2+}$ ions to the i_{18} peak current is in the range of 10^{-13} A, which is about one order of magnitude lower than the typical H_2O^+ ionic contribution. Contrary to that, the $^{40}Ar^{2+}$ ion contribution to i_{20} is much higher than the D_2O^+ one.

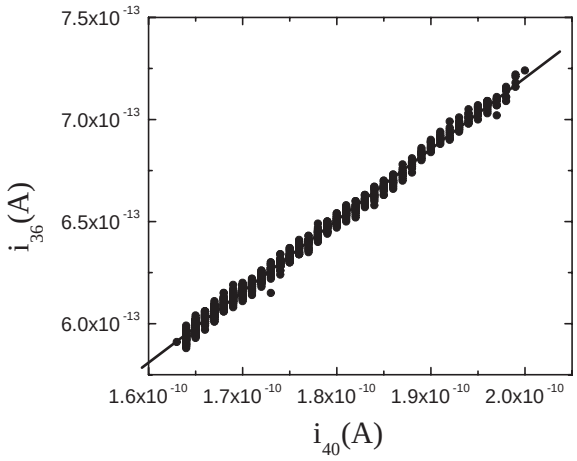

Fig.2.27. Plot of the i_{36} peak current as a function of the i_{40} one obtained from the analysis of a D_2-Ar mixture. The solid line is the linear fit to the experimental data.

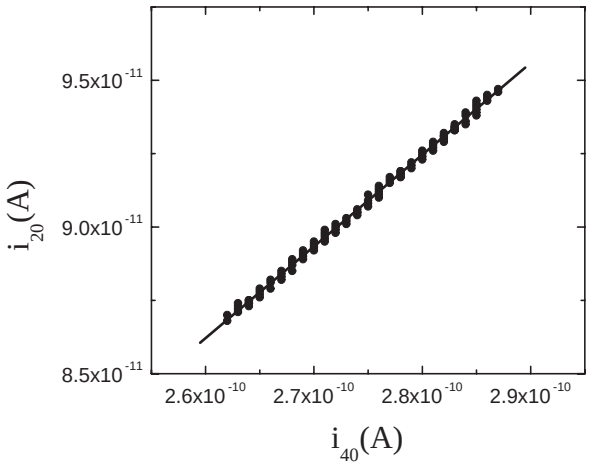

Fig.2.28. Plot of the i_{20} peak current as a function of the i_{40} one obtained from the analysis of a D_2-Ar mixture. The solid line is the least square fit to the experimental data.

Another interesting observation relies on the formation of the ArH^+ and ArD^+ molecular ions. Those ions are produced by ion-molecule reactions between the Ar and the H_2/HD/D_2 species present in the analysis chamber [2.21]. The peak

currents associated to these ions, namely i_{41} and i_{42}, respectively, have been found to vary linearly with the H_2^+ and D_2^+ peak currents in the Ar+H_2 and Ar+D_2 analyses, as shown in Fig.2.29. The slopes of the experimental points in these figures (namely, $a_{41/2}$ and $a_{42/4}$) appear in Table 2.9. As a matter of fact, the $a_{42/4}$ factors are higher than the $a_{41/2}$ ones. The change from Set A to Set B QMS parameters produces a rise of the $a_{41/2}$ factors, but has a slight influence on the $a_{42/4}$ ones. Finally, it must be noted that the Penning sensor has no influence on the $a_{41/2}$ factors, but it has a small influence on the $a_{42/4}$ factor. This should be attributed to the role of the already mentioned isotope exchange reactions occurring within the Penning sensor.

Table 2.9. Influence of the QMS operating parameters and of the Penning sensor on the $a_{41/2}$ and $a_{42/4}$ factors.

QMS parameters	Penning sensor	$a_{41/2}$	$a_{42/4}$
Set A	On	$(2.8\pm0.1)\cdot10^{-3}$	$(4.5\pm0.2)\cdot10^{-3}$
Set B	On	$(3.9\pm0.1)\cdot10^{-3}$	$(5.1\pm0.1)\cdot10^{-3}$
	Off	$(3.9\pm0.1)\cdot10^{-3}$	$(4.8\pm0.1)\cdot10^{-3}$

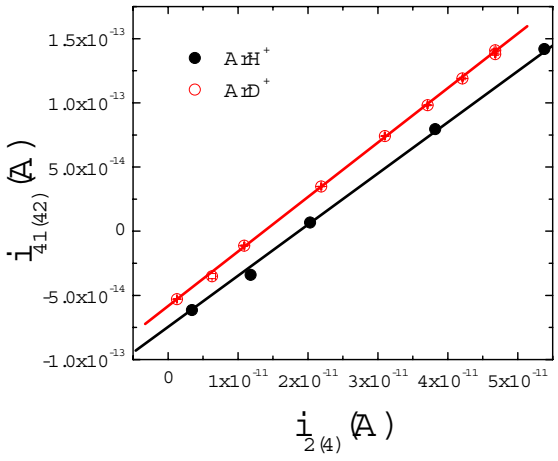

Fig.2.29. Plot of the i_{41} and i_{42} peak currents corresponding to ArH^+ and ArD^+ ions as a function of the i_2 and i_4 ones, respectively, obtained during the analysis of H_2-D_2-Ar mixtures. The solid lines are the linear fits to the experimental data.

2.5.2 H_2O sensitivity

The H_2O detection sensitivity has been obtained from the analysis of the thermal desorption of H_2O from $Mg(OH)_2$ (Panreac). The $Mg(OH)_2$ samples have been

heated in a Differential Scanning Calorimeter and the desorbed H_2O flows have been carried to the gas analysis system by means of a constant Ar flow. Further details of the TDS-DSC technique are given in Chapter 4.

The H_2O desorption reaction is expressed as:

$$Mg(OH)_2 \Rightarrow MgO + H_2O \tag{2.32}$$

According to this reaction, the amount of desorbed H_2O molecules can be known from the initial mass of the $Mg(OH)_2$ samples. Therefore, σ_{18}^{H2O} can be obtained by relating the integral of the i_{18} peak current (substracting the i^0_{18} base line) to the H_2O molar fraction in the H_2O-Ar mixture. Due to the H_2O-induced H_2 formation effect occurring in the Penning sensor (see section 2.3.3), the measurements have been made by switching off this sensor. The typical shape of the obtained thermal desorption spectra is shown in Fig.2.30.

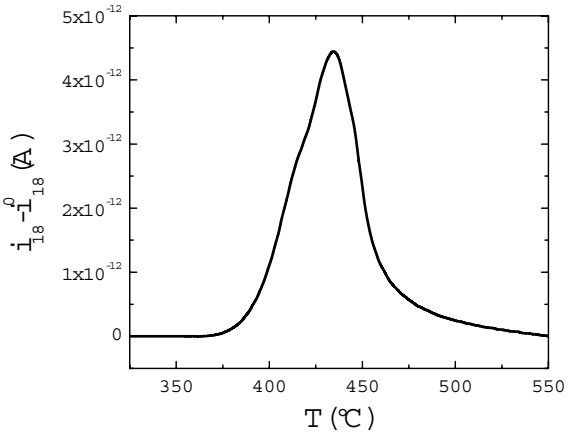

Fig.2.30. Thermal desorption spectra of H_2O from $Mg(OH)_2$. The spectrum has been recorded by applying a constant heating rate equal to 0.167 K s^{-1}.

The mean σ_{18}^{H2O} value obtained with Set B operating parameters is equal to $(2.3\pm0.1)\cdot10^{-10}$ A. Besides, the $a_{1/18}$ and $a_{2/18}$ factors (which express the ratio between the H^+ and H_2^+ ionic currents and the H_2O^+ one) are equal to 0.098±0.002 and 0.020±0.001, respectively. No data were taken with Set A parameters. The $a_{1/18}$ factor obtained from these experiments is lower than that obtained from the analysis of the residual atmosphere (see Table 2.2). This effect could be due to the increase of the H^+ ion concentration coming from the ionization of H_2O molecules induced by the Penning sensor.

2.5.3 O_2 sensitivity

The O_2 detection sensitivity has been determined from the analysis of the O_2 gas evolved from a Pt anode during the electrolysis of 0.1M LiOH-LiOD mixtures. Further details of the experimental procedure used in these experiments are given in Chapter 3. When applying a constant electrolytic current through the cell, the O_2 flow reaches, after a transient time (see section 3.5.2), a steady state value proportional to the electrolytic current imposed to the cell, according to Faraday's law. The produced O_2 flow is carried, together with the H_2-HD-D_2 flow evolved from the cathode, to the gas analysis system by means of an Ar flow. Fig.2.31 shows the dependence of the i_{32} peak current (corresponding to O_2^+ ions) with the partial O_2 flow in the analyzed gases. The partial O_2 flow can be calculated from the electrolytic current and the Ar flow value. The O_2 detection sensitivity (σ_{32}^{O2}) is obtained from the slope of the least square fit of the experimental points in Fig.2.31. The mean σ_{32}^{O2} value obtained from ten experiments is equal to $(1.18\pm0.08)\cdot10^{-10}$ A for Set A parameters. No measurements were done with Set B parameters.

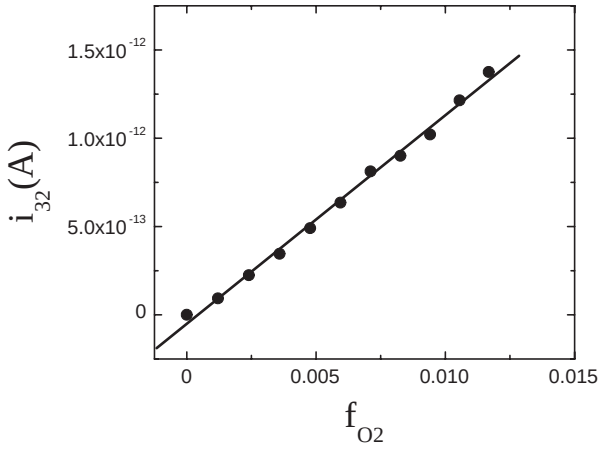

Fig.2.31. Experimental correlation between the i_{32} peak current and the partial O_2 flow evolved from the electrolysis of LiOH/LiOD mixtures. The solid line represents the linear fit to the experimental data.

2.6 Discussion of the obtained results

In this section, the results obtained from the calibration experiments are analyzed and discussed from a global point of view. Table 2.10 summarizes the detection sensitivities of H_2, HD, D_2, H_2O, O_2 and Ar molecules reported in the preceeding sections. We will focalize in two fundamental aspects. Firstly, it is important to

investigate the time stability of the gas analyser. This parameter determines how often calibration is required to assure a desired level of accuracy. This point will be treated in section 2.6.1. Secondly, it is interesting to understand the origin of the great differences among the detection sensitivities of different gas species, in particular, the differences among σ_2^{H2}, σ_3^{HD} and σ_4^{D2}. As it has been stated in the previous sections, several mass discrimination effects are present at the different stages of the gas analysis process. In addition, the e^--impact ionization cross sections depend on the the chemical nature of the atoms/molecules. Both effects determine the detection sensitivity of a particular gas specie. The relative contribution of e^--impact ionization and mass discrimination effects to $\sigma_{m/q}^{\chi}$ will be analyzed and discussed in section 2.6.2.

Table 2.10. Summary of the detection sensitivities obtained from the calibration experiments of the gas analysis system. Data correspond to the results obtained by switching off the Penning sensor.

Detection sensitivity	QMS parameters	
	Set A	Set B
σ_2^{H2}(A)	$(2.75\pm0.05)\cdot10^{-9}$	$(4.8\pm0.1)\cdot10^{-9}$
σ_3^{HD}(A)	$(1.7\pm0.1)\cdot10^{-9}$	$(1.8\pm0.1)\cdot10^{-9}$
σ_4^{D2}(A)	$(6.6\pm0.1)\cdot10^{-10}$	$(9.4\pm0.5)\cdot10^{-10}$
σ_{18}^{H2O}(A)	---	$(2.3\pm0.1)\cdot10^{-10}$
σ_{32}^{O2}(A)	$(1.18\pm0.08)\cdot10^{-10}$	---
σ_{40}^{Ar}(A)	$(1.2\pm0.2)\cdot10^{-10}$	$(3.3\pm0.3)\cdot10^{-10}$

2.6.1 Time stability of the gas analysis system

As it has been stated above, the time stability of the gas analyser determines how often calibration is required to assure a desired level of accuracy or, conversely, it determines the level of accuracy that can be reached as a function of time since calibration. In order to investigate the time stability of the gas analysis system we will analyze the errors of the obtained detection sensitivities. We will distinguish between the error in the determination of a given detection sensitivity from a single measurement and the standard deviation among the results obtained from different measurements.

From the point of view of a single calibration experiment, the errors in the determination of $\sigma_{m/q}^{\chi}$ values are typically below 1%. An exception to this rule is found for the Ar detection sensitivity, σ_{40}^{Ar}, whose errors are typically higher than 2 %, probably due to the high partial Ar flow used in its determination. In any case, it can be concluded that the gas analysis results are well reproducible within short time scales, *i.e.*, if they are performed within a period of one day.

The errors given in Table 2.10, however, represent the standard deviation among the $\sigma_{m/q}^{\chi}$ values obtained from different experiments. These errors depend on the chemical nature of the analyzed species. The obtained $\sigma_{m/q}^{\chi}$ values for H_2 are within 2 %, whereas for D_2 higher errors are observed, typically within 2-5 %. This seems to be caused by the slight influence of isotope exchange reactions on D_2 analysis. This hypothesis is further supported by the fact that higher σ_4^{D2} errors are obtained when switching on the Penning sensor (see Table 2.5). The obtained values of the H_2O and O_2 detection sensitivities have standard deviations of 4 and 8 %, respectively. For Ar, the standard deviation is even higher, being about 10-15 %.

The errors given in Table 2.10 also depend on the number of probes involved in the determination of a particular $\sigma_{m/q}^{\chi}$ value and on the time elapsed between them. The time window among the calibration experiments presented in sections 2.4 and 2.5 is of several months. The values of the standard deviations of the obtained detection sensitivities indicate long-time changes in the detection sensitivities of the gas analysis system. Similar changes have been observed by other authors [2.9, 22-24]. For instance, the week to week variations of the detection sensitivity of a QMS with a tungsten filament obtained by Blanchard *et al.* were typically <10 % [2.22]. Calcatelli *et al.* observed sensitivity changes of up to 20 % during a year long history of a QMS [2.23]. Similarly, Holme *et al.* reported deviations of about 1 and 10 % over one-day and one-year periods, respectively [2.24]. Some authors speculate that these changes could be related to changes in the surface properties of the ionizing filament and the ion detectors.

On the other hand, for many applications (such as the measurement of the relative content of hydrogen and deuterium in the analysed gas) only the relative sensitivities are important. They generally are one order of magnitude more stable than the absolute sensitivities, according to values reported by Ellefson and his coworkers [2.25]. The present results also point out in this direction, as it can be deduced from the experimental data shown in Fig.2.25. In that figure, a comparison among the H_2, HD and D_2 flows evolved from different electrolytic experiments is made. The slope of that figure is related to the relative detection sensitivities ($\sigma_2^{H2}/\sigma_3^{HD}$ and $\sigma_4^{D2}/\sigma_3^{HD}$) according to equation (2.31). The standard deviation of these slopes, obtained from nine measurements over a 4-month period, is <4 %. This implies that the relative H_2, HD and D_2 detection sensitivities are also stable to within ~2 % over this period.

In summary, the present calibration results show that gas analysis can be performed to within 1 % accuracy if calibrations are done before accomplishing the analysis. Conversely, the accuracy level that one can reach over a period of months since the last calibration depends on the nature of the chemical species under analysis, and range between 2 and 15 %. On the other hand, the relative detection sensitivities for the three hydrogen isotopologues are reproducible to within ~2 %

over a 4-month period. This result will allow us to safely use the obtained relative detection sensitivities for the quantitative analysis of H_2-HD-D_2 mixtures.

2.6.2 Discussion of the mass discrimination effects

The detection sensitivities summarized in Table 2.10 show a strong dependence on the chemical nature of the analyzed gases. This is quite evident when comparing σ_2^{H2}, σ_3^{HD} and σ_4^{D2} values. The strong isotope effect affecting these sensitivities seems to be due to mass discrimination effects, since the e^--impact ionization cross sections of the three hydrogen isotopologues are the same to within 5 % (see Fig.2.3).

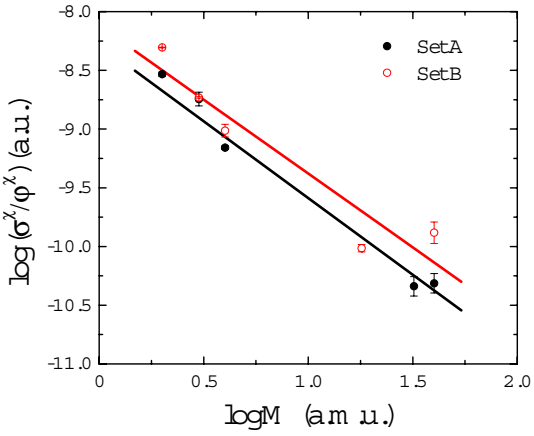

Fig.2.32. Logarithmic plot of the detection sensitivities (divided by the e^--impact ionization cross sections) as a function of the mass of the atoms/molecules. Results obtained with Set A and Set B parameters have been included. The lines represent the least square fits of the experimental data points.

In order to understand the relative influence of e^--impact ionization and mass discrimination effects on $\sigma_{m/q}{}^{\chi}$, the obtained detection sensitivities of H_2, HD, D_2, H_2O, O_2 and Ar have been normalized by the e^--impact ionization cross sections of the atoms/molecules, φ^{χ}. These cross sections have been calculated from the experimental points in Fig.2.3 at the two values of the e^--beam energy tuned with Set A and Set B parameters. $\sigma_{m/q}{}^{\chi}/\varphi^{\chi}$ values are plotted in Fig.2.32 as a function of the mass of the parent atoms/molecules in a logarithmic scale for both sets of QMS operating parameters. The slopes obtained from the linear fits of the experimental data points in that figure are equal to -1.4±0.1 and -1.3±0.2 for Set A and Set B parameters, respectively.

The dependence of $\sigma_{m/q}^{\chi}/\varphi^{\chi}$ values on the mass of the chemical species can be understood from the analysis of the mass discrimination effects present at the different stages of the gas analysis process. According to equation (2.15), $\sigma_{m/q}^{\chi}$ depends on the mass of the atoms/molecules through its dependence on $s_{m/q}^{\chi}$, α_{χ} and B_{χ}. The factor α_{χ} has a $m^{-1/2}$ dependence because the molecular flow of gases through the gas collection system. The pumping speed varies as $m^{1/2}$ [2.2]. Finally, $s_{m/q}^{\chi}$ can be assumed to be proportional to $m^{-1/2}$, due to the molecular flow of the produced ions through the hole between the ion source and the ion filter (see bottom of Fig.2.4). Taking all these contributions, it is deduced a $m^{-3/2}$ dependence of the $\sigma_{m/q}^{\chi}/\varphi^{\chi}$ values:

$$\sigma_{m/q}^{\chi} \propto m^{-3/2} \tag{2.33}$$

The mass dependence of $\sigma_{m/q}^{\chi}$ appearing in equation (2.33) is in agreement with the present experimental results. There exists, however, some dispersion among the experimental data appearing in Fig.2.32 with respect to the straight line behaviour. This can be due to the effect of spatial charge effects that could modify the ionization cross sections of the atoms-molecules or induce additional mass discrimination effects in the ion filtering process. In fact, the strong isotope effect observed between the H_2 and D_2 cracking patterns (see the difference between the $a_{1/2}$ and $a_{2/4}$ factors in Tables 2.4 and 2.5) could be due, at least in part, to this effect.

It is worth to emphasize that the results obtained from the calibration experiments of the gas analysis system imply the existence of a strong isotope effect affecting the detection sensitivities of the three hydrogen isotopologues. For instance, the relative detection sensitivities, $\sigma_2^{H2}/\sigma_4^{D2}$ and $\sigma_3^{HD}/\sigma_4^{D2}$, obtained in the present work with Set A parameters are equal to 4.3±0.1 and 1.66±0.05, respectively. A somewhat similar result was reported by Harada [2.26], who measured the relative detection sensitivities of a MMS for the three molecular isotopes. The $\sigma_2^{H2}/\sigma_4^{D2}$ and $\sigma_3^{HD}/\sigma_4^{D2}$ values reported by him were equal to 5.82 and 1.2, respectively. On the other hand, the existence of such differences among σ_2^{H2}, σ_3^{HD} and σ_4^{D2} values are not mentioned in many of the experimental works dealing with H/D isotope analyses (see for example [2.27-2.29]). In these works, it seems that the authors considered that there are no isotope effects among the detection sensitivities of H_2, HD and D_2. According to the present results, that hypothesis can induce great errors in the quantitative analysis of H_2-HD-D_2 mixtures.

To conclude this section, I want to remark that the obtained dependence of the $\sigma_{m/q}^{\chi}/\varphi^{\chi}$ values with the mass of the atomic/molecular species allows the calculation of the detection sensitivity of the gas analysis system from the e^--impact ionization cross section of the desired specie. This is a quite remarkable result

because it allows extending the present experimental technique to the analysis of any gas mixture.

2.7 References

[2.1] Holland L, Steckelmacher W and Yarwood J *Vacuum Manual* (London, E & FN Spon, 1974) Ch.1
[2.2] Dixon-Warren StJ, Pasteur AT and King DA 1995 *J. Chem. Phys.* **103** 2261
[2.3] Dylla HF and Blanchard WR 1983 *J. Vac. Sci. Technol. A* **1** 1297
[2.4] Bennett JR J and Elsey RJ 1993 *Vacuum* **44** 647
[2.5] Cowling IR and Fletcher J 1973 *J. Phys. B: Ato. Molec. Phys.* **6** 665
[2.6] Kim Y-K and Rudd ME 1994 *Phys. Rev. A* **50** 3954
[2.7] Hwang W, Kim Y-K and Rudd ME 1996 *J. Chem. Phys.* **104** 2956
[2.8] Stephan K, Helm H and Märk TD 1980 *J. Chem. Phys.* **73** 3763
[2.9] Lieszkovszky L., Filipelli R.A. and Tilford C.R. 1990 *J. Vac. Sci. Technol. A,* **8** (5) 3838
[2.10] Titov VV 1995 *Int. J. Mass Spectrom. Ion Processes* **141** 57
[2.11] Reagan NR and Frees LC 1987 *J. Vac. Sci. Technol. A* **5** 2389
[2.12] Souers PC 1986 'Hydrogen Properties for Fusion Energy', Univ. California Press
[2.13] Urey HC and Rittenberg D, 1933 *J. Chem. Phys.* **1** 137
[2.14] Lifshitz A, Bidani M and Carroll HF 1983 *J. Chem. Phys.* **79** 2742
[2.15] Farkas A and Farkas L 1935 *Proc. Roy. Soc. London Ser. A* **152** 124
[2.16] Rittenberg D, Bleakney W and Urey HC 1934 *J. Chem. Phys.* **2** 48
[2.17] Hammerli M, Mislan JP and Olmstead WJ 1969 *J. Electrochem. Soc.* **116** 779
[2.18] Lécluse C and Robert F 1994 *Geochimica et Cosmochimica Acta* **58** 2927
[2.19] Stahl D, Houriet R and Gäumann T 1972 *Chimia* **26** 243
[2.20] Cussler EL 2002 *'Diffusion. Mass Transfer in Fluid Systems'*, Cambridge Univ. Press
[2.21] Phelps AV 1992 *J. Phys. Chem. Ref. Data* **21** 883
[2.22] Blanchard WR, McCarthy PJ, Dylla HF, LaMarche PH and Simpkins JE 1986 *J. Vac. Sci. Technol. A* **4** 1715
[2.23] Calcatelli A, Bergoglio M and Rumiano G 1987 *J. Vac. Sci. Technol. A* **5** 2464
[2.24] Holme AE, Thatcher WJ and Lek JH 1974 *Vacuum* **24** 7
[2.25] Ellefson R.E., Cain D. and Lindsay C.N. 1987 *J. Vac. Sci. Technol. A* **5** 134
[2.26] Harada S 1996 *Mater. Transac. JIM* **37** 45
[2.27] Hahn P, Bertino MF, Toennies JP, Ritter M and Weiss W 1998 *Surface Science* **412/413** 82
[2.28] Salmerón M, Gale RJ and Somorjai GA 1979 *J. Chem. Phys.* **70** 2807
[2.29] Basallote MG, Bernal S, Gatica JM and Pozo M 2002 *Applied Catalysis A* **232** 39

Chapter 3

On the electrolytic separation factor of hydrogen and deuterium

3.1 Introduction

In this chapter, we will centre our attention in a particularly important effect: the electrolytic separation of H and D. The electrolytic separation factor (*S*) of H and D is defined as:

$$S = \frac{(H/D)_{gas}}{(H/D)_{liq}} \tag{3.1}$$

where $(H/D)_{gas}$ and $(H/D)_{liq}$ refer to the fraction of H and D in the gas evolved from the electrolysis and in the electrolyte, respectively. In general, *S* is greater than 1, given that the rate of the hydrogen evolution reaction (HER) is higher for H than for D. This allows separating both isotopes by means of electrolysis of natural water, in which the deuterium to hydrogen ratio is less than 1 part in 5000. Originally, this was the industrial method used to obtain heavy water. Nowadays, there are other methods less expensive to separate the hydrogen isotopes and water electrolysis is only used in the final separation stage. However, electrolytic separation of H and D could become a profitable process at the primary separation stage if voltage efficiencies of the water electrolysis process are increased [3.1]. On the other hand, the electrolytic separation factor has a great importance from a fundamental point of view. A complete description of the HER must account for this effect and one can obtain considerable information about the HER by investigating the electrolytic separation of H and D. Although the HER is one of the most investigated phenomena in chemistry, it is far to be a closed question and further efforts must be done in order to completely understand its mechanisms. By

this reason, it has been believed convenient to repay attention to the H/D isotope effects in the HER, employing modern experimental tools to perform precise *S* measurements.

The fundamental investigations on the electrolytic separation between H and D since its discovery up to nowadays are analyzed and discussed from different points of view in section 3.2. The theoretical treatment of the electrolytic separation factor has been done based on the absolute reaction rate theory. The dependence of *S* values on several variables (temperature, electrode potential and reaction mechanism of the HER) is discussed. In addition, a detailed compilation of *S* data for different metallic cathodes is presented. The analysis of these experimental data has allowed the obtaining of an empirical correlation between *S* values and electronic structure of the metallic cathodes.

The experimental methods used to investigate this phenomenon have been also reviewed in section 3.3. This review aims helping the interested reader to perform *S* measurements and to analyze the different sources of error that could affect them.

In section 3.4, the experimental setup designed and built to perform on-line measurements of the separation factor is presented. This system allows to measure the time evolution of *S* during the electrolysis itself, in contrast with traditional techniques that only allows to measure *S* at the end of the whole electrolytic process. Details about the calibration procedures of the experimental system will be given. Experimental results obtained with this technique for the time evolution of *S* at a Pt cathode will be also presented, discussed and compared with results from other authors.

The last section is devoted to the description of some representative experiments, which can illustrate the capabilities of the present experimental system as an analytical tool in electrochemistry.

3.2 About the theories of the electrolytic separation of hydrogen isotopes

3.2.1 Historical background

The possibility to separate isotopes by means of chemical equilibria was first pointed out by Lindemann and Aston [3.2] in 1919. This proposal was used by Urey, Brickwedde and Murphy [3.3-5] to obtain deuterium enriched hydrogen samples and it was a key factor to discover that isotope in 1931. Soon after, Urey and Washburn [3.6] discovered the electrolytic separation of hydrogen and deuterium. Then, many laboratories all around the world centred their investigations on the properties of this new isotope and, in particular, on the electrolytic separation of hydrogen isotopes.

The aim of explaining the pronounced differences in chemical properties of H and D arose immediately. On the basis of classical physical-chemistry it is expected a ratio of molecular velocities of both isotopes of $2^{1/2}$, due to their mass

differences. However, this difference alone could not by itself account for the observed chemical differences between them. Nevertheless, progresses were made by considering the rising quantum theory. Exact calculations of several gaseous equilibriums involving H and D were made by Urey and Rittenberg [3.7] at the light of the *Bose-Einstein* and *Fermi-Dirac* statistics. They also showed that differences in electrode equilibrium potentials of both isotopes cannot give any appreciable separation by fractional electrolysis. At this point the theory about the electrolytic separation factor was focused on the difference in the reaction rates of H and D instead of the difference in the equilibrium constants. It was pointed out by Cremer and Polanyi [3.8] and Eyring [3.9] that differences in zero point energies (ZPE) of both isotopes affect to their relative reaction rates in chemical reactions. In addition, a second quantum effect, namely the tunnel effect through the energy barriers, was considered [3.10] in order to explain the electrolytic separation of hydrogen isotopes. This tunnelling or leaking through the energy barriers was considered in more detail by Bawn and Ogden [3.11], who calculated the numerical values of the separation factors of H and D for some typical cases. They also pointed out that in certain conditions the reaction rates for deuterium can be larger than for hydrogen.

3.2.2 Absolute reaction rate theory and electrolytic separation factor

A convenient starting point to outline the theory about the electrolytic separation of hydrogen isotopes is found in the early work of Topley and Eyring [3.12], based on the absolute reaction rate theory developed by Eyring [3.13]. They made the assumption that tunnelling was negligible and criticized the results obtained by Bawn and Ogden who, in fact, reported *S* values much greater than the experimental ones.

In chemistry, it is usually assumed that there is a step which determines the reaction rate of the whole process, the rate determining step (r.d.s.), while the rest of steps are considered at equilibrium. Absolute reaction rate theory postulates that the rate of the r.d.s. when the reaction is proceeding irreversibly (forward direction only), is the same as the rate in either direction at equilibrium. In order to obtain an expression for the reaction rates, the number of atoms in the transition state (TS) corresponding to the r.d.s. (in equilibrium with the number of atoms in the initial state for that step) must be calculated and multiplied by the average velocities with which they travel in the forward direction.

The possible mechanisms for the HER include the discharge step:

$$AqH + M + e^- \Leftrightarrow Aq^- + MH \tag{3.2}$$

where AqH is the discharging specie (H_2O molecule in alkaline solution or H_3O^+ ion in acidic media), M is the electrode surface, e^- is an electron and MH is a hydrogen atom bounded to the electrode surface. This step is followed by the

desorption step, what can takes place either by recombination:

$$MH + MH \Leftrightarrow H_2 + 2M \quad (3.3)$$

or by electrochemical desorption:

$$MH + AqH + e^- \Leftrightarrow H_2 + M + Aq \quad (3.4)$$

In order to obtain an expression for *S*, one must calculate the ratio between the equilibrium constants of H and D atoms in the TS and in the initial states of the r.d.s. If the r.d.s. is either reaction (3.3) or (3.4), we can use the fact that reaction (3.2.) is at equilibrium to relate the initial state of the r.d.s to the initial state of reaction (3.2). Besides, the high rate of the reaction:

$$2H_2O \quad \Leftrightarrow \quad H_3O^+ \quad + \quad OH^- \quad (3.5)$$

allows to relate the initial state of reaction (3.2) to the concentration of H and D atoms in liquid water. Thus, whichever be the r.d.s., to calculate the value of the electrolytic separation factor one must calculate the ratio of H and D atoms in the TS of the r.d.s. in equilibrium with atoms in the electrolyte and multiply this number by the ratio of the average velocities with which H and D atoms pass out of the TS.

3.2.2.1 The maximum separation factor according to the theory

The simplest case that one can solve in the light of this theory is that in which the TS of the r.d.s. consists of free hydrogen and deuterium atoms. This is the TS of highest possible energy and in it the difference in ZPE for H and D is zero, since the atoms have only translational energy. This situation should give the maximum separation factor because the difference in activation energies for H and D is the full difference in ZPE in liquid water (see Fig.3.1). In spite of the fact that this simplification is very strong to be valid for real systems, it forms a basis on which a complete description of the electrolytic separation can be built. It is expected that the TS of a real system consists of partially bounded states of the atoms. In this case the difference in activation energies for hydrogen and deuterium will be reduced and a lower value of the separation factor will be obtained.

Instead of the direct equilibrium between H and D atoms in the TS and in liquid water, Topley and Eyring considered the equilibria with water vapour:

$$H_2O + 2D \Leftrightarrow D_2O + 2H \quad (3.6)$$

$$H_2O + D_2O \Leftrightarrow 2HDO \quad (3.7)$$

with equilibrium constants K_6 and K_7, respectively. These constants allow calculating the relative number of H and D atoms at the TS in equilibrium with water vapour of any isotopic composition. K_6 and K_7 can be obtained from the partition functions of different molecules, which are known from spectroscopic data of the corresponding molecules. Then, the reported values of H_2O and D_2O vapour pressures have to be used to finally relate the H and D relative concentrations in the TS to the isotopic composition of liquid water. Topley and Eyring multiplied the relative number of isotopes in the TS by $2^{1/2}$ to obtain the relative velocities with which they pass out of that state.

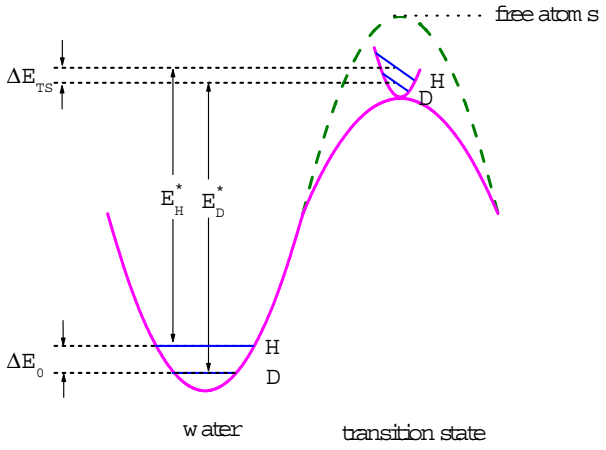

Fig.3.1. Simplified potential energy diagram for reacting H and D atoms (from [3.14]). E_H* and E_D* represent the activation energies for H and D atoms, respectively, while ΔE_0 and ΔE_{TS} are the differences in ZPE for both isotopes in liquid water and at the TS. The potential energy surface for the free atoms TS is shaped by the green dashed line.

Following the same ideas, Rowland [3.14] recalculated the theoretically maximum separation factor from more recent spectroscopic data to obtain the relative numbers of H and D in the TS. In addition, he took into account the reaction coordinate factor, r_0*, that is the ratio of velocities with which H and D atoms pass out of the TS of the r.d.s. Actually, this factor depends on the mechanism of the HER. Rowland obtained r_0*=1 for the discharge step and r_0*=1.28 for both the recombination and the electrochemical desorption reactions. Topley and Eyring assumed that the atoms move out of the TS by diffusion, hence r_0*=$2^{1/2}$.

Rowland took into account the influence of the H and D atomic mole fractions

in the electrolyte to calculate *S*. He obtained an expression valid for any electrolyte composition. Even more, he estimated that the optimum D_2O concentration in the electrolyte is ~70-80% whenever one wishes to simplify the theoretical treatment and to minimize the experimental error in the separation factor measurement. The general expression for the maximum electrolytic separation factor (S_{max}) obtained by Rowland is:

$$S_{\max} = S_0 \cdot c(x_H / x_D) \cdot r_0 * \cdot \left[f(x_H / x_D) \right]^{n-1} \tag{3.8}$$

where:

$$S_0 = 0.525 \cdot e^{\frac{1840}{RT}} \tag{3.9}$$

is what he called 'datum line', that is the equilibrium constant of reaction (3.6) for a 1/1 mixture of H and D in the electrolyte. In equation (3.9), *R* is equal to 1.986 cal equiv.$^{-1}$ K^{-1} and *T* is the absolute temperature. The factor $c(x_H/x_D)$, termed the datum line composition coefficient, accounts for the influence of the H and D mole fractions in the electrolyte (x_H and x_D, respectively). This factor is ~1, with a maximum deviation of ±0.07 and can be considered temperature independent. The factor $f(x_H/x_D)$, termed the TS composition coefficient, is applied when the r.d.s. is bimolecular (*n* is the number of reacting hydrogen atoms). Its influence is estimated to be lower than about ±3%.

3.2.2.2 Application to real systems

The theoretically maximum separation factor poses problems of interpretation. The choice of the free atom state as the TS complex should give activation energies prohibitively large, not observed in practice. To deal with this problem, Topley and Eyring [3.12] and Rowland [3.14] considered an equilibrium between the atoms in free states and the atoms in the actual TS of the r.d.s. Then, to calculate *S* one must multiply S_{max} by the corresponding equilibrium constant. According to Rowland, the general expression for *S* is:

$$S = \frac{\phi_H}{\phi_D} S_{\max} \tag{3.10}$$

where ϕ_H and ϕ_D are the reduced partition functions for H and D atoms in the TS. They can be calculated from the vibrational frequencies of H and D modes in that state. As a matter of fact, as these vibrational frequencies increase, *i.e.* as the atoms in the TS are more tightly bounded, *S* diminishes. This is expected because the ZPE

differences between H and D atoms in the TS compensate for those in the electrolyte. Furthermore, for TS with low vibrational frequencies (namely, below 300 cm^{-1}), the actual *S* value rapidly approaches S_{max}.

On the other hand, Farkas [3.15], based on experimental results obtained by Horiuti [3.16] and Oliphant [3.17], pointed out that if equilibrium between the adsorbed gas at the electrodes and the electrolyte is established, the observed separation factor will be equal to the equilibrium constant of the reaction:

$$HD + H_2O \Leftrightarrow H_2 + HDO \tag{3.11}$$

which is equal to 3.7 at room temperature.

3.2.3 Electrolytic separation factor and reaction mechanism of the HER

Different electrochemical methods show discrepancies on concluding on the r.d.s. of the HER. For this reason, *S* measurements have been taken as an additional criterium. Several calculations [3.18-24] of *S* for different r.d.s. have been done and they appear to be very sensitive to the initial assumptions made. For example, Keii and Kodera [3.18] obtained a minimum value of 13 for the discharge step (3.2) by taking a double degenerate bending frequency for the TS. Conway and Salomon [3.19] showed that this value can be as low as 3.8 by considering that proton is being discharged interstitially between two or three metal atoms (equivalent to take five or eight vibration modes for the TS). In another paper [3.20], Conway calculated a value of 3 for the same step, quite close to that obtained by Bockris and Srinivasan [3.21].

Conway [3.20] gave S=6.1 when the r.d.s is the electrochemical desorption reaction (3.4). Horiuti and his co-workers [3.22] obtained a value of 3 for the same mechanism. Bockris and Srinivasan [3.23] took into account the influence of the cathode overpotential and the effect of tunnelling corrections and gave values ranging from 8.3 to 10.7 for low and intermediate overpotentials and from 3.4 to 4.4 for higher ones.

Bockris and Srinivasan [3.24] obtained *S* equal to 5.4-6.4 and 4.9-5.5 for Ni and Pt, respectively, by considering that the r.d.s. is the slow recombination mechanism (3.3). The *S* value reported by Okamoto and his co-workers [3.24] is 6-7 in that case.

It can be seen that *S* obtained by different authors differ substantially. In fact, Rowland showed [3.14] that for systems with low electrolytic separation factors (strongly bound TS systems), errors due to the assigned frequencies of the atoms in the TS have a larger effect than for systems with high *S* values (weakly bounded TS systems). Therefore, he stated that in order to unequivocally identify the mechanism of the HER, one must study the temperature dependence of *S* in systems with high *S* values. This point will be discussed in more detail in the next section.

3.2.4 Dependence of *S* on temperature

The variation of *S* with temperature has been studied by several workers [3.25-31] in different cathode materials and electrolytes. As a matter of fact, *S* diminishes as the temperature increases, following *Arrhenius* lines with positive slopes.

According to equations (3.8) and (3.9), *Arrhenius* plots of the theoretically maximum separation factor will have a slope of 1840 cal·equiv.$^{-1}$. In addition, the limiting values of the *Arrhenius* lines for $T^{-1}\rightarrow 0$ allow the obtaining of r_0* and hence establishes the r.d.s. for the HER. The existence of real systems with *Arrhenius* lines indistinguishable from the theoretically maximum one has been confirmed experimentally [3.28, 29] with iron cathodes in alkaline solutions under properly chosen conditions. It has been observed that certain additives, such as EDTA (ethylenediaminetetraacetic acid) and urea, adsorb onto the cathode and maintain its surface in a definite and reproducible state. Maximal, reproducible separation factors are obtained by combining these techniques with the electrolytic deposition of cathode material during the HER. *Arrhenius* lines when $T^{-1}\rightarrow 0$ has stated that the reaction was controlled by the slow discharge mechanism. Possible explanations of the free-atom TS state corresponding to those systems have been also given.

On the other hand, it can be seen from equation (3.10) that the difference in the slopes of the *Arrhenius* plots of the electrolytic separation factors with respect to the maximum one gives a measurement of ϕ_H/ϕ_D, *i.e.* of the H and D vibration frequencies in the H and D TS of the r.d.s.

3.2.5 Dependence of S on the electrode potential

Variations of *S* with the potential applied to the cathode was first investigated by Vielstich and Schuchard [3.32] and subsequently treated by other authors [3.30, 33-38]. Some of them explain this potential dependence of the separation factor by considering a switching of the reaction mechanism on varying the electrode potential (see for example [3.39]).

Within the framework of absolute reaction rate theory, the variation of the separation factor with electrode potential at constant temperature and constant electrolyte composition must be due to the change of the H and D vibrational frequencies in the TS. The cathode potential may modify these frequencies through different processes.

i) TS energy may be altered by changes of the H-D surface coverage induced by the electrode potential. Such variations would indeed be expected in some metals like Pt whose H adsorption heat falls with surface coverage [3.40-42]. Therefore, H and D atoms will be more weakly bounded as the surface coverage increases and the TS will similarly have lower vibrational frequencies and higher *S* values. H and D surface coverage increases with overpotential and, therefore, one

should expect that *S* would increase as the electrode potential is made more negative. This view is consistent with the separation factors measured by Hammerli and his co-workers [3.30, 38].

ii) In order to explain the influence of the anion of the electrolyte on the variation of *S* with potential of Pt cathodes, it has been considered [3.37] that hydrogen can be adsorbed at different surface sites. As the tendency of the ions of the electrolyte to be specifically adsorbed increases, H and D will find sites of lower binding energy and *S* will tend to increase.

iii) For metals with low hydrogen coverage, such as Hg, Pb and Ag, the variation of *S* with electrode potential should be due to changes of the electrolyte-metal interaction induced by the applied potential. For instance, the ordering of water molecules in the electrode-electrolyte interface in silver (111) surfaces is voltage dependent [3.43]. The slight decrease of *S* on decreasing the potential of Hg cathodes observed by Salomon and Conway [3.37] agrees with this hypothesis. It is also consistent with the differential double layer capacity increase induced by increasing the Hg cathode overpotential, what reflects that H_3O^+ ions become more tightly bounded to the electrode surface.

On the other hand, it has to be mentioned the work by Krishtalik [3.44-46], based on the DKL model, to account for the variation of *S* with electrode potential when the HER is controlled by the discharge reaction. The DKL model was developed by Dogonadze, Kuznetsov and Levich [3.47]. It is a quite general theory that considers a quantum tunnelling mechanism for proton transfer reactions. In it, the origin of the preexponential factor and the activation energy of the reaction rate are separated. The former quantity depends on the overlapping of the H(D) wave functions in the initial and final states, while the latter is related to on the solvent reorganization, what influences the hydrogen energy levels in the initial state.

3.2.6 Semiempirical correlations between S and electronic structure of metals

'Difference of separation factors seems to have no parallelism with the catalytic activity of metals in hydrogenation nor with that in recombination of active hydrogen'. This assertion was made by Horiuti and Okamoto in 1936 [3.48]. Since then, it has been usually accepted that *S* values fall into two groups, according to the ideas of Horiuti and his co-workers [3.24, 48, 49]. The first group includes metals such as Ni, Au, Cu, Pt (at high overpotentials) and Pb (in alkaline solution) with *S* values around 6-7. The second one includes Hg, Sn and Pt (at low overpotentials) and Pb in acidic solution with *S* values around 3. This difference in *S* values has been ascribed to different r.d.s. of the HER. In the first group of metals the r.d.s. would be the slow recombination mechanism, while the electrochemical desorption mechanism would operate in the second group. However, as it was shown in section 3.2.3, the assignation of *S* values to a certain r.d.s. for the HER is not univoquelly determined. Therefore, the usual clasification of *S* values depending on the reaction mechanism of the HER is questionable.

Table 3.1. Values of the electrolytic separation factors for fifteen metals at different experimental conditions.

Metal	S	Electrolyte	% D	η(mV)	i_d(A cm^{-2})	T (K)	Ref.
Fe	7.6	0.5N KOH	7		1	293	3.12
	6.9	0.5N KOH	8		1	293	3.12
	13.2	5% KOH	10		0.05	288	3.50
	10	1M KOH	10		0.2	298	3.51
	12.3	1M KOH	10		0.2	298	3.51
Ni	5.5	0.5N KOH	7		1	293	3.12
	6.7	1N H_2SO_4	6	-350		293	3.48
	7.0	0.5N H_2SO_4	30-50		$5\cdot10^{-4}$-10^{-3}	288	3.25
	8.0	5% KOH	10		0.05	288	3.50
	6.5	5% NaOH	5.5		0.5	298	3.52
	9.5	30% KOH	0.1		0.05	263	3.53
Cu	6.8	0.5N KOH	7		1	293	3.12
	5.5	0.5N H_2SO_4	7		1	293	3.12
	5.8	0.75N H_2SO_4	8		1	293	3.12
	7.4	1N H_2SO_4	6	-350		293	3.48
	10.5	5% KOH	10		0.05	288	3.50
Zn	5.1	5% KOH	10		0.05	288	3.50
Ga	4.1	0.5N H_2SO_4	8		1.5	293	3.12
	4.6	0.5N H_2SO_4	10		1.5	293	3.12
Zr	4	5% KOH	10		0.05	288	3.50
Pd	4.3	2N H_2SO_4	26		$2.5\cdot10^{-3}$	293	3.15
	4.1	2N H_2SO_4	52			293	3.15
	4.7	2N H_2SO_4	69			293	3.15
	6.8	2N H_2SO_4	26		$2.5\cdot10^{-3}$	293	3.15
	7.8	5% KOH	10		0.05	293	3.50
	4.3	1N H_2SO_4	70		0.05	298	3.54
	13.5	1N H_2SO_4	70		0.05	298	3.54
	7.7	5% NaOH	5.5		0.5	298	3.52
Ag	5.3	0.5N KOH	7		1	293	3.12
	5.8	0.5N KOH	8		1	293	3.12
	6.0	0.5N H_2SO_4	8		1	293	3.12
	5.6	0.5N H_2SO_4	10		1	293	3.12
	6.0	1N H_2SO_4	6	-350		293	3.48
	10.2	5% KOH	10		0.05	288	3.50
	8.4	5% NaOH	5.5		0.5	298	3.52
	6.0	0.5N H_2SO_4	30-50		$5\cdot10^{-4}$-10^{-3}	288	3.25
Cd	5.9	5% KOH	10		0.05	288	3.50

Sn	3.1	1N H_2SO_4	6	-350		293	3.48
	5.5	5% KOH	10		0.05	288	3.50
	3.0	0.5N H_2SO_4	30-50		$5 \cdot 10^{-4}$-10^{-3}	288	3.25
W	5.3	0.5N H_2SO_4	12		6	293	3.12
Pt	7.6	0.5N KOH	7		1	293	3.12
	6.5	0.5N KOH	8		1	293	3.12
	5.7	0.5N H_2SO_4	8		1	293	3.12
	5.7	0.5N H_2SO_4	9		1	293	3.12
	5.7	0.5N H_2SO_4	8		14	293	3.12
	6.4	0.75N H_2SO_4	12		14	293	3.12
	6.3	1N H_2SO_4	18		14	293	3.12
	6.9	1N H_2SO_4	6	-350		293	3.48
	5	0.05N H_2SO_4	50		1.5	298	3.31
	8.8	5% KOH	10		0.05	288	3.50
	7.4	5% NaOH	5.5		0.5	298	3.52
	9	1N HCl	10	-300		298	3.37
	6.8	1N H_2SO_4		-200		288	3.34
	4	1N $HClO_4$	10	-500		298	3.37
	6.5	1.2N HCl	10	-400		298	3.38
	4.1	1.2N HCl	10	-50		298	3.38
	5.3	0.5N H_2SO_4	30-50		$5 \cdot 10^{-4}$-10^{-3}	288	3.25
Au	6.4	1N H_2SO_4	6	-350		293	3.48
	5.3	0.5M H_2SO_4	1.04	-100		299.5	3.55
	5.3	0.5M H_2SO_4	1.04	-600		299.5	3.55
Hg	2.8	0.5N H_2SO_4	8		0.7	293	3.12
	2.9	0.5N H_2SO_4	9		0.7	293	3.12
	2.7	0.75N H_2SO_4	10		0.7	293	3.12
	2.8	1N H_2SO_4	15		0.7	293	3.12
	3.1	1N H_2SO_4	6	-350		293	3.48
	4	1N HCl	10	-900		298	3.37
	2.9	1N $HClO_4$	10	-850		298	3.37
	3.3	0.5N H_2SO_4	30-50		$5 \cdot 10^{-4}$-10^{-3}	288	3.25
Pb	7.4	0.5N KOH	7		1	293	3.12
	7.2	0.5N KOH	8		1	293	3.12
	6.2	0.5N H_2SO_4	8		1.3	293	3.12
	6.6	0.5N H_2SO_4	9		1.3	293	3.12
	6.3	0.5N H_2SO_4	12		1.5	293	3.12
	10.6	5% KOH	10		0.05	288	3.50
	6.8	1N KOH	6	-350		293	3.48
	3.0	1N H_2SO_4	6	-350		293	3.48

Nowadays, it is well known that almost all physical and chemical properties of metals show a regular periodicity when plotted along the Periodic Table [3.56]. This behaviour has been associated to the periodicity of the electronic configuration of the elements along the transition series. Therefore, it has been stated that there exists a common factor governing the physical and chemical properties of a metal, namely the *Fermi* wave vector.

Within this context, some authors have pointed out that there exists a correlation between the electrocatalytic activity for the HER and the electrolytic separation factor [3.57, 58]. However, such correlation has not been investigated in detail and the statement of such assertions has been relegated to a secondary plane. As a consequence, I have believed convenient to examine the dependence of *S* values on the electronic structure of the metallic cathodes. To this aim, an extensive compilation of the reported *S* values have been done. Table 3.1 shows *S* values of 15 metallic cathodes together with the experimental conditions (electrolyte, D content in the electrolyte, overvoltage, current density and temperature) at which they have been measured. Mean values of *S* data given in Table 3.1 are plotted in Fig.3.2(a) against the metal atomic number. The comparison of *S* from different metals is obscured due to all the factors (temperature, electrolyte composition, applied electrode potential/current density, state of the electrode surfaces (oxide layers, impurities and hydrogen-deuterium surface coverage) and presence of impurities in the electrolyte) that can affect the results. Besides, the experimental errors in *S* measurements are not always reported and in many works experimental details to evaluate them are lacking. In the next section, special attention will be put on the possible sources of error in these measurements. In addition, it is worth to note that *S* values of Pb cathodes seem to be strongly affected by the pH of the electrolyte. For this element, higher *S* values are found in alkaline electrolytes as compared to acidic media. This effect seems to be due to the oxidation of the Pb surface in alkaline electrolytes (see the Pourbaix phase diagram of Pb [3.59]). Therefore, for Pb cathodes, only *S* values in acidic electrolytes have been considered in the plot of Fig.3.2(a).

In spite of the large dispersion in *S* values, it can be seen in Fig.3.2(a) that mean *S* values have a regular periodicity when plotted against the atomic number. For each long period *S* rises when increasing the number of d-electrons and it reaches a maximum around d^8-electronic configuration. Then, *S* sharply decreases with further increase of the electron number. Fe has a singular behaviour with the highest mean value of *S*. However, this is not surprising because Fe (as well as Mn) possesses singular characteristics for other physical and chemical properties.

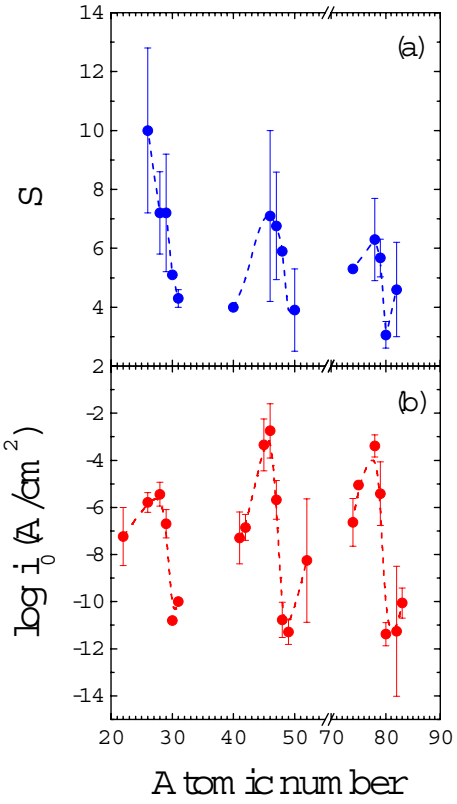

Fig.3.2. Plot of the mean *S* values reported in Table 3.1 (a) and of the electrocatalytic activity data for the HER taken from [3.60] (b) as a function of the atomic number of the metallic electrodes. Error bars represent the standard deviation of the experimental data points. Dashed lines in these figures are a guide for the eyes.

Volcano plots like that in Fig.3.2(a) resemble those observed for the electrocatalytic activity for the HER ($logi_0$). The mean values of $logi_0$ data compiled by Kita [3.60] are plotted in Fig.3.2(b) as a function of the atomic number of the metallic cathodes. As in the case of *S* values, a large dispersion is found among different electrocatalytic activity data of the same element. In spite of that, the plots appearing in Figs.3.2 (a) and (b) suggest that both *S* and $logi_0$ are similarly influenced by the cathode electronic structure. This parallelism should imply the existence of some correlation between them. In Fig.3.3, the mean electrolytic separation factors obtained from the data reported in Table 3.1 have been plotted as a function of the mean

electrocatalytic activity data reported by Kita for the transition metals of the third (a), fouth (b) and fifth (c) period. A relatively good correlation is observed.

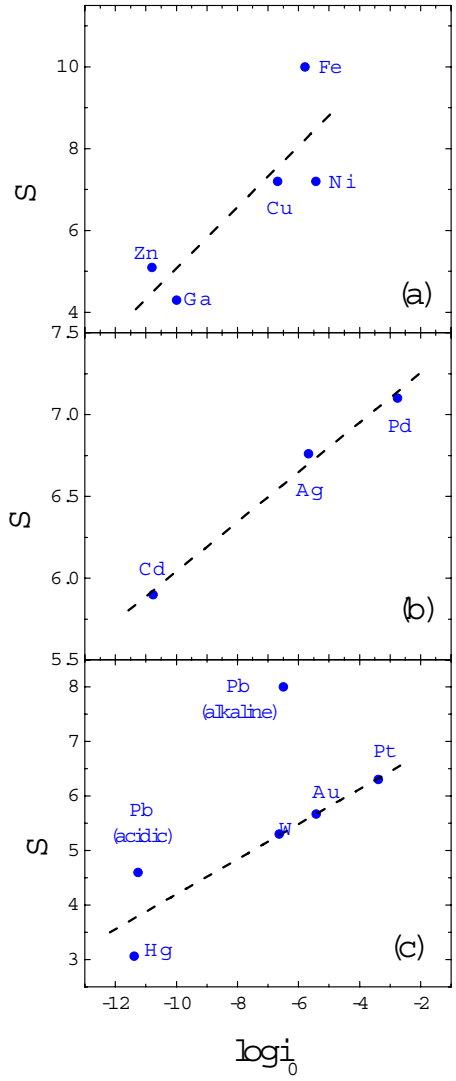

Fig.3.3. Plot of the mean *S* values reported in Table 3.1 as a function of the mean $logi_0$ data for the HER taken from [3.60] for the transition metals of the third (a), fourth (b) and fifth (c) periods. Dashed lines in these figures are the linear fits of the experimental data.

Eperimental data in Fig.3.3 can be qualitatively understood from a microscopic point of view with a simple and intuitive model. Metals having low electrocatalytic activity will have higher activation energies for the H/D reaction steps than metals with high $logi_0$ values. On the other hand, metals with low *S* values will have higher differences between the ZPE levels at the TS of the r.d.s. than those with high *S* values. As a consequence, it seems that the relationship between *S* and $logi_0$ values is determined by the degree of corrugation of the potential energy surface (PES) which experiment H and D atoms during the HER. A high PES corrugation will imply high activation energies and ZPE differences at the TS, as shown schematically in Fig.3.4.

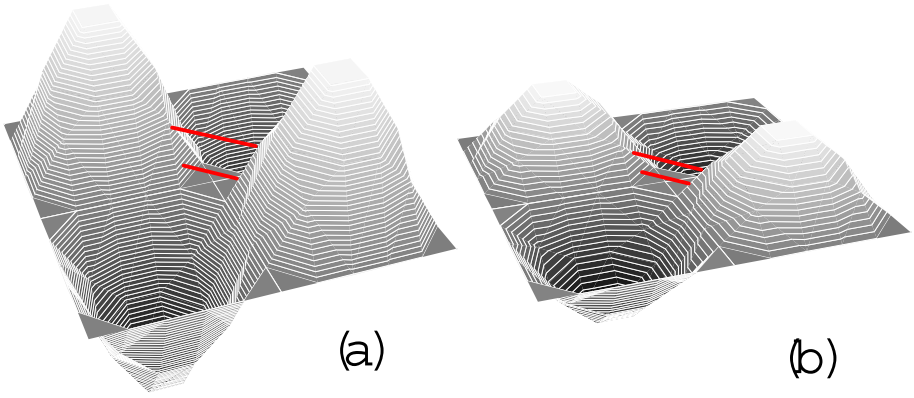

Fig.3.4. Schematic representations of the PES of H and D atoms during the HER. Metals having low $logi_0$ values (a) have higher activation energies and ZPE differences at the TS than metals with high $logi_0$ values (b). Red lines represent ZPE levels of H and D atoms at the TS.

To conclude this section, it must be pointed out that there are further experimental findings which evidence some correlation between *S* and $logi_0$. For instance, it has been observed that iron thin film electrodes electrodeposited in the presence of a magnetic field show a highest electrocatalytic activity and a highest separation factor than those prepared in the absence of magnetic field [3.51]. Moreover, correlations between *S* and $logi_0$ values have been observed for Ti-Ni intermetallic phases and alloys [3.53]. It has been shown that both properties obey similar volcanic plots when plotted along the phase diagram of the Ti-Ni system. Besides, the highest values of *S* and $logi_0$ are found at about the d^8-electronic configuration ($TiNi_3$). The formation enthalpy of Ti-Ni intermetallic phases has also been found to correlate with these properties. This effect could explain the relationships between *S* and the formation enthalpy of intermetallic phases

previously reported [3.61] for Ti-Pt, Pd-Ta, Fe-Mo, Ni-V, Ni-Mo and Ni-W alloys. As a consequence, it seems that *S* is influenced by the electronic structure of metals similarly to other physical and chemical properties of pure metals [3.56] and intermetallic phases [3.62]. In any case, the statement of such types of semiempirical correlations between *S* values and the electronic structure of metals demands for additional investigations on other metals.

3.3 Experimental methods used to measure the electrolytic separation factor

From the definition in equation (3.1), it is clear that to determine *S* it is necessary to measure the relative content of H and D in the electrolyte and in the gases evolved from the electrolysis. The former quantity is generally known, because electrolytes are usually prepared by mixing known volumes of H_2O and D_2O. Then, from density and molecular weight data of heavy and regular water, one can calculate the molar fractions of hydrogen and deuterium in the electrolyte. However, the knowledge of the hydrogen to deuterium ratio in the evolved gases is a more delicate problem. The original method used by Urey, Brickwedde and Murphy [3.63, 3.64] consists on the spectrographic analysis of the Balmer series in atomic spectra excited in a hydrogen discharge tube. However, their results were qualitative due to the low amount of deuterium in the analysed hydrogen. In any case, the development of other quantitative analytical techniques rapidly replaced this method. These new procedures will be described in what follows. Although we will deal with the analysis of gases evolved from the electrolysis of heavy and regular water, the experimental methods can also be used to measure the ratio of hydrogen and deuterium for gases coming from other sources.

I must comment here on a problem which is normally present in all the procedures used to measure the H/D ratio in gases. Gases evolved from the electrolysis are usually stored in a close vessel until a sufficient amount of hydrogen molecules are obtained for analysis. Therefore, it is necessary to use water traps (as dry ice-acetone, solid CO_2, metal-packed at low temperatures, silica gel, etc.) in order to eliminate the water vapour from the electrolyte dragged by the evolved gases. Isotope exchange reactions between hydrogen and water are of importance and they will influence the hydrogen to deuterium ratio in the gases, mainly if they remain stored for a long period. This problem is reduced when on-line methods are used.

3.3.1 Analysis of the water formed by oxidation of hydrogen-deuterium mixtures

A widely used technique consists in the analysis of the water obtained by oxidation of the evolved hydrogen isotopes. It is applied in two steps, H-D oxidation to form water and the analysis of the H to D ratio in the obtained water.

3.3.1.1 Oxidation procedures

There are various methods to oxidize hydrogen-deuterium mixtures to form water. For example, Topley and Eyring used a thin jet of Pyrex to burn oxygen and hydrogen isotopes mixtures evolved from the electrolysis [3.12]. A catalyst, for example a 3% Pt on alumina pellets at 300ºC [3.33] or copper oxide at about 550ºC [3.29] can also be used. It is expected that the isotopic abundance of oxygen atoms in the oxide did not depart far from that on air or natural water. To avoid all risks of explosion during the hydrogen oxidation, some amount of fine sand placed near the jet or the dilution of the hydrogen flow in an inert atmosphere, such as N_2 or Ar, is advisable. Eventually, a condenser must be used to liquate the formed water vapour.

The ratio of ^{18}O and ^{16}O isotopes (^{17}O is usually negligible) evolved from the electrolysis may differ from that in natural water because electrolytic separation of oxygen isotopes takes place at the anode. Thus, if the produced hydrogen isotope mixture is burned in the oxygen evolved from the electrolysis, some error can be introduced in the determination of the hydrogen to deuterium ratio in the formed water. This error can be particularly important on analysing the water by specific gravity measurements. An increment of the water density of 1ppm can be attributed to an increment of 8.75 ppm mol of $^{18}O/^{16}O$ or to 9.27 ppm mol of D/H. As a consequence it is more convenient to use a two compartment electrolytic cell to separate hydrogen and oxygen and burn the hydrogen isotopic mixture in oxygen having a natural isotopic ratio.

3.3.1.2 Analysis of hydrogen to deuterium ratio in the formed water

The analysis of the H/D ratio in water can be done by several techniques. Picnometric measurements of the resulting water specific gravity have been applied by several workers [3.12, 28, 29, 65]. This kind of measurement requires the use of very accurated scales, a thermostat sensitive to 0.01 ºC and at least 3 mg of water are needed for every determination. The precision in the hydrogen to deuterium ratio is about 10 ppm mol D/H but the procedure is very tedious and every single measurement can take several hours. The long time required for each measurement introduces two relevant error sources: the isotope exchange of the analysed water with atmospheric moisture and the water isotope fractionation due to the different partial pressures of heavy and regular water.

Analysis of the resulting water samples can also be done by infrared spectrophotometry as described by Guant [3.66]. Two different absorption bands at 2.946 μm and 3.980 μm correspond to OH and OD groups. The band at 2.946 μm can be used to measure low hydrogen concentration water samples where all hydrogen atoms are in HDO molecules greatly diluted in the mass of D_2O. The 3.980 μm absorption band is used for the analysis of low deuterium concentration water samples. The measurement of intermediate deuterium concentrations is more complicated because significant quantities of all three molecular species (H_2O,

HDO and D_2O) are present. In this case, a combination of other absorption bands of the three molecules can be used [3.67]. In addition, water samples can be diluted to the range of low deuterium concentrations, although this can introduce further errors in the analytical procedure. Anyway, calibration curves of optical density *vs.* deuterium concentration are required mainly due to the effect of temperature and instrument drift. The application of this technique to the measurement of the electrolytic separation factor was done by Lewis and Ruetschi [3.33].

3.3.2 Analysis of H_2-HD-D_2 mixtures by the micro-thermo-conductivity method

The micro-thermo-conductivity method for H_2-HD-D_2 analysis was developed by A. Farkas and L. Farkas in 1934 [3.68]. It is based on the different specific heats of H_2, HD and D_2 molecules. Equilibrium between the three molecules is established by using a hot Ni wire that catalyses exchange reactions. The measurement of the thermal conductivity of the samples before and after the exchange, allows estimating the concentrations of the three molecules. The original apparatus yielded an accuracy of 0.2% in the measurement of deuterium concentration in a sample of 0.002 ml of gas at standard conditions. This technique presents some difficulties. The first one is the maintenance of the fine wire surface used for thermal-conductivity measurements. The second one is that separation of H_2-HD-D_2 mixtures can take place in the apparatus due to their different diffusion coefficients. Methods for overcoming these difficulties were reported by Walton [3.69]. The application of this technique to the measurement of the electrolytic separation factors can be found in the papers by Walton and Wolfenden [3.25] and Farkas [3.15].

3.3.3 Gas chromatographic analysis

A convenient method to analyse hydrogen isotopes is gas chromatography. The H_2-HD-D_2 mixtures pass through a column that separates the three molecular isotopes. A suitable flow detector at the end of the column gives the amount of each molecular isotope in the analysed sample. Calibrations by using H_2-HD-D_2 standards are needed.

Any substance with different adsorption affinities for the hydrogen isotopes which catalyses the conversion of *ortho* and *para*-hydrogen should make the complete separation of the species possible. However, it should not catalyse the hydrogen-deuterium exchange. An effective column for hydrogen isotopes separation was reported by Hunt and Smith [3.70]. It consisted in a copper tube fulfilled with a mixture of chromia and alumina powder operating at 77 K. Pure alumina and silica gel columns have also been proved to be effective for hydrogen isotopes separation. The application of gas chromatography to the measurement of electrolytic separation factors can be found in several works [3.50, 54, 71].

3.3.4 Analysis of H_2-HD-D_2 mixtures by mass spectrometry

The most used technique to analyse H_2-HD-D_2 mixtures evolved from electrolysis and thus to measure *S* is mass spectrometry (MS) [3.30, 31, 37, 38, 51, 53, 55, 61, 72]. The analysis of H_2-HD-D_2 mixtures by means of MS has been treated in detail in Chapter 2. It has been shown that the precise calibration of the gas analysis system is imperative whenever quantitative results are to be obtained due to all the factors that can affect the measurements. Among them, it is of significant importance the influence of the mass discrimination effects on the detection sensitivities of the three hydrogen isotopomers. However, in the majority of the experimental works that used MS to measure *S*, the existence of such effects is omitted. In addition, experimental details about the calibration procedures of the MS are lacked.

Some authors [3.55] have used the technique known as 'electrochemical mass spectrometry' (EMS) for the measurement of *S*. This is an on-line method introduced by Bruckenstein and Gadde [3.73], which couples a porous electrode to the gas-inlet system of a MS. One of the major advantages of this method is the short time needed, of the order of a few minutes, to perform an experiment. In addition, it allows obtaining information about the time evolution of the separation factor during the electrolysis itself. The previously described techniques give the mean value of the separation factor of the whole electrolytic process.

3.4 Experimental results: on-line measurements of the electrolytic separation factor on Pt cathodes

In this work, EMS has been the experimental technique used to investigate the electrolytic separation of H and D. There are, however, some differences between the present experimental set-up and that described in the previous section. For instance, smooth electrodes instead of porous hydrophobic electrodes have been used. This is because hydrogen molecules are volatile and they can be directly carried to the gas inlet of the gas analysis system by means of an Ar flow. In addition, the system has been optimised to reduce to a few seconds the time elapsed between desorption of hydrogen molecules from the cathode and their detection. This allows obtaining relevant information about the time evolution of *S* during the electrolysis.

In what follows, I will describe the experimental apparatus used to measure *S* and the calibration experiments performed with Hg cathodes. Experimental *S* measurements obtained with Pt cathodes are also presented and discussed. Finally, some additional results which illustrate how EMS can be employed to investigate different phenomena are presented.

3.4.1 Description of the experimental system

The scheme of the experimental EMS setup is depicted in Fig.3.5. It consists in two main parts: the electrolytic system and the gas analyser. The latter has been

described in detail in Chapter 2. The electrolytic system is formed by a sealed electrolytic cell with a gas inlet and outlet, what is connected to a potentiostat Princeton Model 362. PVC tubes were attached to the gas inlet and outlet. High purity Ar (99.999%) was flushed through the cell to carry the electrolysis evolved gases to the gas analysis system. The Ar flow has been measured and controlled by a flow meter Ucar F201C-UA. No water traps have been used to dry the gases evolved from the electrolysis, in order to minimize the delay time for molecules detection. The absence of water traps increases the amount of $H_2O/HDO/D_2O$ molecules in the gas analysis system due to the draft of electrolyte by the evolved bubbles. Indeed, the relation between the i_{18} peak current (corresponding to H_2O^+ ions) and the i_2 one (corresponding to H_2^+) was approximately one order of magnitude greater on analyzing the electrolytic gases than the values obtained by using high purity hydrogen. This can lead to a higher isotope exchange between the hydrogen and water isotopomers than that observed during the calibration experiments of the gas analysis system (see section 2.4.4). The presence of a water trap would diminish the effect of isotope exchange reactions inside the gas analysis chamber. However, the use of a water trap would increase the free volume between the electrolytic cell and the analyser, with the subsequent increase of the isotope exchange reactions in this volume. On the other hand, the effect of isotope exchange reactions during the electrolytic experiments can be lowered by using $H_2/HD/D_2$ and $H_2O/HDO/D_2O$ mixtures in which the H and D amounts are of the same order of magnitude. In that case, isotope exchange reactions would compensate for each other and the H and D concentrations in the hydrogen molecular isotopes would remain practically unchanged.

The electrolytic cell consists in a glass vessel sealed with a rubber top supporting the electrodes and the gas inlet and outlet (see Fig.3.5). A small electrolytic cell has been designed and built for several reasons. First, to minimize the amount of dissolved gaseous hydrogen and deuterium in the electrolyte and to reduce as much as possible the time elapsed between gas desorption from the cathode and its detection at the QMS. Second, for economy, due to the cost of heavy water. Volume of electrolyte was 10 ml, whereas the free volume of the cell and the PVC tubes was about 2 ml. The reference electrode (RE) was a polycrystalline Pt wire (Johnson Mathey, Grade 1) sealed with a glass tube. Its geometrical area in contact with the electrolyte was about 2 mm^2. The counter electrode (CE) was a polycrystalline Pt foil (Goodfellow, 99.95% purity) 0.25 mm thick and geometrical area equal to 1 cm^2. Electrical contact was made with a Pt wire sealed with a glass tube and welded to the Pt foil. The electrodes were etched in hot sulphuric acid (Merck, 96% vol.) during 60 min and subsequently washed in H_2O (18.2 MΩ cm) before the experiments.

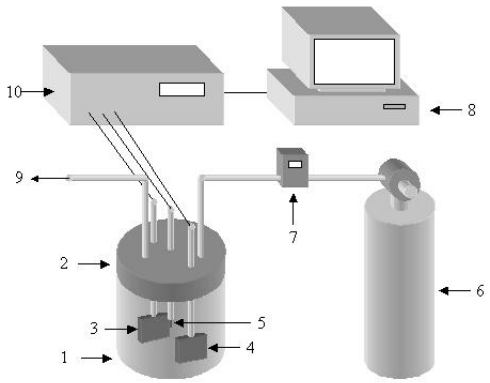

Fig.3.5. Scheme of the electrolytic cell: (1) glass vessel; (2) rubber top; (3) cathode; (4) anode; (5) reference electrode; (6) Ar bottle; (7) flow meter and controller; (8) data acquisition card; (9) PVC tube connecting the cell to the gas analysis system; (10) potentiostat.

3.4.2 Calibration experiments of the EMS system by using Hg cathodes

The experimental EMS system has been tested by using a Hg cathode because it neither absorb [3.74] nor adsorb [3.75] hydrogen at normal conditions. Therefore, it is expected that the amount of hydrogen measured with the gas analysis system varies linearly with the electric charge passed through the Hg cathode, according to *Faraday's* law.

The Hg cathode (Panreac, high purity) was deposited in a small glass vessel located at the bottom of the electrolytic cell. Electrical contact was made with a Pt wire immersed in the Hg and sealed with a glass tube. Geometrical area of the Hg cathode in contact with the electrolyte was ~3.8 cm^2. 1M H_2SO_4 electrolyte was prepared by diluting high purity H_2SO_4 (Merck, 96% vol.) in H_2O (18.2 MΩ cm). In these experiments, a Hg/Hg_2SO_4 RE joined to the electrolyte through a salt bridge was used.

Cathodic polarizations were done to remove the oxide traces in the Hg surface prior to the electrolysis. In order to check the effectiveness of the surface cleaning, cyclic voltammetry was applied to the Hg electrode. A typical voltammogram run between -800 and -1400 mV at a sweep rate of 1 mV s^{-1} is shown in Fig.3.6. The inset of this figure shows the Tafel plot of the experimental data corresponding to the positive scan. The Tafel slope obtained from the mean square fit of the experimental data points is equal to 127±5 mV. This value is in agreement with that reported for Hg in acidic media, namely ~120 mV [3.75]. From this result it can be safely assumed that the Hg electrode is not poisoned by surface oxides.

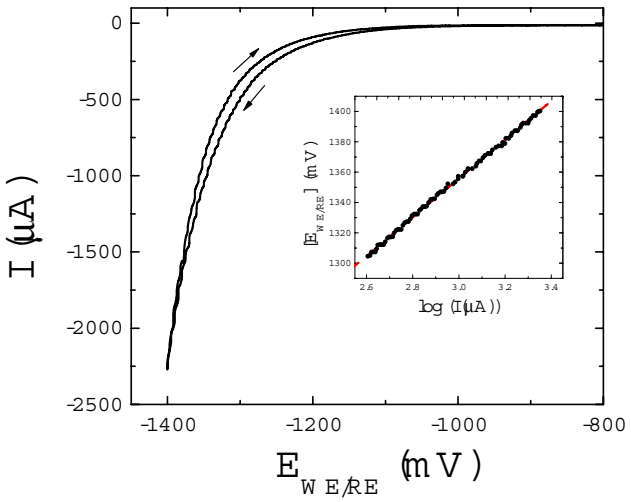

Fig.3.6. Typical voltammogram of the Hg electrode in 1M H_2SO_4 electrolyte run between -800 and -1400 mV at a sweep rate of 1 mV s^{-1}. The inset shows the Tafel plot of the experimental data recorded during the positive scan.

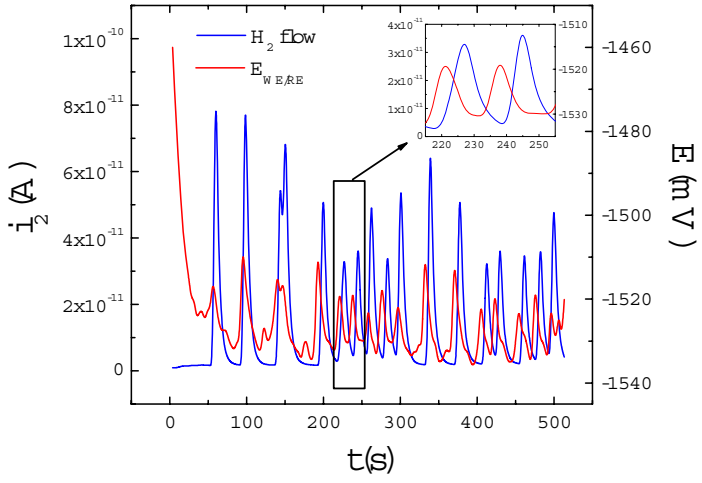

Fig.3.7. Time evolution of the H_2 evolved from the Hg cathode (blue line) and of the cathode potential (red line) when applying a constant electrolytic current (I_d=15 mA cm^{-2}) at t=0. The inset shows a detail of the cathode potential and the H_2 flow to emphasize the delay time between these signals.

Fig.3.7 shows the typical time evolution of i_2 peak current (corresponding to the H_2 flow evolved during the electrolysis) when applying a constant electrolytic current (I_d=15 mA cm^{-2}) at t=0. Sharp peaks in the time evolution of the H_2 flow are observed, due to the evolved bubbles after their nucleation and growth at the Hg cathode. Each peak corresponds to the detection of a bubble what allows to determine the hydrogen production by the electrolysis. It can be observed in Fig.3.7 that the potential of the Hg cathode is influenced by the bubble desorption from the cathode. The growth of a bubble on the Hg surface reduces the area of the electrode in contact with the electrolyte and, therefore, produces an increase of the electrolytic current density and of the overpotential. Accordingly, minima of the electrode potential are observed when H_2 bubbles are desorbed from the Hg cathode.

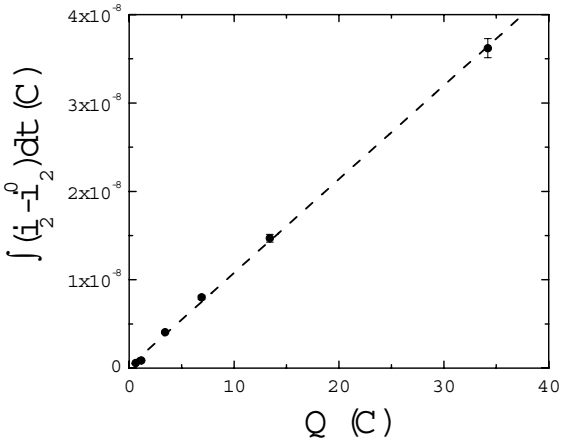

Fig.3.8. Total amount of H_2 evolved from the Hg cathode as a function of the electric charge passed during the electrolysis.

The i_2 peak current can be taken proportional to the evolved H_2 flow. By integrating the i_2 signal minus the i_2^0 background signal one obtains a measurement of the total amount of evolved H_2. This is plotted in Fig.3.8, as a function of the electric charge passed through the cathode. A linear correlation is obtained in agreement with *Faraday's* law.

On the other hand, one can use the fact that H_2 desorption from the cathode is governed by the bubble nucleation and growth to calculate the delay time between H_2 liberation and its detection at the QMS. By measuring the time difference between H_2 bubbles liberation from the cathode (monitored by the electrode potential minima) and the maximum of the peaks corresponding to bubble

detection (see the inset in Fig.3.7), a delay time of about 5 s is obtained. This time agrees well with the estimation done by considering the conductance of the capillary tube for gas collection, the free volume of the electrolytic system and the value of the Ar flow.

In resume, it has been shown that experiments with Hg cathodes allow calibrating the EMS system. From these experiments, it can be concluded that the relationship between the H_2 flow evolved from the electrolysis and the i_2 peak current is linear (given that the H_2 flow is much lower than the carrier Ar flow). In addition, it has been demonstrated that the response time of the EMS system is of about 5 s.

3.4.3 Measurements of the electrolytic separation factor of Pt in alkaline solution

The Pt-H_2 system has significance for many practical systems, such as water electrolysis, fuel cells and organic reductions. Indeed, Pt is one of the most investigated metals in electrochemistry, including the electrolytic separation of hydrogen isotopes (see Table 3.1). However, the HER at Pt cathodes is far to be a closed question and many papers about this subject are still published [3.76, 77]. In what follows, I will present some results on the time evolution of *S* at Pt cathodes, obtained with the EMS system already described. The dependence of *S* on the isotopic composition of the electrolytes will be also investigated.

3.4.3.1 Experimental details

The Pt cathode used was similar to the Pt anode already described (section 3.4.1). It was etched like the anode and reference electrode before the electrolysis. In addition, cathodic polarizations at 0.1 A cm^{-2} were done prior to the electrolytic experiments in order to remove the oxide film from the Pt surface.

0.1M LiOH and 0.1 M LiOD electrolytes were prepared by dissolving metallic granulated Lithium in light (18.2 MΩ cm) and heavy water (>99.6% isotopic purity), respectively, under Ar atmosphere. D_2O was kindly supplied by the European Organization for Nuclear Research (CERN). The purity of D_2O in regard to ionic impurities has been checked by ICP analysis and electrical conductivity. It contains 1 ppm of potassium. Other impurities are well below the ppm range. The electrical conductivity of D_2O at room temperature was 12.3 μS cm^{-1}. From K^+ and OD^- ionic concentrations, the electrical conductivity is calculated to be 11.0 μS cm^{-1}. ICP analyses of the LiOH and LiOD electrolytes revealed that the impurity levels coming from the Li grains are well below the ppm range.

The LiOH and LiOD electrolytes were mixed in different proportions to obtain the desired $(H/D)_{liq}$ ratios. To this aim, a given volume of LiOH electrolyte was measured with a micropipette Gilson P1000. This volume was put into a volumetric flask of 10 ml (Pobel Clase A) and then the LiOD electrolyte was added. The electrolytes were thermostatized at 300 K before the volumetric

measurements. The dependence of $(H/D)_{liq}$ on the volume of LiOH and LiOD electrolytes (V_{H2O} and V_{D2O}, respectively) can be approximated by:

$$\left(\frac{H}{D}\right)_{liq} = \frac{\rho_{H2O} M_{D2O} V_{H2O}}{\rho_{D2O} M_{H2O} V_{D2O}} \tag{3.12}$$

where ρ_{H2O} and ρ_{D2O} are the densities of light and heavy water, respectively, and M_{H2O} and M_{D2O} are their molecular masses.

The experiments were controlled galvanostatically by applying a given current density during time intervals of about 10 min. Currents were applied without following a determinate increasing or decreasing sequence to avoid systematic errors in the measurements. Time intervals (of about 10 min) of zero applied current were kept between two successive measurements in order to allow the cathode to reach a stationary potential value (~100 mV respect to the Pt reference electrode). The temperature of the electrolyte was maintained at 298 K within the experiments.

3.4.3.2 Time evolution of the electrolytic separation factor on Pt cathodes

On applying a constant electrolytic current to the cell, it is observed a transitory evolution of the H_2, HD and D_2 flows evolved from the cathode. A typical result is shown in Fig.3.7, where i_2, i_3 and i_4 peak currents are plotted as a function of time. At the present experimental conditions, these peak currents are respectively proportional to the H_2, HD and D_2 flows evolved from the Pt cathode. The dispersion in the experimental points of Figs.3.9(a)-(c) is mainly due to hydrogen bubbles evolved time by time from the cathode. Bubble formation is affected by the roughness of the electrode surface. As a matter of fact, as the electrode surface is smoother, the size of the desorbed bubbles increases and the H_2, HD and D_2 flows show more irregular profiles.

The experimental points in Figs.3.9(a)-(c) can be well fitted by simple exponential functions of the form:

$$i_{m/q}(t) - i^0{}_{m/q} = i^*{}_{m/q}\,(1 - e^{-t/\tau_{m/q}}) \tag{3.13}$$

These fits are represented by solid lines in Fig.3.9. The steady state values of the current peaks, $i_{m/q}$*, are plotted in Fig.3.10 as a function of the applied electrolytic current. It is observed that $i_{m/q}$* are proportional to the electric current passed through the cell. This implies that the ratio $(H/D)_g$ remains constant and the separation factor is independent of the applied current density, in good accordance with the results reported by Harada [3.31] on Pt cathodes. Furthermore, the total flow of evolved hydrogen molecular isotopes varies linearly with the electrolytic current intensity, according to *Faraday's* law.

Another interesting observation is that the ratio $K=[HD]^2/([H_2][D_2])$ for the evolved gases (see equations (2.28-2.29)) does nor depends neither on the electrolytic current applied through the cell nor the isotopic composition of the electrolytes (see Fig.2.25). This fact was used to obtain the relative detection sensitivity of the gas analysis system for the HD molecule (section 2.4.5).

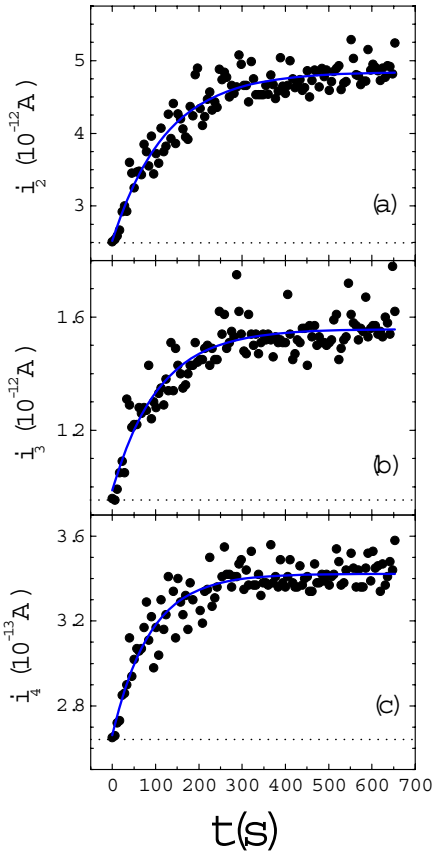

Fig.3.9. Time evolution of: (a) i_2 peak current corresponding to H_2 ; (b) i_3 peak current corresponding to HD and (c) i_4 peak current corresponding to D_2 when applying in t=0 a current density of 5 mA cm^{-2} through the cell. Dotted lines shows the background signals ($i^0_{m/q}$) corresponding to the residual atmosphere present in the system. Solid lines in these figures represent the fits of the $i_{m/q}$ currents by exponential functions $i_{m/q}(t)-i^0_{m/q}=i^*_{m/q}(1-exp(-t/\tau_{m/q}))$.

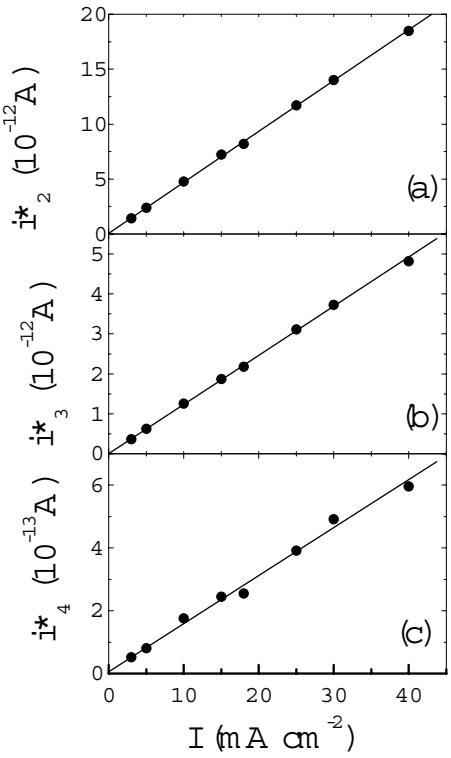

Fig.3.10. Stationary values of the QMS peak currents as a function of the electrolytic current density. (a) i^*_2 peak current corresponding to H_2 ; (b) i^*_3 peak current corresponding to HD; (c) i^*_4 peak current corresponding to D_2. Solid lines are the mean square fits of the experimental data points.

Time constants ($\tau_{m/q}$) obtained from the fits like these appearing in Fig.3.9 are plotted in Fig.3.11 as a function of the applied current density. It is observed that $\tau_{m/q}$ diminishes from 160 to 5 s on increasing the electrolytic current density, reaching a steady value at electrolytic current densities above ~40 mA cm^{-2}. The limiting values of the transient times agree with the response times of the gas analysis system obtained in the preceding section. On the other hand, it can be seen in Fig.3.11 that time constants for hydrogen molecular isotopes are different and decrease in the order $\tau_2 > \tau_3 > \tau_4$ when compared at the same electrolytic current. These time constants seem to be associated with the adsorption/absorption of H and D atoms at/in the Pt cathode. At the early stages of electrolysis, some of the discharged H and D atoms remain adsorbed/absorbed until the saturation coverage

is reached. Then, all the discharging H and D atoms are desorbed as H_2 molecules according to Fig.3.10. The decrease of the time constants when increasing the current density can be attributed to the fact that the H and D coverage reaches faster the saturation state for higher the electrolytic current.

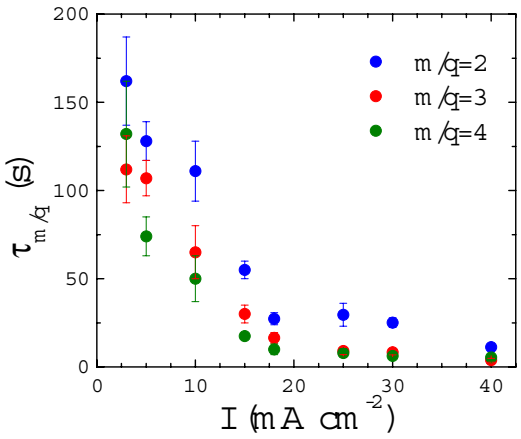

Fig.3.11. Time constants for the evolution of $i_{m/q}$ peak currents as a function of the applied electrolytic current density.

As it has been stated above, time constants decrease in the order $\tau_2 > \tau_3 > \tau_4$ when compared at the same electrolytic current. This difference can not be due to the transport of molecules from the electrode surface to the QMS because the diffusion coefficient of H_2 is higher than that of D_2. Thus, the difference between the time constants for H_2, HD and D_2 evolution reflects a change in *S* as a function of the time of electrolysis. The separation factor has been calculated from the i_2, i_3 and i_4 peak currents by using the relative detection sensitivities $\sigma_2^{H2}/\sigma_4^{D2}$ and $\sigma_3^{HD}/\sigma_4^{D2}$ obtained in the calibration experiments of the gas analysis system (see section 2.4). Experimental errors in *S* values are of the order of 10-15%. These errors come mainly from the dispersion induced by bubble desorption and from the errors in the determination of the relative detection sensitivities.

The typical time evolution of *S* is plotted in Fig.3.12(a). It shows an increase from ~1.8 at t=0 to a limiting value of ~6.4. As a matter of fact, the higher the electrolytic current density, the stationary *S* value is reached faster. There exist an excellent similarity between the evolution of *S* during the electrolysis time shown in Fig.3.10(a) and the corresponding evolution with the electrode potential obtained by Hammerli *et al.* [3.38] with Pt. The experimental results obtained by Dandapani and Fleischmann [3.71] also have some parallelism with them. These authors investigated the H/D ratio of the gases evolved from the electrolysis by applying

short current pulses. According to their results, the separation factor tends to ~1.5 for very short pulses in good agreement with the limiting value at t=0 shown in Fig.3.12. On increasing the pulse length they observed an increase in the separation factor.

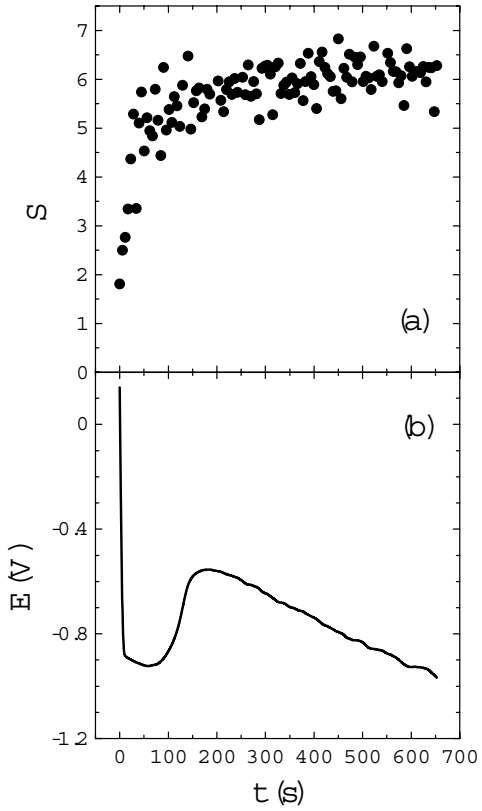

Fig.3.12. Time evolution of the separation factor (a) and the electrode potential (b) on applying a constant electrolytic current (5 mA cm^{-2}) at t=0.

Hammerli *et al.* [3.38] considered that the dependence of S on the electrode potential in Pt cathodes is due to a change in the mechanism of the HER on increasing the overpotential. On the other hand, Dandapani and Fleischmann [3.71] considered that the dependence of S on the length of the current pulses can be explained within the framework of the theory on the electrolytic separation factor exposed in section 3.2. They argued that for short current pulses, H and D atoms are adsorbed at the Pt surface on strongly chemisorbed states. If one assumes that the corresponding TS are similarly strongly bonded, high ZPE differences will

appear at the TS and, therefore, low *S* values will be obtained. On increasing the length of the current pulses, the atoms adsorb on weakly bonded states and *S* increases. This hypothesis is in agreement with the present experimental results. The TS of the r.d.s would be less bounded on increasing the H and D coverage and *S* will increases until the coverage reaches the saturation value. Therefore, it is reasonable to conclude that the surface coverage by H and D is governing the time evolution of *S* at Pt.

The time evolution of the cathode potential is shown in Fig.3.12(b). This evolution can also be related to the adsorption of H and D at the cathode surface. In fact, the changes in the cathode potential have a great similarity to the changes of the work function of Pt surfaces on increasing the amount of adsorbed hydrogen [3.78-80]. The existence of a maximum in the work function when increasing the H coverage has been observed at polycrystalline Pt [3.78, 79] and at Pt (110) (1x2) surfaces [3.80] and it is associated with the existence of different surface sites for H adsorption.

3.4.3.3 Dependence of the electrolytic separation factor on Pt cathodes on the isotope composition of the electrolytes

The dependence of *S* values on the H/D fraction in the electrolyte has been investigated both theoretically [3.14, 81] and experimentally [3.12, 15, 31, 55] by some authors. However, the results are not clear and reproducible and strong differences are observed between the theoretical and experimental results. For instance, a sharp increase of *S* has been predicted for Pt on decreasing the D content in the electrolyte [3.81]. By contrast, experimental results with Pt cathodes [3.31] have shown that S remains practically unchanged when varying the isotopic composition of the electrolytes. In order to solve this discrepancy, *S* values have been measured with Pt cathodes in alkaline media and the results are now reported.

The dependence of *S* values on the D mole fraction in the electrolyte has been obtained by measuring the H to D ratio in the gases evolved from the electrolysis of 0.1M LiOH/LiOD electrolytes with different $(H/D)_{liq}$ ratios. The $(H/D)_{gas}$ ratios in the gases evolved from the electrolysis have been obtained by plotting the stationary values of the H flow as a function of the D flow, as shown in Fig.3.13.

The stationary *S* values are plotted in Fig.3.14 as a function of the D mole fraction in the electrolytes. It can be seen from this figure that *S* does not depend on the atomic percent of D in the electrolytes to within the experimental error bars. The dispersion of the experimental data points is about 5%, that is, about a half of the experimental error associated to *S* measurements.

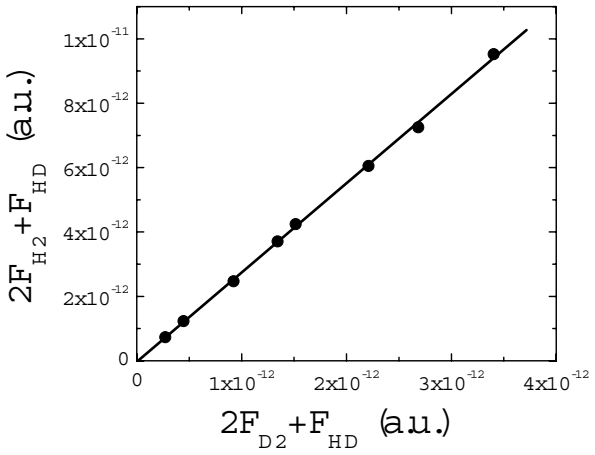

Fig.3.13. Plot of the stationary values of the H flow versus the D flow evolved from the electrolysis of 0.1M LiOH/LiOD mixtures. The slope of the least square fit of the experimental data points (solid line) gives the H to D ratio in the evolved gases.

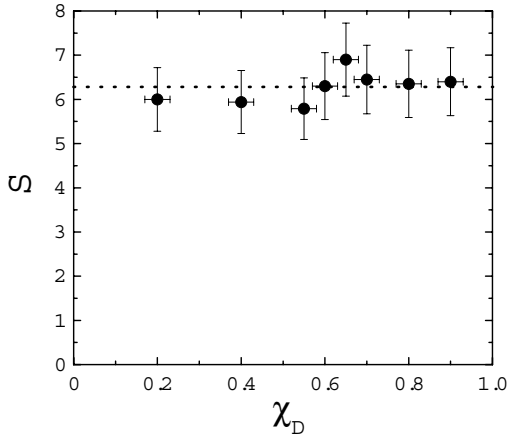

Fig.3.14. Plot of the experimental *S* values of the Pt cathode as a function of the D molar fraction in the 0.1M LiOH/LiOD electrolytes. Dotted line represents the mean value of the experimental points.

The independence of *S* of Pt cathodes on the $(H/D)_{liq}$ ratios was also observed by Harada in acidic media [3.31]. However, the present experimental *S* value, namely, 6.3±0.7, is a 20 % higher than that reported by him (*c.a.*, *S*=5.0±0.2). The

present value is closer to the mean value of the experimental data appearing in Table 3.1 for Pt, namely 6.3±1.4. This close agreement confirms the quality of the experimental setup constructed to measure *S*.

3.5 Additional applications of EMS

In this section, I will show some additional results on the use of a gas analysis system coupled to an electrochemical cell, in order to emphasize the capabilities of the EMS technique. For this reason, the problems treated here will be analyzed at a lower level of detail than in the previous sections.

3.5.1 Kinetics of Hydrogen absorption on Pt

The kinetics of H absorption by metallic cathodes is a problem which has a great interest from a fundamental point of view. EMS technique has been applied to investigate the kinetics of H absorption in Pt in acidic media and the results are now reported.

The electrolytic experiments have been performed in the EMS setup already described in section 3.4. 1M H_2SO_4 electrolytes have been prepared from high purity H_2SO_4 (Merck, 96% vol.) and Milli-Q H_2O (18.2 MΩ cm). A Pt foil of 0.1x10x10 mm^3 (Johnson Mathey, Grade 1) has been chosen as WE. The working and counter electrodes have been etched with *aqua regia* and then rinsed with deionised water prior to the electrolysis. In those experiments, a $Hg/HgSO_4$ RE filled with a saturated K_2SO_4 aqueous solution has been used. This electrode was electrically connected to the cell by means of a salt bridge.

The time evolution of the H_2 flow has been measured by appying constant electrolytic currents through the cell and analyzing the composition of the gases evolved from the electrolysis. In Fig.3.15(a), the H_2 flow evolved from the Pt cathode has been plotted as a function of the electrolysis time. It shows a transitory behaviour until a steady state value of the H_2 flow is reached. This transitory has been fitted by considering an exponential-time dependence, like that given by equation (3.13). The time evolution of the electrode potential has been plotted in Fig.3.15(b). It presents a transitory evolution, decreasing with time, which is indicative of some dynamic process taking place at the Pt electrode.

The steady values of the i_2 peak currents obtained from the fits of the time dependence of the H_2 flow are plotted in Fig.3.16 as a function of the applied electrolytic current. Again, a linear relationship is observed, according to *Faraday's* law. The slope of the linear fit of the experimental points in Fig.3.16 allows calculating the sensitivity of detection of H_2 by the gas analysis system. The obtained σ_2^{H2} value is equal to $2.20 \cdot 10^{-4}$ A mol^{-1} s, to within ±1%. This value agrees with that obtained during the calibration probes exposed in section 2.4.2.

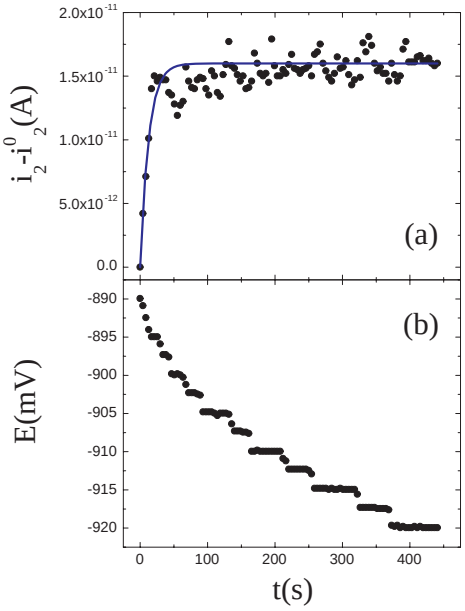

Fig.3.15. Typical time evolution of the H_2 flow evolved from the Pt cathode (a) and of the electrode potential (b) when applying a constant electrolytic current through the cell.

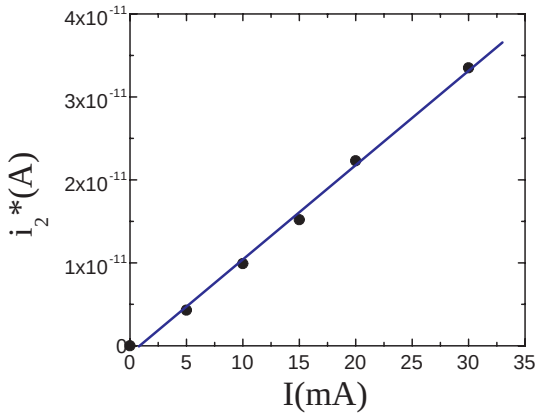

Fig.3.16. Relationship between the steady values of the i_2 peak currents and the electrolytic current applied through the cell. The blue line is the least square fit of the experimental data points.

In order to investigate the origin of the transient behaviour of the H_2 flow shown in Fig.3.15(a), the differences between the total amount of discharged atoms and that evolved from the cathode as H_2 molecules have been calculated. The first quantity can be known from the electric charge passed through the cell, whereas the latter can be obtained from the time integrals of the i_2 peak current divided by σ_2^{H2}. The calculated differences have been plotted in Fig.3.17 as a function of the electrolytic current. The experimental point at 10 mA shows a H amount much higher than these of the other electrolytic currents. This point corresponds to the first charging step, which implies that an irreversible trapping of is taking place. The origin of this irreversible trapping is unknown. It coud be caused by the trapping of H atoms within the Pt cathode (irreversible H absorption) or in the electrolyte (as H_2 dissolved molecules).

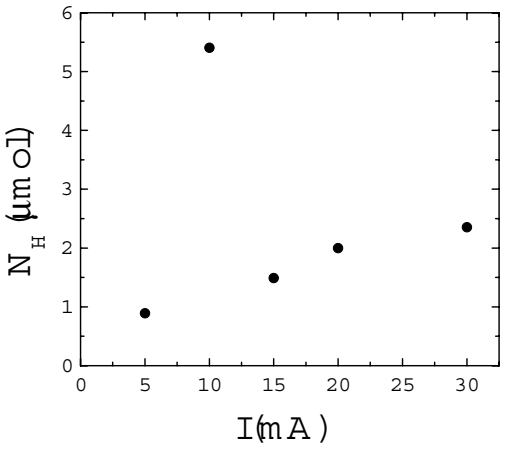

Fig.3.17. Difference between the amounts of H atoms discharged at the Pt cathode and evolved as H_2 molecules as a function of the electrolytic current applied through the cell.

In order to understand the results shown in Fig.3.17, it will be assumed that H atoms are adsorbed/absorbed at/in the Pt cathode. If the number of H adsorbed/absorbed atoms is small, the kinetic equations governing the time evolution of the amount of H atoms adsorbed/absorbed within the electrode (N_H) are given by:

$$\frac{dN_H}{dt} = \frac{I}{F} - 2 \cdot k_d \cdot {N_H}^2 \qquad (3.14)$$

where I is the electrolytic current density, F the *Faraday's* constant and k_d is the rate constant of surface recombination. The first term in the right hand side of equation (3.14) is the rate at which H atoms are discharged at the cathode surface, whereas the second term represents the number of H atoms leaving the cathode in the form of H_2 gaseous molecules. According to the present model, H_2 molecules are formed by recombinative desorption of H atoms, instead of by electrochemical desorption. If it is assumed that k_d is independent of N_H (Langmuir desorption process), the solution of equation (3.14) is:

$$N_H(t) = \sqrt{\frac{I}{2 \cdot F \cdot k_d}} \cdot tgh\left(\sqrt{\frac{2 \cdot k_d \cdot I}{F}} \cdot t + C\right) \tag{3.15}$$

where C is the integration constant, which can be calculated from the initial conditions (C=0 when $N_H(0)$=0). According to the present model, the steady state value of the number of H adsorbed/absorbed atoms varies as the square root of the electrolytic current. This behaviour is equivalent to that described by the *Sievert's* law forn solid-gas reactions, by changing the electrolytic current by the H_2 pressure. In Fig.3.16, the amount of H atoms adsorbed/absorbed at/in the Pt cathode is plotted against the square root of the electrolytic current. Experimental data corresponding to the first charge step at 10 mA has not been included in the plot in Fig.3.16. It can be seen that experimental data points fit well to the proposed model. However, there is a point which requires further discussion. The mol number of H adsorbed/absorbed atoms found experimentally (in the range of 10^{-6} moles) seems to be very high to be due to H adsorption at the Pt surface. In fact, the saturation coverage of the typical Pt surfaces is of about $2 \cdot 10^{-9}$ moles cm^{-2}. Therefore, the roughness factor of the Pt electrode surface should be in the range of 10^2-10^3. These values are typical of Pt black, but they seem to be unrealistic for Pt bright electrodes. Another possibility is considering that H atoms are absorbed in the electrode bulk. In that case, the H to Pt ratio would be in the range of 10^{-3}. These values are about 10^3-10^4 times higher than those estimated from solid-gas equilibrium data [3.82] at ambient conditions. This discrepancy, however, can be explained by taking into account the different thermodynamic behaviours in solid-gas and electrochemical processes. As a matter of fact, the driving force for H absorption in metals by the electrochemical route is equivalent to that found in solid-gas reactions at very high pressures. Several experimental evidences avale this assertion. Although H absorption by Pt is ususlly regarded as negligible by most electrochemists, there is a number of repports which point out its role in different phenomena. For instance, Gileadi *et al.* [3.83] observed H absorption in thin Pt foils. In these experiments, the reported H/Pt ratio within the Pt foils at 343 K was as high as $2.5 \cdot 10^{-4}$. On the other hand, H absorption has been suggested by a number of authors [3.84] in order to explain some voltammetric features of Pt

electrodes. Somewhat similar results have been reported in Ni electrodes. Thin layers of non-stoichiometric NiH_x have been observed in Ni cathodes both in acidic [3.85] and alkaline [3.86] solutions, although it is quite hard to prepare it by solid-gas reaction at ambient temperature (the equilibrium plateau pressure on absorption is about $6 \cdot 10^3$ bar [3.87]).

A critical reader could think that there are no sound arguments to conclude that H atoms are absorbed in the Pt electrode. It can be though that the difference between the amounts of H atoms discharged at the electrode and the mol number of H_2 molecules detected at the QMS could be caused by the dissolution of molecular hydrogen in the electrolyte. Indeed, the mole fraction of dissolved H_2 in water can be as high as 10^{-5} [3.88], *i.e.*, of the same order of magnitude than the H amounts found in the present experiments. However, there is an additional argument to conclude in favour of H absorption in the Pt cathode, namely, the time evolution of the rest electrode potential.

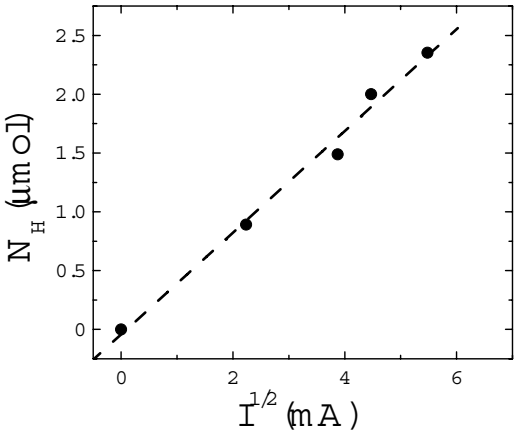

Fig.3.18. Difference between the amounts of H atoms discharged at the Pt cathode and evolved as H_2 molecules as a function of the square root of the electrolytic current applied through the cell. The dashed line is the mean square fit of the experimental data points.

The relationship between the electrode potential (in millivolts) and the amount of adsorbed H atoms at equilibrium (*i.e.*, at zero applied current) is given by the Nernst equation [3.89]:

$$E = K - 59 \cdot \log\left(\frac{\theta_H}{1-\theta_H}\left[H^+\right]\right) \qquad (T\text{=}298\text{ K}) \qquad (3.16)$$

where K is a constant, $[H^+]$ is the proton concentration in the electrolyte and θ_H is the H surface coverage. θ_H is assumed to be proportional to the number of absorbed H atoms per Pt atom (n_H), given that n_H is small. If it is also assumed that the surface coverage decreases with time due to recombination of H atoms at the surface, the following equation must be obeyed:

$$\frac{d\theta_H}{dt} = -\kappa \cdot \theta_H{}^2 \tag{3.17}$$

The solution of equation (3.17) is given by:

$$\theta_H(t) = \frac{1}{\theta_0{}^{-1} + \kappa \cdot t} \tag{3.18}$$

where κ is the rate constant of the surface recombination process and θ_0 is the initial surface coverage. By introducing equation (3.18) into (3.16), an expression for the time evolution of the electrode potential is obtained. There are some unknowns (such as κ, θ_0, etc.) which avoid fitting the experimental data to the present model. To circumvent this difficulty, we must extrapolate the time evolution of E at large times (i.e., $\kappa t >> \theta_0^{-1}$). In that case, the Nernst equation takes the form:

$$E = K' + 59 \cdot \log(t) \tag{3.19}$$

being K' a constant (independent of time). Thus, the model predicts a linear dependence between the rest potential of the Pt electrode and the decimal logarithm of time, whose slope is equal to 59 mV. The typical time evolution of the rest potential of the Pt electrode has been plotted in a semilogarithmic scale in Fig.3.19. A linear dependence is observed at large times. The mean value of the slopes obtained from the linear fit of experimental data points give 58±5 mV, which is in excelent agreement with the results predicted by equation (3.19). This result agrees with the hypothesis of H absorption within the Pt electrode. In any case, further endeavours are needed in order to understand the features of the electrolytic H absorption in Pt.

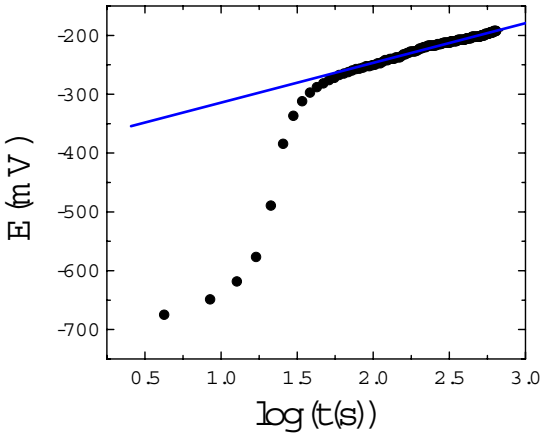

Fig.3.19. Rest potential of the Pt cathode as a function of the decimal logarithm of time. The blue line represents the linear fit of experimental data at large times.

3.5.2 The Oxygen Evolution Reaction on Pt

The oxygen evolution reaction (OER) is another fundamental reaction involved in many electrochemical processes. In particular, the kinetics of anodic oxidation of metallic electrodes is closely related to the OER. In this section, I will show some results which illustrate how EMS can be applied to investigate these phenomena.

The O_2 flows evolved from Pt anodes have been measured simultaneously to the H_2 (or H_2-HD-D_2) flows during the EMS experiments described in the preceding sections. The typical time evolution of the i_{32} peak current (corresponding to O_2^+ ions) on applying a constant electrolytic current through the cell is displayed in Fig.3.20. Three characteristic regions can be observed. In the initial part of the curve (region i)), the O_2 flow rises very quickly with the electrolysis time. The slope of the time evolution of the O_2 flow is lowered in region ii). Finally, a steady state region is observed in region iii).

The time evolution of the evolved O_2 flow has a great similarity with the time evolution of the overpotential (η) of a Pt anode at galvanostatic conditions. Unfortunately, the electrode potentials of the Pt anodes were not monitored during the experiments, because these electrodes were used as counter electrodes. In spite of that, the general shape of the Pt electrode overpotential at constant electrolytic current is well known [3.90]. In Fig.3.21, η is plotted as a function of the electric charge passed through the electrode (which is proportional to the electrolysis time). As for the time evolution of the O_2 flow shown in Fig.3.20, three definite regions can be distinguished. In the first ascending section of the curve, the charge of the double layer takes place. This produces a marked increase of the overpotential until the electrode potential reaches the oxidation potential of H_2O molecules. Then, an

oxide layer is formed on the electrode surface, which correspond to region ii). Usually, it is assumed that the charge passed though the electrode within this region (Δq_0) corresponds to a monoatomic layer of oxygen atoms. Finally, in region iii) the evolution of gaseous oxygen molecules occurs and a stationary η value is observed.

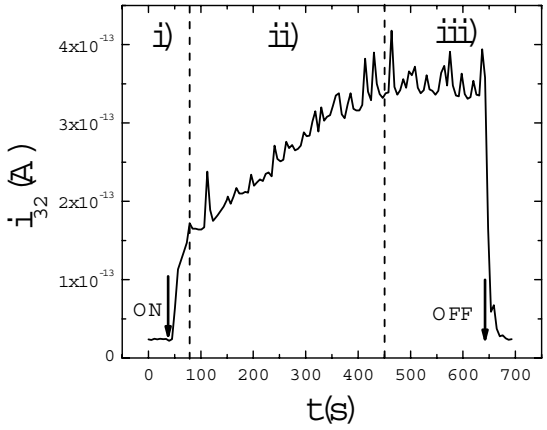

Fig.3.20. Typical time evolution of the i_{32} peak current (proportional to the O_2 flow) on applying a constant electrolytic current through the cell. Three regions separated by vertical dashed lines are observed. The arrows indicate the times at which the electrolytic current is switched on and off.

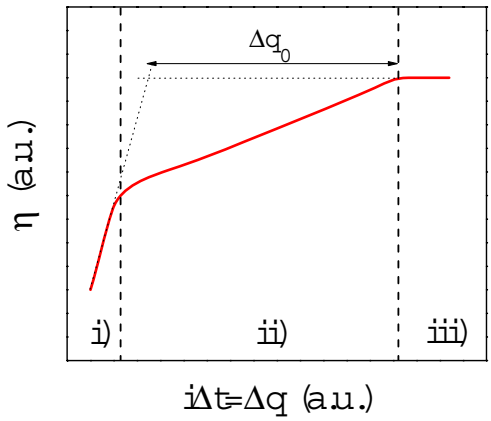

Fig.3.20. Typical time evolution of the overpotential (η) of a Pt anode at galvanostatic conditions (taken from [3.90]). Three regions (marked as i), ii) and iii)) are observed. Δq_0 represents the electric charge passed through the electrode in region ii).

The mean i_{32} values in region iii) of Fig.3.20 have been found to be proportional to the applied electrolytic current, according to *Faraday*'s law (see Fig.3.22). This observation agrees with the interpretation of region iii) in the overpotential-time curve shown in Fig.3.21. Besides, the slope of the i_{32}-I plots allows calculating the O_2 detection sensitivity (σ_{32}^{O2}) by the gas analysis system. The obtained σ_{32}^{O2} values have been used to calculate the difference (N_O) between one half of the mol number of electrons passed through the Pt electrode and the mol number of O atoms evolved as O_2 molecules. This difference is plotted in Fig.3.22 as a function of the electrolytic current. In spite of the large dispersion of experimental data points, a positive correlation between N_O and I can be appreciated.

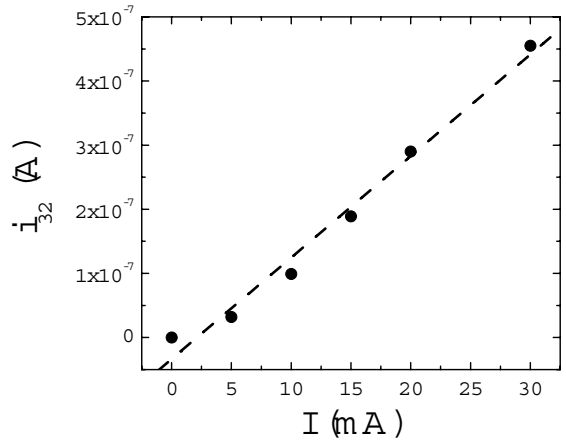

Fig.3.21. Typical experimental correlation between the steady state values of the i_{32} peak current and the electrolytic current applied through the cell. The dashed line represents the linear fit of the experimental data points.

The similarity between the shapes of the intermediate regions in the plots in Fig.3.20 and 3.21 may lead to think that N_O is the amount of oxygen atoms in the Pt oxide layer formed by electrooxidation of H_2O molecules. However, experimental N_O values seem to be very high to be due to Pt oxide formation. These values imply that the thickness of the Pt oxide layer would be in the range of about 1000 monolayers. Therefore, although the hypothesis of Pt oxide formation is not discarded, other possibilities must be considered. For instance, N_O could be caused by the dissolution of O_2 molecules in the electrolyte or the formation of other oxidized species during the electrolysis, such as H_2O_2. In any case, it is clear

that further efforts are needed to ascertain the causes governing the O_2 flow evolution.

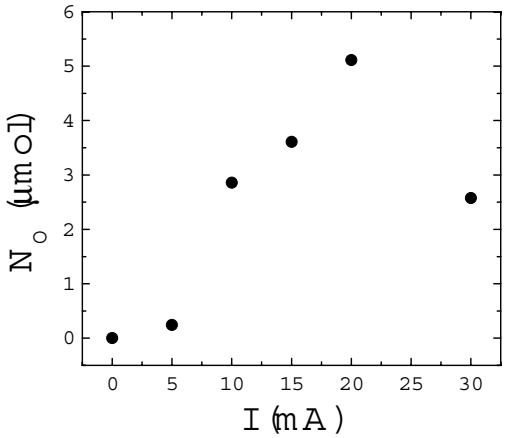

Fig.3.22. The difference between one half of the mol number of electrons passed through the Pt electrode and the mol number of O atoms evolved as O_2 molecules (N_O) is plotted as a function of the electrolytic current passed through the cell.

3.5.3 Coupling EMS with cyclic voltammetry

EMS can be coupled to other electrochemical techniques in order to complement the information provided by them. In order to illustrate this, I will show some results obtained from the analysis of the gases evolved during the cyclic voltammetry of a Pt electrode.

Cyclic voltammetry has been done at the same experimental conditions than the experiments described in section 3.5.1. The Pt electrode was also the same than that used in these experiments. In Fig.3.23(b) it is shown portion of a typical voltammogram of the Pt electrode run between 30 and -965 mV at a constant sweep rate equal to 1 mV s^{-1}. At the same time, the H_2 flow evolved through the cell has been plotted in Fig.3.23(a) in order to show the correlation between the electrolytic current and the amount of evolved H_2 molecules. In both cases, some hysteresis is observed between the negative and positive scans. Both the electrolytic current and the H_2 flow evolved from the Pt electrode are higher in the positive than in the negative scan.

The present results show that the coupling between Cyclic Voltammetry and QMS can be useful to investigate electrochemical processes in which gas evolution reactions take place.

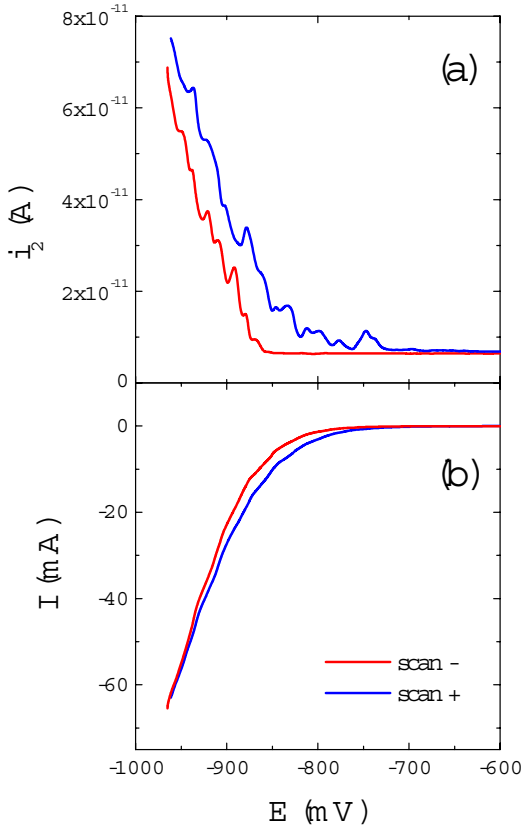

Fig.3.23. Typical results obtained by cyclic voltammetry of a Pt foil electrode in 1M H_2SO_4. (a) and (b) show the dependence of the i_2 peak current (proportional to the H_2 flow) and of the electrolytic current, respectively, on the electrode potential. Red lines refer to the scan towards negative potentials, whereas blue lines represent the positive sweeps.

The results obtained in this section show several prototypic problems in which EMS can be used. Although the obtained experimental results are not concluding, they point out that the experimental system is suitable to perform on-line measurements of the amount of molecules evolved from the electrolysis of any substance. The present technique can provide relevant information in the fields of electrochemical hydrogen production and metal-hydride formation.

3.6 References

[3.1] Matsushima H, Nohira T, Kitabata T and Ito Y 2005 *Energy* **30** 2413
[3.2] Lindemann FA and Aston FW 1919 *Phil. Mag.* **33** 523
[3.3] Urey HC, Brickwedde FG and Murphy GM 1932 *Phys. Rev.* **39** 164
[3.4] Urey HC, Brickwedde FG and Murphy GM 1932 *Phys. Rev.* **40** 1
[3.5] Urey HC, Brickwedde FG and Murphy GM 1932 *Phys. Rev.* **40** 464
[3.6] Washburn EW and Urey HC 1932 *Proc. Nat. Acad. Sci.* **18** 496
[3.7] Urey HC and Rittenberg D 1933 *J. Chem. Phys.* **1** 137
[3.8] Cremer E and Polanyi M 1932 *Z. Physik. Chem.* **19B** 443
[3.9] Eyring H 1933 *Proc. Nat. Acad. Sci.* **19** 78
[3.10] Polanyi M 1933 *Naturwiss* **21** 316
[3.11] Bawn CEH and Ogden G 1934 *Trans. Farad. Soc.* **30** 432
[3.12] Topley B and Eyring H 1934 *J. Chem. Phys.* **2** 217
[3.13] Glasstone S, Laidler KJ and Eyring H *'The Theory of Rate Processes'* McGraw-Hill (1941 New York)
[3.14] Rowland PR 1971 *J. Electroanal. Chem.* **32** 89
[3.15] Farkas A 1937 *Trans. Farad. Soc*, **33** 552
[3.16] Horiuti J and Polanyi M 1933 *Nature* **132** 931
[3.17] Oliphant ML 1933 *Nature* **132** 765
[3.18] Keii T and Kodera T 1957 *J. Res. Inst. Catalysis Hokkaido Univ.* **5** 105
[3.19] Conway BE and Salomon M 1964 *Ber. Bunsenges.* **68** 331
[3.20] Conway BE 1958 *Proc. Roy. Soc. (London)* **A247** 400
[3.21] Bockris JO'M and Srinivasan S 1964 *J. Electrochem. Soc.* **111** 844
[3.22] Horiuti J, Keii T and Hirota K 1951-3 *J. Res. Inst. Catalysis Hokkaido Univ.* **2** 1
[3.23] Bockris JO'M and Srinivasan S 1964 *J. Electrochem. Soc.* **111** 853
[3.23] Bockris JO'M and Srinivasan S 1964 *J. Electrochem. Soc.* **111** 858
[3.24] Okamoto G, Horiuti J and Hirota K 1936 *Sci. Pap. Inst. Phys. Chem. Res. Tokyo* **29** 223
[3.25] Walton HF and Wolfenden JH 1938 *Trans. Farad. Soc.* **34** 436
[3.26] Roy LP 1962 *Can. J. Chem.* **40** 1452
[3.27] Raman MS, Kumar R and Datta RL 1963 *Z. Naturforsch.* **18A** 347
[3.28] Rowland PR 1968 *Nature* **218** 945
[3.29] Rowland PR 1971 *J. Electroanal. Chem.* **32** 109
[3.30] Hammerli M, Mislan JP and Olmstead WJ 1970 *J Electrochem. Soc.* **117** 751
[3.31] Harada S 1996 *Mater. Transac. JIM* **37** 45
[3.32] Vielstich W and Schuchard H 1959 *Z. Elektrochem.* **63** 1014
[3.33] Lewis GP and Ruetschi P 1962 *J. Phys. Chem.* **66** 1487
[3.34] Fukuda M and Horiuti J 1962 *J. Res. Inst. Catalysis Hokkaido Univ.* **10** 43
[3.35] Vielstich W, Schuchardt H and Stackelberg Mv 1963 *Ber. Bunsenges. Phys. Chem.* **67** 645
[3.36] Buttlar H, Vielstich W and Barth H 1963 *Ber. Bunsenges.* **67** 650
[3.37] Salomon M and Conway BE 1964 *J. Phys. Chem.* **68** 2009

[3.38] Hammerli M, Mislan JP and Olmstead WJ 1969 *J. Electrochem. Soc.* **116** 779
[3.39] Horiuti J in '*Physical Chemistry. An Advanced Treatise*', chapter 6, vol. IX, part B, H. Eyring (editor), Academic Press (1970)
[3.40] Thomas JGN 1961 *Trans. Farad. Soc.* **57** 1603
[3.41] Parsons R 1958 *Trans. Farad. Soc.* **54** 1053
[3.42] Dolin, Eshler and Frumkin 1940 *Acta Physicochim.* **13** 779
[3.43] Toney MF, Howard JN, Richer J, Borges GL, Gordon JG, Melroy OR, Wiesler DG, Yee D and Sorensen LB 1994 *Nature* **368** 444
[3.44] Krishtalik LI and Tsionsky VM 1971 *J. Electroanal. Chem.* **31** 363
[3.45] Krishtalik LI 2000 *Biochim. et Biophys. Acta* **1458** 6
[3.46] Krishtalik LI 2001 *Electrochim. Acta* **46** 2949
[3.47] Dogonadze RR, Kuznetsov AM and Levich VG 1968 *Electrochim. Acta* **13** 1025
[3.48] Horiuti J and Okamoto G 1936 *Sci. Pap. Inst. Phys. Chem. Res. Tokyo* **28** 231
[3.49] Horiuti J, Keii T and Hirota K 1951-3 *J. Res. Inst. Catalysis Hokkaido Univ.* **2** 1
[3.50] Brun J, Varberg Th, Gundersen W and Solli R 1956 *Kgl. Nor. Vidensk. Selsk. Forh.* **29** 5
[3.51] Matsushima H, Nohira T and Ito Y 2004 *Electrochim. Acta* **49** 4181
[3.52] Bucur RV and Stoicovici L 1972 *J. Electroanal. Chem.* **36** 243
[3.53] Stojic DLJ, Miljanic SS, Grozdic TD, Petkovska LT and Jaksic MM 2000 *Int. J. Hydrogen Energy* **25** 819
[3.54] Dandapani B and Fleischmann M 1972 *J. Electroanal. Chem.* **39** 323
[3.55] Kretschmer J and Heitbaum J 1979 *J. Electroanal. Chem.* **97** 211
[3.56] Jaksic JM, Ristic NM, Krstajic NV and Jaksic MM 1998 *Int. J. Hydrogen Energy* **23** 1121
[3.57] Baba R, Nakabayashi S, Fujishima A and Honda K 1985 *J. Phys. Chem.* **89** 1902
[3.58] Stojic DLJ, Miljanic SS, Grozdic TD and Jaksic MM 1996 *Bulletin of Electrochem.***12** 436
[3.59] Pourbaix M *'Atlas d'Equilibres Électrochimiques'* Gauthier-Villars & C^{ie} (Paris, 1963) pp485-492
[3.60] Kita H 1966 *J. Electrochem. Soc.* **113** 1095
[3.61] Stojic DLJ, Miljanic SS, Grozdic TD, Bibic NM and Jaksic MM 1991 *Int. J. Hydrogen Energy* **16** 469
[3.62] Jaksic MM 2001 *Int. J. Hydrogen Energy* **26** 559
[3.63] Urey HC, Brickwedde FG and Murphy GM 1932 *Phys. Rev.* **39** 164
[3.64] Urey HC, Brickwedde FG and Murphy GM 1932 *Phys. Rev.* **40** 1
[3.65] Bell RP and Wolfenden JH 1934 *Nature* **133** 25
[3.66] Guant J 1956 *Spectrochim. Acta* **8** 57
[3.67] Stevens WH and Thurston WM *Canadian Report CRC* **568** March 1954 (Reprinted, June 1956)
[3.68] Farkas A and Farkas L 1934 *Proc. Roy. Soc. A* **144** 467

[3.69] Walton HF 1938 *Trans. Farad. Soc.* **34** 450
[3.70] Hunt PP and Smith HA 1961 *J. Phys. Chem.* **65** 87
[3.71] Dandapani B and Fleischmann M 1972 *J. Electroanal. Chem.* **39** 315
[3.72] Hammerli M and Olmstead WJ 1973 *J. Appl. Electrochem.* **3** 37
[3.73] Bruckenstein S and Gadde RR 1971 *J. Amer. Chem. Soc.* **93** 5941
[3.74] Hard DT *'An Introduction to the Chemistry of Hydrides'* John Wiley & Sons (New York 1987)
[3.75] Frumkin AN 1947 *Disc. Farad. Soc.* **1** 57
[3.76] Conway BE and Jerkiewicz G 2002 *Solid State Ionics* **150** 93
[3.77] Xu X, Wu DY, Ren B, Xian H and Tian Z-Q 1999 *Chem. Phys. Lett.* **311** 193
[3.78] Mignolet JCP 1957 *J. Chim. Phys.* **54** 19
[3.79] Voronina GF, Larin LA and Kalish TV 1978 *Soviet Electrochem.* **14** 252
[3.80] Engstrom JR, Tsai W and Weinberg WH 1987 *J. Chem. Phys.* **87** 3104
[3.81] Bockris JO'M and Koch DFA 1961 *J. Phys. Chem.* **65** 1941
[3.82] Mueller WM, Blackedge JP and Libowitz GG in *'Metal Hydrides'* Academic Press (New Cork, 1968) p633
[3.83] Gileadi E, Fullenwider MA and Bockris JO'M 1966 *J. Electrochem. Soc.* **113** 926
[3.84] Martins ME, Zinola CF, Andreasen G, Salvarezza RC and Arvia AJ 1998 *J. Electroanal. Chem.* **445** 135
[3.85] Baranowski B and Smialowski M 1959 *Int. J. Phys. Chem. Solids* **12** 206
[3.86] Bernardini M, Comisso N, Davolio G and Mengoli G 1998 *J. Electroanal. Chem.* **442** 125
[3.87] Baranowski B in *'Hydrogen in Metals II'* G. Alefeld and J. Völk (ed.) Topics in Applied Physics vol. 29, Springer-Verlag (Berlin, 1978) p174
[3.88] CRC handbook of chemistry and physics (84th edition) Lide DR (ed) CRC Press 2003
[3.89] Franklin T, Naito M, Itoh T and Mcclella DH 1970 *J. Electroanal. Chem.* **27** 303
[3.90] Forker W in *'Elektrochemische kinetik'* Akademie, Verlag (Berlin, 1966) (versión en castellano: *Cinética Electroquímica*, Editorial Universitaria de Buenos Aires, 1971)

Chapter 4

Isotope effects in the kinetics of simultaneous H and D thermal desorption from Pd

4.1 Introduction

One of the main issues in the field of H storage in metal hydrides (MH) concerns the kinetics of hydrogen absorption/desorption. The formation/decomposition of a MH involves both bulk (hydride to solid solution phase transformations, diffusion of H atoms through the bulk and from the bulk to the surface) and surface (dissociation of H_2 molecules/H-H recombination at the surface) processes. In most cases, the H absorption/desorption kinetics by/from a MH is limited by surface reaction steps [4.1]. Accordingly, there is a growing interest on the catalysis of surface reactions in MH [4.2, 3]. In this context, the microscopic description of the MH formation/ decomposition processes is of fundamental importance.

A suitable approach to investigate the kinetics of H atoms in the course of chemical reactions is the analysis of the H/D isotope effects. Owing to their relative mass differences, different zero point energies (ZPE) and local mode vibrations are experienced by the hydrogen isotopes within the wells of the potential energy surface (PES). As a consequence of these energy shifts, the reaction rates are usually higher for the lighter isotope. This is denoted as the normal isotope effect. However, there are some exceptions to this rule. A typical case is the inverse isotope effect observed in the H/D diffusion in Pd [4.4].

The simplest reaction involving H and D atoms is the isotope exchange reaction:

$$H_2 + D_2 \Leftrightarrow 2HD \tag{4.1}$$

Reaction (4.1) has been has been proved to be very useful to investigate the kinetics and mechanisms of the interaction of H_2 with metal surfaces. In fact, this reaction has been extensively investigated on mono- and polycrystalline transition metal surfaces [4.5-13] as well as on transition metal supported catalysts [4.14-17]. H/D kinetic isotope effects in hydride forming metals have been also widely investigated, mainly due to the potential applications of MH for isotope separation processes. This kind of studies is usually performed by heterophase hydrogen isotope exchange (H_2/MD and D_2/MH) experiments [4.18-20].

In the present chapter, the kinetics of simultaneous hydrogen and deuterium desorption from bulk PdH_xD_y material is investigated by means of thermal desorption spectroscopy (TDS). TDS was initially developed for the study of the desorption kinetics of chemical species from surfaces, but lately it has been proved to be also a valuable technique to investigate the kinetics of MH decomposition [4.21-23]. Two relevant facts support the election of Pd hydride to perform this investigation. Firstly, the Pd/H_2 system is the prototypic MH system. Historically, it was the first MH that attracted research activities [4.24] and it has been the most investigated MH since then. Secondly, Pd is well-known for its selectivity and activity in hydrogenation reactions and it is one of the most used catalysts. Indeed, Pd thin film overlayers are usually used to enhance the kinetics of hydrogen uptake and release from metal hydrides [4.25, 26].

To my knowledge, there is only one previous TDS study on the simultaneous H and D desorption from MH [4.27]. This investigation was carried out in V and V-Ti intermetallic compounds. However, no quantitative analysis of the desorption kinetics was reported in that paper.

A novel experimental approach for the study of the transition state (TS) characteristics of the surface recombination reaction is proposed here based on the analysis of the H and D distribution into H_2, HD and D_2 molecules. This method gives complementary information on the TS to that obtained from quantum-state resolved experiments [4.28] and quantum-state integral measurements [4.13].

4.2 Experimental details

Pd foils from Goodfellow (99.95% purity) have been simultaneously hydrogenated-deuterated by electrolysis in 0.1M LiOH-LiOD electrolytes at room temperature (RT). The foils were washed in an ultrasound bath with ethanol and then with deionised water (18.6 MΩ cm) prior to the electrolytic experiments. The LiOH and LiOD electrolytes were prepared by dissolving metallic granulated lithium in H_2O (18.6 MΩ cm) and D_2O (>99.6% isotopic purity, 0.08 MΩ cm), respectively, under Ar atmosphere. Then, the LiOH and LiOD were mixed to obtain the desired H/D ratio in the electrolytes. The electrolyses were performed with a Princeton Mod.362 potentiostat in a three-electrode open cell all constructed in Teflon. Pd foils of 0.25x10x10 mm^3 were placed at the bottom of the electrolytic cell with only one face in contact with the electrolyte. The area of the foils in

contact with the electrolytes was delimited by an o-ring made of Viton of 8.5 mm of internal diameter. A Pt grid located opposite to the cathode was used as counter electrode. The reference electrode was a Pt wire placed near the cathode.

Structural characterization of the samples at RT has been carried out by means of X-ray diffraction (XRD) accomplished with the CuK_α radiation in a θ-2θ Siemens D-5000 powder diffractometer. Sample surface morphology has been studied by Optical Microscopy (OM) with a Nikon Eclipse E400 microscope and by Scanning Electron Microscopy (SEM) with a Phillips XL30 apparatus, which is also equipped with electron dispersive X-ray (EDAX) analysis.

Electrical resistivity measurements have been done by Van der Pauw method [4.29] with a Keithley Mod. 2400 current source and a Keithley Mod.182 digital voltmeter. Thermopower measurements have been performed as described elsewhere [4.30].

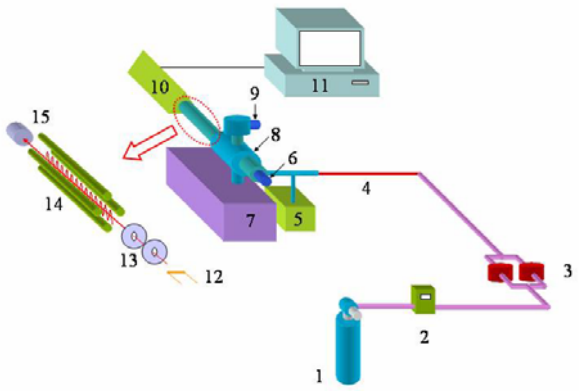

Fig.4.1. Scheme of the experimental system used for TDS measurements: (1) Ar bottle; (2) flow meter and controller; (3) differential scanning calorimeter; (4) capillary tube; (5) rotary pump; (6) dosing valve; (7) turbomolecular pump; (8) vacuum chamber; (9) Penning sensor; (10) electronic setup; (11) PC acquisition data and controller system; (12) ion source; (13) electrodes; (14) quadrupolar filter; (15) ion detector.

Thermal desorption spectroscopy (TDS) has been performed in the experimental setup depicted in Fig.4.1. A differential scanning calorimeter (Perkin Elmer DSC4) is connected through a quartz capillary tube and a dosing valve (Balzers UDV 040) to the gas analysis system described in Chapter 2. A more detailed description of the whole experimental setup can be found in [4.23].

A constant Ar flow (57.6 sccm, 99.999% purity) passing symmetrically through both heaters of the calorimeter has been used to carry the desorbed gases to the QMS. Mass of the samples before and after TDS experiments were measured with an Ohaus Analytical Plus balance.

The analyses of the gases thermally desorbed from the samples have been done by tuning the Set A QMS parameters, as shown in Table 2.1. The detailed calibrations of the gas analysis system performed prior to TDS experiments are described in Chapter 2. At the experimental conditions of the present TDS experiments, the i_2, i_3 and i_4 current peaks are essentially due to H_2^+, HD^+ and D_2^+ ions, respectively (the contribution of D^+, H_3^+ and H_2D^+ ions to these current peaks were below 1%). In addition, the influence of isotope exchange reactions among the hydrogen ionic/molecular isotopes during the gas analysis process can be neglected. Therefore, the H_2, HD and D_2 desorbed flows (F_χ) are related to the i_2, i_3 and i_4 current peaks, respectively, according to:

$$i_{m/q}(\chi) - i^0_{m/q}(\chi) = \sigma_{m/q}(\chi) \cdot F_\chi \tag{4.2}$$

where $i_{m/q}{}^0$ represent the background signals from the residual atmosphere present in the vacuum chamber and $\sigma_{m/q}(\chi)$ is the detection sensitivity of the specie χ. Experimental base lines have been recorded before the TDS experiments to obtain the temperature dependence of the $i_{m/q}{}^0$ peak currents.

4.3 Preparation and characterization of the PdH_xD_y samples

4.3.1 Electrolytic H and D charging

The electrochemical behaviour of the Pd foils has been investigated by means of cyclic voltammetry and current transient analyses prior to the electrolytic H/D charging. The electrodes have been cycled several times between 0.6 and -0.7 V at 0.02 V s^{-1} in order to obtain stabilized results.

A typical voltammogram of the working Pd electrode in 0.1M LiOH/LiOD electrolyte run between 0.6 and -0.7 V at 0.02 V s^{-1} is shown in Fig.4.2 (blue line). It exhibits a broad current region (c_1) during the scan at potentials more positive than -0.25 V. That region is associated to PdO formation. This oxide layer is reduced in the scan to negative potentials at the peak current (a_1) appearing at $E_{Pd/Pt}$=-0.43 V. When the voltammogram is run towards more negative potentials, namely -1 V (red line in Fig.4.2), an additional peak current (a_2) is observed at potentials more negative than -0.75 V. This region is associated to H atom electroadsorption and α-Pd formation. Finally, the electrooxidation of the adsorbed/absorbed H atoms is observed at the broad peak current (c_2) occurring in the positive scan at $E_{Pd/Pt}$=-0.61 V. The voltammetric results are in agreement with those reported by other authors in alkaline media [4.31, 32].

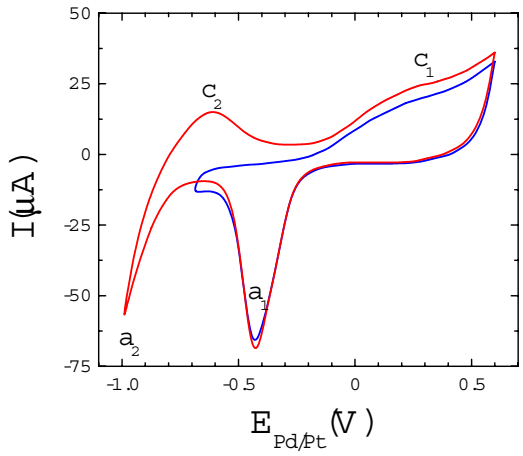

Fig.4.2. Typical voltammograms of the Pd electrodes in 0.1M LiOH/LiOD electrolyte recorded between 0.6 and -0.7 V (blue line) and between 0.6 and -1 V (red line) at 0.02 V s^{-1}. The current peaks observed in the negative and positive scans are indexed.

Current transient analyses have been done at different electrode potentials in the cathodic polarization region. The time evolution of the electrolytic current at $E_{Pt/Pd}$=-1.15 V is depicted in Fig.4.3a. At these experimental conditions, no β-Pd hydride/deuteride formation takes place and the evolution of the electrolytic current is governed by the electroadsorption of H/D atoms and their diffusion through the bulk of the α-Pd phase. For more negative potentials, namely $E_{Pt/Pd}$=-1.6 V, the electrolytic current shows a maximum (see Fig.4.3b). The appearance of a maximum in the electrolytic current during the H/D charging is associated to the nucleation and growth of the β-$PdH(D)_x$ phase [4.31].

According to the above results, the Pd electrodes have been charged by cathodic polarization at a constant electrode potential more negative than that needed to form the hydride/deuteride phase, namely $E_{Pd/Pt}$= –3 V. A typical time evolution of the electrolytic current during electrode charging is depicted in Fig.4.4. The shape of the time evolution of the electrolytic current is different to that obtained at more positive potentials (see Fig.4.3b), although the maximum associated to the nucleation and growth of the β-PdH_xD_y phase is also observed. After the maximum, hydrogen-deuterium evolution took place, which was evidenced by the observation of H_2-HD-D_2 gas bubbles evolved from the cathode accompanied by a sharp decrease of the electrolytic current.

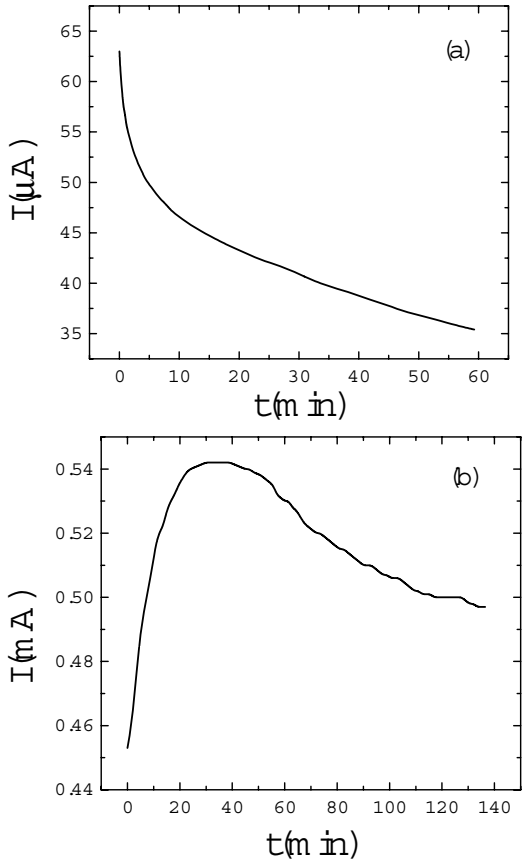

Fig.4.3. Time evolution of the electrolytic current at $E_{Pd/Pt}$=-1.15 (a) and -1.6 V (b).

It is worth to note that the time scales of the electrolytic charge processes were large enough to allow the H and D atoms reaching a homogeneous concentration within the sample along to the coordinate normal to their faces. The time scale (τ) of the H(D) diffusion process can be estimated from:

$$\tau = \frac{L^2}{\pi^2 D_c} \tag{4.3}$$

where L is the diffusion length and D_c is the diffusion coefficient of H(D) through Pd. By taking D_c~10^{-7} cm^2 s^{-1} [4.33] and L=0.025 cm, it is obtained τ~10^3 s. This

time is much lower than the time scales of the electrolytic charge processes and, therefore, no H(D) gradients are expected to appear along the direction normal to the faces of the electrodes. The situation is somewhat different for the diffusion of H(D) atoms along the coordinates parallels to the sample faces (*i.e.*, from the circular region in contact with the electrolytes to the outside region). In this case, the typical diffusion lengths were one order of magnitude higher than along the normal direction and the diffusion times were similar to the time scales of the electrolysis. As a consequence, it is expected that the H plus D concentration within the outside region will correspond mainly to the α-Pd phase. These concentrations gradients will not be homogenized after the electrolytic charge process, because the circular β-PdH_xD_y region keeps stable, and the diffusion of H/D atoms between this region and the adjacent ones of α-Pd should occur much more slowly than within each phase.

Three Pd samples have been charged with different H and D concentrations. The total charge passed through the electrodes during the cathodic polarization (Q) and the original mass of the Pd samples are shown in Table 4.1.

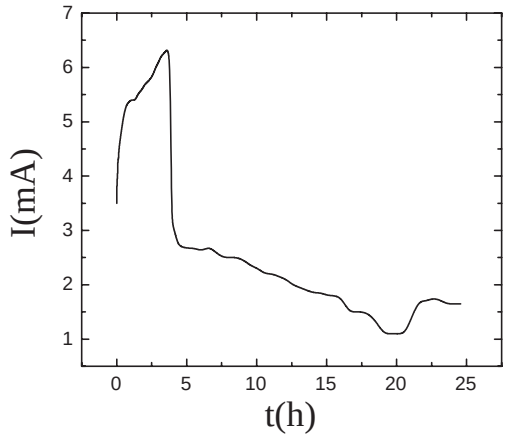

Fig.4.4. Typical time evolution of the electrolytic current during the cathodic polarization of the Pd electrodes at $E_{Pd/Pt}$= -3 V.

The samples were washed with deionised water (Milli-Q) and then with ethanol after the electrolytic experiments. During this process, H_2/HD/D_2 bubbles desorbing from the samples were observed. In order to investigate the rate of H and D desorption from the Pd electrodes, the masses of the samples were measured after the electrolysis as a function of time. A typical result is shown in Fig.4.5, where the mass increment (Δm=mass at different times after electrolysis minus mass prior electrolysis) is plotted as a function of time. It can be seen from Fig.4.5 that Δm exponentially decays with time due to H_2/HD/D_2 desorption until a

stationary value is reached after about 1 month. This behaviour has been ascribed to two different effects. On the one hand, a high $H_2/HD/D_2$ desorption rate takes place in the sample during the decomposition of highly concentrated β-PdH_xD_y. In fact, when increasing the H+D concentration above the two phase coexistence limit, the chemical potential of H and D atoms in the hydride/deuteride phase rises very fast. Accordingly, H and D atoms in β-PdH_xD_y (whose concentration is higher than β_{min}) have a low stability. The hydride phase is more stable in the two phase coexistence region and, therefore, the $H_2/HD/D_2$ desorption rate must be slower once the H+D concentration reaches this region. On the other hand, and at the same time, the progressive reduction of the $H_2/HD/D_2$ desorption rate must be also due to the formation of an oxide layer over the sample's surfaces. It is well known that monolayer amounts of oxygen in polycrystalline transition metals hinder the atom-atom recombination reaction and reduce the hydrogen desorption rate by orders of magnitude [4.1]. Experiments in Pd surfaces [4.34] in ultrahigh vacuum conditions have showed that the surface oxygen coverage is nearly saturated after an exposure of 4L ($1L=10^{-6}$ torr s) at 298 K. This implies that surface oxidation must occur very fast in the samples during air exposure. In addition to O, the surface layer can contain C, OH groups, N and possibly further elements, mixed together in ill-defined composition and morphology.

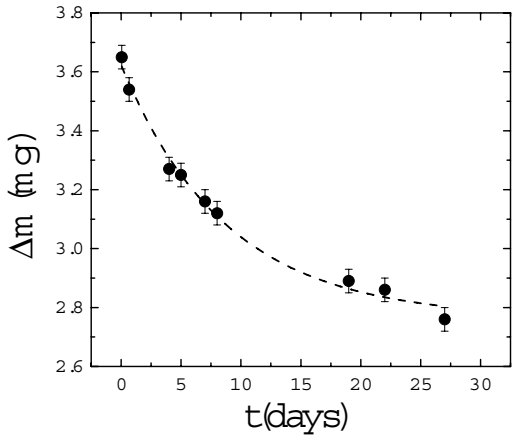

Fig.4.5. Time evolution of the mass of the H plus D atoms absorbed in a Pd foil due to $H_2/HD/D_2$ desorption.

The H/D ratios in the electrolytes ($(H/D)_{liq}$) and in the Pd samples after the electrolysis ($(H/D)_{Pd}$) have been also measured and the results are included in Table 4.1. From these ratios, the separation factor (S_L^M) of the electrolytic hydrogenation/deuteration reaction can be evaluated. For hydride forming electrodes, (S_L^M) is defined as:

$$S_L^M = \frac{(H/D)_{liq}}{(H/D)_M} \tag{4.4}$$

The $(H/D)_{liq}$ ratios appearing in Table 4.1 are affected by a 5 % of error due to the influence of isotope exchange between the electrolytes and the air moisture during the experiments. To evaluate the increment of the H concentration in the electrolytes as a consequence of that exchange process, the electrolyte's densities were measured before and after the electrolytic experiments (see the analysis done in section 5.3.4). On the other hand, the $(H/D)_{Pd}$ ratios have been evaluated from the area of the H_2, HD and D_2 desorption peaks obtained from TDS experiments (see Table 4.6). The error in the $(H/D)_{Pd}$ values comes from the error in the determination of the H_2, HD and D_2 detection sensitivities. It must be noted that the $(H/D)_{Pd}$ ratios in the samples could be affected by the H_2/HD/D_2 desorption since the sample's preparation and the TDS experiments. In principle, it is expected that this effect should increase the measured $(H/D)_{Pd}$ values, because the desorption rate of D is higher than that of H, as it will be shown in section 4.4. Therefore, the calculated S_L^M values should be taken as a lower limit of the real values. The obtained S_L^M values are also listed in Table 4.1 and are in agreement with those reported by Farkas [4.35] (S_L^M =6.6) and Dandapani and Fleischmann [4.36] (S_L^M ~7.2).

Table 4.1. Experimental variables of the electrolytic H/D charge of the Pd electrodes.

Sample	***Q (C)***	m_{Pd} **(g)**	$(H/D)_{liq}$	$(H/D)_{Pd}$	S_L^M
S1	210	0.35295(2)	0.21(1)	1.31(8)	6.2(6)
S2	195	0.34341(2)	0.059(3)	0.38(2)	6.4(7)
S3	230	0.35214(2)	0.080(6)	0.52(3)	6.5(7)

4.3.2 Sample characterization: structure and transport properties

The surface morphology and composition of the Pd cathodes have been investigated by means of OM, SEM and EDAX analyses before and after the electrolytic experiments. In addition, XRD, electrical resistivity and thermopower measurements have been accomplished after the electrolytic H/D charging in order to evaluate the amounts of H and D atoms present in the samples. Experimental data obtained from Pd samples before their electrochemical hydrogenation-deuteration have been also analysed and compared with previously reported values in order to test the accuracy of the measurements.

4.3.2.1 Surface morphology and composition

A typical SEM picture of the Pd surface after the electrolytic hydrogenation /deuteration can be seen in Fig.4.6. The foils present surface bands due to the cold rolling of Pd. In addition, small pores and inclusions can be observed in the sample surface. These inclusions were mainly composed by Si and Al, with traces of Fe and Mg in some of them, as revealed by EDAX analysis. They were already present in the original Pd foils and, thus, they are not attributed to surface contamination during the electrolysis. It is worth to note, however, that the SEM images of the hydrogenated/deuterated Pd samples exhibited weak spatial charge effects. This is indicative of the presence of a surface oxide layer. Unfortunately, the EDAX analyses could not detect the X-ray emissions of O atoms, due to the characteristics of the available equipment.

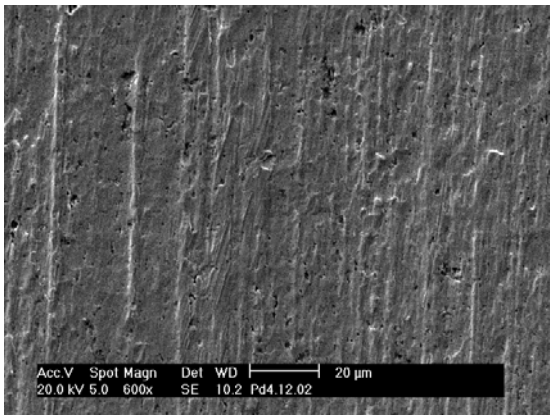

Fig.4.6. SEM picture of the Pd surface after the electrolytic hydrogenation /deuteration.

On the other hand, remarkable differences have been observed in the surface morphology before and after the electrolytic charging of the samples. The expansion of the Pd lattice due to hydrogenation/deuteration produces the appearance of strain fields. These fields are concentrated at the edges of the zone of the electrodes in contact with the electrolyte. In this region, the strain generated by the lattice expansions of Pd is the maximum one. These strain fields give rise to the plastic deformation of the samples, which is evidenced by the appearance of macroscopic furrows. In most cases, these furrows exhibit a radial symmetry (Fig.4.7), extending outside the circular area of the electrodes in contact with the electrolytes. However, some regions presented a rhombic structure, as seen in Fig.4.7.

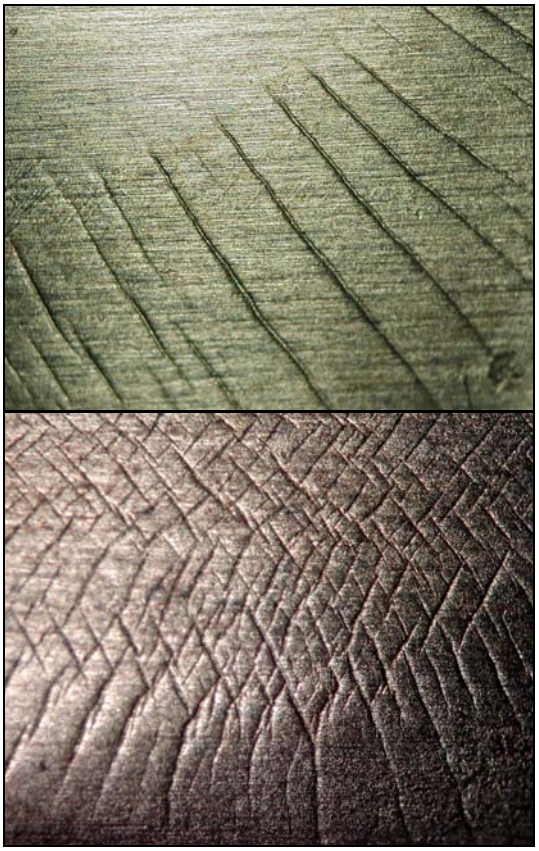

Fig.4.7. The strain fields generated by the lattice expansion of Pd upon hydrogenation/deuteration produce the appearance of macroscopic furrows forming either radial (up) or rhombic (bottom) structures (x15).

4.3.2.2 Structural characterization by XRD

The XRD patterns of Pd samples before (sample S0) and after (samples S1-S3) the electrochemical hydrogenation/deuteration are shown in Fig.4.8. These patterns can be indexed in the *Fm3m* crystallographic space group, characteristic of Pd and β-Pd hydride-deuteride. The positions of the diffraction peaks of Pd are indicated by vertical dotted lines. Diffracting planes corresponding to each XRD peak have been indexed. Non-labelled small peaks correspond to the diffraction produced by non filtered Cu K_β radiation. The diffraction peaks of β-PdH_xD_y are the same that those of Pd, but shifted to lower angles due to the lattice expansion of the hydride/deuteride-phase.

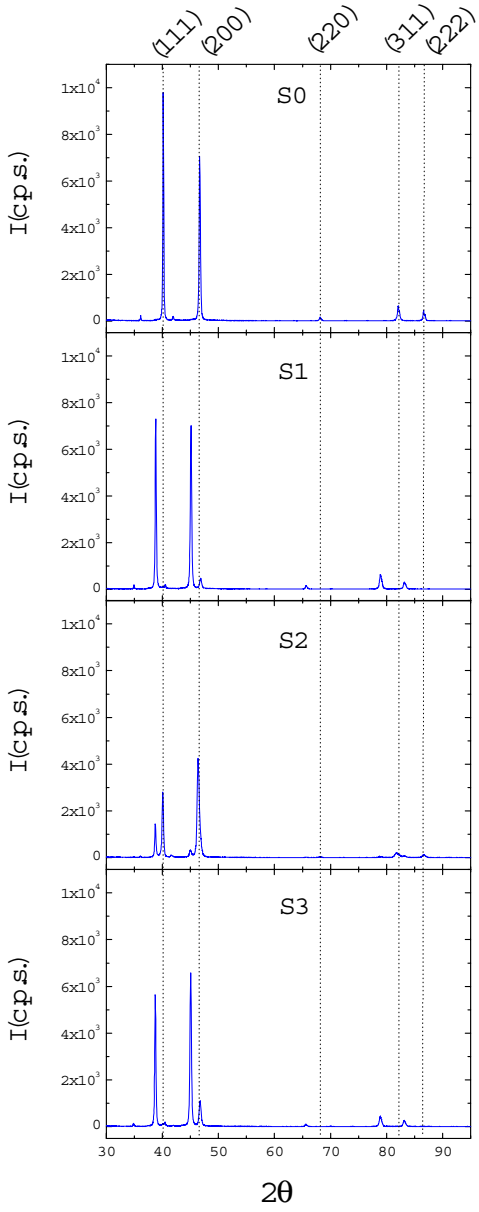

Fig.4.8. XRD patterns of the Pd samples before (S0) and after (S1-S3) the electrochemical H/D charging. Vertical dotted lines show the position of the diffraction peaks of Pd. Diffracting planes corresponding to each XRD peak of Pd are indexed in the upper part of the figure.

Similar XRD patterns of Pd foils after the electrolysis have been obtained from the two sample faces, indicating that the total H and D concentration along the thickness of the foils is quite homogeneous. On the other hand, lower diffracted intensities are observed for the XRD patterns of the hydrogenated/deuterated samples. This effect has been ascribed to the lower diffracting power of the β-PdH_xD_y phase due to its lower density.

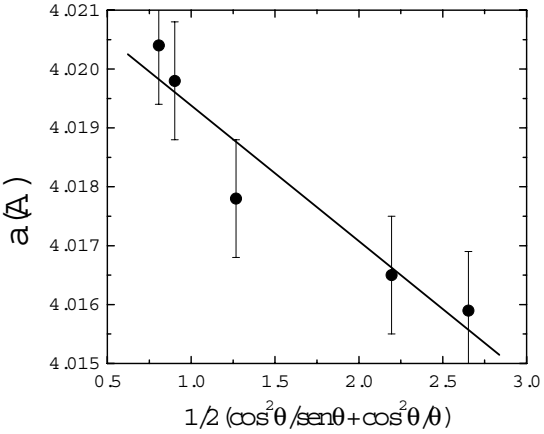

Fig.4.9. Fit of the set of values of the lattice parameters obtained from the diffraction peaks of the XRD patterns of β-PdH_xD_y to Eq.4.5.

The lattice parameters of the Pd and β-PdH_xD_y phases in the samples have been obtained from the XRD patterns in Fig.4.8. By using Bragg's law, a set of values (a_n), one from each diffraction peak, can be obtained. By plotting a_n *vs.* θ_n and fitting the obtained points to the formula [4.37]:

$$a_n = a_0 + \frac{1}{2}\left(\frac{\cos^2 \theta_n}{\sin \theta_n} + \frac{\cos^2 \theta_n}{\theta_n} \right) \tag{4.5}$$

the lattice parameter (a_0) is obtained. A typical fit of a_n values of β-PdH_xD_y to equation (4.5) is shown in Fig.4.9. The obtained lattice parameters of Pd and β-PdH_xD_y are summarized in Table 4.2. For sample S2, the lattice parameters of both the α-Pd and β-PdH_xD_y phases have been calculated. However, only the lattice parameters of the hydride/deuteride phase have been obtained for samples S1 and S3, due to the low amount of α-Pd in these samples. Indeed, these samples exhibit

only one diffraction peak corresponding to α-Pd and, therefore, the calculation of the corresponding lattice parameter according to the method exposed above is not possible. It can be seen from Table 4.2 that there is a good agreement between the present experimental values and those previously reported for Pd [4.38], β-$PdH_{0.6}$ [4.39] and β-$PdD_{0.6}$ [4.40]. By taking the values of the lattice parameters of Pd and β-PdH_xD_y, the calculated cell expansion of Pd due to the transformation from the α to the β phase is about 10.3 %.

Table 4.2. Lattice parameters of the α-Pd and β-PdH_xD_y phases of the samples before and after their electrochemical hydrogenation /deuteration.

	a_0(Å)	
Sample	**α-Pd**	**β-PdH_xD_y**
S0	3.892(3)	
S1		4.022(3)
S2	3.895(5)	4.022(3)
S3		4.021(3)
Pd	3.8902[4.38]	
β-$PdH_{0.6}$		4.025 [4.39]
β-$PdD_{0.6}$		4.025 [4.40]

4.3.2.3 Electrical resistivity and thermopower

There is a well known relationship between the hydrogen/deuterium content in a Pd sample and its electrical resistivity. In fact, the measurement of the electrical resistivity has been extensively used as an *in situ* probe to evaluate the amount of H/D absorbed in Pd [4.41].

Table 4.3. Resistivities and Seebeck coefficients of the samples before and after their electrochemical hydrogenation/deuteration.

Sample	ρ(μΩ cm^{-1})	S(μV K^{-1})
S0	9.9(1)	-11.0(5)
S1	18.5(2)	5.1(5)
S2	17.0(2)	-4.1(5)
S3	19.1(2)	2.6(5)
Pd	10.54 [4.42]	-11.5 [4.44]
$PdH_{0.6}$	17.9 [4.43]	5 [4.44]
$PdD_{0.6}$	20.0 [4.43]	

The measured resistivities of the Pd and PdH_xD_y samples are shown in Table 4.3, together with the values reported for Pd [4.42], $PdH_{0.6}$ and $PdD_{0.6}$ materials. The electrical resistivities of $PdH_{0.6}$ and $PdD_{0.6}$ have been calculated from the reported ratios [4.43] between the electrical resistances of $PdH_{0.6}$ and $PdD_{0.6}$ and the original resistance of Pd, by taking into account the increment in sample dimensions due to hydrogenation/deuteration. It can be seen that there is a relatively large isotope effect that affects the resistivities of Pd hydride and deuteride.

The values of the Seebeck coefficients of the samples are also included in Table 4.3, together with those of Pd and $PdH_{0.6}$ [4.44]. As far as I know, no data on the Seebeck coefficient of Pd deuteride have been previously reported.

4.3.2.4 Evaluation of the H and D content in the samples

The experimental results obtained from XRD, electrical resistivity, thermopower and TDS measurements have allowed the calculation of the amounts of H and D atoms absorbed in the samples.

Firstly, the XRD patterns of samples S1 and S3 exhibit only a weak diffraction peak from the (200) plane of α-Pd (see Fig.4.8). It has been assumed that this diffraction peak comes mainly from α-Pd regions outside the circular area in contact with the electrolytes. This implies that the H+D amount in the hydrogenated/deuterated regions of the samples is close to the limit of the β-PdH_xD_y phase (β_{min}). At RT this limit corresponds to a content of $x+y=0.61$ H+D atoms per Pd atom [4.39]. This value, together with the x/y ratios obtained from TDS measurements (see Table 4.2) allow an estimation of the x and y values in samples S1 and S3, as shown in Table 4.4. On the other hand, the XRD peaks of α-Pd in sample S2 are much more intense, indicating that the amount of β-PdH_xD_y in this sample is lower than in samples S1 and S3. However, the quantitative determination of the relative amounts of α-Pd and β-PdH_xD_y from the integration of the XRD peaks of the corresponding phases has not been possible for sample S2, due to the different diffracting powers of the corresponding phases.

The measured electrical resistivities of the samples have been also used to evaluate the H and D amount in the samples. By considering that the electrical resisitivity of β-$Pd(H\text{-}D)_{0.6}$ depends linearly on the relative H and D content, the electrical resistivity of samples S1 and S3 would be 18.7 and 19.3 $\mu\Omega$ cm^{-1}, respectively. These values agree with the experimental results shown in Table 4.3 and confirm the calculation of the H and D concentration in the Pd matrix. On the other hand, the measured electrical resistivity of sample S2 can be used to estimate the H plus D amount in this sample. By taking the results reported by McKubre *et al.* [4.43] on the dependence of the electrical resistance of $PdH(D)_x$ with the amounts of H(D) and the x/y value obtained from TDS measurements (Table 4.1), the calculated $x+y$ value of sample S2 is equal to 0.45(2).

Table 4.4. *x* and *y* values in the samples deduced from XRD, electrical resistivity and thermopower measurements.

Sample	*x*	*y*
S1	0.35(1)	0.26(1)
S2	0.11(1)	0.34(1)
S3	0.20(1)	0.39(1)

The measured Seebeck coefficients of the samples are plotted in Fig.4.10 as a function of the total H plus D fraction in Pd. Data reported by Szafranski [4.45] and Foiles [4.44] have been also included for comparison purposes. The results show a non-linear dependence of the Seebeck coefficient with the H(D) content. This dependence can be calculated within the two phase region by using the model proposed by Yoo *et al.* [4.46]. These authors considered the general case of heterogeneous mixtures of two solid phases with different thermoelectric powers. If it is assumed that the α and β phases are arranged in parallel, the Seebeck coefficient of PdH_xD_y samples must obey the equation:

$$S = \frac{S^{\alpha} + \frac{V^{\beta}\rho^{\alpha}}{V^{\alpha}\rho^{\beta}} S^{\beta}}{1 + \frac{V^{\beta}\rho^{\alpha}}{V^{\alpha}\rho^{\beta}}} \tag{4.6}$$

where ρ^{α} and ρ^{β} are the electrical resistivities, $S_c{}^{\alpha}$ and $S_c{}^{\beta}$ the Seebeck coefficients and V^{α} and V^{β} the volumes of α-Pd and β-PdH_xD_y, respectively. In order to fit the experimental points in Fig.4.10 to equation (4.6) the fraction of α and β phase volumes have been calculated by applying the lever rule that gives the relative fractions of α and β phases in the samples within the two phase coexistence region. To this aim, the concentration limits of the α and β phases have been taken from [4.39]. The ratios between the electrical resistivities of both phases have been obtained from the values reported in Table 4.3. It is worth to note that the isotope effect in the electrical resistivity of Pd hydride does not essentially affects to the calculated Seebeck coefficients. On the contrary, the results depend more strongly on $S_c{}^{\alpha}$ and $S_c{}^{\beta}$ values. It has been assumed that the Seebeck coefficient of α-Pd is the same as that of Pd. In addition, $S_c{}^{\beta}$ has been taken from the thermoelectric coefficient of β-$PdH_{0.6}$ appearing in Table 4.3, because no data on the Seebeck coefficient of β-$PdD_{0.6}$ are available. The calculated dependence of S_c on the H(D) content in Pd within the two phase coexistence region has been also plotted in Fig.4.10 (black line). A good agreement between theoretical and experimental values is observed for the Seebeck coefficients of PdH_x samples reported by

Szafranski (red points). The present experimental data, however, present slight deviations with respect to the theoretical values. This could be due, at least in part, to the existence of an isotope effect on the Seebeck coefficients of Pd hydride and deuteride. Additional investigations are needed to clearify this question.

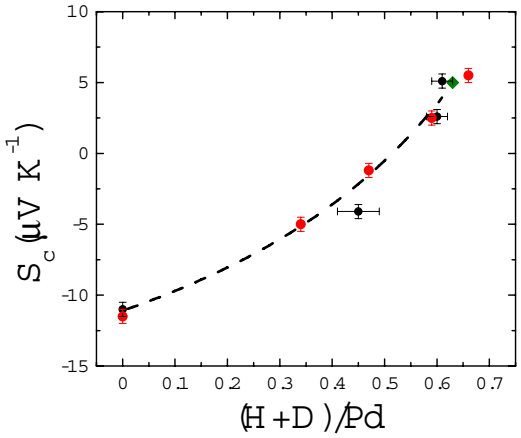

Fig.4.10. Plot of the Seebeck coefficient as a function of the H+D content in Pd. Black points refer to the experimental points obtained in this work, whereas red and green points have been taken from references [4.45] and [4.44], respectively. The dashed line is the fit of the experimental points during the two phase coexistence region by equation (4.6).

As it will be shown in section 4.4.1, the *x* and *y* values obtained from XRD, electrical resistivity and thermopower measurements are further supported by the mass loss measurements of the samples due to H/D desorption during TDS experiments.

4.4 Thermal Desorption Spectra

Thermal Desorption Spectroscopy (which is sometimes called Temperature-Programmed Desorption, TPD) is commonly used to investigate the kinetics and thermodynamics of desorption processes or decomposition reactions. The technique consist on applying a temperature program to the sample $b(t)=dT/dt$ (with T usually being a linear function of time) and measure the flows of the atoms/molecules evolved from the sample, *e.g* by mass spectrometry. Here, TDS has been applied to investigate the kinetics of simultaneous H and D desorption from PdH_xD_y samples.

4.4.1 H_2, HD and D_2 desorption

TDS of PdH_xD_y samples have been obtained by heating them between 298 and 623 K at a constant heating rate b=0.333 K s^{-1}. To this purpose, small portions (of about ten milligrams) were taken from the centre of the hydrogenated/deuterated foils and putted into Al pans. Two TDS measurements (S1a and S1b) were done with sample S1 (in different days and by taking different portions of the sample) in order to investigate the reproducibility of the results.

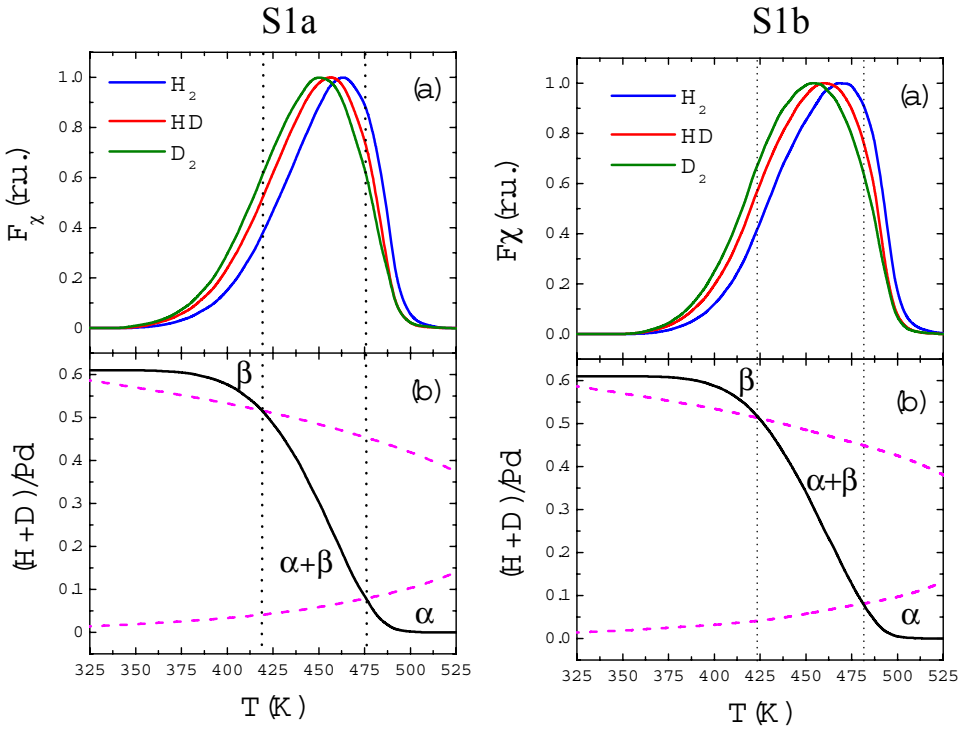

Fig.4.11. (a) Temperature dependence of the H_2, HD and D_2 flows desorbed from sample S1. (b) Temperature evolution of the H+D concentration in Pd (black line). The pink dashed lines indicate the limits of the two phase coexistence region. Vertical dotted lines indicate the temperatures at which the H plus D concentration crosses the two phase coexistence limits. Two TDS measurements are shown in the right (S1a) and left (S1b) parts of the figure.

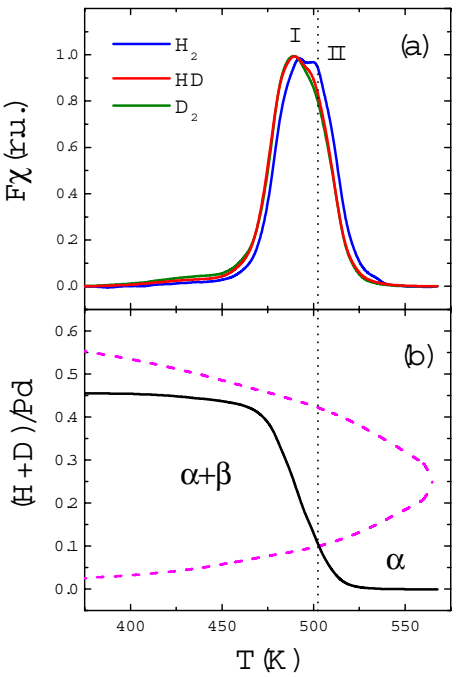

Fig.4.12. (a) Temperature dependence of the H_2, HD and D_2 flows desorbed from sample S2. (b) Temperature evolution of the H+D concentration in Pd (black line). The pink dashed lines indicate the limits of the two phase coexistence region. The vertical dotted line indicates the temperature at which the H plus D concentration crosses the two phase coexistence limit.

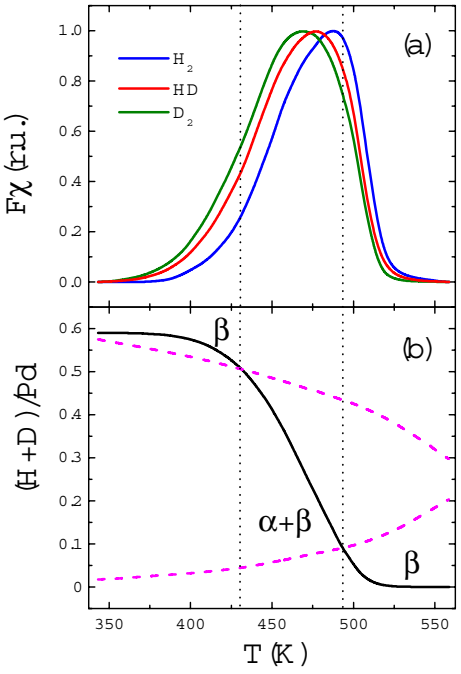

Fig.4.13. (a) Temperature dependence of the H_2, HD and D_2 flows desorbed from sample S3. (b) Temperature evolution of the H+D concentration in Pd (black line). The pink dashed lines indicate the limits of the two phase coexistence region. Vertical dotted lines indicate the temperatures at which the H plus D concentration crosses the two phase coexistence limits.

TDS of samples S1, S2 and S3 are shown in Figs.4.11a, 4.12a and 4.13a, respectively. The spectra of samples S1 and S3 consist of a single desorption peak for each one of the hydrogen molecular isotopes. On the contrary, two desorption peaks (I and II) are observed in sample S2. In addition, it shows a shoulder at ~425 K, which is not observed in TDS of S1 and S3. The H_2, HD and D_2 flows in these figures have been normalized to their maximum values in order to clarify the comparison among them. The absolute values of the desorbed flows at the maxima of desorption peaks are shown in Table 4.5. The temperatures at which the maxima of the peaks occur are also summarized in Table 4.5 for each one of the samples. An inverse isotope effect is observed. Desorption peaks are shifted to higher

temperatures for H_2 than for D_2, being the HD peak between the H_2 and D_2 ones. It should be noted that these temperature shifts can not be caused by the time required for the transport of the desorbed molecules from the sample surface to the gas analysis system. In fact, the observed shifts are opposite to what would be observed if they were caused by the transport of gases because the diffusion of the heavier molecule towards the QMS is slower. Besides, the experimental system has been constructed to reduce the transport time as much as possible and it has been estimated to be <10 s [4.23].

The shapes of the TDS peaks of samples S1 and S3 are quite similar. The TDS peaks of the three hydrogen molecular isotopes are asymmetric, with a relatively sharp fall of the desorbed flows at temperatures higher than that corresponding to their maxima. A detailed examination reveals that this fall is sharper for HD than for H_2 and D_2. Similar H_2 desorption peaks have been reported from TDS of β-PdH_x powder [4.47] and β-PdH_x foils [4.48] formed by solid-gas reactions and from thermo gravimetric analysis of electrochemically loaded PdH_x foils [4.49]. On the other hand, the shapes of the TDS peaks of sample S2 are more symmetric than those of S1 and S3.

Table 4.5. Temperatures at which the maxima of the H_2, HD and D_2 desorption peaks occur in the three samples and H_2, HD and D_2 desorbed flows at the corresponding maxima.

	T(K)			F(μmol s^{-1})		
Sample	H_2	HD	D_2	H_2	HD	D_2
S1a	462	458	449	0.067	0.096	0.031
S1b	468	461	454	0.058	0.091	0.035
S2	492(I)	489(I)	489(I)	0.019	0.109	0.137
	500(II)	497(II)	497(II)			
S3	486	477	469	0.034	0.113	0.104

The detection sensitivities of H_2, HD and D_2 molecules in TDS experiments are somewhat different to those obtained in the calibration experiments of the gas analysis system (see Chapter 2). Such differences are caused by the different opening of the needle valve (see Fig.4.1) during TDS and calibration experiments. However, this fact does not affect to the relative detection sensitivities $\sigma_2^{H2}/\sigma_4^{D2}$ and $\sigma_3^{HD}/\sigma_4^{D2}$, which are the same in both experiments. The detection sensitivities of H_2, HD and D_2 molecules in TDS experiments have been calculated from the ratio between the integrals of the corresponding ionic signals normalized by the relative detection sensitivities and the amounts of H and D atoms desorbed from the samples. These amounts have been obtained from the *x* and *y* ratios reported in Table 4.4 and the mol number of Pd in the samples used for TDS. The calculated H and D amounts are in agreement with the mass loss measurements of the samples due to H/D desorption. The integrals of the H_2, HD and D_2 flows, the mol number

of Pd in the desorbed samples and the mass loss after TDS experiments are summarized in Table 4.6.

Table 4.6. Mol number of Pd in the samples, integrals of the H_2, HD and D_2 desorbed flows and calculated and experimental mass loss of the samples due to H/D desorption.

		$\int F_\chi dt$ (mol)			Δm(mg)	
Sample	n_{Pd}(mol)	H_2	HD	D_2	Calc.	Exp.
S1a	$1.092\cdot10^{-4}$	$1.25\cdot10^{-5}$	$1.90\cdot10^{-5}$	$6.31\cdot10^{-6}$	0.105	0.10(2)
S1b	$1.254\cdot10^{-4}$	$1.15\cdot10^{-5}$	$1.90\cdot10^{-5}$	$7.48\cdot10^{-6}$	0.110	0.12(2)
S2	$1.370\cdot10^{-4}$	$2.18\cdot10^{-6}$	$1.26\cdot10^{-5}$	$1.59\cdot10^{-5}$	0.106	0.11(2)
S3	$1.855\cdot10^{-4}$	$6.62\cdot10^{-6}$	$2.48\cdot10^{-5}$	$2.39\cdot10^{-5}$	0.183	0.17(2)

The integration of the TDS curves also allows calculating the temperature variation of the H plus D fraction in Pd, as shown in Figs. 4.11b, 4.12b and 4.13b. The two phase coexistence limits [4.39] have been also plotted in these figures (pink dashed lines), in order to emphasize the temperatures at which the total H plus D concentration crosses the limits of the β-PdH_xD_y and α-Pd phases. The small H/D isotope effects in the limits of the β-PdH_xD_y and α-Pd phases [4.50] have been neglected.

4.4.2 H_2O/HDO/D_2O desorption

It is of interest to analyze the possible influence of H_2O/HDO/D_2O desorption on TDS results. It is well known that H(D) atoms can react with O atoms adsorbed at the Pd surface and evolve as water molecules [4.51]. In Fig.4.14 it is shown the correlation between the i_{18} peak current and the i_2 one (corresponding to H_2O and H_2 molecules, respectively) during a typical TDS experiment. Similar correlations were observed between the HDO and HD peak currents. On the other hand, the correlation between the D_2O and D_2 ionic signals could not be obtained because of the high contribution of Ar^{2+} ions to the i_{20} peak current.

The measured i_{18}/i_2 and i_{19}/i_3 ratios lie in the range of 10^{-3}-10^{-2}. These ratios are of the same order of magnitude than those obtained during the calibration experiments of the gas analysis system (see section 2.3.3), which were ascribed to hydrogen-induced water formation within the vacuum chamber. In the present TDS experiments, however, the amounts of desorbed H_2O/HDO/D_2O molecules are expected to be much lower than those corresponding to H_2/HD/D_2, because the former are limited by the O concentration at the surface, which is several orders of magnitude lower than the amounts of H and D in the bulk. Even if it is assumed that all the oxygen atoms present as impurities in the carrier Ar flow (whose concentration is <1 ppm) react with the desorbing H and D atoms at the Pd surface to form water molecules, the estimated i_{18}/i_2 and i_{19}/i_3 ratios would be in the range of 10^{-4}-10^{-3}, *i.e.*, about one order of magnitude lower than these found

experimentally. It must be concluded that the amounts of $H_2O/HDO/D_2O$ molecules desorbed from the samples were low and, therefore, could not be detected in the present TDS experiments due to the influence of the hydrogen-induced water formation processes in the gas analysis chamber.

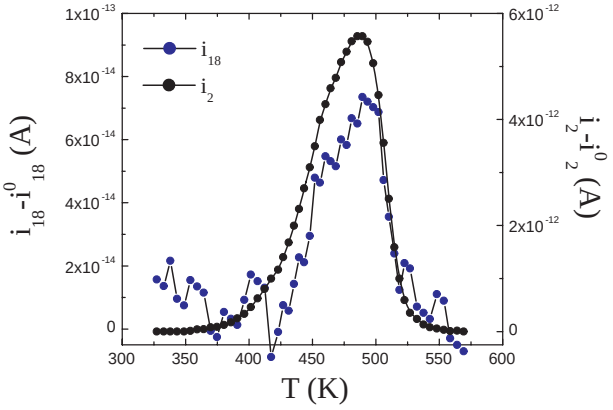

Fig.4.14. Typical profile of the i_{18} and i_2 peak currents (corresponding to H_2O^+ and H_2^+ ions, respectively) during TDS experiments.

4.5 Discussion

4.5.1 Partitioning of H and D atoms into H_2, HD and D_2 molecules

The desorbed H_2, HD and D_2 molecules are formed at the Pd surface by recombination of H and D atoms. Therefore, the way in which H and D surface atoms are partitioned into the three molecular isotopes must depend on the characteristics of these reactions. Owing to ZPE differences, significant isotope effects are expected among the kinetics of the H-H, H-D and D-D recombination reactions. However, earlier kinetic studies on the isotope exchange reaction (4.1) on metal surfaces have usually assumed no isotope effects in the rates of H and D recombination reactions [4.8-12], in order to simplify the theoretical analysis. This assumption implies a statistical partitioning of H and D atoms into H_2, HD and D_2 molecules. In other works [4.19], the relative concentrations of the hydrogen molecular isotopes in the gas phase have been assumed to be determined by the equilibrium constant of reaction (4.1):

$$K_{eq} = \frac{[HD]^2}{[H_2]\cdot[D_2]} \qquad (4.7)$$

The statistical value of K_{eq} for equally probable combination of H and D atoms is 4. However, a lower value is found in practice due to the fact that a pair of H_2 and D_2 molecules is energetically more favourable than two of HD. Exact calculations of K_{eq} were made by Urey and Rittenberg [4.52] based on the partition functions of the different molecules. In the temperature range of the present TDS experiments their results can be approximated by:

$$\ln K_{eq} = \frac{-6.75 \cdot 10^{-3}}{kT} + 1.4471 \tag{4.8}$$

where k is the Boltzmann constant expressed in eV K^{-1}.

The integration of the H_2, HD and D_2 flows desorbed from $PdH_{0.35}D_{0.26}$ yields ratios among the three molecular isotope concentrations completely different to those expected either from statistical or equilibrium partitioning of H and D atoms into H_2, HD and D_2 molecules (see Table 4.6). This is not a new finding. A detailed examination of the relative amounts of H_2, HD and D_2 desorbed molecules reported in previous experimental works also reveals deviations from statistical or equilibrium partitioning among the molecules [4.10, 19, 53, 54]. In particular, experimental results on hydrogen-deuterium exchange on Pd [4.19] showed departures from the equilibrium value predicted by equation (4.8), although equilibrium was later assumed to simplify the theoretical analysis. It is worth to note, however, that the origin of such deviations from the statistical or equilibrium partitioning has not been discussed in previous works. On the other hand, experimental values of the relative amounts of H_2, HD and D_2 molecules are not given in most of them [4.5-9, 11, 12, 14-17].

It will be shown here that the assumptions of equilibrium or statistical partitioning of H and D atoms into the three molecular isotopes are only valid under certain circumstances. We will deal with the general case in which H_2, HD and D_2 molecules are formed by surface recombination of H and D atoms. Two limiting cases must be distinguished:

i) surface recombination reaction is at equilibrium (*i.e.*, takes place in the forward and backward directions).

ii) surface recombination is out of equilibrium (*i.e.*, takes place in the forward direction only).

In case *i)*, the molecules are continuously dissociated and formed by recombination at the surface and, therefore, equilibrium partitioning of H and D atoms into hydrogen molecules is expected. On the other hand, in the majority of the experiments involving H and D atoms to form H_2, HD and D_2 molecules by surface recombination (such as TDS), the molecules are rapidly removed from sample surface by means of a pumping system or a carrier gas flow. Under these circumstances it is reasonable to assume that surface recombination reaction occurs in the forward direction only (*i.e.*, case *ii)* holds), whichever be the rate

determining step of the whole reaction. Accordingly, the H_2, HD and D_2 desorbed flows (F_{HH}, F_{HD} and F_{DD}, respectively) can be written as:

$$F_{HH} = \nu_{HH} \exp\left(-\frac{E^*_{HH} - 2E^p_H}{kT} \right) \theta_H{}^2 \tag{4.9a}$$

$$F_{HD} = \nu_{HD} \exp\left(-\frac{E^*_{HD} - E^p_H - E^p_D}{kT} \right) \theta_H \theta_D \tag{4.9b}$$

$$F_{DD} = \nu_{DD} \exp\left(-\frac{E^*_{DD} - 2E^p_D}{kT} \right) \theta_D{}^2 \tag{4.9c}$$

where ν_{HH}, ν_{HD} and ν_{DD} are the prexponential factors of the H-H, H-D and D-D recombination processes; $E_{HH}{}^*$, $E_{HD}{}^*$ and $E_{DD}{}^*$ are the corresponding energy levels of the transition states; $E_H{}^p$ and $E_D{}^p$ are the energy levels of H and D atoms at the precursor (surface) states of molecular formation and θ_H and θ_D are their respective concentrations.

In order to quantify the relationship among the H_2, HD and D_2 desorbed flows let us to define, in analogy with equation (4.7):

$$K = \frac{F_{HD}{}^2}{F_{HH} \cdot F_{DD}} \tag{4.10}$$

Introducing equations (4.9a)-(4.9c) into (4.10) and taking logarithms, it is obtained:

$$\ln K = \ln\left[\frac{\nu_{HD}{}^2}{\nu_{HH}\nu_{DD}} \right] - \frac{2E^*_{HD} - E^*_{HH} - E^*_{DD}}{kT} \tag{4.11}$$

In the absence of isotope effects in the atom-atom recombination reaction, the following equalities are valid: $\nu_{HD}=2\,\nu_{HH}=2\,\nu_{DD}$ and $E_{HH}{}^*=E_{HD}{}^*=E_{DD}{}^*$, what implies a statistical partitioning of atoms into the molecular isotopes (*i.e.*, K=4). However, this assumption seems to be unrealistic because large ZPE differences among H-H, H-D and D-D pairs at the TS are expected.

Experimental TDS data of PdH_xD_y samples have been analyzed according to equation (4.11). The results obtained for samples S1a, S1b, S2 and S3 are shown in Figs.4.15. The low and high temperature tails of the TDS peaks have not been

included in the analysis of *K* values due to the higher uncertainty of these data. The line predicted by the equilibrium exchange reaction (4.8) has been also plotted in these figures (blue dashed line) for comparison purposes.

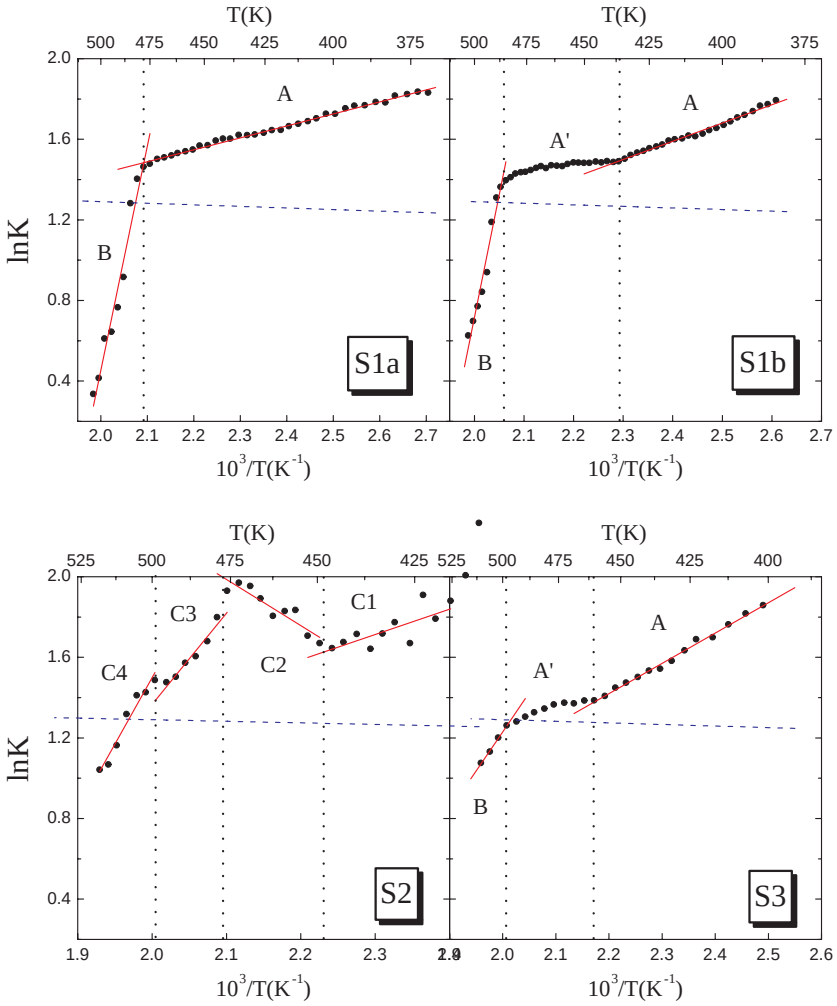

Fig. 4.15. Arrhenius plot of the relative H_2, HD and D_2 flows desorbed from samples S1a, S1b, S2 and S3 (black points). Various regions (separated by vertical dotted lines) with different activation energies are observed. Red lines represent the linear fit to the data in each region. The line predicted by the equilibrium exchange reaction between H_2 and D_2, equation (4.7), has been also plotted (blue dashed line) for comparison purposes.

Experimental points of samples S1a, S1b and S3 show two regions (A and B) which can be fitted to equation (4.11). An additional intermediate region (A') where K is nearly constant is observed in samples S1b and S3. On the other hand, the behaviour of sample S2 is more complex than those of samples S1a, S1b and S3. In this case, up to four regions (denoted as C1-C4) are observed.

According to equation (4.11), the observed changes in the slopes of the plots of lnK *vs* T^{-1} denote some changes in the energy levels of the TS of the atom-atom recombination. The $2E_{HD}$*-E_{HH}*-E_{DD}* values obtained from the least square fits of experimental points in Fig.4.15 (red lines) in each region are summarized in Table 4.7. The temperature range of each region has been also included in this table. It must be noticed that the appearance of negative energies simply reflects that the TS energy of the H-D recombination is below the mean value of those corresponding to H-H and D-D recombinations. This finding contrast with the predictions of simple quantum considerations, as it will be shown in section 4.5.3.

Table 4.7. Activation energies of the Arrhenius plots of the relative desorbed flows obtained from the linear fits of the experimental points in Fig4.15.

Sample	Region	T range (K)	$2E_{HD}$*-E_{HH}*-E_{DD}* (ev molec^{-1})
S1a	A	370-480	-0.051(1)
	B	480-510	-0.96(7)
S1b	A	380-425	-0.078(2)
	B	490-505	-1.05(8)
S2	C1	420-445	-0.11(4)
	C2	445-475	0.20(3)
	C3	475-495	-0.39(4)
	C4	495-515	-0.57(5)
S3	A	400-470	-0.130(3)
	B	502-515	-0.34(0.1)

It is worth to note that although the rates of H_2, HD and D_2 desorption may depend on other steps of the whole process, the relationship among these flows defined by equation (4.10) is uniquely determined by the atom-atom recombination reaction, according to equation (4.11). Therefore, the logarithmic plots appearing in Fig.4.15 give direct information on the TS of the surface recombination reaction. The changes in the energy levels of those TS can be easily monitored by observing the changes in the slopes of the Arrhenius plots of the relative desorbed flows, whichever be the r.d.s. of the desorption reaction.

4.5.2 Kinetic analysis of the thermal desorption spectra

In order to analyze the kinetics of the thermal desorption process, one should consider the desorption mechanism, which can be summarized in up to six sequential steps (see Fig.4.16):

a) Diffusion of H and D atoms through β-PdH_xD_y

b) Transformation of β-PdH_xD_y into α-Pd

c) Diffusion of H and D atoms through α-Pd

d) Transition of H and D atoms from bulk to surface states

e) Surface recombination of H and D atoms to form H_2, HD and D_2 physisorbed molecules.

f) Desorption of physisorbed molecules into the gas phase.

It should be noted that these steps are not simultaneously present during the complete desorption reaction. According to Fig.3b, the total H and D concentration crosses the limits of the β-PdH_xD_y and α-Pd phases. During desorption from the β-PdH_xD_y phase steps *b)* and *c)* are absent, whereas the same occurs with steps *a)* and *b)* during desorption from α-Pd. Therefore, one should analyze separately the desorption kinetics depending on the steps involved in each phase.

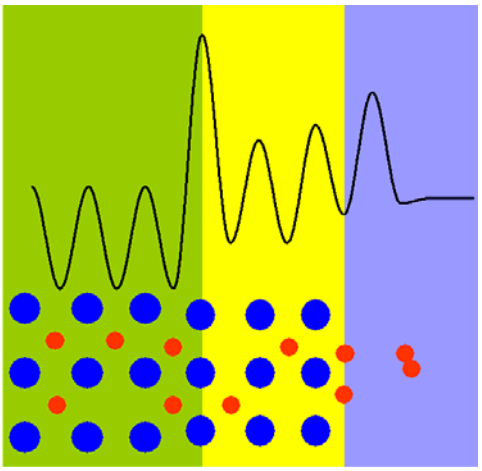

Fig.4.16. Scheme of the β-PdH_xD_y (green region), α-Pd (yellow region) and gas (violet region) phases. Blue and red circles represent Pd and H(D) atoms, respectively. The black line shapes the potential energy surface of H(D) atoms during their desorption from PdH_xD_y samples.

4.5.2.1 Influence of bulk diffusion on the kinetics of H and D desorption

Prior to analyze the kinetics of H(D) thermal desorption from Pd samples, it is important to estimate the role that plays bulk diffusion on this processes. To this

aim, the temperature evolutions of the H and D concentration gradients within the samples during the course of the TDS experiments (Δx and Δy, respectively) have been analyzed. If these gradients are small compared to the total H and D concentrations in the samples (*i.e.*, $\Delta x/x, \Delta y/y << 1$), it can be safely assumed that diffusion does not limit the kinetics of H(D) desorption. Δx and Δy can be evaluated from the variations of the H and D concentrations inside the sample during a typical diffusion time $\tau_{H(D)}$ [4.47]:

$$\Delta x = F_H \tau_H \tag{4.12a}$$

$$\Delta y = F_D \tau_D \tag{4.12b}$$

where F_H and F_D are the H and D desorption rates, which can be experimentally determined from the H_2, HD and D_2 desorbed flows ($F_H = 2F_{HH} + F_{HD}$ and $F_D = 2F_{DD} + F_{HD}$). The diffusion times can be estimated according to equation (4.3), where L is the diffusion length (*i.e.*, the half of the thickness of the Pd foils) and D_c is the diffusion coefficient of H or D within the samples:

$$D_c = D_0 \exp\left(\frac{-E_d}{kT}\right) \tag{4.13}$$

H(D) diffusion coefficients in the samples have been calculated by interpolating between the diffusion coeficients in the hydride and solid solution phases, depending on the relative amounts of α and β phases in the samples during the course of the TDS experiments. The diffusion coefficient of H in β-Pd hydride is given by $D_0 = 0.9 \cdot 10^{-3}$ cm^2 s^{-1} and $E_d = 0.228$ eV [4.55]. Hydrogen diffusion is faster in α-Pd than in β-Pd hydride. According to Völk and Alefeld [4.56], the best fit to diffusion coefficient data of H in α-Pd is given by $D_0 = 2.9 \cdot 10^{-3}$ cm^2 s^{-1} and $E_d = 0.230$ eV. Deuterium diffusion coefficients have been obtained from reported data [4.56] of the ratio between H and D diffusion coefficients in Pd as a function of temperature. The $\Delta x/x$ and $\Delta y/y$ values corresponding to each TDS experiment obtained by using this procedure are plotted in Fig.4.17.

The results appearing in Fig.4.17 show that the H(D) concentration gradients are below the 5% of the total H(D) concentrations within the samples during the most part of the desorption processes. These gradients increase up to the 7-8% of the H and D concentrations at the end of the TDS. From those results it seems reasonable to assume that the desorption processes can not be fitted by a diffusion limited mechanism. As a consequence, the kinetics of H and D thermal desorption will be analyzed in what follows by considering surface and phase transformation processes as the only possible rate limiting mechanisms.

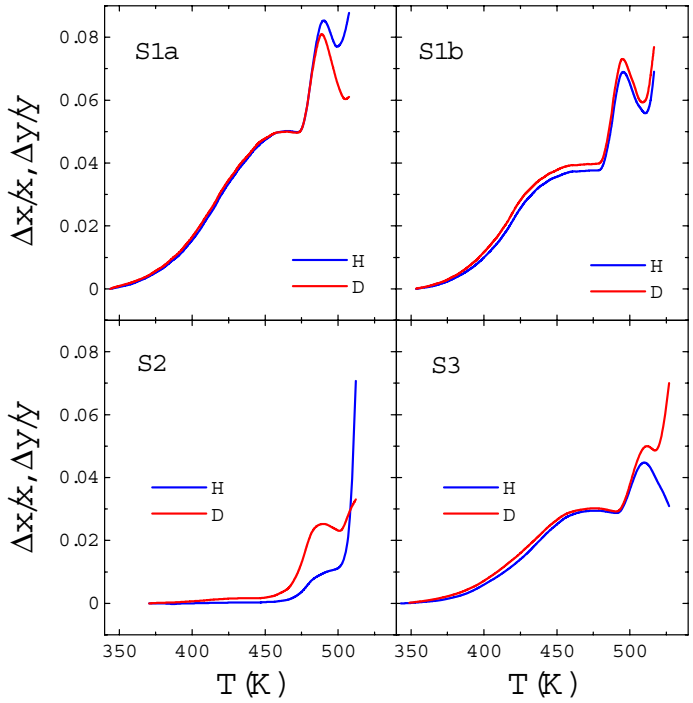

Fig.4.17. Estimated H and D concentration gradients (divided by the H and D concentrations in Pd) within the samples during the course of TDS experiments.

4.5.2.2 Desorption from β-PdH$_x$D$_y$

Samples S1 and S3 show a range of temperatures where desorption of H_2, HD and D_2 molecules takes place from β-PdH$_x$D$_y$ (see Figs.4.11b-13b). It has been found that the desorption pocesses are rate limited within these temperature ranges by the kinetics of recombination of H and D atoms at the β-PdH$_x$D$_y$ surfaces. The analysis of the thermal desorption curves of bulk metal hydrides in the case of a process limited by surface recombination was done by Stern *et al.* [4.21, 22] and was successfully applied to Pd hydride powder [4.47]. These authors considered two limiting cases, depending on the relative position of the H(D) energy levels in the bulk and at the precursor (surface) states of the recombination reaction (see Fig.4.16). The chemical potential of H(D) atoms in bulk sites ($\mu_{H(D)}$) is known from the pressure-composition isotherms of the Pd-H_2(D_2) system. It depends on the H and D content and temperature. According to the results of Stern *et al.*, for a H/Pd ratio in the sample below 0.7, the H bonding energy in the bulk is higher than at the

precursor states. Under these circumstances the H concentration at the precursor states is low and the H_2 flow can be written:

$$F_{HH} = M_s^A \nu_{HH}^A \exp\left(-\frac{E_{HH}^{A*} - 2\mu_H}{kT}\right) \tag{4.14}$$

where M_s^A is a constant and ν_{HH}^A is the frequency factor of H-H recombination. By writing analogue expressions for HD and D_2 flows and taking the chemical potential of H and D atoms given by lattice gas theory (see [4.57]), it is obtained:

$$F_{HH} = M_s^A \nu_{HH}^A \exp\left(-\frac{E_{HH}^{A*} - 2E_H^\beta}{kT}\right)\left(\frac{x}{1-x}\right)^2 \tag{4.15a}$$

$$F_{HD} = M_s^A \nu_{HD}^A \exp\left(-\frac{E_{HD}^{A*} - E_H^\beta - E_D^\beta}{kT}\right)\left(\frac{x}{1-x}\right)\left(\frac{y}{1-y}\right) \tag{4.15b}$$

$$F_{DD} = M_s^A \nu_{DD}^A \exp\left(-\frac{E_{DD}^{A*} - 2E_D^\beta}{kT}\right)\left(\frac{y}{1-y}\right)^2 \tag{4.15c}$$

where E_H^β and E_D^β are the energies of H and D atoms, respectively, in bulk β-PdH_xD_y sites. The superscript A in the TS energies of the atom-atom recombination reaction denotes that this is the TS corresponding to regions 'A' in Fig.4.15.

Fits of the H_2, HD and D_2 flows desorbed from samples S1a, S1b and S3 by equations (4.15a)-(4.15c) are shown in Fig.4.18. Regression coefficients very close to 1 have been obtained from these fits. The activation energies obtained from the least square fits of the experimental points in Fig.4.18 are listed in Table 4.8. Mean values of the activation energies for H_2, HD and D_2 molecules are also listed. The reproducibility of the results obtained from the three samples is reasonably good. The standard deviations of the obtained mean values are around 5-6%. It can be seen that the activation energies decrease in the order H_2>HD>D_2, as expected from the temperature shift of the H_2, HD and D_2 desorption peaks (see Figs.4.11a and 4.13a). On the other hand, these activation energies are higher than the formation enthalpies of β-Pd hydride and deuteride (about 0.4 eV molec^{-1} [4.50]) and, therefore, imply the existence of an activation barrier of about 0.4 eV molec^{-1} for the surface recombination reaction. Stern *et al.* [4.47] also observed an activation barrier for surface recombination, although its height was substantially lower, namely about 0.06 eV molec^{-1}. Such differences should be attributed to the different surface conditions of the Pd samples. It is well known that the height of the activation barrier for recombinative desorption is extremely sensitive to the presence of oxides [4.58, 59] and other surface impurities [4.60].

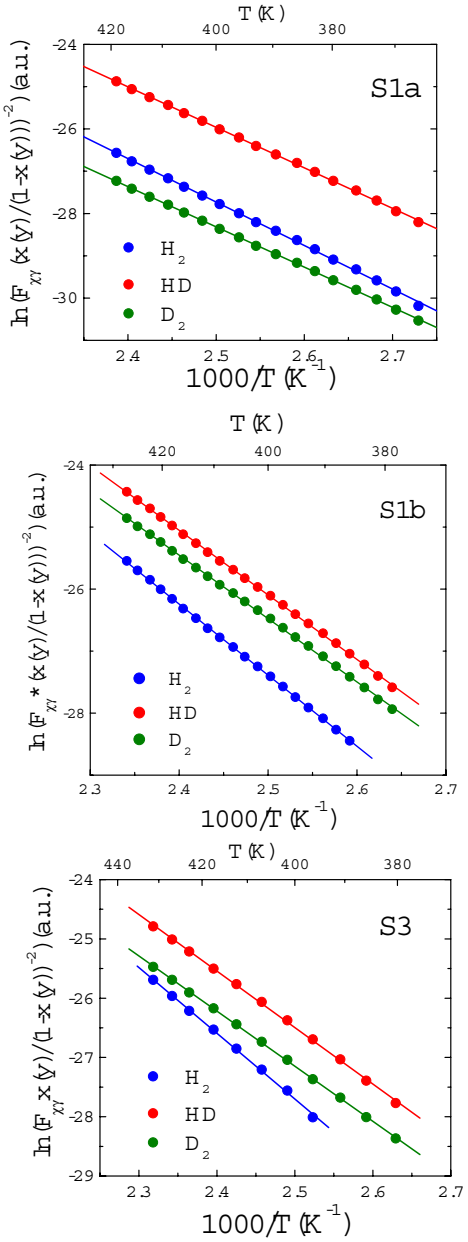

Fig.4.18. Arrhenius plots of the H_2, HD and D_2 desorption from β-PdH_xD_y by considering a surface recombination mechanism. Solid lines in those figures are the linear fits of experimental data.

Table 4.8. Activation energies of H_2, HD and D_2 desorption from β-PdH_xD_y obtained by considering a surface recombination mechanism.

		E^{act}(eV molec^{-1})		
Sample	T range (K)	H_2	HD	D_2
S1a	375-420	0.878(4)	0.822(4)	0.818(3)
S1b	380-425	0.988(3)	0.897(3)	0.881(3)
S3	380-430	0.96(1)	0.821(7)	0.800(4)
Mean		0.94(6)	0.85(4)	0.83(4)

4.5.2.3 Desorption during the coexistence of α and β phases

Once the total H plus D concentration in samples S1a, S1b and S3 crosses the limit of the two phase coexistence region, a layer of α-Pd will grow from the surface to the bulk of the samples. Therefore, the desorbing samples must be regarded as a shrinking core of β-PdH_xD_y enveloped by a growing layer of α-Pd [4.61], as shown squematically in Fig.4.19a. A different geometric distribution of the α and β phases must be expected in sample S2. In this case, the initial H and D concentration within the sample lies within the two phase coexistence region. Thus, it seems to be more reasonable to assume an inhomogeneous distribution of β-PdH_xD_y nucleous dispersed over the sample, as shown squematically in Fig.4.19b.

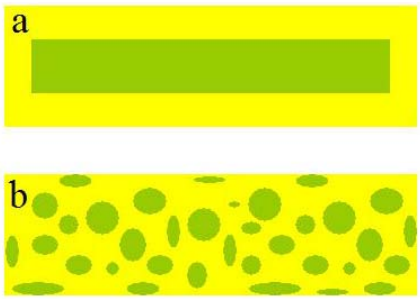

Fig.4.19. Schemes of the two possible geometric distributions (**a** and **b**) of the α (yelow) and β (green) phases within the samples during the two phase coexistence region.

During the coexistence of the α and β phases, the chemical potential of H(D) atoms in the samples is constant. Therefore, if surface recombination is rate limiting in this region, the molecular desorbed flows should be described by zero order processes [4.47] (see equation (4.14)). However, the experimental H_2, HD and D_2 desorbed flows do not fit to zero order processes.

If it is assumed that the desorption is rate limited by the kinetics of H and D transition from β-PdH_xD_y to α-Pd, the rates of H and D desorption can be written:

$$F_H = M_\beta \nu_H \exp\left(-\frac{E_H^{\beta/\alpha} - E_H^{\beta}}{kT}\right) x_{\beta/\alpha} \tag{4.16a}$$

$$F_D = M_\beta \nu_D \exp\left(-\frac{E_D^{\beta/\alpha} - E_D^{\beta}}{kT}\right) y_{\beta/\alpha} \tag{4.16b}$$

where M_β is a constant, ν_H and ν_D are the frequency factors of the β to α transformation, $E_H^{\beta/\alpha}$ and $E_D^{\beta/\alpha}$ are the correspoding TS energies for H and D atoms and $x_{\beta/\alpha}$ and $y_{\beta/\alpha}$ are the numbers of H and D atoms at the β/α interface. These numbers will depend on the β-phase concentration (β_{min}, which changes with temperature according to the dashed line shown in Fig.3b) and on the area of the β/α interface ($A_{\beta/\alpha}$):

$$x_{\beta/\alpha} = \frac{x}{x+y}\beta_{\min} A_{\beta/\alpha} \tag{4.17a}$$

$$y_{\beta/\alpha} = \frac{y}{x+y}\beta_{\min} A_{\beta/\alpha} \tag{4.17b}$$

The factors *x/(x+y)* and *y/(x+y)* account for the probability of a H or D atom be located at the β/α interface, respectively.

In order to fit the experimental data to the model described by equations (4.16)-(4.17), one should express $A_{\beta/\alpha}$ in terms of the experimental variables obtained from the TDS curves. To this purpose, it has been assumed that all the H and D atoms within the sample are in the β phase. This assumption is based on the fact that the hydrogen and deuterium partial pressures in the volume near the samples are much lower than the equilibrium pressures of the β/α transformation. Therefore, as surface recombination is not rate limiting, the H and D concentration in α-Pd can be safely assumed to be negligible. From this hypothesis, it can be deduced that the volume of the β phase should be proportional to the total number of atoms in the sample ($x+y$), while the area of the β/α interface should be proportional to $(x+y)^{2/3}$. The constant of proportionality will depend on the geometric distribution of the α and β phases within the samples. By taking into account those considerations, equations (4.16a) and (4.16b) take the form:

$$F_H = M'_{\beta}\nu_H \exp\left(-\frac{E_H^{\beta/\alpha} - E_H^{\beta}}{kT}\right)\beta_{\min} x(x+y)^{-1/3} \tag{4.18a}$$

$$F_D = M'_{\beta}\nu_D \exp\left(-\frac{E_D^{\beta/\alpha} - E_D^{\beta}}{kT}\right)\beta_{\min} y(x+y)^{-1/3} \tag{4.18b}$$

The experimental H and D flows desorbed from the samples within the two phase coexistence region have been fitted to equations (4.18a) and (4.18b), respectively, and the results are shown in Fig.4.20. It can be seen that the model does not fit the experimental data of sample S2. The kinetic analysis of the TDS data of sample S2 will be discussed in section 4.5.2.5. On the other hand, the TDS curves of samples S1a, S1b and S3 are well fitted by a phase transformation limiting mechanism. In principle, the β to α phase transformation should control the process until the end of the desorption, because all the H and D atoms in the samples are in the β-PdH_xD_y inner core. However, it can be seen from Fig.4.20 that the model only fit the experimental data up to a certain temperature, which is slightly different for each sample. These temperatures coincide with those at which the transition from regions 'A' to regions 'B' are observed in the Arrhenius plots of the relative desorbed flows (Fig.4.15). According to the analysis done in section 4.5.1, these transitions reflect that the kinetics of the surface recombination reaction is modified on passing from A to B. Therefore, it must be concluded that the desorption is controlled by the phase transformation within the bulk until surface recombination becomes again rate limiting at higher temperatures. This point will be further discussed in the next section.

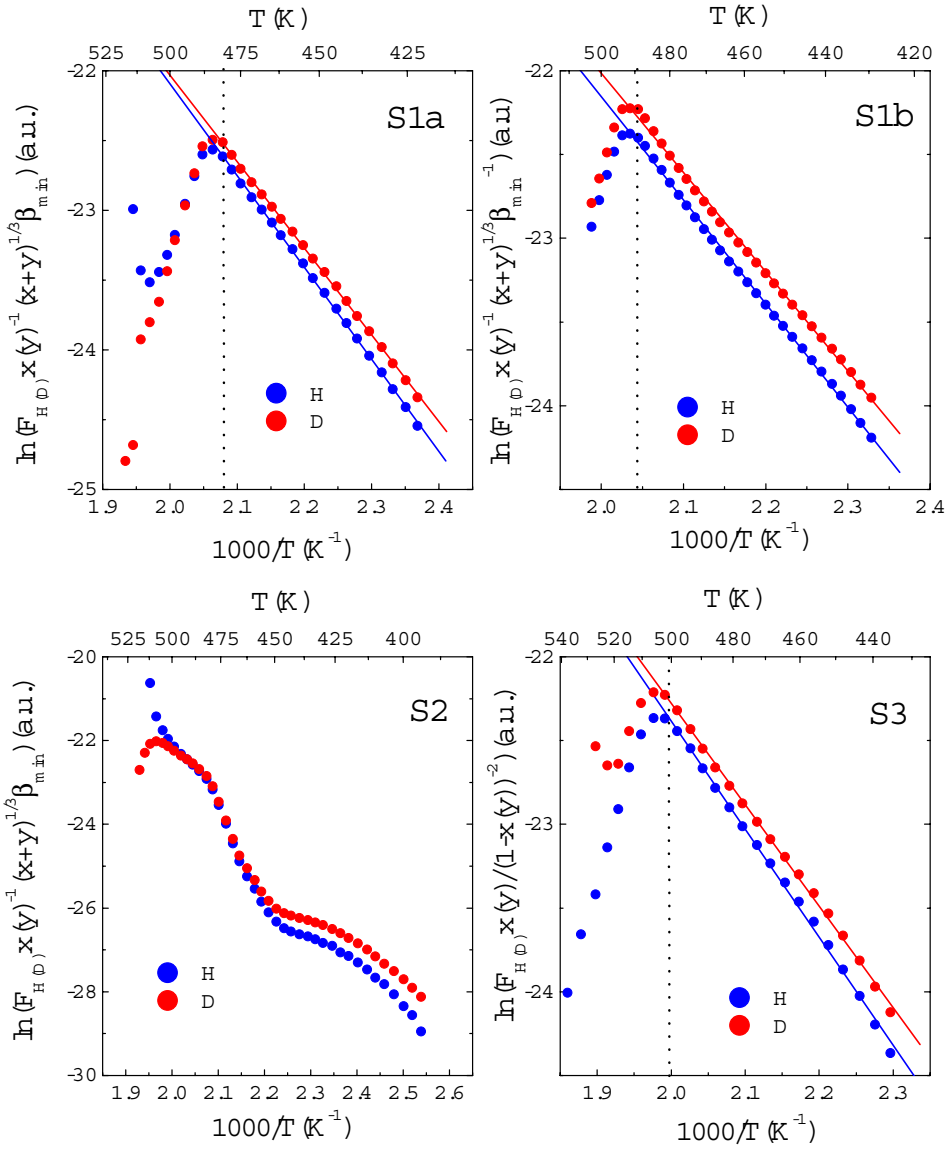

Fig.4.20. Arrhenius plots of the H and D flows by considering a β to α transformation mechanism. Solid lines in those figures are the linear fits of experimental data. Vertical dotted lines show the temperatures at which surface recombination reaction becomes rate limiting.

Table 4.9. Activation energies of the α to β phase transformation process obtained from the least square fits of the experimental points in Fig.4.20.

		E^{act}(eV atom^{-1})	
Sample	T range (K)	H	D
S1a	420-480	0.569(3)	0.535(3)
S1b	425-490	0.533(3)	0.511(4)
S3	430-500	0.555(7)	0.522(5)
Mean		0.55(2)	0.52(1)

The activation energies of the α to β phase transformation process obtained from the least square fits of experimental points in Fig.4.20 are listed in Table 4.9. A good agreement is found among the values corresponding to the three samples. The deviation of the obtained activation energies with respect to the mean values are of about 2-3%. The obtained values reflect the existence of an inverse isotope effect in the β to α transition. As far as I know, no previous results on this isotope effect have been reported. In addition, there is only one previous estimation of the activation energy of the β to α transition in the Pd-D system [4.62]. It was obtained from the analysis of the effective diffusion coefficient of D in single crystal Pd within the two phase coexistence region. The reported activation energy value was 0.45 eV atom^{-1}. By taking into account that the method used to estimate that value is only approximate, the agreement with the present results can be considered to be good.

4.5.2.4 Final stage of desorption

As it has been stated in the previous section, the desorption kinetics is not controlled by the β to α phase transition above a certain temperature. This has been ascribed to the change in the kinetics of the surface recombination reaction, which becomes again rate limiting above this temperature. This implies that the rate of the β to α phase transition is then faster than the whole desorption rate. Given that the mean H plus D concentration in the sample in this temperature range is below the α-Pd phase limit (see Figs.4.11-4.13), it is expected that the inner β-nucleus will disappear and the samples will be completely transformed into α-Pd.

Following the analysis done in section 4.5.2.2 for a surface recombination limiting mechanism, the H_2, HD and D_2 flows will be described by the equations:

$$F_{HH} = M_s^B \nu_{HH}^B \exp\left(-\frac{E_{HH}^{B*} - 2E_H^\alpha}{kT}\right)\left(\frac{x}{1-x}\right)^2 \qquad (4.19a)$$

$$F_{HD} = M_s^B \nu_{HD}^B \exp\left(-\frac{E_{HD}^{B*} - E_H^\alpha - E_D^\alpha}{kT}\right)\left(\frac{x}{1-x}\right)\left(\frac{y}{1-y}\right) \quad (4.19b)$$

$$F_{DD} = M_s^B \nu_{DD}^B \exp\left(-\frac{E_{DD}^{B*} - 2E_D^\alpha}{kT}\right)\left(\frac{y}{1-y}\right)^2 \quad (4.19c)$$

where M_s^B is a constant, ν_{HH}^B, ν_{HD}^B and ν_{DD}^B are the frequency factors of the H-H, H-D and D-D recombination in region 'B' (see Fig.4.15) and E_H^α and E_D^α are the energies of H and D atoms, respectively, in α-Pd sites.

The fits of the experimental data of samples S1a, S1b and S3 to equations (4.19a)-(4.19c) are shown in Fig.4.21. The obtained activation energies from the least square fits of the H_2, HD and D_2 data in Fig.4.21 are summarized in Table 4.10, together with the mean values corresponding to each molecule. The dispersion of the experimental values is higher than for the activation energies obtained in the preceding sections (about 10% for H_2, 3% for HD and 7% for D_2).

Table 4.10. Activation energies of H_2, HD and D_2 desorption from α-Pd obtained by considering a surface recombination mechanism.

		E^{act}(eV molec^{-1})		
Sample	T range (K)	H_2	HD	D_2
S1a	480-510	4.20(6)	3.65(2)	4.08(5)
S1b	490-505	4.1(1)	3.76(6)	4.3(1)
S3	500-515	3.5(1)	3.6(1)	3.8(1)
Mean		3.9(4)	3.7(1)	4.1(3)

The most significant result is that the obtained activation energies are about 4-5 times greater than those found for the atom-atom recombination in β-PdH_xD_y at lower temperatures (see Table 4.8). Similar increments in the activation energies of the atom-atom recombination have been observed in TDS experiments of TaD_x foils [4.63]. In these experiments, the surface composition was *in situ* monitored by means of Auger spectroscopy. The change of the activation energy occurred at the same temperature where a decrease in the oxygen surface concentration was observed. The authors argued that the increment in the activation energy of the H-H recombination reaction was due to the energy involved in the process of diffusion of oxygen atoms from the surface layer to the bulk.

Later experiments [4.64] performed in ultrahigh vacuum conditions with TaH_x and ZrH_x foils with different degrees of oxidation confirmed the observation of a rise in the activation energy of the H-H surface recombination. In this case, however, the effect was ascribed to the energy involved in the O desorption in the form of H_2O molecules.

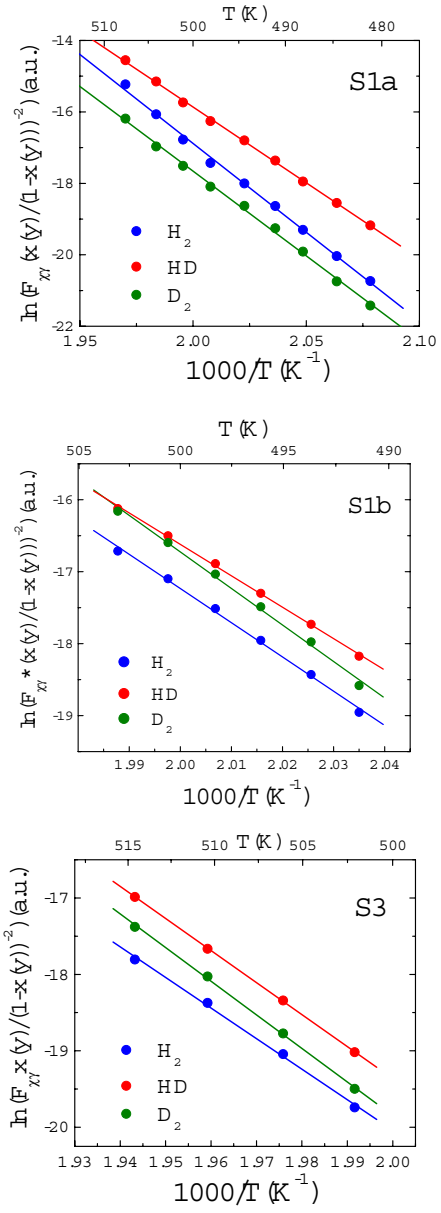

Fig.4.21. Arrhenius plots of the H_2, HD and D_2 desorption from α-Pd by considering a surface recombination mechanism. Solid lines are the linear fits of experimental data.

As it has been exposed in section 4.4.3, the $H_2O/HDO/D_2O$ desorption rates could not be monitored in the present TDS experiments, due to the effect of hydrogen-induced water formation in the gas analysis chamber. In any case, the estimated $H_2O/HDO/D_2O$ desorption rates seem to be very low compared to the $H_2/HD/D_2$ ones to account for the observed increments in the activation energies.

There is an additional argument to rule out both O diffusion into the bulk and $H_2O/HDO/D_2O$ desorption as the cause of the rise of the activation energies. Within these models, the change of the activation energy is due to the extra energy needed either to diffuse O atoms into the bulk or to desorb them forming $H_2O/HDO/D_2O$ molecules. Both processes would lead to a similar increment in the activation energies of H_2, HD and D_2 molecules. By contrast, it is observed that the activation energy increments are different for the three hydrogen molecular isotopes. Accordingly, it seems more reasonable to assume that the increment of the activation energies of the H-H, H-D and D-D recombination reactions are due to a change of the surface catalytic properties due a modification of the surface composition. This modification would shift the energy levels of the TS of the surface recombination reaction, which are different for each one of the molecular isotopes. This interpretation is further supported by the fact that the change in the activation energies occurs in the same temperature range than the change in the TS energies deduced from the analysis of the relative H_2, HD and D_2 distributions (Fig.4.15). The modification of the surface composition should be ascribed to the diffusion of bulk impurities to the surface or to the growing of the surface oxide layer. Oxygen transitions from surface to subsurface or bulk sites have been reported in Pd [4.34] at temperatures between ~350 and 500 K. This would imply that the oxide layer present at the sample surface could growth, assisted by the oxygen diffusion into the bulk, due to the impurity levels of oxygen in the carrier Ar gas (~1ppm). Further experiments in ultrahigh vacuum conditions would be of great importance in order to test the present hypothesis.

4.5.2.5 Kinetic analysis of the thermal desorption spectra of sample S2

The kinetic models used to describe TDS of samples S1a, S1b and S3 do not fit the results from sample S2. In fact, TDS of sample S2 shows qualitative differences with those of samples S1a, S1b and S3. These differences seem to be related to two effects. On the one hand, the initial H+D content in sample S2 lies within the two phase coexistence region. The geometric distribution of α-Pd and β-PdH_xD_y phases within the sample must be inhomogeneous, as shown in Fig.4.19b. Therefore, it seems reasonable to assume that H and D atoms desorb simultaneously from α-Pd and β-PdH_xD_y regions near the sample surface. As the model described in section 4.5.2.3 failed to explain the TDS of this sample, one can consider that surface recombination is rate limiting. The relative fraction of H(D) atoms desorbed from each phase can be calculated from the fraction of α and β phases in the sample

obtained by using the lever rule. This fraction is plotted in Fig.4.22 as a function of temperature. According to this figure, it seems that H(D) atoms desorb mainly from β-PdH_xD_y regions up to about 480 K. At 500 K all the atoms would be desorbed from α-Pd. This qualitative model can account for the observation of two desorption peaks in the TDS, because each desorption peak can be ascribed to desorption from a different phase.

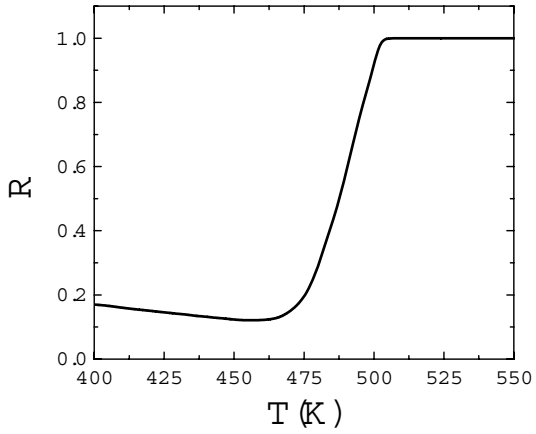

Fig.4.22. Evolution of the fraction of H+D atoms in the α phase during the course of the TDS of sample S2.

On the other hand, the kinetics of H(D) desorption is further complicated by surface modifications. The Arrhenius plot of the relative desorbed flows (see Fig.4.15) indicates that complex changes take place in the sample surface during the course of the TDS experiment. The results obtained in the preceding sections have shown that these surface modifications can lead to drastic changes in the kinetics of H_2, HD and D_2 desorption. This fact, together with the presence of two phases from which H(D) are desorbed simultaneously, makes extremely difficult the kinetic analysis of TDS data from this sample.

4.5.3 Transition state energies

From the activation energies obtained in the kinetic analysis of TDS data, the energy levels of the β to α phase transformation and of the atom-atom surface recombination TS can be calculated. The schematic diagram appearing in Fig.4.23 shapes the potential energy levels of H and D atoms during the desorption reaction. The zero energy level has been taken as the energy of a pair of free H atoms. The energy levels of H_2, HD and D_2 molecules in the gas phase (E_{HH}^0, E_{HD}^0 and E_{DD}^0) have been calculated from the reported dissociation energies of the three molecular

isotopes [4.65]. It must be noted that dissociation energies refer to H_2, HD and D_2 dissociation into atoms in their fundamental states. Therefore, the energy difference between free H and D atoms ($3.6 \cdot 10^{-3}$ eV) must be taken into account in the calculation of H_2, HD and D_2 energies. The energy level of H atoms in bulk α-Pd sites (E_H^{α}) has been obtained from E_{HH}^{0} and the enthalpy of solution of H_2 in α-Pd. [4.39]. From E_H^{α} and the reported ZPE difference between H and D atoms in α-Pd [4.50], E_D^{α} can be calculated. On the other hand, H and D energies in bulk β-PdH_xD_y sites (E_H^{β} and E_D^{β}) can be obtained from the enthalpies of the β to α transition of Pd hydride and deuteride [4.50], respectively. The energies of all these states are summarized in Table 4.11.

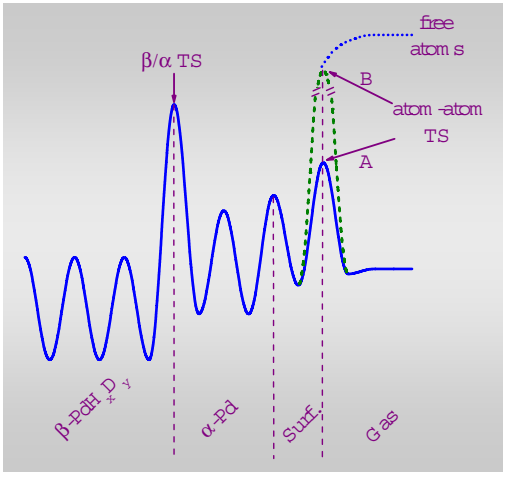

Fig4.23. Schematic potential energy diagram for H and D atoms in their desorption from PdH_xD_y.

The energies of H and D atoms at the TS of the β to α phase transformation have been calculated from the energy levels in β-PdH_xD_y sites (Table 4.11) and the activation energies obtained in the analysis of the TDS curves (Table 4.9) for samples S1a, S1b and S3. These energies are summarized in Table 4.12. A good agreement is found among the TS energies of the three samples. The observed isotope effect in the TS energies can be understood in the following terms. The TS is usually represented as a saddle point at the PES, with a maximum along the reaction coordinate and a minimum in at least one of the normal coordinates. The dynamics of atoms or molecules along these normal coordinates generates quantized energy levels at the TS, which will depend on the mass of the atoms/molecules. The existence of such quantized states in the TS of chemical reactions is supported by some experimental evidences and it has been the subject of recent reviews [4.66, 67]. TS energies of the β to α transition shown in Table

4.12 are more positive for H than for D atoms, as expected from ZPE considerations. Moreover, these differences are higher at the TS of the β to α transition than in bulk β-PdH_xD_y sites. This is the cause of the inverse isotope effect in the activation energies of the β to α phase transformation. A similar situation is observed for the TS of H and D diffusion in α-Pd. Differences between ZPE of H and D atoms are higher at the TS of the diffusion process that in α-Pd octahedral sites, which is the reason to observe a higher diffusion coefficient for D than for H [4.4, 68].

Table 4.11. Energy levels of H and D atoms in the fundamental states of the diatomic molecules and in bulk α-Pd and β-PdH_xD_y sites.

State	Symbol	Energy (eV)
H_2 molecule	E_{HH}^{0}	-4.478[a]
HD molecule	E_{HD}^{0}	-4.517 [a]
D_2 molecule	E_{DD}^{0}	-4.563 [a]
H in α-Pd	E_H^{α}	-2.339(7) [b]
D in α-Pd	E_D^{α}	-2.369(7) [b]
H in β-PdH_xD_y	E_H^{β}	-2.441(5) [b]
D in β-PdH_xD_y	E_D^{β}	-2.466(5) [b]

[a]: energies per molecule; [b]: energies per atom

Table 4.12. Energy levels of H and D atoms at the TS of the β/α phase transformation.

Sample	$E_H^{\beta/\alpha}$ (eV $atom^{-1}$)	$E_H^{\beta/\alpha}$ (eV $atom^{-1}$)
S1a	-1.87(1)	-1.93(1)
S1b	-1.91(1)	-1.96(1)
S3	-1.89(1)	-1.94(1)
Mean	-1.89(2)	-1.94(2)

TS energies of the surface recombination reactions in regions 'A' and 'B' have been evaluated from the activation energies given in Tables 4.8 and 4.10 and the energy levels of H(D) atoms in β-PdH_xD_y and α-Pd sites, respectively. The obtained $E_{XY}^{A^*}$ and $E_{XY}^{B^*}$ values (*X* and *Y* represent H or D atoms) are plotted in Fig.4.24 (a) and (b), respectively, as a function of the mass number of the hydrogen isotope molecules. It is worth to note that when these TS energies are introduced into equation (4.11), this equation reproduces experimental points in Fig.4.15 (see Table 4.7) within the experimental error. This accordance confirms the goodness of the calculation of the TS energies and, therefore, corroborates the kinetic analyses of the TDS curves. On the other hand, the reproducibility of these energy levels

among the three TDS experiments is not as good as for $E_{H(D)}^{\beta/\alpha}$ values. This must be ascribed to the different surface conditions of the samples.

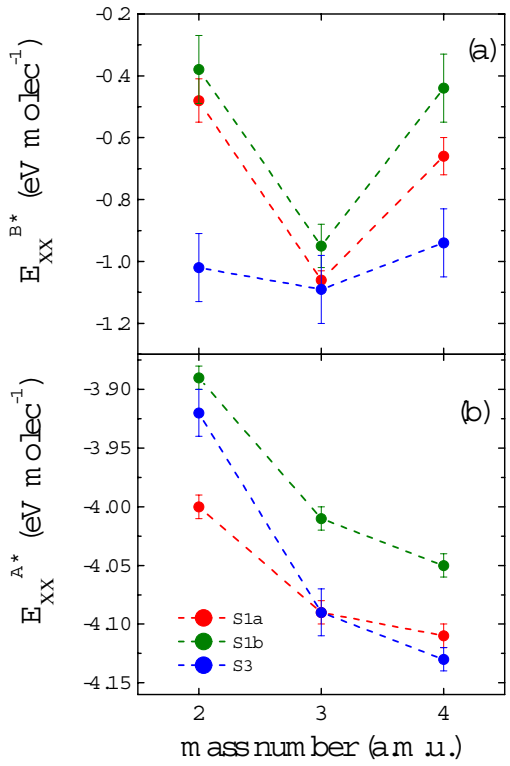

Fig.4.24. Plot of the TS energies of the atom-atom recombination reaction as a function of the mass number of the molecules. Energies are referred to the free atom states, which have been taken as the zero energy levels. (a) and (b) stand for regions A and B, respectively. Data corresponding to samples S1a (red), S1b (green) and S3 (blue) have been included.

The energy spacing among the H-H, H-D and D-D TS show anomalous behaviours. Considering the simplest case of a two dimensional PES in which the potential along the normal coordinate is harmonic, the relative ZPE differences at the TS of H-H, H-D and D-D recombination can be calculated. Applying the rule for calculating isotopic energy levels [4.69], the difference between ZPE of H-H and H-D TS should be ~0.45 times the difference between H-H and D-D. This implies that ZPE of H-D TS should lie slightly above the mean value between H-H

and D-D ones. This picture describes well the differences between ZPE of H_2, HD and D_2 molecules in the gas phase (see Fig.1.1). However, as it can be seen in Fig.4.24, H-D TS energies lay below the mean values of H-H and D-D TS energies. The effect is more pronounced in region B, in which TS energy of H-D is even lower than the corresponding value for D-D.

Anomalous behaviours among H_2, HD and D_2 molecules desorbed from Pd have been also observed by Schröter *et al.* [4.70]. They found that the energy spacing between the two first vibrational levels in the TS of the atom-atom recombination does not scale with the isotopic mass ratio of the molecules. Assuming that the energy difference between vibrational states is proportional to ZPE, as in the case of a harmonic potential, the ratio between the ZPE differences for the three molecular isotopes can be obtained from the experimental results of Schröter *et al*. [4.70]. It is found that ZPE of H-D recombination lies also below the mean value between H-H and D-D ones.

Tentative explanations of the above mentioned anomalies can be given on the basis of the heteronuclear character of the HD molecule. This gives rise to the breakdown of the inversion symmetry and to the appearance of several properties qualitatively different from those of the homonuclear species. A review of the phenomena associated to the inversion symmetry breakdown in HD has been recently done by de Lange *et al.* [4.71]. One of such phenomena is the existence of a permanent dipolar moment in the ground state of the HD molecule. This implies that TS energy of HD could be lowered by the presence of a surface electric field. However, by considering a typical electric field of 10^7 V m^{-1}, the dipolar moment of the HD molecule in the TS should be 6-7 orders of magnitude greater than the corresponding value in the fundamental state in the gas phase (~10^{-3} D [4.72]) if the observed energy shifts are to be explained. Such a value seems to be unreasonable. On the other hand, the breaking of the inversion symmetry also produces the electronic coupling between states of *g* and *u* symmetry and this can lead to the appearance of new states not observed in the homonuclear species. This effect is stronger near the dissociation threshold of the molecule [4.71]. The fact that the anomalies observed in the TS energies are more pronounced in region B, for which the TS energy is closer to the free atoms state, could be related to the former view. Present results should motivate further experiments in order to clarify the origin of these anomalies, such as quantum-state integral measurements (*i.e.*, the analysis of the angular and velocity distributions) and quantum-state resolved experiments (*i.e.*, the analysis of the rotational and vibrational distributions) of the desorbed molecular isotopes.

4.6 References

[4.1] Schalpbach L 1992 in *Hydrogen in Intermetallic Compounds*, vol.II, ed. L. Schalpbach, Springer (Berlin) Ch.2

[4.2] Borgschulte A, Westerwaal R.J., Rector J.H., Schreuders H., Dam B. and Griessen R. *J. Catalysis* **239** (2006) 263

[4.3] Kyung Sub Jung, Dong Hyun Kim, Eun Young Lee and Kyung Sub Lee *Catalysis Today* **120** (2007) 270

[4.4] Sicking G 1984 *J. of the Less Common Metals* **101** 169

[4.5] Lu KE and Rye RR 1974 *Surface Science* **45** 677

[4.6] Bernasek SL and Somorjai GA 1975 *J. Chem. Phys.* **62** 3149

[4.7] Wachs IE and Madix RJ 1976 *Surface Science* **58** 590

[4.8] Salmerón M, Gale RJ and Somorjai GA 1979 *J. Chem. Phys.* **70** 2807

[4.9] Engel T and Kuipers H 1979 *Surface Science* **90** 162

[4.10] Dixon-Warren StJ, Pasteur AT and King DA 1995 *J.Chem. Phys.* **103** 2261

[4.11] Bertino MF and Toennies JP 1999 *J. Chem. Phys.* **110** 9186

[4.12] Hahn P, Bertino MF, Toennies JP, Ritter M and Weiss W 1998 *Surface Science* **412/413** 82

[4.13] Lin TH and Somorjai GA 1984 *J. Chem. Phys.* **81** 704

[4.14] Magnusson J 1987 *Industrial & Engineering Chemistry Research* **26** 877

[4.15] Backman H, Jensén J, Klingstedt F, Wärna J, Salmi T and Murzin DY 2004 *Applied Catalysis A* **273** 303

[4.16] Basallote MG, Bernal S, Gatica JM and Pozo M 2002 *Applied Catalysis A* **232** 39

[4.17] Backman H, Rahkamaa-Tolonen K, Wärna J, Salmi T and Murzin DY 2005 *Chemical Engineering Journal* **107** 89

[4.18] Outka D.A. and Foltz G.W. 1991 *J. Catalysis* **130** 268

[4.19] Foltz GW and Melius CF 1987 *J. Catalysis* **108** 409

[4.20]Andreev B.M. Magomedbekov E.P. 2001 *Separation Science and Technology* **36** 2027

[4.21] Stern A, Kreitzman SR, Resnik A, Shaltiel D and Zevin V 1981 *Solid State Communications* **40** 837

[4.22] Stern A, Resnik A and Shaltiel D 1982 *J. of the Less Comm. Met.* **88** 431

[4.23] Fernández JF, Cuevas F and Sánchez C 2000 *J. of Alloys and Comp.* **298** 244

[4.24] Graham T. *Phil. Trans. Roy. Soc. (London)* **156** (1866) 415

[4.25] Pick MA, Davenport JW, Strongin M and Dienes GJ 1979 *Phys. Rev. Lett.* **43** 286

[4.26] Cuevas F and Hirscher M 2000 *J. Alloys Comp.* **313** 269

[4.27] Hayashi S 2003 *J. of Alloys and Comp.* **359** 281

[4.28] Schöter L, Zacharias H and David R 1989 *Phys. Rev. Lett.* **62** 571

[4.29] Van der Pauw LJ 1958 *Phil. Res. Rep.* **13** 1

[4.30] Ares JR, Leon M, Arozamena NM, Sánchez-Paramo J, Celis P, Ferrer IJ and Sánchez C 1998 *J. Phys.: Condens. Matter* **10** 4281
[4.31] Salvarezza RC, Montemayor MC, Fatas E and Arvia AJ 1991 *J. Electroanal. Chem.* **313** 291
[4.32] Bolzán AE 1995 *J. Electroanal. Chem.* **380** 127
[4.33] Seymour EFW, Cotts RM and Williams WD 1975 *Phys. Rev. Lett.* **35** 165
[4.34] He J-W, Memmert U and Norton PR 1989 *J. Chem. Phys.* **90** 5088
[4.35] Farkas A 1937 *Trans. Farad. Soc.* **33** 552
[4.36] Dandapani B and Fleischmann M 1972 *J. Electroanal. Chem.* **39** 323
[4.37] Azároff LD 1968 *Elements of Crystallography* (International Student Edition; McGraw-Hill) p477
[4.38] Kern A and Eysel W, Mineralogisch-Petrograph 1993 *Inst., Univ. Heidelberg, Germany, ICDD Grant-in-Aid*
[4.39] Wicke E and Brodowski H in '*Hydrogen in Metals II'* Topics in Applied Physics vol 29 ed. G Alefeld and J Völk (Berlin: Springer-Verlag, 1978) pp73-155
[4.40] Felici R, Bertalot L, DeNinno A, LaBarbera A and Violante V 1995 *Rev. Sci. Istrum.* **66** 3344
[4.41] Lewis FA *'The Palladium Hydrogen System'* Academic Press 1967 (London/New York)
[4.42] *CRC Handbook of Chemistry and Physics (82nd edition)* 2001-2002 ed. DR Lide (Boca Raton: CRC Press)
[4.43] McKubre MCH, Crouch-Baker S, Riley M, Rocha-Filho RC, Schreiber M, Smedley SI and Tanzella FL 1991, *Aspects of the Electrochemical Loading of Hydrogen and its Isotopes into Palladium*, presented at ECS mtg. (Phoenix, Arizona)
[4.44] Foiles CL 1980 *Solid State Commun.* **33** 125
[4.45] Szafranski AW 2001 *J. Alloys and Comp.* **316** 82
[4.46] Yoo H-I, Sinn D-S and Hong J-O 1998 *J. Electrochem. Soc.* **145** 1008
[4.47] Stern A, Resnik A and Shaltiel D 1984 *J. Phys. F.: Met. Phys.* **14** 1625
[4.48] Cabrera AL, Morales E and Amor JN 1995 *J. Mater. Res.* **10** 779
[4.49] Berlouis LEA, Hall PJ, MacKinnon AJ, Wark AW, Manuelli D, Gervais V and Robertson JE 1997 *J. Alloys and Comp.* **253/254** 207
[4.50] Läser R and Klatt KH 1983 *Phys. Rev. B* **28** 748
[4.51] Petersson LG, Dannetun HM and Lundström I 1984 *Phys. Rev. Lett.* **52** 1806
[4.52] Urey HC and Rittenberg D 1933 *J. Chem. Phys.* **1** 137
[4.53] Liu Z, Feldmann LC, Tolk LH, Zhang Z, Cohen PI 2006 *Science* **312** 1024
[4.54] Franzen P, Behrisch R, García-Rosales C, Schleussner D, Rösler D, Becker J, Knapp W and Edelmann C 1997 *Nuclear Fusion* **37** 1375
[4.55] Seymour EFW, Cotts RM and Williams WD 1975 *Phys. Rev. Lett.* **35** 165

[4.56] Völk J and Alefeld G 1978 Hydrogen in Metals I *Topics in Applied Physics* vol 28 ed G Alefeld and J Völk (Berlin: Springer-Verlag) pp321-348
[4.57] Lacher JR 1937 Proc. Roy. Soc. (London) A **161** 525
[4.58] Krenn G, Eibl C, Mauritsch W, Hebenstreit ELD, Varga P and Winkler A 2000 *Surface Science* **445** 343
[4.59] Petersson LG, Dannetum H, Fogelberg J and Lundström I 1986 *Appl. Surf. Sci.* **27** 275
[4.60] Castro FJ, Meyer G and Zampieri G 2002 *J. Alloys comp.* **330-332** 612
[4.61] Castro FJ and Meyer G 2002 *J. Alloys and Comp.* **330-332** 59
[4.62] Chen WC and Heuser BJ 2000 *J. Alloys and Comp.* **312** 59
[4.63] Pörschke E, Shaltiel D, Klatt KH and Wenzl H 1986 *J. Phys. Chem. Solids* **47** 1003
[4.64] Shleifman DE, Shaltiel D and Steinberger IT 1995 *J. Alloys and Comp.* **223** 81
[4.65] Herzberg G 1969 *Phys. Rev. Lett.* **23** 1081
[4.66] Liu K 2001 *Annu. Rev. Phys. Chem.* **52** 139
[4.67] Skodje RT and Yang X 2004 *Int. Reviews in Physical Chemistry* **23** 253
[4.68] Ke X and Kramer GJ 2002 *Phys. Rev. B* **66** 184304
[4.69] Herzberg G *Molecular Spectra and Molecular Structure I. Spectra of Diatomic Molecules* (1950, New York: Nostrand Reinhold)
[4.70] Schröter L, Küchenhoff S, David R, Brening W and Zacharias H 1992 *Surface Science* **261** 243
[4.71] De Lange A, Reinhold E and Ubachs W 2002 *Int. Reviews in Physical Chemistry* **21** 257
[4.72] Bradley Nelson J and Tabisz GC 1983 *Phys. Rev. Lett.* **48** 1393

Chapter 5

H/D isotope effects in $LaNi_5$-type metal hydride electrodes

5.1 Introduction

Thermodynamic isotope effects in MH are related to the energy differences of the hydrogen isotopes in the gas phase and in the metal. They are evidenced by different plateau pressures in Pressure-Composition-Isotherms (PCI). Owing to ZPE differences, a lower plateau pressure is expected for the heavier isotope [5.1]. This is denoted as the normal isotope effect. It has been observed, for instance, in V, Nb, and Ta [5.1, 2]. For some metals, such as Pd and Ni, the inverse isotope effect is, however, observed [5.1, 3]. The hydride is more stable that the deuteride. This modification results from the fact that H(D) atoms are located in tetrahedral interstices for the former metals, whereas they occupy octahedral sites for the latter ones. The zero-point vibration energy of hydrogen in tetrahedral sites is higher than that in octahedral ones due to the smaller hole radius of the tetrahedrons. Thermodynamic isotope effects have also been reported for intermetallic compounds. $LaNi_5$ [5.2, 4], $ZrCr_2$ [5.5] and $TiCr_{1.5}V_{1.7}$ [5.6] exhibit a normal behavior whereas TiFe [5.2], TiNi [5.7] and Mg_2Ni [5.2, 8, 9] have an inverse behavior. This is consistent with the location of H(D) atoms in tetrahedral sites for the former compounds and octahedral sites for the latter.

It is worth to say that the use of the terms ‘normal’ and ‘inverse’ referred to the H/D isotope effects in MH is somewhat misleading. Indeed, there are some authors [5.2, 10] who use these terms in the opposite sense to that mentioned in the previous paragraph. These authors argue that absolute entropy of hydrogen gas is lower than that of deuterium gas and, therefore, metal hydrides are expected to be more stable than deuterides. They conclude that the normal isotope effect is that in which the hydride is more stable than the deuteride. However, we will refer

hereafter to the normal isotope effect as that in which the deuteride is more stable than the hydride, as stated in the previous paragraph.

As it was stated in Chapter 1, isotope effects in hydrogenation kinetics arise from ZPE differences in the reactants and at the transition state (TS) of the reaction [5.11, 12], which give place to different activation energies for the hydrogen isotopes. In general, ZPE differences are more pronounced in the reactants than at the TS, which imply faster dynamics for the lighter isotope. However, some anomalies exist. For instance, a higher diffusion coefficient is observed for D than for H in Pd metal [5.1, 13].

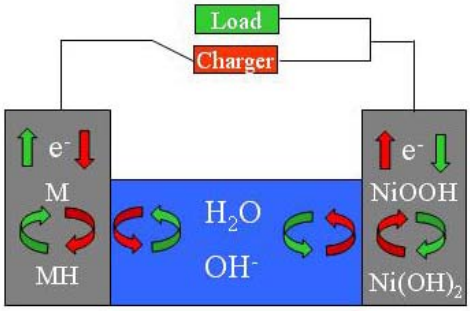

Fig.5.1. Schematic drawing of the charge (red arrows) and discharge (green arrows) reactions of a Ni/MH battery (from [5.14]).

Among the current applications of MH, the most important is their use as negative electrodes in rechargeable Ni-MH batteries [5.14-16]. These batteries were developed in the 1980's as substitutes of Ni-Cd batteries, due to the environmental problems associated to Cd handling and the low availability of this element in ore deposits. The schematic drawing of the cell reactions taking place in a Ni-MH battery upon charging and discharging is shown in Fig.5.1. During the charge, the nickel hydroxide ($Ni(OH)_2$) electrode is oxidized to nickel oxyhydroxide (NiOOH), while the metal (M) electrode is reduced to MH. The reverse processes occur in discharge. Thus, the whole reactions are the H transfer between the $Ni(OH)_2$ and the MH electrode through an alkaline electrolyte acting as a proton conductor.

So far, research on isotope effects in MH electrodes has attracted very little attention, in spite of the fact that structural studies require, in practice, the use of deuterated samples to ascertain the position of hydrogen atoms by neutron diffraction (see [5.17] and references therein). As a matter of fact, electrochemical charging in heavy water seems to be much more sluggish than in normal water, as it has been observed during in-situ neutron diffraction of Ti_2Ni compound [5.18].

As concerns thermodynamics, there are only a few studies on the Pd-H and Pd-D systems in acidic media [5.19-21]. These reports showed that D atoms are relatively more stable than H in the electrolyte than in the deuteride (hydride) phase.

In this chapter, both the thermodynamic and kinetic isotope effects in $LaNi_{4.5}Mn_{0.5}$ and $LaNi_{5.4}$ electrodes are investigated. $LaNi_5$-type electrodes are commonly used in commercial Ni-MH batteries, due to their good hydrogenation properties. Substitutional derivatives of $LaNi_5$ are usually employed to tune its hydrogenation properties by changing the microscopic structure of the alloy. For instance, Ni substitution by Mn facilitates the electrochemical cycling by decreasing the plateau pressure below 1 atm [5.15]. The overstoichiometric $LaNi_{5.4}$ is formed by partial substitution of Ni atoms by Ni dimmers along the *c* axis (see Fig.5.2). This compound presents a plateau pressure above 1 atm, what makes it unsuitable for MH electrode applications. However, it is interesting to compare the H/D isotope effects in this compound with those present in the $LaNi_{4.5}Mn_{0.5}$ alloy.

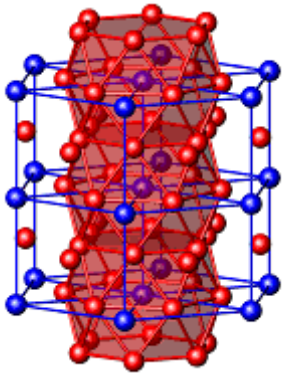

Fig.5.2. Crystallographic structure of the $LaNi_5$ intermetallic compound. Blue and red spheres represent La and Ni atoms, respectively.

The alloys have been characterized by conventional metallurgical methods. PCI diagrams obtained by solid gas reactions have been measured with H_2 and D_2 at two different temperatures in order to evaluate the isotope effects between hydrides and deuterides. The electrochemical behaviour of the samples has also been investigated both in H_2O and D_2O media. The influence of isotopic substitution on the electrochemical isotherms and cycling of the electrodes have been analysed. Thermodynamic isotope effects are discussed on the basis of the Nernst equation whereas kinetic isotope effects are explained by different permeation rates for H and D atoms across electrode surface barriers as well as H/D differences on the charge transfer reaction rate.

5.2 Experimental details

$LaNi_{4.5}Mn_{0.5}$ and $LaNi_{5.4}$ intermetallic compounds have been prepared by melting the pure elements in an induction furnace (Celes GHF 25AP). In order to homogenize the samples they have been annealed under vacuum in a resistance furnace before quenching them. $LaNi_{5.4}$ has been annealed at 1200 ºC during 3 days. Two $LaNi_{4.5}Mn_{0.5}$ alloy ingots have been prepared by induction melting and subsequently annealed at 900 ºC, one for 3 hours and the other for 3 days. We will refer to them hereafter as Mn05A1 and Mn05A2 alloy, respectively.

Alloy composition and structure have been determined by electron probe microanalysis (EMPA) and powder X-Ray diffraction (XRD), respectively. EPMA analyses have been done with a Cameca SX100 apparatus. The XRD patterns have been obtained with Cu K_α radiation in a θ-2θ Bruker D8 Advance diffractometer equipped with backscattered rear graphite monochromator. The determination of the unit cell parameters has been performed by full-pattern refinement of XRD data using Fullprof software [5.22].

Composite electrodes have been made from the powdered intermetallic compound (<63 μm) mixed with carbon black and PTFE in the weight ratio 90:5:5. This mixture was spread out in 0.25 mm thick sheets and compressed (~500 MPa) on Ni grids that were spot welded to Ni wires acting as current collectors. $Ni(OH)_2$ was used as a counter electrode. The capacity and surface area of the counter electrode were chosen to be much larger than that of MH electrode in order to avoid oxygen evolution and the limitation of kinetics by this electrode. One-compartment open plastic electrolytic cells were used. Polyamide insulators were introduced between the working and the counter electrodes. Electrode potentials were monitored against Hg/HgO electrodes (Radiometer Analytical XR430 and XR400) both in normal and heavy water experiments. These electrodes were filled with 1M KOH (H_2O), unless otherwise stated. The potential stability of the reference electrodes was checked 20 times during a period of one month. Variations were found to be within ±1 mV. The scheme of the electrochemical cell is shown in Fig.5.3.

Electrolyte concentrations were 1M, unless otherwise stated. The electrolytes were prepared by dissolving KOH pellets (RP Normapur AR, Prolabo) in deionised water (Milli-Q) and heavy water (>99.6 mol% isotopic purity). D_2O was kindly supplied by the European Organization for Nuclear Research (CERN). The purity of D_2O in regard to ionic impurities has been checked by ICP analysis and electrical conductivity. It contains 1 ppm of potassium. Other impurities are well below the ppm range. The electrical conductivity of D_2O at room temperature was 12.3 μS cm^{-1}. From K^+ and OD^- ionic concentrations, the electrical conductivity is calculated to be 11.0 μS cm^{-1}. This close agreement excludes a significant level of other ionic impurities not detected by ICP. The impurity level for both KOH-H_2O

and KOH-D_2O electrolytes is, therefore, very similar and mostly due to the impurities introduced by the KOH pellets (0.02 % for CO_3 and about 0.1 ppm for each of the following species: Pb, N, Cl, PO_4, SiO_4, Al, Ca, Cu, Fe, Na and Ni). The amount of hydrogen impurity in D_2O coming from KOH pellets and from the discharge of nickel hydroxide electrodes has been estimated to be less than 2 at%.

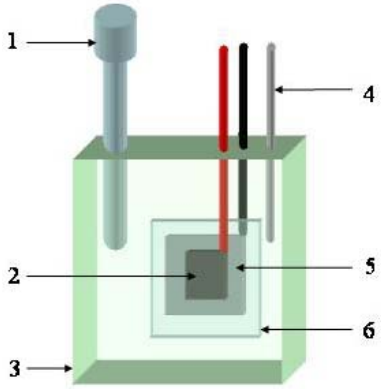

Fig.5.3. Scheme of the electrochemical cell used in the experiments: (1) HgO/Hg reference electrode; (2) MH electrode; (3) PVC cell; (4) Ar line; (5) NiOOH electrode; (6) Polyamide separator.

Electrolytic experiments were galvanostatically controlled by using a Biologic Mac-Pile potentiostat. Electrolytic cells were placed inside a thermostat to maintain the temperature constant within ±0.3 K. The air dissolved in the electrolytes and in the pores of the electrodes was evacuated with a rotatory pump prior to the electrolytic experiments. During the electrolysis Ar was bubbled through the cells to avoid the contamination of the electrolytes with dissolved air species.

PCI curves both with H_2 and D_2 were obtained with Sievert's type apparatus by pressure variation measurements using thermalised and calibrated volumes. About 0.5 g of intermetallic powder was used. The samples were activated by cycling the 5 times before PCI measurements.

5.3 Results

5.3.1 XRD and EMPA characterization

5.3.1.1 Mn05A1 alloy

A Back-scattered electron (BSE) image of Mn05A1 sample is shown in Fig.5.4. Darker zones reveal a higher Mn/Ni atomic ratio, showing that alloy composition is not homogeneous. Mn atoms seem to be preferentially segregated around grain boundaries.

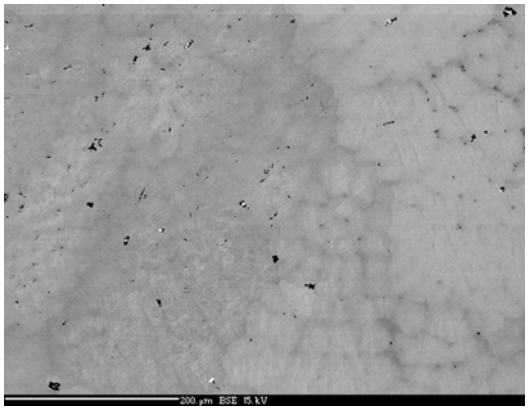

Fig.5.4. BSE image of Mn05A1 alloy. Mn atoms seem to be preferentially segregated around grain boundaries.

Electron Microprobe Analysis (EMPA) confirmed the alloy inhomogeneity. Fig.5.5 displays the concentration profiles of La, Ni and Mn atoms along a line scan. Lanthanum concentration is quite homogeneous, but Ni and Mn exhibit an inhomogeneous profile. It must be noted that the variations of Ni and Mn concentrations are complementary and present periodic trends along the line scan. This periodicity is attributed to the segregation of Mn atoms around grain boundaries. The ratios Ni/La and Mn/La obtained from the average of these measurements are 4.5±0.3 and 0.5±0.2, respectively.

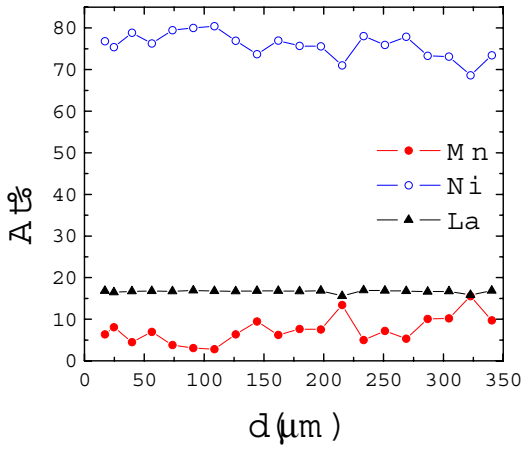

Fig.5.5. EMPA of Mn05A1 alloy along a line scan.

The XRD pattern of Mn05A1 alloy is shown in Fig.5.6. All diffraction peaks are indexed in the hexagonal $CaCu_5$-type structure (*P*6/*mmm* space group). Full pattern refinement yields as lattice parameters *a*=5.048(1) Å and *c*=4.012(1) Å and a unit cell volume of 88.62(1) $Å^3$.

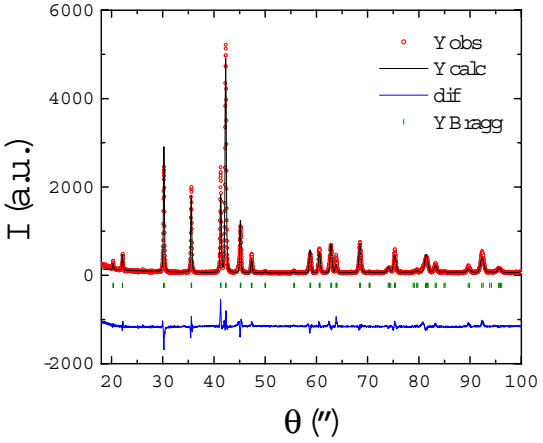

Fig.5.6. Rietveld analysis of the XRD pattern of Mn05A1 alloy.

5.3.1.1.2 Mn05A2 alloy

A BSE image of Mn05A2 alloy is shown in Fig.5.7. As compared to Mn05A1 alloy, this sample presents a more homogeneous aspect. This is due to the higher annealing time applied to Mn05A2 sample. Fig.5.8 shows the concentration profiles of La, Ni and Mn along a line scan. The small dispersion of these profiles confirms the good alloy homogeneity. The ratios Ni/La and Mn/La obtained from this analysis were 4.48±0.05 and 0.52±0.03, respectively.

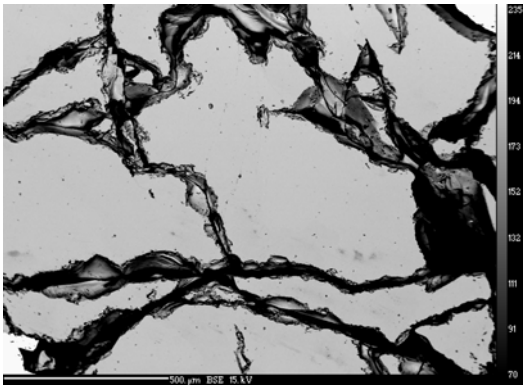

Fig.5.7. BSE image of Mn05A2 alloy.

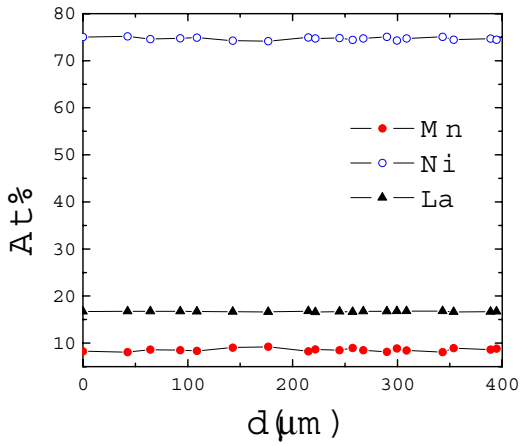

Fig.5.8. EMPA line scan of Mn05A2 alloy.

The XRD pattern of Mn05A2 alloy is shown in Fig.5.9. The alloy is single phase ($CaCu_5$–type structure). The small diffraction peak observed at 27.24º is due to surface alloy contamination from Wood alloy used for EMPA encapsulation. The lattice parameters obtained from the fit of the XRD pattern are a=5.052(1) Å and c=4.021(1) Å and the unit cell volume is 88.86(1) $Å^3$.

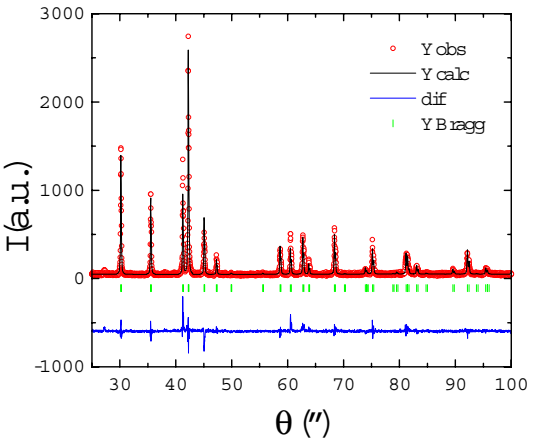

Fig.5.9. Rietveld analysis of the XRD pattern of Mn05A2 alloy.

5.3.1.3 $LaNi_{5.4}$

Fig.5.10 shows a BSE image of $LaNi_{5.4}$ alloy. Small Ni precipitates, appearing in black in this picture, are observed. Small white precipitates are also detected,

corresponding presumably to lanthanum oxide. Different crystallographic orientation of the grains of the $LaNi_5$-phase produces a clear contrast in the number of backscattered electrons, as can be appreciated in this figure.

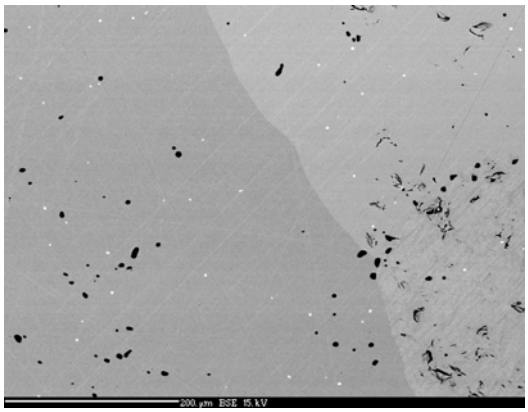

Fig.5.10. BSE image of $LaNi_{5.4}$ alloy. Black and white precipitates correspond presumably to Ni and lanthanum oxide, respectively. The contrast in the background of this picture is due to the different crystallographic orientation of $LaNi_5$-type crystallites.

EPMA of this alloy reveals a good homogeneity (Fig.5.11). The stoichiometry of the alloy has been obtained by averaging 80 measurements in different parts of the sample, giving a Ni/La ratio equal to 5.37±0.04.

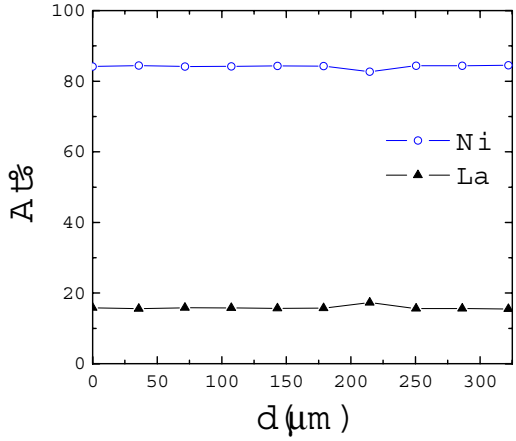

Fig.5.11. EMPA line scan of $LaNi_{5.4}$ alloy.

Fig.5.12 shows a XRD pattern of this alloy. This pattern has been fitted by using two phases: a $TbCu_7$-type structure (*P6/mmm* space group) for the over-stoichiometric $LaNi_{5+x}$ matrix and a Cu-type structure ($Fm\bar{3}m$ space group) corresponding to Ni precipitates. The lattice parameters of the $LaNi_{5+x}$ phase obtained from the fit are a=4.989(1) Å and c=3.998(1) Å and the unit cell volume is 86.182(2) $Å^3$. The measured overstoichiometry is x = 0.37 ±0.04.

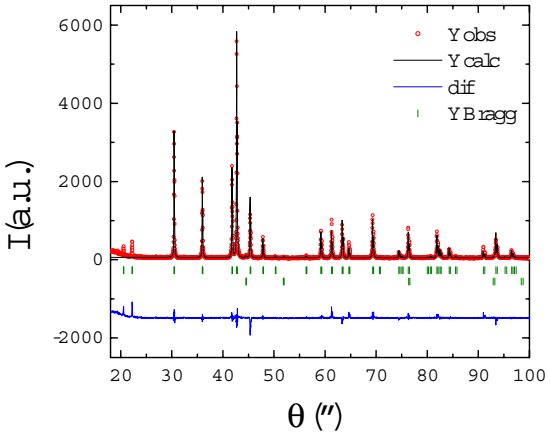

Fig.5.12. Rietveld analysis of the XRD pattern of $LaNi_{5.4}$ alloy.

To summarize, the composition and structural parameters of all studied samples are given in Table 5.1.

Table 5.1: Thermal treatments and characterization of intermetallic compound samples

Sample name	Nominal composition	Annealing treatment	Lattice parameters			Composition(EMPA)	
			a(Å)	*c*($Å^3$)	*V*($Å^3$)	Ni/La	Mn/La
Mn05A1	$LaNi_{4.5}Mn_{0.5}$	900ºC/3h	5.048(1)	4.012(1)	88.62(1)	4.5(3)	0.5(2)
Mn05A2	$LaNi_{4.5}Mn_{0.5}$	900ºC/3d	5.052(1)	4.021(1)	88.86(1)	4.48(5)	0.52(3)
$LaNi_{5.4}$	$LaNi_{5.4}$	1200ºC/3d	4.989(1)	3.998(1)	86.18(1)	5.37(4)	

5.3.2 Pressure-composition isotherms

5.3.2.1 Mn05A1 alloy

Absorption and desorption isotherms were obtained at 313 K with H_2 gas. Results are depicted in Fig.5.13. Both the absorption and desorption curves of the isotherm show sloping plateaux. The desorption equilibrium pressure varies from 0.952 bar at 5.46 hydrogen atoms per unit cell (H/u.c.) down to 0.057 bar at 0.44 H/u.c. Sloping plateaux are characteristic of alloys with inhomogeneous composition. At the light of this result it was preferred to investigate the isotope effects with more

homogeneous samples, because the presence of sloping plateaus would make difficult the comparison between the H_2 and D_2 isotherms.

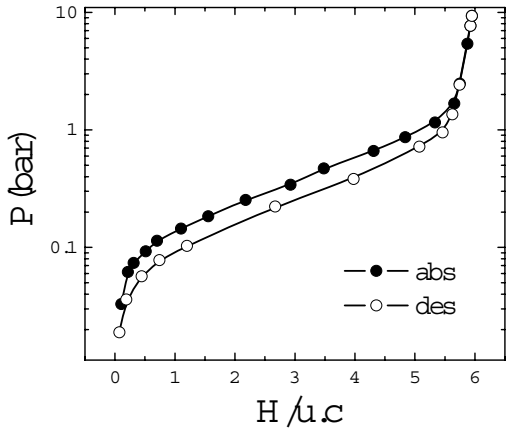

Fig.5.13. Hydrogen absorption and desorption isotherms of Mn05A1 alloy at 313 K.

5.3.2.2 Mn05A2 alloy

Absorption and desorption isotherms by solid gas reactions have been measured with Mn05A2 alloy at 298 K and 313 K both with H_2 and D_2 gases. The isotherms at 313 K and 298 K are depicted in Fig.5.14. Contrary to the case of Mn05A1 alloy, relatively flat plateaux have been obtained. This reflects the fact that Mn05A2 sample has a good homogeneity, as revealed by EMPA and XRD analysis. Equilibrium pressures at 3 H(D)/u.c. are listed in Table 5.2 for absorption (P_{abs}) and desorption (P_{des}) isotherms. The reversible capacities between 0.1 bar and 9 bar at 313 K and between 0.05 bar and 9 bar at 298 K are also given. At 298 K, no significant isotopic differences are appreciated in the plateau pressures. At 313 K, slightly higher plateau pressures are observed for the deuteride than for the hydride. On the other hand, reversible capacities are higher for H than for D at both temperatures indicating an isotope effect in the hydrogen solubility.

Table 5.2. Absorption and desorption plateau pressures at H(D)/u.c.=3 and reversible capacities (*RC*) of Mn05A2 alloy at 298 and 313 K.

	T=298 K		**T=313 K**	
	H_2	**D_2**	**H_2**	**D_2**
***P_{abs}* (bar)**	0.150	0.151	0.339	0.375
***P_{des}* (bar)**	0.077	0.076	0.166	0.199
***RC* (H(D)/u.c.)**	6.11	5.90	5.89	5.76

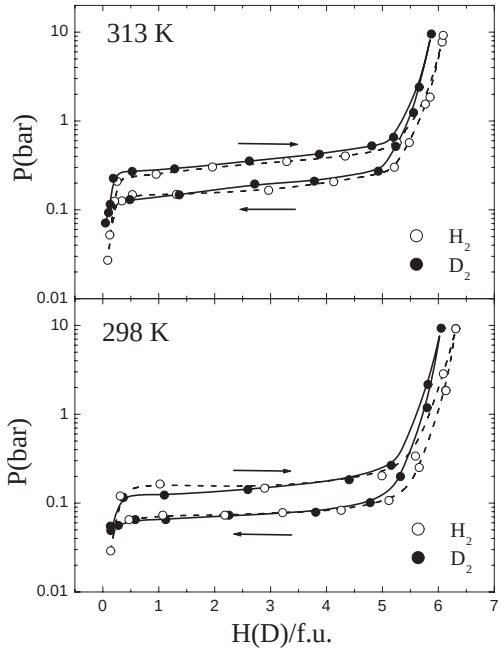

Fig.5.14. Absorption and desorption isotherms of Mn05A2 alloy with H_2 (open circles) and D_2 (full circles) at 313 K (up) and 298 K (bottom).

5.3.2.3 $LaNi_{5.4}$ alloy

Absorption and desorption isotherms of $LaNi_{5.4}$ hydride and deuteride at 298 K and 313 K are depicted in Fig.5.15. These isotherms show a flat plateau pressure in the α-β coexistence region, as for Mn05A2 alloy. Equilibrium pressures at 3 H(D) atoms per unit cell during absorption (P_{abs}) and desorption (P_{des}) isotherms at both temperatures are listed in Table 5.3. Reversible capacities between 1.5 bar and 20 bar are also shown.

Desorption isotherms show higher equilibrium pressures for the hydride than for the deuteride, whereas absorption isotherms exhibit the opposite trend. Therefore, the hysteresis factor between absorption and desorption isotherms is larger for the deuteride than for the hydride. No isotope effects are observed in the reversible capacities within the experimental accuracy.

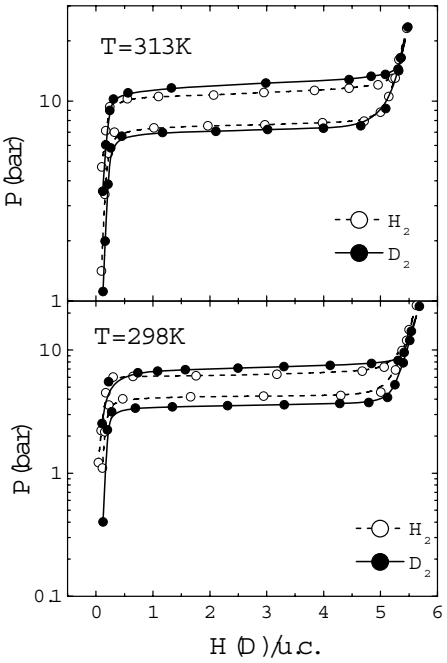

Fig.5.15. Absorption and desorption isotherms of $LaNi_{5.4}$ alloy with H_2 (open circles) and D_2 (full circles) at 313 K (up) and 298 K (bottom).

Table 5.3. Absorption and desorption equilibrium pressures at H(D)/u.c.=3 and reversible capacities (*RC*) of $LaNi_{5.4}$ alloy at 298 K and 313 K.

	T=298 K		**T=313 K**	
	H_2	**D_2**	**H_2**	**D_2**
***P_{abs}* (bar)**	6.33	7.25	11.07	12.36
***P_{des}* (bar)**	4.24	3.59	7.64	7.22
***RC* (H(D)/u.c.)**	5.46	5.47	5.31	5.29

5.3.3 Electrochemical behaviour

5.3.3.1 Mn05A1 electrode

The electrochemical properties of Mn05A1 alloy have been investigated in 5M KOH solution at 313 K, in order to compare desorption isotherms obtained by solid-gas reaction and by electrochemical discharge. The Hg/HgO reference electrode was also filled with 5M KOH in these experiments.

The time evolution of the working electrode potentials during galvanostatic charge and discharge steps are plotted in Figs.5.16 (a) and (b), respectively. Charge

and discharge steps were performed at a high current density: 100 mA g^{-1}. During discharge steps a cut off-voltage equal to –0.7 V versus Hg/HgO reference electrode was imposed to limit oxidation of the working electrode. The particular behaviour of the charging electrode potential in the first cycle is related to the activation process. Surface oxides produce a strong overpotential (*i.e.*, large negative potentials) which is gradually reduced during charging.

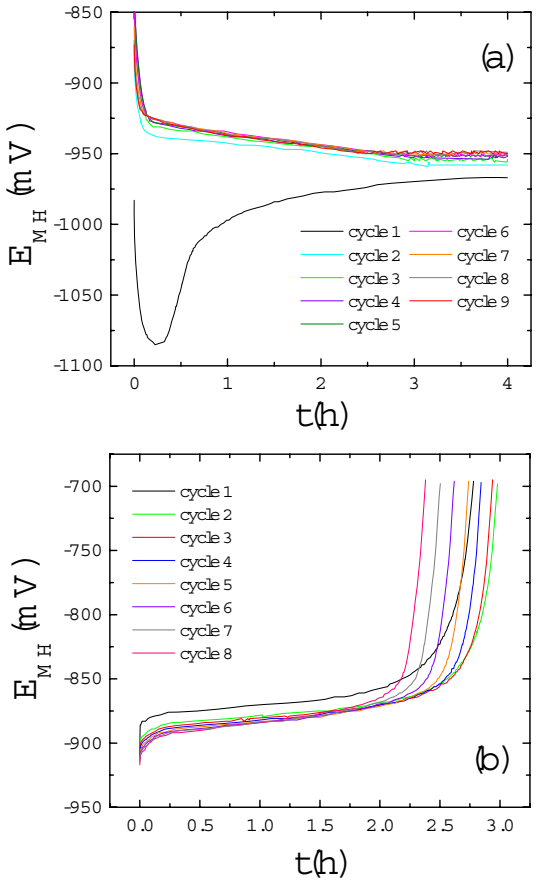

Fig.5.16. Time evolution of the working electrode potential during charge (a) and discharge (b) steps with Mn05A1 electrode at 313 K in 5M KOH.

Current was switched off during 0.5 h between charge and discharge steps to smear hydrogen concentration gradients within the working electrode. The cycling evolutions of the rest potentials after charge and discharge steps are plotted in

Figs.5.17 (a) and (b), respectively. The rest potential after charge steps is quite stable (with exception of the first cycle) and the mean value is -927±1 mV. However, the rest potential after discharge steps exhibit a significant variation with cycle number.

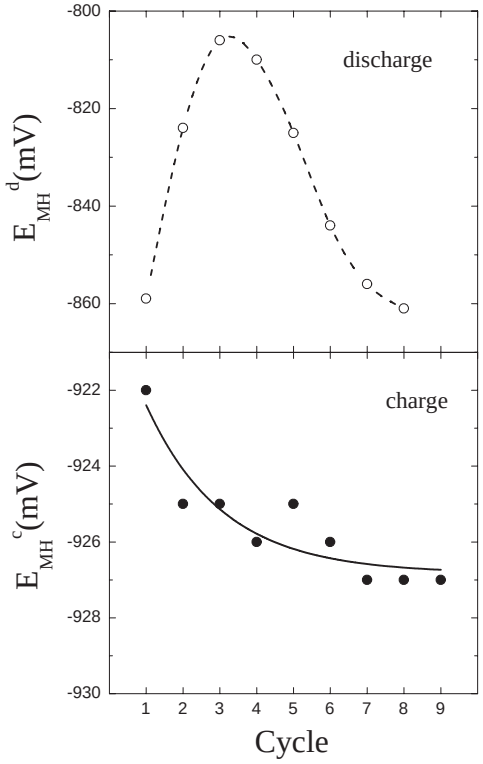

Fig.5.17. Cycling behaviour of the rest potentials of Mn05A1 electrode after discharge (up) and charge (bottom) steps.

Electrode capacities have been calculated by integration of the electrolytic current during discharge steps. The variation of the electrochemical capacity with cycle number is plotted in Fig.5.18. The electrode capacity reaches a maximum in the second cycle and then linearly decreases with cycle number.

After the cycling procedure, an electrochemical potential-composition isotherm at 313 K in 5M KOH was obtained. This was done by measuring the open circuit potential voltage (OCP) during a stepwise discharge process. The electrode was completely charged at 100 mA g^{-1} for 4 h and then discharged by steps of 0.17 h at the same current density. A relaxation time of 1 h was imposed to the electrode between successive steps. Fig.5.19 depicts the electrode equilibrium potential as a

function of discharged capacity. As for the solid-gas isotherm (Fig.5.13), three regions are observed in the electrochemical isotherms in Fig.5.19. The initial potential rise corresponds to H discharge from the hydride phase. Next, a plateau occurs within the two phase coexistence region. Finally, a rise of the electrode potential is observed during H discharge from the solute phase. The electrochemical isotherm shows a sloping plateau, as for the solid-gas isotherm. The equilibrium electrode potential varies between -916 and -893 mV within the plateau region.

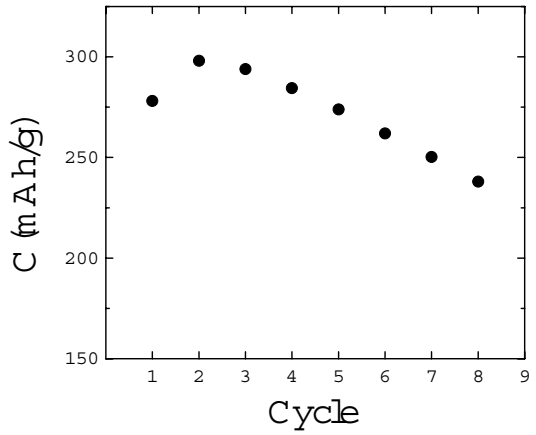

Fig.5.18. Evolution of Mn05A1 capacity with cycle number at 313K in 5M KOH.

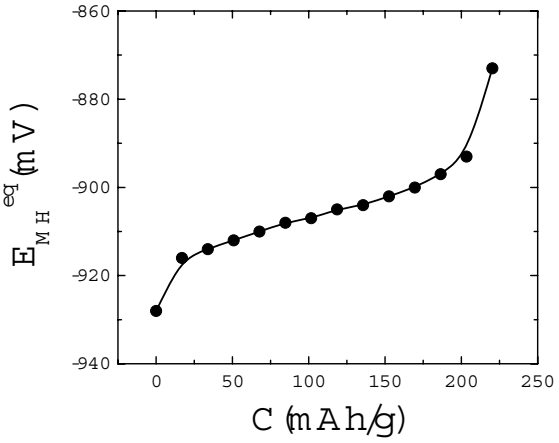

Fig.5.19. Equilibrium electrode potential of Mn05A1electrode in 5M KOH at 313K as a function of discharged capacity.

5.3.3.2 Mn05A2 electrode

The cycling behaviour of Mn05A2 alloy has been investigated in 1M KOH-H_2O and 1M KOH-D_2O electrolytes at 298 K. Two series of experiments for each electrolyte type have been done, in order to test the reproducibility of the measurements. Similar results have been obtained from the two series of experiments. For H_2O, first and second series were performed at current densities of 108 and 117 mA g^{-1}, respectively. For D_2O, the current density was 120 mA g^{-1} for both series. For both electrolytes, the electrolyte loss by drafting of Ar bubbles was compensated in the second series by refilling with the corresponding electrolytes. No refilling was done for the first series. The cut-off voltage and the relaxation time were equal to those used with Mn05A1 electrode.

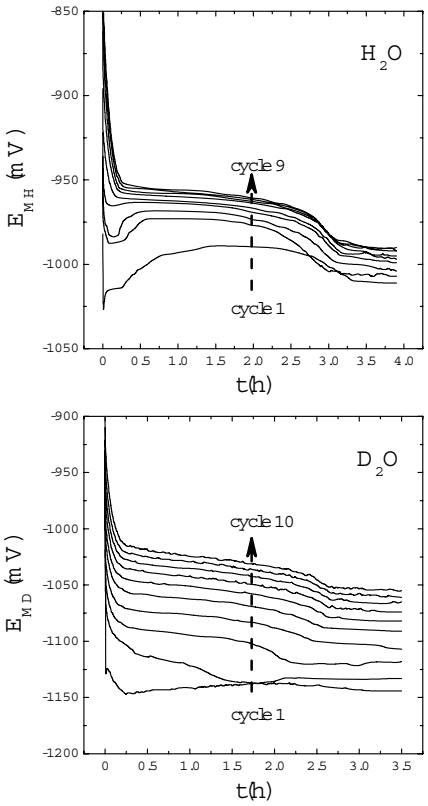

Fig.5.20. Time evolution of electrode potentials during charge steps with Mn05A2 electrodes at 298 K in 1M KOH-H_2O (up) and 1M KOH-D_2O (bottom) electrolytes.

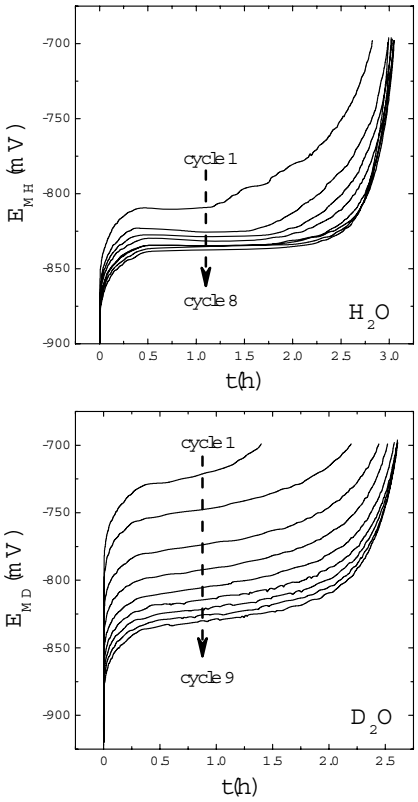

Fig.5.21. Time evolution of electrode potentials during discharge steps with Mn05A2 electrodes at 298 K in 1M KOH-H_2O (up) and 1M KOH-D_2O (bottom) electrolytes.

The time evolutions of electrode potentials during charge steps in H_2O and D_2O media are plotted in Fig.5.20. Within a given charging step, three regions can be distinguished. At short charging time, a minimum is observed. This region is clearly recognized for H_2O-experiments during the first four charging steps. The evolution of the electrode potential in D_2O-electrolytes is different since the minimum is only observed in the first cycle. At medium charging time, a potential plateau occurs due to the coexistence of solid solution and hydride (deuteride) phases. Finally, after a potential kink, a second plateau takes place. This last stage corresponds to the HER (DER) reaction. The potential kink indicating the start of the DER is not clearly observed in the first cycles in D_2O-electrolyte.

For both electrolytes, charging potentials increase on cycling indicating a gradual diminution of the overpotential. The potential curves tend to be stationary after several cycles. When comparing H_2O to D_2O experiments, a strong isotope

effect is observed: electrode potentials are more negative in D_2O medium and require more cycles to stabilize.

The potential time evolution during discharge steps is displayed in Fig.5.21. Discharge occurs through a potential plateau, corresponding to the gradual transformation from the hydride to the solute phase, which tends to stabilize after cycling. Flat plateaux can be observed in H_2O-electrolyte. The potential plateau is short in the first cycles and is followed by a progressive rise of electrode potential. On cycling, the potential plateau widens at the expense of the rising part of the curve. For D_2O-electrolyte, sloping plateaux are observed. The potentials are more positive (*i.e.*, higher overpotentials occur) and more cycles are necessary to reach a stationary behaviour.

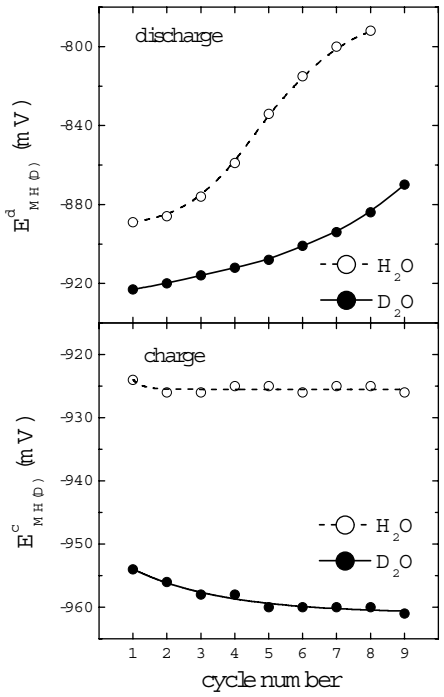

Fig.5.22. Cycling evolution of the relaxation potential of Mn05A2 electrodes after discharge (up) and charge (bottom) steps in 1M KOH-H_2O and 1M KOH-D_2O at 298 K.

Fig.5.22 displays the evolution of the rest potentials on cycling after discharge and charge steps. The rest potentials after discharge steps ($E_{MH(D)}{}^d$) increase on cycling for both electrolytes, the increase being more pronounced for H_2O. The potentials are more negative in D_2O medium. The rest potentials after charge steps

($E_{MH(D)}^{c}$) are stationary except for the first cycles. This effect is more evident in D_2O-electrolyte. A clear isotope effect is observed. Stationary E_{MH}^{c} and E_{MD}^{c} rest potentials are -926±1 mV and -960 ± 1 mV, respectively.

Electrode capacities have been calculated by integration of the discharge current. The evolution of electrode capacities with cycle number in H_2O and D_2O media are plotted in Fig.5.23. Cycling yields an increase of the electrode capacity up to a maximum. This transient period is known as electrode activation. Longer activation period is observed in D_2O. Maximum electrode capacities in H_2O are 4% higher than in D_2O.

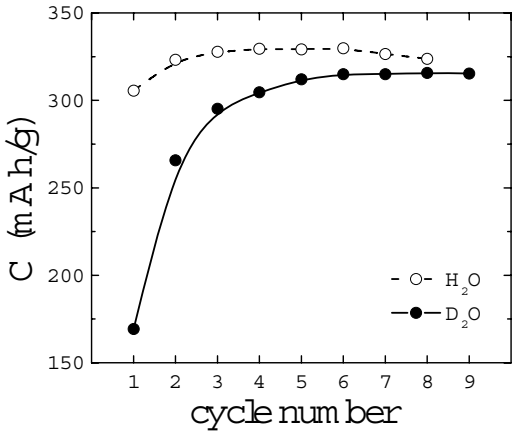

Fig.5.23. Discharge capacity of Mn05A2 electrodes as a function of cycle number in H_2O and D_2O electrolytes at 298 K.

Electrochemical desorption isotherms were measured at 298 and 313 K in 1M KOH-H_2O and 1M KOH-D_2O electrolytes after cycling series. The electrodes were discharged by steps of 0.5 h at a current density of 65 mA g^{-1} at both temperatures. A relaxation time of 1 h was imposed to the electrodes between successive current steps. The equilibrium electrode potentials at both temperatures are plotted in Fig.5.24 versus the discharged capacities.

Nearly constant potentials are observed in the electrochemical isotherms within the plateau region, as for the solid gas isotherms (Fig.5.14). On increasing the temperature, potentials become more negative and discharging capacity decreases. Furthermore, a clear isotope effect in electrode potentials can be observed. Equilibrium electrode potentials are ~33 mV more negative in heavy water than in normal water for both 298 K and 313 K measurements.

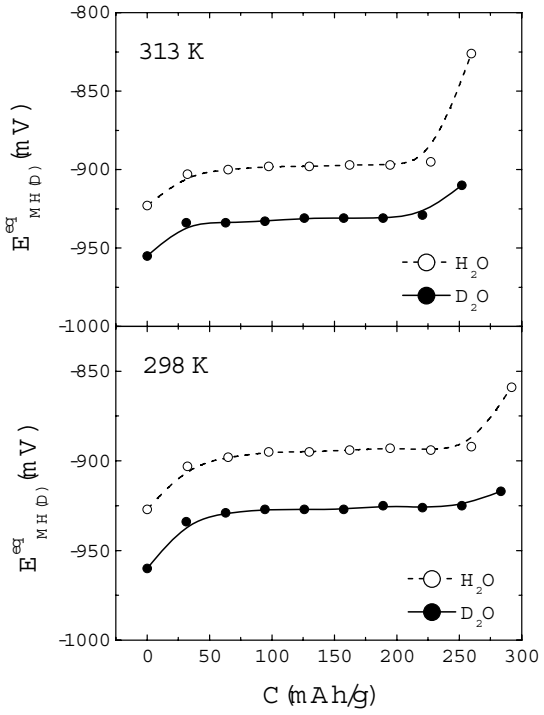

Fig.5.24. Equilibrium electrode potentials of Mn05A2 electrodes as a function of discharged capacities in H_2O and D_2O-electrolytes at 313 K (up) and 298 K (bottom).

5.3.3.3 $LaNi_{5.4}$ electrode

The cycling response of $LaNi_{5.4}$ electrode in 1M KOH-H_2O and 1M KOH-D_2O at 298 K has been investigated. Charge and discharge steps have been performed at 90 mA g^{-1} up to the fourth cycle. Subsequent cycles have been done at 20 mA g^{-1}. During discharge steps a cut off voltage equal to –0.5 V versus Hg/HgO reference electrode has been imposed to the electrodes.

The time evolution of the electrode potentials in H_2O and D_2O electrolytes during charge steps are plotted in Fig.5.25. It can be seen that the lowering of the electrolytic current from 90 to 20 mA g^{-1} has a strong effect on the electrode potentials, both in their shape and their magnitude. For the first charging steps, the electrode potential shows a monotonic behaviour, with a wide plateau at quite negative potentials, characteristic of the HER/DER reaction. This plateau also occurs at lower charging currents, but at much lower potentials. In addition, an initial transient region is observed, corresponding to the H/D absorption reaction within the electrode.

As for Mn05A2 electrode, a gradual diminution of the overpotential is produced on cycling. In addition, a strong isotope effect is observed. The overpotentials are much higher in D_2O than in H_2O electrolytes.

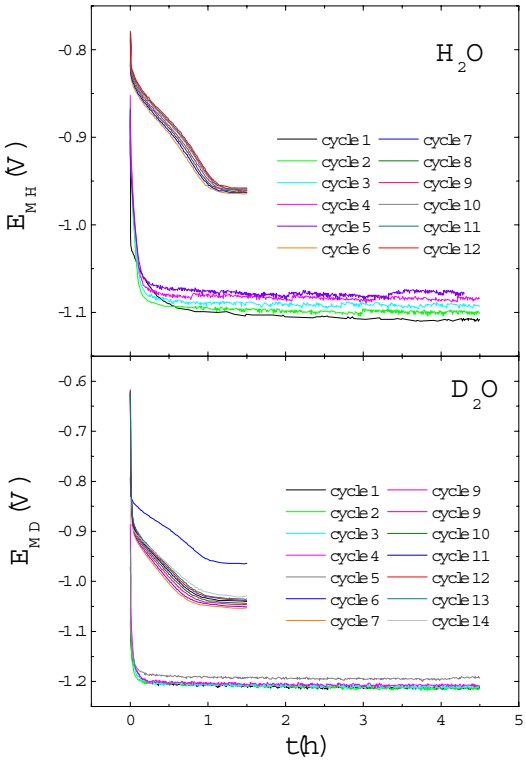

Fig.5.25. Time evolution of electrode potentials during charge steps with $LaNi_{5.4}$ electrodes at 298 K in 1M KOH-H_2O (up)and 1M KOH-D_2O (bottom) electrolytes. Charge steps were performed at 90 mA g^{-1} up to the fourth and fifth cycles in D_2O and H_2O electrolytes, respectively. Subsequent cycles were performed at 20 mA g^{-1}.

Fig.5.26 depicts the time evolution of the electrode potentials on discharge. As for charge steps, a strong effect of the electrolytic current density on the electrode discharge overpotentials is observed. In addition, it can be seen a gradual decrease of overpotentials on cycling, being this effect more pronounced in D_2O electrolytes.

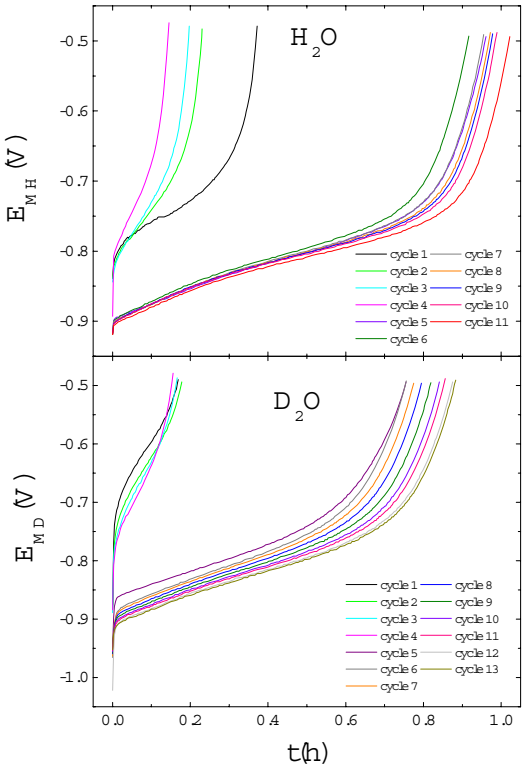

Fig.5.26. Time evolution of electrode potentials during discharge steps with $LaNi_{5.4}$ electrodes at 298 K in 1M KOH-H_2O (up) and 1M KOH-D_2O (bottom) electrolytes. Discharge steps were performed at 90 mA g^{-1} up to the fourth cycle. Subsequent cycles were performed at 20 mA g^{-1}.

The cycling evolution of electrode capacities is plotted in Fig.5.27. This compound shows low electrode capacities in both electrolytes due to the fact that equilibrium plateau pressures are well above 1 atm. Electrode capacities are slightly higher for hydrogen than for deuterium, as in the case of the Mn05A2 electrodes. However, the relative differences are much higher in $LaNi_{5.4}$ electrodes.

The evolution of electrode capacities is not monotonic. After an initial diminution up to the fourth cycle a continuous rise of electrode capacities can be observed. This effect seems to be associated to the diminution of charge / discharge current density imposed in the fourth cycle.

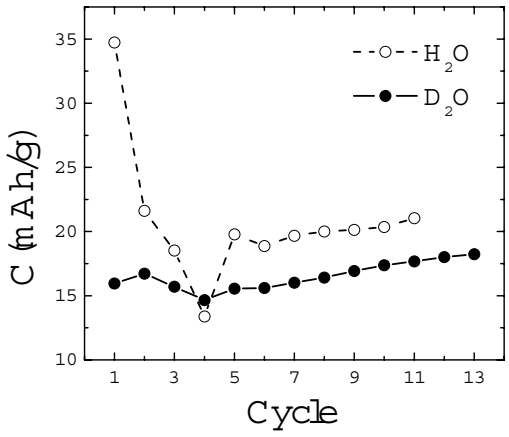

Fig.5.27. Evolution of $LaNi_{5.4}$ electrode capacities with cycle number in 1M KOH-H_2O and 1M KOH-D_2O electrolytes at 298 K.

Electrochemical isotherms at 298 K in both electrolytes were measured after the cycling experiments. The electrodes were charged at 90 mA g^{-1} during 4.5 h and then stepwise discharged for 0.5 h at 3.4 mA g^{-1}. A relaxation time of 1 h was imposed to the electrode between successive steps. The obtained results are plotted in Fig.5.28. Discharged capacities have been normalised to unity for the sake of comparison. As for the electrochemical isotherms obtained with Mn05A2 electrodes, the equilibrium electrode potentials are more negative for the deuterated electrolyte.

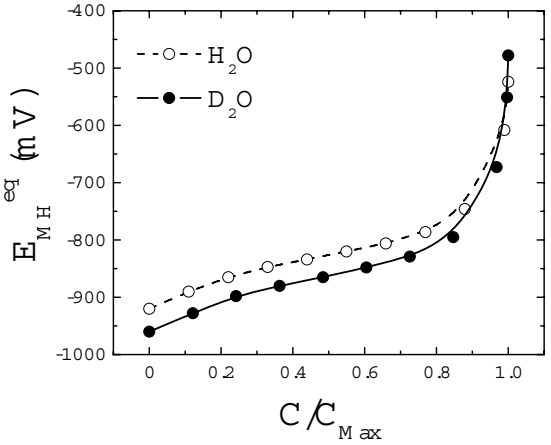

Fig.5.28. Equilibrium electrode potentials of $LaNi_{5.4}$ electrode as a function of normalized discharged capacities in 1M KOH-H_2O and 1M KOH-D_2O electrolytes at 298 K.

5.3.4 Influence of isotope exchange reactions on the electrochemical isotherms

The protium concentration in the deuterated electrolyte coming from the original H concentration in D_2O (<0.4 at%) and from the H atoms in the KOH pellets has been estimated to be less than 2 at%. However, this concentration can increase during the electrolytic experiments due to isotope exchange of the D_2O-electrolyte with the H_2O-electrolyte from the reference electrode, with H atoms from the NiOOH counter electrode or with air moisture. Previous experiments carried out with LiOD electrolytes revealed that the last process is not negligible. The time evolution of the density of a LiOD electrolyte let in contact with the laboratory atmosphere is plotted in Fig.5.29. The decrease of electrolyte density is due to the increment in protium concentration induced by isotope exchange with air moisture. This process depends on the contact surface between the electrolyte and the atmosphere, the ambient humidity and the temperature. From density measurements, the protium mole fraction (χ_H^L) in LiOD after 7 days was estimated to be of about 0.4. The present experiments, however, have been performed under Ar purge. Under these circumstances it is expected that isotope exchange with air moisture should be lower than for the experimental data shown in Fig.5.29.

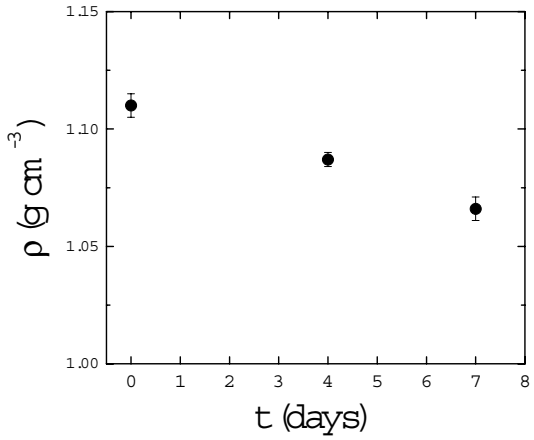

Fig.5.29. Time evolution of the density of LiOD electrolyte in contact with the laboratory atmosphere. The density decrease is due to the increment in protium concentration coming from the isotope exchange between the electrolyte and the air moisture.

In order to evaluate the rise of the H concentration in D_2O-electrolytes during the experiments, electrolyte's densities have been measured before and after the electrolysis. This has been done by weighting known volumes of electrolytes (measured with a Gilson P1000 micropipette) in sealed recipients. The electrolytes

were let to thermally equilibrate with the temperature of the room that was also measured. Each value was taken as the average of 3-5 measurements and in some cases the procedure was repeated different times. Errors were taken as the standard deviation of all measurements and were typically less than ~0.4%. Standards of deionised water (Milli-Q) and of D_2O were used each time to calibrate the experimental procedure. The densities of these standards agreed well with tabulated values at the same temperature, within the experimental accuracy.

Table 5.4. Mean density values (ρ(g cm^{-3})) of 1M KOH-H_2O and 1M KOH-D_2O electrolytes at 295 K before and after electrolytic experiments with Mn05A2 and $LaNi_{5.4}$ electrodes.

	KOH-H_2O	KOH-D_2O	χ_H^L
Before electrolysis	1.042±0.004	1.147±0.004	<0.02
After Mn05A2 series 1	1.051±0.004	1.138±0.004	0.12±0.11
After Mn05A2 series 2	1.050±0.004	1.151±0.002	0.04±0.09
After $LaNi_{5.4}$	1.044±0.004	1.145±0.003	0.04±0.09

Mean density values of 1M KOH-H_2O and 1M KOH-D_2O electrolytes at 295 K before and after electrolysis are listed in Table 5.4. In the cycling experiments with $LaNi_{5.4}$ electrodes and in the second series with Mn05A2 electrodes, the electrolyte loss by drafting of Ar bubbles was compensated by refilling with the corresponding electrolytes. No refilling was made during the first series with Mn05A2 electrodes. A density increase after cycling experiments with Mn05A2 electrodes in H_2O electrolytes can be observed. For $LaNi_{5.4}$ electrodes, the electrolyte does not essentially change its density. This observation seems to be due to the fact that the increment of H_2O electrolyte densities in Mn05A2 experiments can be due to the dissolution of Mn atoms from Mn-containing electrodes in the electrolyte. On the other hand, it is assumed that the D_2O electrolyte density changes are also affected by isotope exchange processes. These processes would tend to decrease the electrolyte density. According to this view, it is expected that the increment in protium concentration should be lowered when refilling the electrolyte and, thus, the density decrease should be smaller, what is coherent with the present results.

In order to estimate χ_H^L from electrolyte's densities, it has been assumed that the increment in protium concentration in the electrolytes comes from isotope exchange with air moisture. As a consequence, the KOH-D_2O electrolyte density after the electrolytic experiments (ρ_{D2O}*) must be related to χ_H^L according to:

$$\rho_{D2O}^{*} = \chi_H^L \rho_{H2O} + \left(1 - \chi_H^L\right)\varepsilon\rho_{D2O} \tag{5.1}$$

where ρ_{D2O} is the original KOH-D_2O density, ρ_{H2O} is the density of pure water and ε is a factor that accounts for the increment of the KOH-D_2O density due to Mn dissolution. This factor has been estimated from the ratio between KOH-H_2O densities after and before electrolysis. Using the density data shown in Table 5.4 one can solve for χ_H^L in equation (5.1). The obtained χ_H^L values are listed in Table 5.4. Inaccuracy in χ_H^L is very large due to the error in density measurements. As KOH-H_2O and KOH-D_2O densities only differ by a ~10%, the accuracy in density measurements (~0.4%) is traduced in a great uncertainty in χ_H^L.

The electrochemical desorption isotherms of Mn05A2 electrodes obtained from both series of experiments have been plotted in Fig.5.30. The measurements in H_2O, with and without refilling, give the same results. However, the equilibrium electrode potentials in D_2O series are slightly different. Electrode potentials of the first series (no refilling) are ~7 mV more positive than those of the second series (refilling), which is attributed to more H content in the electrolyte for the first series. This point will be treated in more detail in section 5.4.1.3.

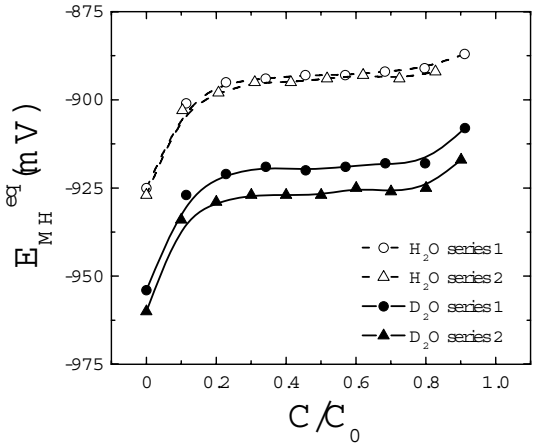

Fig.5.30. Comparison between electrochemical desorption isotherms of Mn05A2 electrodes for the two electrolytes and the two series of experiments. For comparison purposes, equilibrium electrode potentials have been plotted as a function of discharged capacities normalized to the maximum values.

5.4 Discussion

5.4.1 Equivalence between electrochemical and solid-gas isotherms

In this section, the equivalence between electrochemical and solid gas isotherms will be analyzed. Special attention will be paid to the isotope effects obtained with

Mn05A2 electrodes. Equilibrium electrode potentials obtained from electrochemical isotherms have been found to be lower in D_2O than in H_2O media. No significant isotope effect has been found, however, in solid-gas PCI curves of Mn05A2 alloy. To understand the observed isotope effect in electrolytic medium, one must focus on the Nernst equation.

5.4.1.1 The Nernst equation

The Nernst equation establishes the relationship between the electrode potential at equilibrium ($E_{MH(D)}^{eq}$) and the equivalent hydrogen (deuterium) pressure in solid-gas reaction ($P_{H2(D2)}$). Under the present experimental conditions, the fugacity equals the hydrogen (deuterium) pressure and the Nernst equation is [5.14, 23]:

$$\ln P_{H_2(D_2)} = -\frac{2F}{RT}\left[E_{MH(D)}^{eq} - \left(E_{H(D)}^{0} - E_{HgO/Hg}^{0}\right)\right] + \ln a_{H(D)_2O} \tag{5.2}$$

where $E_{H(D)}^{0}$ and $E_{HgO/Hg}^{0}$ are the standard electrode potentials of the H_2O/H_2 (D_2O/D_2) and the HgO/Hg couples, respectively, $a_{H(D)2O}$ is the electrolyte activity, F is the Faraday's constant, R is the gas constant and T is the absolute temperature. According to equation (5.2), differences in the equilibrium potential between H_2O and D_2O media can arise from differences between H_2 and D_2 equilibrium pressures, E_H^0 and E_D^0 potentials or H_2O and D_2O activities.

E_H^0-$E_{HgO/Hg}^0$ potentials and electrolyte activity in KOH-H_2O solutions are reported in the literature [5.23, 24]. When considering non standard conditions, they depend on electrolyte concentration and temperature as follows:

$$E_H^0 - E_{HgO/Hg}^0 = -1.18041 + \left(4.4666 \cdot 10^{-3} - 6.93606 \cdot 10^{-4} \ln T\right) \cdot T + 1.0788 \cdot 10^{-6} T^2 - 4.512 \cdot 10^{-10} T^3 + \frac{5.232}{T} \tag{5.3}$$

$$\ln a_{H_2O} = -0.05181m + 0.003302m^2 + \frac{3.178m - 2.131m^2}{T} \tag{5.4}$$

where m is the electrolyte concentration in mol/kg, which is related to the electrolyte concentration in mol/l (M) according to [5.25]:

$$m = 0.0022 + 0.9984M + 0.0092M^2 + 0.00114M^3 \quad (1 \le M \le 8) \tag{5.5}$$

As concerns deuterated electrolytes, Wakao and Yonemura have estimated the equivalent deuterium pressure from the equilibrium electrode potentials in alkaline medium [5.26]. However, numerical values of E_D^0-$E_{HgO/Hg}^0$ and KOD-D_2O activity have not been reported. To circumvent this difficulty, it has been adopted an alternative empirical method. It has been hypothesized that the electrode rest potentials after complete charging ($E_{MH(D)}^c$) in an open electrolytic cell correspond to an equivalent pressure ($P_{H2(D2)}$) of 1 atm. Thus, the rest potential equals the e.m.f. of the cells:

$$H_2(1atm)\,|\,1M\ KOH\ (H_2O)\,|\,HgO\,|\,Hg \tag{5.6}$$

and

$$D_2(1atm)\,|\,1M\ KOH\ (D_2O\,|\,H_2O)\,|\,HgO\,|\,Hg \tag{5.7}$$

The H_2O/D_2O interphase appearing in equation (5.7) accounts for the filling of Hg/HgO reference electrode with 1M KOH-H_2O electrolyte.

If we use now the present hypothesis, the Nernst equation (equation (5.2)) is modified as:

$$\ln P_{H_2(D_2)} = -\frac{2F}{RT}\left(E_{MH(D)}^{eq} - E_{MH(D)}^{c}\right) \tag{5.8}$$

By combining Eqs.5.2 and 5.8, the following relation is easily derived:

$$E_{MH(D)}^{c} = \left(E_{H(D)}^{0} - E_{HgO/Hg}^{0}\right) + \frac{RT}{2F}\ln a_{H(D)_2O} \tag{5.9}$$

E_{MH}^c potentials calculated from Eqs.5.3-5.5 and 5.9 are listed in Table 5.5 for various electrolyte concentrations and temperatures. The measured E_{MH}^c potentials of the activated electrodes are also shown. A good agreement is found between the experimental and calculated values. This validates the initial hypothesis for light water experiments, so we can confidently extend the present approach to heavy water ones.

The equilibrium E_{MH}^c potentials obtained from the numerical values appearing in the Nernst equation reported by other authors are also listed in Table 5.5 for the sake of comparison. According to those values, it can be seen that there is some lack of rigour when using the Nernst equation. In some cases, there is a good accordance between the values calculated from equation (5.9) and those reported in previous works. However, significant differences are observed in other cases. Due to the fact that the Nernst equation relates the electrode potential to the logarithm

of the equivalent pressure, small deviations in the numerical E_{MH}^{c} values used in the Nernst equation can produce great deviations in the calculated pressures. The non-proper use of the Nernst equation may be the reason to obtain different equilibrium pressures from electrochemical and solid-gas methods, as it is sometimes observed.

Table 5.5. Calculated E_{MH}^{c} values at different electrolyte concentrations and temperatures. The experimental values obtained in the present work as well as those reported by other authors are also listed.

Electrolyte	T(K)	E_{MH}^{0} (mV) calculated	E_{MH}^{0} (mV) experimental/reported
1M KOH	293	-927.5	
	298	-926.1	-926(1) [This work]
	303	-924.7	
	313	-921.9	-922(1) [This work]
5M KOH	293	-931.2	
	298	-929.8	-930.1 [5.27]
	303	-928.4	
	313	-925.7	-927(1) [This work]
5.5M KOH	293	-931.8	
	298	-930.4	
	303	-929.0	-932.4 [5.28]
	313	-926.3	
6M KOH	293	-932.5	
	298	-931.1	-931 [5.29] -930/-923 [5.30] -926 [5.31]
	303	-929.7	-929.6 [5.32]
	313	-927.0	

The advantage of using the modified Nernst equation (equation (5.8)) is that E_{MH}^{c} is a measurable variable (*i.e.,* the rest potential after complete electrode charging), whereas the parameters appearing in the Nernst equation (equation (5.2)) must be calculated by using equations (5.3)-(5.5). In practice, these parameters are sensitive to unwanted experimental perturbations, such as the oxygen dissolved in the electrolyte or the change of electrolyte concentration due to evaporation. Moreover, the present approach can be used when electrolyte activity or standard potentials of working and reference electrodes are unknown, as for D_2O electrolytes or H_2O-D_2O mixtures.

For a proper use of the modified Nerst equation the $E_{MH(D)}^{c}$ potential should satisfy two conditions: (i) it should be measured with a well-activated electrode and

(ii) it should be stable with time. During the first charging steps of the samples, $E_{MH(D)}^{c}$ potentials are not stationary due to incomplete electrode charging (see Figs.5.17 and 5.22). This results in an equivalent hydrogen pressure lower than 1 atm. On the other hand, the time stability of $E_{MH(D)}^{c}$ potentials during relaxation was good. In fact, investigations on the self-discharge behavior of AB_5-type hydride electrodes show that diminution of their H content is only significant at long relaxation times (some tens of hours) [5.33].

The modified Nernst equation (equation (5.8)) results from an experimental approach that allows determining the $H_2(D_2)$ equivalent pressure from the difference between the electrode equilibrium potential and a reversible hydrogen (deuterium) electrode (RHE(RDE)) which is immersed in the same electrolyte. The rest potential after complete charging have been used to calculate the electrode potential *vs.* the RHE(RDE). In practice, Flanagan and Lewis used this concept to determine the electrode potentials of the Pd-H [5.19] and Pd-D [5.20] systems. They measured the equilibrium potentials of PdH_x and PdD_x in acidic media at 298 K versus RHE and RDE reference electrodes, respectively. The equivalent H_2 and D_2 pressures calculated from electrode potentials reproduced the values obtained by solid-gas measurements.

5.4.1.2 Equivalent equilibrium pressures

The pressure-composition isotherms of the Mn05A1, Mn05A2 and $LaNi_{5.4}$ electrodes have been calculated from the electrochemical isotherms by using the modified Nernst equation (equation (5.8)).

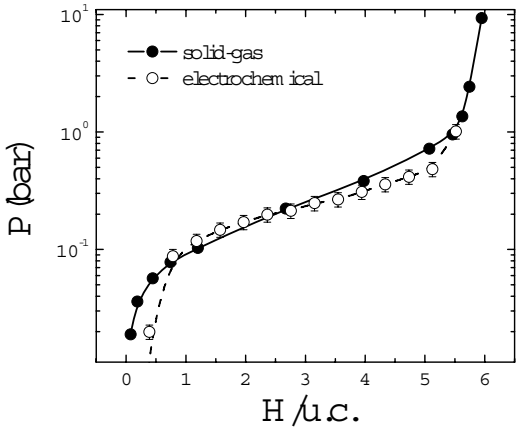

Fig.5.31. Comparison between electrochemical and solid gas isotherms of Mn05A1 alloy at 313 K.

The obtained equilibrium pressures for the Mn05A1 electrode are plotted in Fig.5.31 together with the solid-gas isotherms in order to compare both results. To convert electrochemical capacities into H(D)/u.c. units, it has been considered that the electrochemical capacities at an equivalent pressure of 1 atm (1.013 bar) correspond to those measured by solid-gas reaction. Electrochemical and solid-gas isotherms yield alike plateau pressures at H/u.c.=3. However, the electrochemical isotherm shows a slower slope in the plateau region. This may be tentatively attributed to long-range inhomogeneities within the sample. In addition, significant differences at low hydrogen concentrations are observed. Such differences can be due to electrode corrosion processes during electrochemical measurement. The high electrolyte concentration (5M KOH) and the relatively high temperature (313 K) favour the electrode corrosion. This is clearly manifested in the tendency of the electrode capacity as a function of cycle number (Fig.5.18).

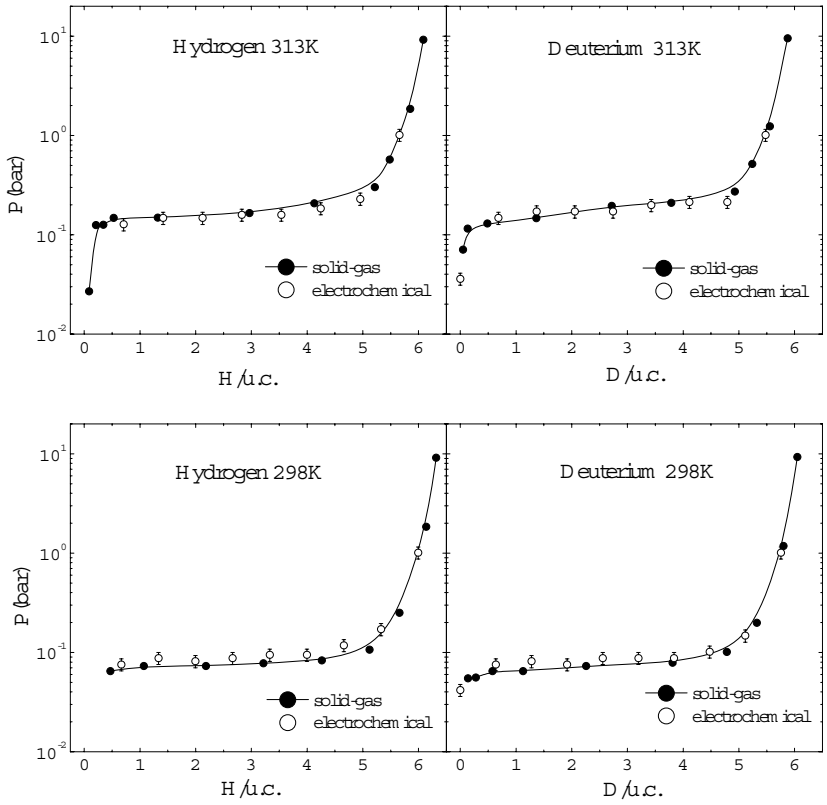

Fig.5.32. Comparison between hydrogen and deuterium electrochemical and solid-gas isotherms of Mn05A2 alloy at 313 and 298K.

Fig.5.32 shows the equivalent H_2 and D_2 pressures of Mn05A2 electrodes in H_2O and D_2O media at 298 K and 313 K after applying equation (5.8), together with the desorption isotherms measured by solid-gas reaction. The electrochemical isotherms agree with those obtained by solid-gas reaction and confirm that no significant isotope effect occurs regarding the thermodynamic stability of the metal hydride. The fair agreement between the solid-gas and the electrochemical isotherms obtained in D_2O media confirms the validity of the experimental approach used to calculate the equivalent pressures.

The equivalent H_2 and D_2 pressures obtained from the electrochemical isotherms of $LaNi_{5.4}$ electrodes at 298 K are shown in Fig.5.33. The amounts of hydrogen and deuterium absorbed within the electrode have been normalized to unity. Equilibrium pressures are slightly higher for hydrogen than for deuterium. This result is qualitatively similar to that obtained from the desorption isotherms measurements by solid-gas reactions at the same temperature (Fig.5.15). Unfortunately, no quantitative results could be obtained for the solid-gas isotherms in the same pressure region of the electrochemical ones, due to the experimental limitations to measure at low equilibrium pressures. Therefore, the quantitative comparison between the solid-gas and the electrochemical isotherms is not possible in this sample.

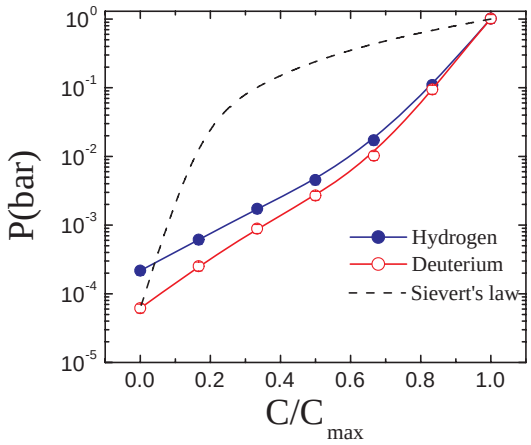

Fig.5.33. Hydrogen and deuterium equilibrium pressures as a function of normalised electrode capacities. The line predicted by Sievert's law is also plotted for comparison purposes.

On the other hand, it is worth to note that the equilibrium pressures shown in Fig.5.33 do not obey the Sievert's law, despite the electrochemical desorption isotherms correspond to the α-region. This can be due to two different processes.

Firstly, the H and D trapping effects in the $LaNi_{5.4}$ electrodes can affect to the calculated capacities and, therefore, to the shape of the pressure-composition isotherms. Secondly, the measured electrode potentials could be affected by electrode oxidation processes. The cut off potential imposed to the electrodes in these experiments (-0.5 V) are appreciably more positive than the redox potential of Ni hydroxide formation (-0.818 V *vs.* Hg/HgO reference electrode in H_2O [5.34]). In fact, the open circuit electrode potentials during electrochemical isotherms measurements were not very stable, mainly at the higher electrode potentials (i.e., the lower equivalent pressures). This is indicative of some dynamic process taking place at the electrode surface, such as electrode oxidation.

5.4.1.3 Isotope effects in the equilibrium potentials

It is interesting to analyze the observed isotope effects in the rest electrode potentials. E_{MD}^{c} potential is more negative than E_{MH}^{c} one in electrolytic experiments. In addition, the results shown in Fig.5.30 imply that the rest electrode potential after charge steps depends on the H mole fraction in the electrolyte. E_{MD}^{c} values obtained during cycling experiments with D_2O electrolytes were -954±1 mV and -960±1 mV in the first and second series, respectively. The corresponding values with H_2O electrolytes were -926±1 and -927±1 mV. The observed shift of E_{MD}^{c} values towards more positive values concurs with the increment in the protium concentration in D_2O electrolytes, as evidenced from electrolyte density measurements.

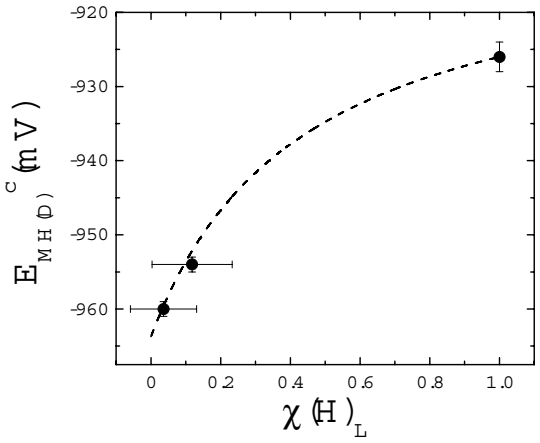

Fig.5.34. Electrode rest potentials after charge steps as a function of the protium molar fraction in the electrolyte. The dashed line corresponds to the fit of the experimental points according to equation (5.12).

Fig.5.34 displays $E_{MH/D}{}^{c}$ values as a function of the protium mole fraction in the electrolyte. In order to explain the observed relationship between $E_{MH/D}{}^{c}$ and $\chi_H{}^{L}$, it has been assumed that there is a linear dependence of $E_{MH/D}{}^{c}$ on the H mole fraction in the metal hydride ($\chi_H{}^{M}$):

$$E^c_{MH/D} = \chi^M_H E^c_{MH} + \left(1-\chi^M_H\right)E^c_{MD} \tag{5.10}$$

The H mole fraction in the metal hydride can be related to the corresponding mole fraction in the electrolyte through the H/D separation factor between the electrolyte and the metal hydride ($S_L{}^{M}$):

$$\frac{\chi^M_H}{1-\chi^M_H} = S^M_L \frac{\chi^L_H}{1-\chi^L_H} \tag{5.11}$$

By combining Eqs.5.10 and 5.11, the following relation between equilibrium electrode potential and H molar fraction in the electrolyte is derived:

$$E^c_{MH/D} = E^c_{MH} + \left(E^c_{MH} - E^c_{MD}\right)\frac{\dfrac{\chi^L_H}{1-\chi^L_H}S^M_L}{1-\dfrac{\chi^L_H}{1-\chi^L_H}S^M_L} \tag{5.12}$$

In order to fit the experimental data shown in Fig.5.34 to equation (5.12), $E_{MH}{}^{c}$ has been taken as -926 mV. On the other hand, the separation factor between H and D in the electrolyte and in the metal hydride can be obtained from the separation factors between the electrolyte and the gas ($S_L{}^{G}$) and between the gas and the metal hydride ($S_G{}^{M}$):

$$S^M_L = S^G_L \cdot S^M_G \tag{5.13}$$

From the H_2 and D_2 equilibrium pressures obtained by solid-gas reactions it is deduced that the last quantity must be approximately equal to 1. The equilibrium separation factor between the electrolyte and the gas phase can be calculated from the partition functions of hydrogen and water molecular isotopes in the gas phase and the H_2O and D_2O vapour pressures [5.35]. In the region of high deuterium concentration in the electrolyte, $S_L{}^{G}$ is approximately equal to 3.3. Therefore, there is only one fitting parameter, the electrode potential of the metal deuteride. By fitting the experimental points with this equation (red line in Fig.5.34), the obtained potential of the deuteride electrode at full charge is equal to -964 mV. This

potential is 38 mV more negative than that of the hydride. This isotope effect implies that deuterium is more stable than hydrogen in the electrolyte than in the gas phase. This is consistent with S_L^M value, which is higher than 1. On the other hand, according to equation (5.9), lower potential in D_2O than in H_2O has to be attributed to differences between E^0_H and E^0_D potentials and/or H_2O and D_2O activities.

Isotope effects on the rest potentials in acidic media have also been reported. For instance, the difference between the e.m.f. of the cells:

$$H_2(1atm) \,|\, HCl\ (H_2O) \,|\, AgCl \,|\, Ag \tag{5.14}$$

and

$$D_2(1atm) \,|\, DCl\ (D_2O) \,|\, AgCl \,|\, Ag \tag{5.15}$$

has been investigated by Noonan and La Mer [5.36] and Wu *et al*. [5.37]. They found a potential difference of 4.47 mV and 9.87 mV, respectively. This discrepancy may be related either to different experimental conditions (H_2(D_2) pressure and electrolyte activity) or to a different level of impurities in their D_2O-electrolytes. In any case, their results agree reasonably well with the calculations performed by McIntyre and Salomon for the potential difference in this electrochemical cell: 5.828 mV [5.38]. The same authors also calculated the e.m.f. difference between the H_2O/H_2 and D_2O/D_2 couples for standard alkaline electrolytes, obtaining a value of about 58 mV at 298 K. The higher e.m.f. difference for alkaline as compared to acidic media concurs with the strong isotope effect on the rest potentials found in the present investigation.

A non-linear relation between the equilibrium electrode potentials and the H molar fraction in the electrolyte was also obtained by Noonan and La Mer [5.36] in acidic media. However, the shape of that curve was different to that predicted by equation (5.12), showing a maximum around χ_H^L=0.7. It is worth to note that other physicochemical properties of aqueous electrolytes (such as the electrical conductivity [5.39, 40] or the rate constants and the Tafel slopes during the HER/DER with Hg drop electrodes [5.41]) also present non-linear behaviours when varying the relative content of hydrogen and deuterium.

5.4.2 Electrochemical cycling

For understanding the cycling behaviour, one should consider the hydrogenation mechanism in electrolytic media. Electrochemical hydrogenation can be resumed in three sequential steps:

i) The charge transfer reaction at the electrode surface:

$$M + H_2O + e^- \rightarrow MH_{ads} + OH^- \quad (5.16)$$

ii) Three near-surface processes in competition:

a) Lattice incorporation of adsorbed hydrogen:

$$MH_{ads} \rightarrow MH_{ss} \quad (5.17a)$$

b) Recombinative desorption:

$$2MH_{ads} \rightarrow 2M + H_2\,(g) \quad (5.17b)$$

c) Electrochemical desorption:

$$MH_{ads} + H_2O + e^- \rightarrow M + H_2\,(g) + OH^- \quad (5.17c)$$

iii) Hydride formation in the electrode bulk:

$$MH_{ss} \rightarrow MH_{hyd} \quad (5.18)$$

where H_{ads} stands for H atoms adsorbed on the surface and H_{ss} and H_{hyd} represent H atoms absorbed in the electrode as solid solution and hydride phases, respectively. Discharge of the electrodes takes place through the reverse reactions of Eqs.5.18, 5.17a and 5.16. These equations also hold for the electrochemical deuteration.

As concerns the electrode potential during dynamic experiments, it can be described as:

$$E_{MH(D)} = E^{eq}_{MH(D)} + \eta \quad (5.19)$$

where $E_{MH(D)}{}^{eq}$ represents the equilibrium potential of the electrode (which depends on the hydrogen content) and η is the overpotential. During electrochemical H(D) charging and discharging, η comprises the charge transfer overpotential at the electrode surface (η_e) and the mass-transfer overpotential (η_m) across the surface and within the bulk of the electrode :

$$\eta = \eta_e + \eta_m = \eta_e + \eta_{ms} + \eta_{mb} \quad (5.20)$$

where η_e relates to equation (5.16), η_{ms} (near-surface permeation overpotential) relates to equation (5.17a) and η_{mb} (bulk diffusion overpotential) relates to equation (5.18).

During the HER(DER) reaction, the overpotential can be expressed as:

$$\eta = \eta_e + \eta_d \tag{5.21}$$

where η_d is the near-surface overpotential associated either to recombinative or electrochemical desorption reactions (equations (5.17b) or (5.17c), respectively), depending on the mechanism of the HER(DER) reaction.

The evolution of the charge and discharge overpotentials as well as that of the HER(DER) reaction upon cycling has been analyzed. The evaluation of these overpotentials is now explained. According to equation (5.19), the overpotential can be obtained from the difference between the dynamic and equilibrium potentials. In order to obtain a representative overpotential for each electrochemical cycle, the equilibrium discharge potentials (obtained from the electrochemical isotherms) have been subtracted from the dynamic discharge potentials at the middle of the plateau region. The same procedure was used to evaluate the charge overpotential. To accomplish this task, the equilibrium charge potentials had to be calculated from the PCI absorption curve using the modified Nernst equation. As for the HER(DER) overpotential, they have been obtained by subtracting the $E_{MH(D)}^{c}$ potential from the dynamic charge potential at the end of charge steps. The values of the equilibrium potentials in charge, discharge and HER(DER) reactions used to calculate the corresponding overpotentials are summarized in Table 5.6.

Table 5.6. Equilibrium potentials of Mn05A1 and Mn05A2 electrodes used to calculate the charge, discharge and HER/DER overpotentials.

		Mn05A1	**Mn05A2**	
		5M KOH-H_2O	1M KOH-H_2O	1M KOH-D_2O
$E_{MH(D)}^{eq}$ (mV)	charge	-913	-902	-936
	discharge	-908	-893	-926
$E_{MH(D)}^{c}$ (mV)		-927	-926	-960

5.4.2.1 Mn05A1 electrodes

The cycling evolution of charge, discharge and HER overpotentials of Mn05A1 electrodes are displayed in Fig.5.35. It can be seen that all the three overpotentials decrease on cycling. This is mainly attributed to the diminution of the charge transfer overpotential as a result of the activation of the electrode surface. Native oxides are formed at the electrode surface due to air exposure during its preparation. On electrochemical cycling, mechanical stresses induced by hydride formation and decomposition lead to defect generation and grain pulverisation. Overpotentials associated to defect generation are evaluated from the plateau pressure measurements reported by Joubert *et al.* [5.42] to be 5 mV at the maximum for $LaNi_{5-x}Mn_x$ alloys (x = 0.4 and 1). Therefore, their contribution to

the measured overpotential is, in practice, negligible. On the other hand, grain pulverisation increases the actual surface area of the electrode. Moreover, fresh surfaces are corroded by potassium hydroxide, yielding the formation of $La(OH)_3$ needles and Ni clusters at the electrode surface [5.43]. Ni clusters are known to have a high electrocatalytic activity for the charge transfer reaction (equation (5.16)). Ni clusters as well as the diminution of the electrolytic current density by the increment of the electrode surface on cycling account for the gradual diminution of the charge transfer overpotential.

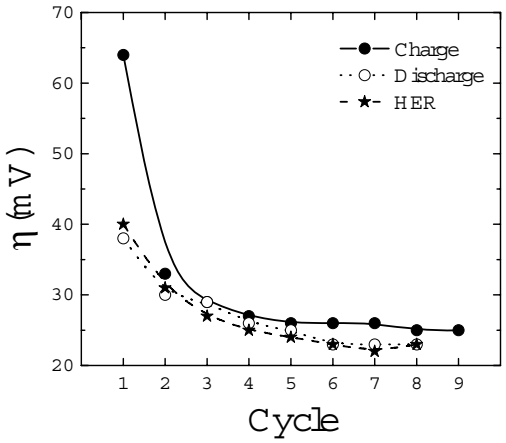

Fig.5.35. Cycling evolution of charge, discharge and HER overpotentials of Mn05A1 electrodes.

It is interesting to compare the evolution of the overpotentials on cycling with that of the electrode capacity. As a matter of fact, the cycling evolution of the electrode capacity results from the competition of two different effects. On one hand, surface activation allows higher H absorption during charge steps, raising the electrode capacity. On the other hand, there are some processes which decrease the electrode capacity, which can arise both from the lowering of the charge/discharge kinetics or from the diminution of the amount of active material for H storage. These two opposite effects give rise to the appearance of a maximum in the electrode capacity upon cycling (see Figs.5.18 and 5.23).

It can be deduced from Fig.5.35 that the activation of the electrode surface takes place mainly during the first charge step, which agrees with the observed evolution of the electrode capacity with cycle number. On the other hand, the observed diminution of the Mn05A1 capacity must not be ascribed to kinetic limitations coming from electrode corrosion processes, because the overpotentials of the charge, discharge and HER reactions do not increase within this region. In fact, the diminution of the electrode capacity must be related to the diminution of

the amount of active material due to the lack of electrical contact among the intermetallic grains as a consequence of the intermetallic pulverization and to the dissolution of the electrode material. This result is further supported by the well-known mechanical and chemical properties of Mn-containing $LaNi_5$ alloys. Mn atoms brittles the alloy. Besides, Mn atoms continuously corrode because its oxides are soluble in KOH as manganite ions. These two effects give rise to the diminution of the electrode cycle life [5.14].

5.4.2.1 Mn05A2 electrodes

Fig.5.36 shows the cycling evolution of charge, discharge and HER/DER overpotentials of Mn05A2 electrodes. As for Mn05A1 electrodes, all the three overpotentials decrease on cycling, for both H_2O and D_2O media. However, higher overpotentials in H_2O electrolytes are observed as compared to Mn05A1 electrodes. This has been ascribed to the lower temperature and the slightly higher electrolytic current density at which charge/discharge cycles have been performed with Mn05A2 electrodes.

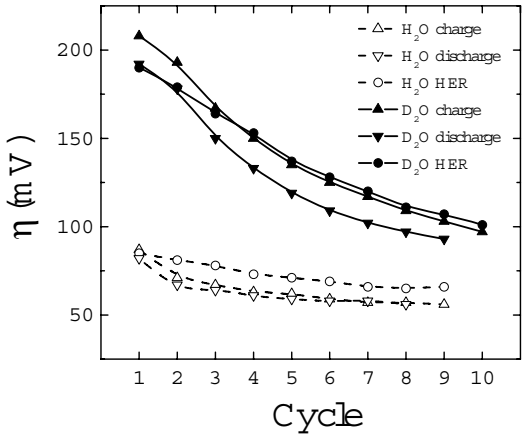

Fig.5.36. Evolution of the overpotential on cycling for charge and discharge reactions and for the HER(DER) in H_2O and D_2O electrolytes with Mn05A2 electrodes.

Again, the decrease of the overpotentials on cycling is mainly attributed to the diminution of the charge transfer overpotential as a result of the activation of the electrode surface. However, the diminution of the overpotentials is not only due to the charge transfer reaction. During the first cycles, the evolution of the charge and discharge overpotentials as a function of the number of cycles and that corresponding to the HER(DER) reaction differ. The diminution of the overpotential is more pronounced for charge and discharge reactions than for the

HER(DER) reaction. This is ascribed to a significant decrease of the near-surface permeation overpotential, η_{ms}. The importance of this permeation transfer on the electrochemical MH formation has been pointed out by other authors [5.44, 45]. According to previous results in mono-substituted $LaNi_5$-type electrodes, the rate of the permeation reaction (equation (5.17a)) decreases by the occurrence of native oxide barriers at the electrode surface [5.46]. The overcoming of these barriers due to the appearance of fresh surfaces on cycling accounts for the diminution of η_{ms} during the activation period.

The occurrence of a permeation-limited mechanism during the activation period is supported by the following observations:

i) The charge efficiency is near 100% for the activated electrodes, but is substantially lower during the activation period. The charge efficiency can be evaluated from the ratio between the discharge and charge capacities. The charge capacity is evaluated from the time elapsed to reach the potential kink that indicates the beginning of the HER(DER) reaction (Fig.5.20).

ii) The rest potentials after charge steps, $E_{MH(D)}{}^{c}$, are not stationary during the activation period (bottom of Fig.5.22). The higher rest potentials observed during the first cycles indicate that the state of charge of the electrodes is lower than that corresponding to a pressure of 1 atm.

iii) The rest potentials after discharge steps, $E_{MH(D)}{}^{d}$ (top of Fig.5.22), during the first cycles are very close to the plateau potentials of the electrochemical isotherms. This indicates that the discharge is not complete during the activation period.

iv) A sudden increase of the discharge overpotential is observed during the first cycles for H_2O-electrolyte (top of Fig.5.21). This rise is attributed to an incomplete and inhomogeneous activation of the electrode. Non-activated grains yield high permeation overpotential. For D_2O-electrolyte (bottom of Fig.5.21), sloping plateaux are observed indicating a smooth increase of the permeation overpotential and a more homogeneous activation process.

According to these results, the low initial electrode capacities (Fig.5.23) have a kinetic origin. Fast permeation of hydrogen atoms through the native oxides allows high hydrogen absorption in the electrode bulk from the first cycle, producing grain pulverisation and creating fresh surfaces. Permeation of deuterium atoms is much more sluggish. This explains the faster activation in H_2O than in D_2O electrolyte. Faster diffusion of H as compared to D atoms through oxide compounds has already been reported [5.47]. The higher ZPE energy for hydrogen causes lower activation energy for its diffusion as compared to deuterium.

Once the blocking effect of the native oxides disappears, H(D) permeation is not rate limiting and the evolution of charge and discharge overpotential parallels that of the HER(DER). This implies that the rate determining step for activated electrodes is the charge transfer reaction (equation (5.16)). The lower overpotential during charge steps than during the HER(DER) in this region can be due to a lower

H(D) surface concentration during β-phase MH(D) formation than during the HER(DER), but also to the appearance of an overpotential associated to the recombinative or electrochemical desorption reactions (Eqs. 5.17b and 5.17c, respectively). On the other hand, the difference between charge and discharge overpotential may be due to a higher H(D) surface concentration during charge steps. In addition, according to the Buttler-Volmer equation, which describes the charge transfer reaction (5.16), a difference between charge and discharge overpotential can be expected. The Buttler-Volmer equation is:

$$i = i_0 \left[e^{-\alpha f \eta} - e^{(1-\alpha) f \eta} \right] \tag{5.22}$$

where i is the electrolytic current density at the overpotential η, i_0 is the equilibrium current density, $f=F/RT$ and α is the transfer coefficient ($0<\alpha<1$) which describes the asymmetry of the potential barrier of reaction 5.16 [5.48]. The first and second terms of the right hand side of equation (5.22) represent the cathodic and anodic currents. During charge steps only the cathodic current is of importance, whereas the opposite is true on discharge. Accordingly, a higher overpotential on charge can arise from a transfer coefficient lower than ½. This would imply the existence of an asymmetric barrier, less sharp in the electrolyte side than in the electrode surface.

Fig.5.36 shows as a general trend that the overpotentials are higher in D_2O than in H_2O electrolytes. This is in good accordance with previous studies on the effect of isotope substitution on the overpotential [5.49, 50]. This also agrees with the results of Luan *et al*. on the electrochemical behaviour of Ti_2Ni in H_2O and D_2O [5.18]. They found that deuteriding was much more difficult than hydriding. Electrochemical a.c. impedance spectra revealed that the reaction resistance was much higher in D_2O than in H_2O. This was attributed to a slower charge transfer reaction in D_2O medium. The charge transfer reaction is so sluggish in the Ti_2Ni/ D_2O system that deuterium charging was not possible. The role of native oxides was not considered by these authors.

Apart from these characteristic behaviours, some transient phenomena can be observed in the evolution of electrode potentials. In the experiments performed with H_2O-electrolytes, the electrode potential during charge steps (Fig.5.20) initially passes over a minimum for the cycles preceding the maximum electrode capacity. Therefore, this minimum is ascribed to surface activation processes occurring in the electrode surface. The evolution of electrode potential during charge steps in D_2O-electrolytes is different and this initial minimum is only observed in the first cycle and appears retarded in the second cycle, whereas electrode capacity continues rising during some cycles. One may conclude that the activation process occurs more slowly in D_2O medium, leading to smaller potential signatures and requiring longer activation cycling.

Finally, isotope effects have been observed in the maximum electrode capacities (Fig.5.23). The maximum Mn05A2 capacities are a ~3-4% higher in H_2O than in D_2O. The same effect has been found on PCI measurements obtained by solid-gas reactions, being higher the reversible capacities for hydrogen than for deuterium (Table 5.2). The difference in H and D solubility can not be due to a difference in the number of atoms trapped after the first activation cycle, since the amount of hydrogen absorbed after this cycle was also ~3% higher than that for deuterium. Therefore, the difference between H and D reversible capacities in Mn05A2 alloys comes from an isotope effect in the solubility limit. Similar results were obtained by Lässer and Klatt, who reported that the β-phase limits of PdH_x, PdD_x and PdT_x obtained by solid-gas reaction decrease when increasing isotope's mass [5.51]. Czerwinski *et al.* found the same isotope effect with thin film Pd electrodes [5.21]. The decrease of solubility limits on increasing the isotope mass might not be, however, a general rule in metal hydrides. As a matter of fact, no isotope effect in the solubility limits is found for $LaNi_{5.4}$ alloy (see Table 5.3).

5.4.2.3 $LaNi_{5.4}$ electrodes

The evolution of the capacity of $LaNi_{5.4}$ electrodes (Fig.5.27) show that cycling at high current densities (90 mA g^{-1}) diminish the electrode capacity while a rise of electrode capacity is observed at lower current densities (20 mA g^{-1}). This could be associated to the fact that MH(D) formation / decomposition during charge / discharge steps at high current densities is limited by the diffusion of H and D atoms through the metal. Accordingly, electrode oxidation during discharge steps at high current densities can occur, decreasing the electrode capacity. When reducing the electrolytic current, the oxidation of electrode surface during discharge steps would be suppressed and electrode capacities would increase with cycling due to surface activation processes.

In addition, it can be observed that the electrode capacity diminution at 90 mA g^{-1} is sharper in H_2O than in D_2O media. A strong isotopic effect is also seen in electrode capacity at 20 mA g^{-1}, being ~50% higher for the hydride than for the deuteride. However, the origin of these effects is not clear and further efforts have to be done to solve these questions.

5.4.3 Isotope effects in PCI curves

It is well known that AB_5-type intermetallic compounds exhibit a logarithmic relation between the hydrogen plateau pressure and the intermetallic cell volume [5.52]. This effect can be qualitatively understood by considering that hydrogen atoms in MH sites behave as particles in a box. Within this model, a decrease of intermetallic cell volume produces a reduction of the volume available for hydrogen and, thus, an increase in ZPE. Fig.5.37 displays the H_2 absorption plateau pressures measured at 298 K for various AB_5-type intermetallic compounds as a

function of intermetallic cell volume. The present results for $LaNi_{5.4}$ and Mn05A2 alloys correlate well with other alloys.

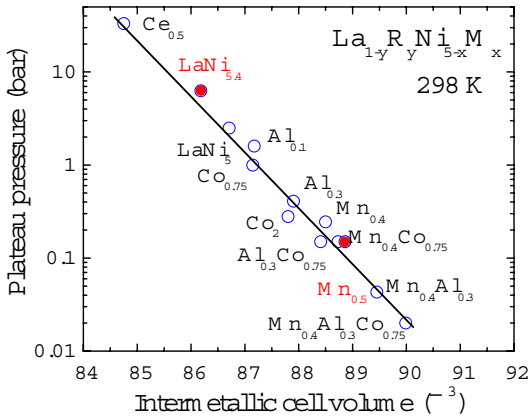

Fig.5.37. Hydrogen absorption plateau pressures of AB_5-type intermetallic compounds as a function of intermetallic cell volume. Red points refer to the present results obtained for $LaNi_{5.4}$ and Mn05A2 alloys. (Kindly provided by Dr. F. Cuevas, CNRS, France).

Within the same theoretical framework, isotope effects in plateau pressures can also be understood. Mn05A2 exhibits the same plateau pressures for H_2 and D_2 gases. This means that ZPE differences of H and D atoms in the solid phase are compensated by those of the gaseous molecules. A reduction of the intermetallic cell volume produces a higher energy gap between ZPE levels of H and D atoms. Accordingly, it is expected that ZPE differences between H and D atoms in $LaNi_{5.4}$ alloy are greater than those of H_2 and D_2 molecules and, therefore, the plateau pressure must be lower for deuterium. In fact, a lower plateau pressure is obtained for the deuteride on desorption (Fig.5.15).

Another interesting isotope effect can be observed in the hysteresis loop between absorption and desorption isotherms for $LaNi_{5.4}$ alloy. Absorption plateau pressures are higher for deuterium than for hydrogen, whereas the opposite behaviour is observed for the desorption isotherms. Therefore, hysteresis is higher for deuterium than for hydrogen. This effect can be helpful to elucidate the origin of the hysteresis. According to the results reported by Joubert *et al.* [5.42], the hysteresis between absorption and desorption plateau pressures in the first activation cycle of $LaNi_5$-type intermetallic compounds is related to the density of dislocations generated during this hydrogen cycle. We believe that the evolution of the X-ray broadening in hydrogenated and deuterated $LaNi_{5.4}$ alloy on cycling can

constitute a unique test to understand the relationship between hysteresis and dislocation formation.

5.5 References

[5.1] Sicking G 1984 *J. Less-Common Met.* **101** 169

[5.2] Wiswall RH and Reilly JJ 1972 *Inorg. Chem.* **11** 1691

[5.3] Wicke E and Brodowsky H, in *"Hydrogen in Metals II",* G. Alefeld and J. Völkl, Editors, Ch. 3, Topics in Applied Physics, vol.29, Springer-Verlag (Berlin, 1978)

[5.4] Lambert I, Percheron-Guégan A and Montel J 1977 *J. Chim. Phys.* **74** 380

[5.5] Andreev BM, Sicking GH and Magomedbekov EP, in *Interaction of Hydrogen Isotopes with transition Metals and Intermetallic Compounds*, Springer Tracts in Modern Physics vol. 132, Springer-Verlag (Berlin, 1996)

[5.6] Cho S-W, Akiba E, Nakamura Y and Enoki H 2000 *J. Alloys Comp.* **297** 253

[5.7] Buchner H, in *Hydrides for Energy Storage,* Proc. Int. Symp. Geilo, Norway, August 1977. A.F. Andresen and A. J. Maeland Eds. Pergamon Press. p. 569

[5.8] Yawny A, Friedlmeier G and Bolcich JC 1989 *Int. J. Hydrogen Energy* **14** 587

[5.9] Nikolić R, Zmbov K and Veljković M 1993 *Int. J. Hydrogen Energy* **18** 743

[5.10] Sandrock G, Suda S and Schalpbach L in *Hydrogen in Intermetallic Compounds II* Topics in Applied Physics vol.67, Schalpbach L (ed.), Springer-Verlag (Berlin, 1992) Ch.5

[5.11] Eyring H 1933 *Proc. Nat. Acad. Sci.* **19** 78

[5.12] Topley B and Eyring H 1934 *J. Chem. Phys.* **2** 217

[5.13] Völkl J and Alefeld G, in *"Hydrogen in Metals I",* G. Alefeld and J. Völkl, Editors, Ch. 12, Topics in Applied Physics vol.28, Springer-Verlag (Berlin, 1978)

[5.14] Sakai T, Matsouka M and Iwakura C, in *Handbook on the Physics and Chemistry of Rare Earths* vol. 21, pp133-178, K.A. Geschneider, Jr Eyring and L. Eyring, Editors, Elsevier (1995)

[5.15] Cuevas F, Joubert JM, Latroche M and Percheron-Guégan A 2001 *Appl. Phys. A,* **72** 225

[5.16] Kleperis J, Wójcik G, Czerwinski A, Skowronski J, Kopczyk M and Beltowska-Brzezinska M 2001 *J. Solid State Electrochem.* **5** 229

[5.17] Latroche M, Chabre Y, Decamps B, Percheron-Guegan A and Noreus D 2002 *J. of Alloys and Comp.* **334** 267

[5.18] Luan B, Kennedy SJ, Liu HK and Dou SX 1998 *J. Alloys Comp.* **267** 224

[5.19] Flanagan TB and Lewis FA 1959 *Trans. Farad. Soc.* **55** 1409

[5.20] Flanagan TB 1961 *J. Phys. Chem.* **65** 280

[5.21] Czerwinski A, Marassi R and Zamponi S 1991 *J. Electroanal. Chem.* **316** 211

[5.22] Rodríguez Carvajal J 1993 *Physica B* **192** 55

[5.23] Wang CS, Wang XH, Lei YQ, Chen CP and Wang QD 1997 *Int. J. Hydrogen Energy* **22** 1117
[5.24] Balej J 1985 *Int. J. Hydrogen Energy* **10** 365
[5.25] *CRC Handbook of Chemistry and Physics*, 69th Edition 1988-89, R.C. Weast, M.J. Astle and W. H. Breyer Editors, CRC Press Inc, Boca Raton, Florida, D-245
[5.26] Wakao S and Yonemura Y 1983 *J. Less-Common Metals* **89** 481
[5.27] Cuevas F, Mirad A and Percheron-Guégan A 2004 *J. Materials Science* **39** 5263
[5.28] Ratnakumar BV, Witham C, Bowman RC, Hightower JrA and Fultz B 1996 *J. Electrochem. Soc.* **143** 2578
[5.29] Niessen RAH, Vermeulen P and Notten PHL 2006 *Electrochimica Acta* **51** 2427
[5.30] Geng M, Han J, Feng F and Northwood DO 1999 *J. Electrochem. Soc.* **146** 2371
[5.31] Notten PHL, Ouwerkerk M, van Hal H, Beelen D, Keur W, Zhou J and Feil H 2004 *J. Power Sources* **129** 45
[5.32] Iwakura C, Oura T, Inoue H, Matsuoka M and Yamamoto Y 1995 *J. Electroanal. Chem.* **398** 37
[5.33] Wang C, Marrero-Rivera M, Serafín MA, Baricuatro JH, Soriaga MP and Srinivasan S 2006 *Int. J. Hydrogen Energy* **31** 603
[5.34] *CRC Handbook of Chemistry and Physics* 2002-2003 (83rd edition), ed DR Lide (CRC Press)
[5.35] Farkas A 1937 *Trans. Farad. Soc.* **33** 552
[5.36] Noonan E and La Mer VK 1939 *J. Phys. Chem.* **43** 247
[5.37] Wu YC, Koch WF and Marinenko G 1986 *J. Solution Chem.* **15** 675
[5.38] McIntyre JDE and Salomon M 1968 *J. Phys. Chem.* **72** 2431
[5.39] Baker WN and La Mer VK 1935 *J. Chem. Phys.* **3** 406
[5.40] Weingärtner H and Chatzidimitrou-Dreismann CA 1990 *Nature* **346** 548
[5.41] Sperling J, Tributsch H, Streffer RMF, Abdul-Redah T and Chatzidimitrou-Dreismann CA 1999 *J. Electroanal. Chem.* **477** 62
[5.42] Joubert JM, Latroche M, Cêrny R, Percheron-Guégan A and Yvon K 2002 *J. Alloys Comp.* **330-332** 208
[5.43] Maurel F, Knosp B and Backhaus-Ricoult M 2000 *J. Electrochem. Soc.* **147** 78
[5.44] Yang QM, Ciureanu M, Ryan DH and Ström-Olsen JO 1994 *J. Electrochem. Soc.* **141** 2108
[5.45] Conway BE and Jerkiewicz G 1993 *J. Electroanal. Chem.* **357** 47
[5.46] Baddour-Hadjean R, Mathlouthi H, Pereira-Ramos JP, Lamloumi J, Latroche M and Percheron-Guégan A 2003 *J. Alloys Comp.* **356-357** 750
[5.47] Soda K, Iizuka E, Tsuchiya B, Morita K and Iwahara H 2002 *J. of Nuclear Science and Technology* **39** 359

[5.48] Bard AJ and Faulkner LR, *Electrochemical Methods. Fundamentals and Applications* (New York: John Wiley & Sons, 1980)
[5.49] Bowden FP and Kenyon HF 1935 *Nature* **135** 105
[5.50] Conway BE 1960 *Proc. Roy. Soc. (London) A* **256** 128
[5.51] Lässer R and Klatt K-H 1983 *Phys. Rev. B* **28** 748
[5.52] Percheron-Guégan A, in *'Hydrogen in Intermetallic Compounds I'* L. Schlapbach, Editor, Ch. 2, Topics in Applied Physics vol.63, Springer-Verlag (Berlin, 1988)

Realizaciones

1. Se ha realizado la caracterización experimental de una instalación de análisis de gases compuesta por un sistema de colección de gases, una cámara de vacío y un espectrómetro de masas (Balzers QMS 200). Se ha investigado la contribución de los diferentes iones moleculares a los distintos picos del espectro de masas, la influencia de los parámetros de funcionamiento del sistema en el resultado de las medidas experimentales y la estabilidad temporal del sistema. Además, se han obtenido las sensibilidades de detección de H_2, HD, D_2, H_2O, O_2 y Ar.

2. Se ha realizado una revisión completa de las investigaciones relativas al factor separación electroquímico (*S*) de H y D desde su descubrimiento hasta nuestros días. Se han expuesto las distintas teorías existentes relativas a este fenómeno, así como los métodos experimentales que se han desarrollado para investigarlo. Por otro lado, se ha realizado una extensa recopilación de las medidas de *S* en los metales de transición.

3. Se ha utilizado la técnica de Espectrometría de Masas acoplada a una celda electroquímica con objeto de analizar de forma cuantitativa los flujos de H_2/HD/D_2 liberados durante la electrolisis de mezclas H_2O/D_2O usando cátodos de Pt policristalino. Se ha investigado la evolución temporal del factor de separación y su dependencia con la corriente electrolítica aplicada y la composición isotópica de los electrolitos. Por otro lado, se ha explorado la posibilidad de usar esta técnica experimental para investigar otros fenómenos, como la cinética de adsorción/absorción de H/D en cátodos metálicos y la oxidación electroquímica de metales.

4. Se han preparado y caracterizado muestras de hidruro-deuteruro de Pd y se ha investigado, por primera vez, el efecto isotópico en la cinética de descomposición de este hidruro, mediante Espectroscopia de Desorción Térmica. Se ha propuesto un nuevo método experimental, basado en el análisis de la concentración relativa de los tres isótopos moleculares, H_2, HD y D_2, que permite obtener información muy relevante acerca del proceso de recombinación superficial de H y D.

5. Se han preparado electrodos de tipo MH a partir de aleaciones de $LaNi_{4.5}Mn_{0.5}$ y $LaNi_{5.4}$. Se ha investigado el efecto isotópico H/D en la cinética de carga y descarga de los electrodos y se ha comparado su estabilidad termodinámica en H_2O y D_2O.

Conclusiones

1. El sistema de análisis de gases es capaz de detectar flujos en el rango de los nano-moles por segundo. La estabilidad de este sistema es razonablemente buena: la variación de la sensibilidad de detección es típicamente menor del 1 % en periodos de un día y del orden del 10 % en un periodo de varios meses. Las sensibilidades relativas de detección son más estables: sus variaciones son del orden del 2 % en un periodo de varios meses.

2. La sensibilidad de detección del sistema de análisis de gases ($\sigma_{m/q}^{\chi}$) depende de la sección eficaz de ionización por impacto electrónico (φ^{χ}) y de la masa (m) de las especies gaseosas de acuerdo con la ecuación:

$$\sigma_{m/q}^{\chi} = G\frac{\varphi^{\chi}}{m^{3/2}}$$

siendo G una constante que depende de los valores de los parámetros de funcionamiento del sistema experimental. La dependencia de $\sigma_{m/q}^{\chi}$ con la masa se debe a los distintos efectos de discriminación de masas presentes en el proceso de colección de gases y en el filtrado de iones.

3. Se ha encontrado una clara correlación entre el valor del factor de separación electroquímico de H y D y la actividad electrocatalítica de los metales de transición, que viene a confirmar los resultados observados en otros metales y compuestos intermetálicos. Esta correlación se explica en base al grado de corrugación de la superficie de energía potencial durante la Reacción de Evolución de Hidrógeno.

4. Se observa una evolución temporal del factor de separación electroquímico del Pt en medio básico, que aumenta desde ~1.8 hasta un valor estacionario entorno a 6.3. Este fenómeno se explica considerando la dependencia de S con el grado de recubrimiento de H/D en la superficie del Pt. Por otro lado, el valor estacionario de S no depende de la densidad de corriente electrolítica ni de la composición isotópica de los electrolitos.

5. La relación entre los flujos de H_2, HD y D_2 desorbidos de las muestras de PdH_xD_y ($K=F_{HD}^2/F_{H2}F_{D2}$) no coincide con la correspondiente a la equipartición estadística de los átomos de H y D en los tres isotopólogos moleculares (K=4), ni tampoco con la concentración de equilibrio de la reacción de intercambio isotópico $H_2+D_2 \Leftrightarrow 2HD$ ($K=K_{eq}$), tal como se asume habitualmente. Por el contrario, se ha encontrado que esta relación está determinada por la diferencia

entre los niveles de energía de los complejos activados (CA) de las reacciones de recombinación superficial H-H, H-D y D-D. Debido a lo anterior, se ha propuesto un nuevo método que permite obtener información muy relevante acerca de la cinética de recombinación superficial a partir del análisis de la relación entre los flujos de los tres isótopos moleculares.

6. A partir del análisis de los espectros de desorción térmica de las muestras de PdH_xD_y se han podido obtener los mecanismos y los parámetros cinéticos del proceso de desorción de H_2, HD y D_2.

Durante la desorción desde la fase β-PdH_xD_y, la cinética del proceso está determinada por la reacción de recombinación de los átomos en la superficie. Las energías de activación muestran un efecto isotópico inverso. Los valores medios de éstas son iguales a 0.94(6), 0.85(4) y 0.83(4) eV $molec^{-1}$ para H_2, HD y D_2, respectivamente.

Durante la zona de coexistencia de fases, el proceso está controlado por la cinética de transformación de fase β en fase α. Nuevamente, se observa un efecto isotópico inverso. Las energías de activación medias para H y D son 0.55(2) y 0.52(1) eV $atomo^{-1}$, respectivamente.

Por último, la reacción de recombinación superficial vuelve a ser limitante a partir de una determinada temperatura, lo que parece estar asociado a un cambio en las propiedades catalíticas de la superficie. Se ha encontrado un aumento considerable de las energías de activación en esta zona (aproximadamente un factor 5). Los valores medios de las energías de activación para H_2, HD y D_2 son 3.9(4), 3.7(1) y 4.1(3) eV $molec^{-1}$, respectivamente.

7. Existe un efecto isotópico anómalo en los niveles de energía del CA de la reacción de recombinación superficial en las muestras de PdH_xD_y. Se observa que el nivel de energía del CA de la recombinación H-D se encuentra por debajo del valor medio entre los niveles de los CA de H-H y D-D, lo cual contrasta con las predicciones de las consideraciones cuánticas más elementales. Esta anomalía se ha relacionado con el carácter heteronuclear de la molécula de HD, que presenta propiedades de simetría cualitativamente diferentes a las de los isotopólogos homonucleares.

8. Existen diferencias sustanciales en el comportamiento electroquímico de $LaNi_{4.5}Mn_{0.5}$ en H_2O y D_2O.

En lo relativo a la termodinámica, se ha encontrado un efecto isotópico muy notable en los potenciales de las isotermas de desorción. Este efecto isotópico, sin embargo, no se ha observado mediante reacción sólido-gas. Se ha propuesto un método empírico que permite convertir los potenciales de electrodo en la escala de los electrodos reversibles de hidrógeno y de deuterio.

Este método se basa en la hipótesis de que los potenciales de equilibrio de los electrodos completamente cargados corresponden a una presión equivalente de $H_2(D_2)$ igual a 1 atm. Usando esta escala de potenciales y la ecuación de Nernst, se han calculado las presiones de H_2 y D_2 equivalentes, obteniéndose un buen acuerdo con las obtenidas mediante reacción sólido-gas.

También se ha encontrado un efecto isotópico muy notable en la cinética de carga/descarga de los electrodos, principalmente durante el periodo de activación. El periodo de activación es mucho más largo en D_2O que en H_2O. Este efecto parece estar relacionado con la cinética de difusión de los átomos de H(D) a través de la capa de óxido superficial, siendo ésta mayor para H que para D. El ciclado electroquímico produce superficies limpias, de modo que el efecto de la barrera de óxido superficial va desapareciendo gradualmente.